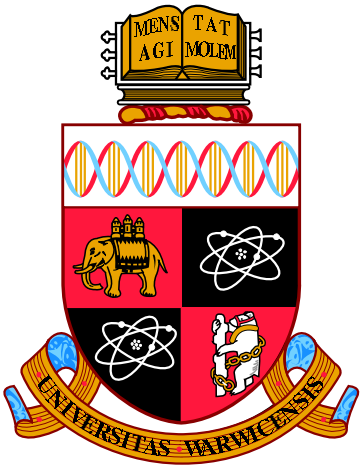

Thermodynamics of Ice Interfaces and Structures within a Coarse-grained Model of Water

by

Michael Ambler

Thesis

Submitted to the University of Warwick

for the degree of

Doctor of Philosophy

Department of Physics

September 2016

THE UNIVERSITY OF WARWICK

Contents

List of Tables

List of Figures

Acknowledgements

First and foremost, I would like to thank my supervisor, Dr David Quigley, for all his advice and guidance over the last four years. Without his support, I would most likely not have begun this work, let alone finished. I would also like to extend my thanks to Prof. Mike Allen, who encouraged me throughout the first several months of this project, and to both Prof. George Rowlands and Dr Bart Vorselaars, who graciously provided help when needed.

I would also like to personally thank the many people I've met during my time at Warwick. It's true that the people make the place, which in turn shapes you. I am extremely grateful for all the experiences I have had during this project; it has been richly rewarding.

To my office mates over the years, I would particularly like to thank Dr Anja Humpert, Dr Gil Rutter, Dr Sally Bridgwater and Dr Sam Brown, who each provided the moral support that only fellow Ph.D. students can; and in one case, a much needed change of perspective.

I would like to thank all of WUSAC for giving me some amazing experiences from around the world. The time I shared with you all allowed me to return to my work refreshed and ready. I would especially like to thank Francesca Parker, Andy Loo, Eleanor Kelly, James Christen, Dr Francesco Fermani, Emma Orton and Heather Barnes; you made WUSAC what it was for me.

To my housemates over the years, particularly Kateryna Taylor, Cyril Chimisov, Adam Griffin and Ting Chen, I thank you for being there and making my house feel like a home.

Sahattaya "Pai" Choochatpong: Thank you for some great times, some great

advice and some great food! You made things just a little bit easier.

Joe and Sam Rearden: I've never met two people who are more affirmative and optimistic. You are both a real inspiration for my determination to keep going.

I would also like to thank many friends from before Warwick, for all their support in one way or another; especially Dr Jonathan Watkins, who has always been an inspiration.

To Eleanor O'Shea, I am truly thankful for the stability you have provided me with and the clarity of mind I needed to get this work completed.

Last but not least, to my family – Nick, Jacqui and Kerri – who have always supported me in any way they can. Thank you for everything you have done for me.

Declarations

This thesis is submitted to the University of Warwick in support of my application for the degree of Doctor of Philosophy. It has been composed by myself and has not been submitted in any previous application for any degree.

The work presented (including data generated and data analysis) was carried out by the author except in the cases outlined below:

- Measurements of the bulk free energy difference between ice-Ih and ice-0, reported in chapter 6, were conducted using lattice switching Monte Carlo and were performed and supplied by Dr David Quigley.

Abstract

This research applies the capillary wave method (CWM) to quasi-2D systems in order to calculate the solid-liquid coexistence interfacial free energy (γ) of ice-Ic, ice-Ih and ice-0, with water, at 1 atm, within molecular dynamics simulations employing the coarse-grained monatomic water (mW) model. Investigations are performed to determine how the measured interfacial stiffness ($\tilde{\gamma}$) is affected using various: i) order parameters, to distinguish between the solid and the liquid; ii) analysis discretisation, for interface profiling; iii) system thicknesses.

The values of γ for the different crystal planes (γ_{plane}) shows that for ice-Ih $\gamma_{\text{basal}} < \gamma_{\text{prism}} \lesssim \gamma_{11\bar{2}0}$, for ice-Ic $\gamma_{111} \lesssim \gamma_{112} \lesssim \gamma_{110} < \gamma_{100}$ and for ice-0 $\gamma_{001} < \gamma_{102} \lesssim \gamma_{110} \lesssim \gamma_{101} \lesssim \gamma_{100}$. It is also found that between ice-Ic and ice-Ih, $\gamma_{110} \approx \gamma_{11\bar{2}0}$ and $\gamma_{\text{basal}} \approx \gamma_{111}$ to 0.3 mJ m^{-2} outside of errors. All structures are weakly anisotropic in γ compared to their $\tilde{\gamma}$, with ice-Ic, ice-Ih and ice-0 having ranges of 1.5(4), 2.5(5) and 3.9(7) mJ m^{-2}, respectively, between their measured planes. The isotropic component of γ for the different structures ($\gamma_{0_{\text{Structure}}}$) shows $\gamma_{0_{\text{Ice-0}}} = 33.8(4)$, $\gamma_{0_{\text{Ice-Ih}}} = 36.0(3)$ and $\gamma_{0_{\text{Ice-Ic}}} = 36.3(3)$ mJ m^{-2}.

The rationality that ice-I nucleation can be catalysed at strong supercooling within a shell of ice-0 is explored. It is found that at 215.2 K such nucleation could occur, forming an ice-0 shell of 3.3 Å thick around a core of ice-Ih.

Free energy perturbation is also applied to the mW model using Monte Carlo simulations, in an attempt to increase the Gibbs free energy gap between ice-Ic and ice-Ih to more closely match values previously reported from experiments and ab initio calculations. However, the Gibbs free energy gap is only increased to 5.6 J mol^{-1}, at 240 K, before the ice-Ic and ice-Ih melting temperatures fall to below 240 K; failing to reach the expected value. This suggests that the mW model, despite its successes, does not capture the true mechanism behind the formation ice-Ic and ice-Ih stacking faults at all degrees of supercooling; the formation of which is rather an artefact of the model itself.

Chapter 1

Introduction

1.1 Motivation

Calculating the interfacial free energy between a crystal and its melt is necessary to properly understand the behaviour of crystal nucleation. On a microscopic scale, the magnitude of the interfacial free energy strongly controls the growth rate, while the anisotropy determines the dendritic growth and morphology of the crystal[1]. Knowledge of the anisotropy is particularly important for being able to reliably perform nucleation calculations which often assume a spherical symmetry of the interfacial free energy. Hence, if there is significant anisotropy present, such calculations are invalid[2].

Practically, being able to control the dendritic growth grants control over the formation of crystal microstructures, which appear as a crystal solidifies[3]. This can be used in metallurgy to create stronger alloys and metals, where, for example, the material sheer stress is inversely correlated to the size of grains within the material[4]. Interfacial free energy calculations are also important in studying ice nucleation in clouds, determining whether nucleation begins within or on the surface of such water droplets, and the subsequent effect this has on crystallisation rates in the presence of other aerosols in the atmosphere[5, 6]. This has direct implications on constructing more accurate climate models, since the radiative properties of cirrus clouds are dependent on the morphology, concentration, distribution and growth rates of the ice crystals within them[7, 8].

The importance of ice nucleation is not restricted to inorganic systems. Organisms exist in supercooled environments that have developed abilities to inhibit complete freezing of themselves, avoiding damage to their cells[9]. Research has shown that whether systems are organic or inorganic, nucleation is also dependent

on the type of ice nuclei precursor[10]. Hence, by knowing the value for the interfacial and bulk free energy of different ice structures, the preferential structure for nucleation can be determined at a specific temperature and pressure. This is useful in the development of solvents to stop these preferential ice nuclei from forming, which is applicable to: cryogenic storage of tissues, to stop ice from destroying cells; and antifreeze agents, to stop ice build up on aircraft wings[11].

However, in general, experimental measurement of the anisotropy of the interfacial free energy is difficult in systems with weak anisotropy[12]. Experiments that rely on measuring the interfacial free energy from classical nucleation theory, yield only averaged interfacial dependence and are typically 10-20% lower in their estimates than reality, while experiments that rely on contact angles do not usually have the precision to resolve the anisotropy[1]. Indeed, there are only a few exceptions where the anisotropy of the free energy has been directly measured, limited to transparent organic systems[13]. Of these, only one experiment has managed to measure the anisotropy in ice via measuring contact angles of water in an ice-I matrix at atmospheric pressure, which revealed the (basal) plane to have a much lower degree of anisotropy than that of the edge planes[14]. Such experimental difficulties and low sensitivity to the anisotropy, provides the necessity to turn to computational methods to more accurately measure the interfacial free energy and its anisotropy.

In order to use computational methods effectively, it is of crucial importance that the model potentials used, accurately reproduce experimentally observed results. Models that yield results to the contrary, cannot be used to make accurate conclusions about the nature of reality. Sufficient effort should therefore be given to developing more accurate models, and to establishing the limitations of such models, to avoid making false claims about reality.

1.1.1 Ice-I

As discussed above, ice nucleation has relevance to the integrity of many kinds of systems, from climate models to mitigating cell damage. The ice being referred to in these terrestrial systems is ice-I. However, there are at least 15 crystalline phases of ice – excluding amorphous phases – currently known, that make up the rich phase diagram of water[15]. This research is concerned with the formation of ice at atmospheric pressure at coexistence with liquid, and so only ice-I need be considered out of the existing 15 phases. Yet, ice-I itself is a richly complicated phase of ice, which may exist as one of two polytypes: hexagonal ice-I (ice-Ih) and cubic ice-I (ice-Ic)[15].

Ice-I is the common crystalline phase of ice that exists on Earth, at atmo-

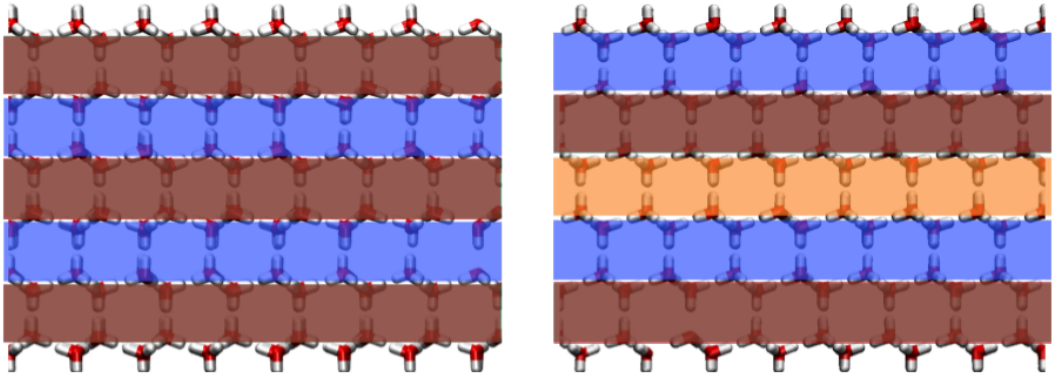

Figure 1.1: ABABAB stacking layers for ice-Ih (*left*) and ABCABC stacking layers for ice-Ic (*right*). The normal of both the ice-Ih (basal) and ice-Ic (111) plane, is parallel to the length of the page.

spheric pressure from 73 K to 273.15 K[15]. The stable form of ice-I is ice-Ih, which is observed experimentally in a pure state at temperatures $T > 263$ K[16]. At lower temperatures, nucleation of ice-I has been observed to form metastable ice-Ic precursor nuclei to that of ice-Ih[16]. The difference between these two polytypes is that of the stacking order in only one direction of the crystal structure. Ice-Ih follows a repeating ABABAB stacking pattern in the direction of the normal of the (basal) plane, while ice-Ic follows an ABCABC stacking pattern in the direction of the normal of the (111) plane, as shown in figure 1.1; additionally, diagrams of the crystal cells are found in chapter 5.

Unlike ice-Ih, pure ice-Ic has never actually been observed experimentally. Instead, there is increasing evidence from neutron diffraction patterns to suggest that metastable ice-Ic is actually stacking disordered ice-I (ice-Isd), consisting of random arrangements of cubic and hexagonal ice-I planes[16]. It also transpires that the quantity of ice-Ic present in ice-Isd is temperature dependent, with increasing cubicity with decreasing temperature to approximately 50% cubicity[15, 16]. This is discussed in much greater detail in chapter 7, but it is worth noting that given ice-Isd – rather than pure ice-Ic – may actually nucleate as a precursor to pure ice-Ih, means that calculated and reported differences between the free energies of ice-Ih and pure ice-Ic, are extrema, rather than reflecting actual experimental conditions.

1.1.2 Ice-0

Similar to how ice-Ic is a metastable state of ice-I, that forms as a precursor to ice-Ih, ice-0 is a theoretical metastable phase of ice that can act as a precursor to the formation of ice-I; as predicted by Russo et al.[17]. At atmospheric pressure,

ice-0 is predicted to form at $T \leq 245$ K; as researched in chapter 6. Under such conditions, ice-0 has a structure that is more similar to that of the liquid than that of ice-Ic or ice-Ih, consisting of tetragonal ordering[17]. Such microscopic similarity to the liquid structure results in a comparatively lower interfacial free energy barrier with that of water, than that of an ice-Ic and water or ice-Ih and water; making homogeneous nucleation of ice-0 favourable. The formation of ice-0 nuclei therefore act as nucleation points for catalysing heterogeneous nucleation of more stable ice-I nuclei, which have similar interfacial free energies with that of ice-0 than with that of the liquid, as predicted by Ostwald's step rule[18]. This is discussed in greater detail in chapters 3 and 6. The unit cell for ice-0 can also be found in chapter 5.

Calculating the solid-liquid interfacial free energies of ice-I and ice-0 crystal systems can help answer questions about how ice nucleates at atmospheric pressures and whether ice-0 has a role in the formation of ice-I[17, 19]. If ice-0 does indeed have an influence in nucleation, this could have wider consequences – as previously mentioned – on accounting for changes in the radiative properties of ice crystals forming in clouds, impacting climate models, or motivating the development of more sophisticated antifreeze agents for operation in extreme environments.

1.2 This Research

This work focuses on the use of the capillary wave method (CWM), to calculate the interfacial free energy of ice-Ic, ice-Ih and ice-0 in contact with water at atmospheric pressure, using the coarse-grained monatomic water (mW) model established by Molinero and Moore[20], through the use of molecular dynamics (MD) simulations. While there are several computational methods that exist to calculate the interfacial free energy and its anisotropy, each method has its own advantages and disadvantages. A review of such methods is conducted in chapter 3, along with a discussion regarding nucleation theory and the nucleation of the ice structures studied in this research.

Before a review of nucleation and free energy methods, the theoretical background for numerical simulations, practicalities and statistical physics are first discussed in detail in chapter 2; upon which this work is heavily dependent. Chapter 2 also reviews the model potentials used in this research. Following, chapters 2 and 3, this thesis begins to describe the research conducted in earnest.

Chapter 4 opens with a detailed discussion of capillary wave theory and how to carefully analyse the interface of solid-liquid coexistence simulations. Basic validation of the CWM is performed by comparing calculated interfacial stiffness

results against those in the literature for the same planar interface orientations of a simple face centred cubic lattice interacting in a Lennard-Jones type potential.

Chapter 5 then discusses how to distinguish between solid-like and liquid-like particles in ice, the choice of interface analysis parameters and how to use spherical harmonics to describe the form of the interfacial free energy. The methods developed in chapters 4 and 5 are then applied to various ice-Ic, ice-Ih and ice-0 systems to calculate the interfacial free energy; the results of which are presented and discussed in chapter 6.

Finally, chapter 7 examines a deficiency of the mW model to correctly reproduce the relative stabilities of ice-Ic and ice-Ih. Thermodynamic perturbation theory is applied to the model in an attempt to alter the Gibbs free energy gap between the two polytypes, to match recent ab initio calculations[21]. The parameters of the mW model are modified via this procedure using a gradient descent approach. The findings of this thesis are then concluded in chapter 8.

Chapter 2

Theoretical Background

2.1 Introduction

The main research conducted in this thesis relies heavily on concepts from statistical physics and scientific computing, aspects of which are discussed here. This chapter begins with a review of ensembles in the context of statistical physics. Following, is a discussion of the principles of molecular dynamics, along with the use of barostating and thermostating, and also performing Monte Carlo simulations. The chapter then covers the practicalities involved with molecular dynamics simulations, before finally covering the model potentials used in the work.

2.2 Ensembles

For a thermodynamic system of N particles, macroscopic quantities such as energy, temperature and pressure, are observed. Such a system evolves classically according to Hamilton's equations of motion and in statistical physics, these macroscopic quantities can be related to the microscopic quantities of position and momentum of each particle in the system. This follows from the Virial theorem[22]

$$\left\langle x_i \frac{\partial \mathcal{H}}{\partial x_j} \right\rangle = k_{\mathrm{B}} T \delta_{ij} \,, \tag{2.1}$$

where x_i is a particle's position or momentum. For example, the temperature of the system can be given by the average kinetic energy of all the particles at that point in time,

$$\left\langle \frac{p_i^2}{2m} \right\rangle = \frac{\nu}{2} k_{\mathrm{B}} T \,, \tag{2.2}$$

where ν is the number of degrees of freedom per particle and p_i is the i^{th} particle's momentum. Therefore, if the "microstate", which is the complete microscopic description of all particles' position and momenta at time t, can be calculated, then it is also possible to calculate all macroscopic quantities of the system at t. The set of macroscopic observables that a system has is called the "macrostate" and there may be many unique individual microstates that describe a single macrostate. Furthermore, there may be many systems, each in a unique microstate, that when evolved in time yield unique trajectories from one microstate to the next, but where the average of one trajectory is equivalent to that the other systems' and all still yield the same macrostate. The collection of such systems is called an "ensemble"[22].

The ensemble exists in a domain known as "phase space". The phase space is a $2dN$ dimensional space – where d is the dimensionality of a system in real space – which describes all the possible microstates that a system of N particles can access. The dimensionality of the phase space is such, due to N particles having d dimensional descriptions of position and momentum. This results in each microstate being described by a unique phase space coordinate: $\mathbf{x} = \{\mathbf{r}_1, ..., \mathbf{r}_N, \mathbf{p}_1, ..., \mathbf{p}_N\}$. However, if a system is described by some ensemble, then the system must have a well defined macrostate. This restricts the accessible microstates of a system's trajectory to within a bound hypervolume of the phase space. Since on average a trajectory will produce the defined macrostate, the microstates are accessible according to the ensemble probability distribution. For example, a finite number of equally accessible microstates exist on a constant energy hypersurface, but this is only true for systems described exactly by Hamilton's equations of motion, since these are energy preserving[22]; see section 2.2.1.

The description of an ensemble implies that it is not necessary to calculate the exact equations of motion for every particle in the system at every instant in time in order to observe the macroscopic properties of the system. Instead, with access to the entire ensemble describing the macrostate of interest, the observables can be recovered from averaging the microscopic description of the observable over the ensemble by the number of microstates that describes the ensemble. Mathematically, this is

$$A = \frac{1}{Z} \int d\mathbf{x} a(\mathbf{x}) F(\mathcal{H}(\mathbf{x})) \,, \tag{2.3}$$

where $a(\mathbf{x})$ is the function giving the microscopic description of the observable A, $F(\mathcal{H}(\mathbf{x}))$ is a function of the Hamiltonian describing the ensemble and Z is known as the partition function of microstates.

Calculation of equation (2.3) is not typically possible analytically. Instead, numerical techniques are required such as molecular dynamics (MD), which is discussed further in section 2.3. Using a technique such as MD, allows the system to evolve from a single microstate and explore the ensemble phase space hypervolume. For equilibrium systems, given infinite time the system will visit each microstate within the hypervolume, which assumes the system is "ergodic". Recording the full evolution of the system over time allows the full recovery of the ensemble, and thus measurement of the necessary macroscopic observable. Hence, to measure any observable, the relevant partition function, Hamiltonian and Virial must be known. The Hamiltonian for each of the ensembles depends upon the type of thermostat or barostat being used in the simulation. As such, these Hamiltonians are discussed in section 2.4.

Ergodicity is an important requirement of the evolution of an ensemble if correct sampling via MD is to be obtained. If a system is not ergodic, then it is not possible to positively state that the MD simulation is sampling the correct ensemble. For a system to be considered ergodic requires: sampling be done at time intervals longer than the longest correlations; the integration scheme to be phase space area preserving, i.e. "symplectic"; and the simulation duration to be long enough that it reproduces the ensemble probability density function[23]. Ergodic processes are time reversible and therefore allow ensemble averaging to be done at any time once the phase space has been thoroughly explored.

There are many ensembles that MD simulations can be used to recover. A brief description of each of the ensembles used throughout this research, follows.

2.2.1 Microcanonical (NVE)

Simulating an isolated system for a constant number of particles, N, over a constant volume, V, and energy, E, generates the microcanonical ensemble. This ensemble follows Hamilton's equations of motion exactly and therefore the Hamiltonian that describes such a system is just[22] $\mathcal{H}(\mathbf{x}) = E$. The partition function for the microcanonical ensemble is therefore[22]

$$\Omega(N, V, E) = \frac{E_0}{N! h^{3N}} \int d\mathbf{x} \delta(\mathcal{H}(\mathbf{x}) - E)\,, \tag{2.4}$$

where E is the fixed total energy of the system, E_0 is a small energy shell above the constant energy hypersurface and h is Planck's constant. The constants E_0 and h arise from the uncertainty in being able to determine the actual energy, position and momentum no better than some small deviation ΔE, Δx and Δp, respec-

tively. It should be further observed that the uncertainty of the phase space vector $\Delta\mathbf{x} \equiv (\Delta x)^{3N}(\Delta p)^{3N} = h^{3N}$, from Heisenberg's uncertainty principle. The factor $N!$, compensates for overcounting, since classically the particles are distinguishable. Since the energy is fixed, this has the effect of fixing the phase space hypersurface and so a simulation can only explore the states within this ensemble with equal probability.

2.2.2 Canonical (NVT)

The microcanonical ensemble generates conditions that are not representative of actual experimental conditions. In reality, the total energy is not fixed but rather other thermodynamic quantities. The canonical ensemble is an example of a such a system, which fixes the number of particles N, the volume of the system V, and fixes the temperature of the system T, to an infinite heat bath. Given that such a system is in contact with a heat bath, the energy can fluctuate as to maintain a fixed temperature. This means the Hamiltonian of the system is not conserved. Instead, the system exists on a constant "Helmholtz free energy" hypersurface; $F = E - TS$.

The partition function that describes such an ensemble is

$$Q(N, V, T) = \frac{1}{N! h^{3N}} \int d\mathbf{x} \exp[-\beta \mathcal{H}(\mathbf{x})] \,, \tag{2.5}$$

where the Hamiltonian follows a Boltzmann distribution.

Normally, experiments are carried out under constant pressure rather than constant volume. An alternative ensemble is the isobaric-isothermal ensemble, discussed in section 2.2.4. However, in the limit of large enough systems, the canonical ensemble actually approximates to the isobaric-isothermal ensemble.

2.2.3 Isobaric-Isoenthalpic (NPH)

Instead of fixing the temperature of the system, it is instead possible to fix the pressure of the system. This leads to the development of an ensemble with constant particles N, pressure P and, by extension, enthalpy $H = E + PV$. Coupling the system to an external piston, allows the volume to fluctuate so that the average internal pressure is fixed. This generates the isobaric-isoenthalpic, or NPH, ensemble and the system evolves under Hamilton's equations across a constant enthalpy hypersurface.

The NPH ensemble is the isobaric equivalent of the microcanonical ensemble

with the partition function

$$\Gamma(N,P,H) = \frac{H_0}{V_0 N! h^{3N}} \int_0^\infty dV \int d\mathbf{x} \delta(\mathcal{H}(\mathbf{x}) + PV - H)\,. \tag{2.6}$$

The partition function is now also dependent on the volume, as the position of each particle is dependent on the number of positions available to it within the volume of the system.

2.2.4 Isobaric-Isothermal (NPT)

Experiments normally report macroscopic observables for systems of N particles under conditions of constant pressure, P, and temperature, T. Therefore, the isobaric-isothermal, or NPT, ensemble is necessary to use to compare simulated conditions to those of actual experiments. The NPT ensemble extends the canonical ensemble, coupling the system to both an external heat bath and an external piston. With the inclusion of pressure, the system now exists on a constant "Gibbs free energy" hypersurface, $G = E - TS + PV$.

The partition function for the NPT ensemble is

$$\Delta(N,P,T) = \frac{1}{V_0 N! h^{3N}} \int_0^\infty dV \int d\mathbf{x} \exp[-\beta(\mathcal{H}(\mathbf{x}) + PV)]\,. \tag{2.7}$$

2.3 Molecular Dynamics Techniques

In principle, a MD simulation is just a virtual collection of particles constrained to behave according to some defined parameters and allowed to evolve in time[22, 24]. Some thermodynamic properties can be extracted from the system as it evolves, while others have to be measured over the duration of the simulation such as the change in the free energy between two states and entropy[24]. The latter case is due to the fact that these quantities are dependent on the partition function of the system, rather than an actual instantaneous physical property. As such, the change in the free energy must be computed via thermodynamic integration over the thermodynamic path between the system's initial and final state. Since the former case is concerned with instantaneous properties of the system, these quantities can be extracted through the use of the Virial theorem[22].

The basic procedure for an MD simulation is as follows[24]:

- The system initialises with specific macroscopic parameters such as temperature, volume and pressure estimators, and also microscopic particle positions.

- The system is evolved over a predetermined number of iterations.
- Each iteration requires the forces between each pair of particles to be calculated, subject to the potential being used, as well as the present positions of each particle.
- Once force calculations have been performed, the equations of motion must be integrated to acquire the next set of particle positions for the next iteration.
- Averages of microscopic properties, such as kinetic energy, can be taken to obtain thermodynamic properties.
- Iterate to the next timestep.
- The simulation terminates once the maximum number of iterations has been reached.

There are many different types of algorithms that exist to perform the simulations, however one of the most widely used and stable is the Verlet algorithm[24].

2.3.1 Verlet Algorithm

The Verlet algorithm is used to compute the next particle positions from the present particle positions, previous particle positions and the forces between the particles[25]. Since it depends on the previous particle location, it is necessary to prepare a fictional previous state at the very beginning of the simulation.

At the beginning of the simulation, the initial state is prepared according to a set of defined conditions. The system can be initialised in a well defined ordered state, such as a solid crystal lattice with all particles at their lattice sites. Liquid systems can then be set up by melting the structure over the equilibration period before performing statistical sampling. It is also important that no particle positions overlap with each other, as this would yield non-physical results; such as highly repulsive forces between particles causing rapid changes in the total energy of the system and explosion of the simulation volume. Particles are then each assigned a velocity, v, sampled from a distribution and scaled so that the centre of mass momentum is zero. In order to obtain the fictional previous state, the system is run backwards in time for a very short timestep, dt, so that all particles move a distance $-vdt$. The program then has access to a set of previous particle locations and present particle locations with which to iterate to the next set timestep.

Before an iteration can be completed, the forces between all pairs of particles must be computed. Consequently, the force calculation is computationally the most

costly part of the program, since for N particles it requires looping over $N(N-1)/2$ unique particle pairs in the system and computing the total force on a particle from each of its neighbours. This is an order N^2 calculation and therefore extremely slow for large systems. The calculation can be performed over fewer pairs by considering the form of the particle potential used in the system. If the potential and force fields are close to zero at some radius away from each particle, as demonstrated in section 2.7, then the calculation only needs to be performed for particle pairs within that radius for each atom.

The calculation itself is simply,

$$\mathbf{f}(\mathbf{r}) = -\nabla U(\mathbf{r})\,, \tag{2.8}$$

where $\mathbf{f}(\mathbf{r})$ is the force in the vector space $\mathbf{r}$ and $U(\mathbf{r})$ is the potential in vector space $\mathbf{r}$. The Verlet algorithm uses a Taylor expansion about the forward time increment, Δt, in position,

$$\mathbf{r}(t+\Delta t) = \mathbf{r}(t) + \dot{\mathbf{r}}(t)\Delta t + \frac{\ddot{\mathbf{r}}(t)\Delta t^2}{2} + \frac{\dddot{\mathbf{r}}(t)\Delta t^3}{3!} + \mathcal{O}(\Delta t^4)\,, \tag{2.9}$$

and, symmetrically, the backward time increment,

$$\mathbf{r}(t-\Delta t) = \mathbf{r}(t) - \dot{\mathbf{r}}(t)\Delta t + \frac{\ddot{\mathbf{r}}(t)\Delta t^2}{2} - \frac{\dddot{\mathbf{r}}(t)\Delta t^3}{3!} + \mathcal{O}(\Delta t^4)\,. \tag{2.10}$$

Simply adding equations (2.9) and (2.10) together and rearranging for the forward time increment gives the Verlet algorithm:

$$\mathbf{r}(t+\Delta t) = 2\mathbf{r}(t) - \mathbf{r}(t-\Delta t) + \frac{\mathbf{f}(t)\Delta t^2}{m} + \mathcal{O}(\Delta t^4)\,. \tag{2.11}$$

In the above equations, $\mathbf{r}$ is the position of the particle as a function of time t, m is particle mass and, $\mathbf{f}(t) = m\ddot{\mathbf{r}}(t)$, is the force on the particle. It is clear from equation (2.11), that the next particle locations only depend on the present particle locations, the previous locations and the force between the present particle locations. In the original Verlet algorithm, terms of order $\mathcal{O}(\Delta t^4)$ and higher are ignored[24], making a single calculation of the Verlet algorithm very rapid to compute. Higher order terms store more information about the present state of the system, at the cost of speed, and hence it is possible to make more accurate predictions about the state of the system further into the future. This could be considered as a desirable quality to have, as the algorithmic speed is not usually of concern during simulations, but rather being able to perform larger iterations with high accuracy, as this reduces the

total number of calculations that need to be performed for the same total duration of the simulation. However, there are two further aspects that need to be considered. These aspects are long-term energy drift, since the equations of motion are energy conserving, and "Lyapunov instability"[24].

Lyapunov instability describes how the trajectory of the system across a phase space hypersurface, for constant energy, will diverge exponentially from the true trajectory of the system. This is actually not that problematic as MD simulations are not concerned with exact simulations of systems, but rather statistical results[22]. Furthermore, evidence suggests the existence of "shadow orbits", which are true trajectories of the system that closely track the computed trajectory of the system, for durations longer than the Lyapunov instability[24, 26]. This implies the computed trajectory does actually match a true trajectory that exists within the system.

Therefore, the more important aspect to consider is whether the system is phase space volume preserving; i.e. the system has access to the same microstates on the constant energy hypersurface, indicating no long-term energy drift in agreement with Hamilton's equations of motion[22]. Algorithms that suffer from this heavily are those that are not time reversible. Despite the time reversibility of the Verlet algorithm, it does not conserve the total energy exactly. Instead it conserves a "shadow" Hamiltonian that tends to the true Hamiltonian with decreasing timestep size[22, 24]. Higher order Verlet-like algorithms do a much better job at accurately following the true trajectory of the system over short timescales, but are much poorer at preventing long-term energy drift[24]. This makes low order, short timestep, Verlet algorithms suitable for long duration MD simulations.

2.4 Barostats and Thermostats

Using MD to sample the desired ensemble requires using the correct equations of motion and Hamiltonian that describes the entire system. As mentioned in section 2.2, integrating Hamilton's equations of motion to iterate the MD simulations reproduces the microcanonical ensemble. If one wishes to use MD to sample other ensembles, then Hamilton's equations of motion can not be used directly. Furthermore the simple Hamiltonian defines a constant energy hypersurface, while the other ensembles conserve different hypersurfaces in phase space and the energy fluctuates about an average due to interactions of the system with its environment.

Systems capable of exchanging heat with their environment, such as in the NVT ensemble, are controlled using a thermostat while those that can affect the

size of their container, such as systems in the NPH ensemble, are controlled by a barostat. These additional controls enter as separate degrees of freedom into the Hamiltonian, and are discussed in sections 2.4.1 and 2.4.2 respectively. The NPT ensemble relies on both a thermostat and barostat and is discussed at the end of section 2.4.2.

2.4.1 Thermostats

The simplest way to control the temperature of the system is to rescale the velocities so the kinetic energy generates the required temperature instantaneously. This procedure lead to the development of the Nosé Hamiltonian[27]

$$\mathcal{H}_{\mathrm{N}} = \sum_{i=1}^{N} \frac{\mathbf{p}_i^2}{2m_i s^2} + U(\mathbf{r}_1, ..., \mathbf{r}_N) + \frac{p_s^2}{2Q} + (dN+1)k_{\mathrm{B}}T \ln s \,, \tag{2.12}$$

where s is a separate entity that scales the instantaneous kinetic energy, p_s is the conjugate momentum to s and Q acts as a fictional mass term effecting how rapidly the kinetic energy is rescaled in the response to thermal fluctuations; the actual dimensionality of Q is energy$\times$time^2. This generates a canonical partition function with the following equations of motion:

$$\begin{aligned}
\dot{\mathbf{r}}_i &= \frac{\partial \mathcal{H}_{\mathrm{N}}}{\partial \mathbf{p}_i} = \frac{\mathbf{p}_i}{m_i s^2} \\
\dot{\mathbf{p}}_i &= -\frac{\partial \mathcal{H}_{\mathrm{N}}}{\partial \mathbf{r}_i} = \mathbf{f}_i \\
\dot{s} &= \frac{\partial \mathcal{H}_{\mathrm{N}}}{\partial p_s} = \frac{p_s}{Q} \\
\dot{p}_s &= -\frac{\partial \mathcal{H}_{\mathrm{N}}}{\partial s} = \frac{1}{s}\left[\sum_{i=1}^{N} \frac{\mathbf{p}_i^2}{m_i s^2} - (dN+1)k_{\mathrm{B}}T\right].
\end{aligned} \tag{2.13}$$

The equations of motion associated with the Nosé Hamiltonian actually act upon a non-standard form of the kinetic energy, as shown in equation (2.12). Therefore, to recover the actual kinetic energy, a noncanonical change of variables is required by transforming, $\mathbf{p'}_i = \mathbf{p}_i/s$, $p'_s = p_s/s$ and $dt' = dt/s$. However, making such a change of variables results in the equations of motion no longer being symplectic, which, as previously mentioned, is a requirement for correct sampling of the ensemble.

A modification to the dynamics of the Nosé Hamiltonian was proposed by Hoover[28], who suggested that the variable s could be removed from the Nosé equations of motion by rescaling the time as $dt_{\mathrm{old}} \equiv s dt_{\mathrm{new}}$. This generates the

Nosé-Hoover equations of motion of the form:

$$\begin{aligned}
\dot{\mathbf{r}}_i &= \frac{\mathbf{p}_i}{m_i} \\
\dot{\mathbf{p}}_i &= \mathbf{f}_i - \zeta \mathbf{p}_i \\
\dot{\zeta} &= \frac{1}{Q}\left[\sum_{i=1}^{N} \frac{\mathbf{p}_i^2}{m_i} - dNk_{\mathrm{B}}T\right],
\end{aligned} \tag{2.14}$$

where the quantity $dN + 1$ has also been redefined as dN. The term $\zeta \equiv p_s/Q$ is described as a "frictional" term by Hoover, which determines how rapidly the temperature of the system adjusts. The Nosé-Hoover equations generate a canonical distribution in an ergodic system, but does not necessarily sample the canonical ensemble properly for a non-ergodic system. Hoover showed that for a harmonic oscillator the phase space was not properly sampled due to the system not being sufficiently chaotic. One reason for this was suggested by Martyna et al.[29], which indicated that the distribution in phase space has a Gaussian dependence on p_i but also on the thermostat momenta. In the Nosé-Hoover equations, the momenta of the particles is controlled by the thermostat, but there is no fluctuation of the thermostat momenta. For the system to be truly ergodic, the thermostat momenta should also be explored across the phase space.

The correction to the Nosé-Hoover approach is to apply Gaussian sampling of the thermostat momenta by applying a Nosé-Hoover thermostat to the original thermostat momenta. However, the second thermostat must have its thermostat momenta also sampled and so a chain of thermostats must be applied to each thermostat momenta. The longer the chain, the closer the phase space is explored ergodically. This results in the following equations of motion for a chain of length

M as presented by Martyna et al.[29]:

$$\begin{aligned}
\dot{\mathbf{r}}_i &= \frac{\mathbf{p}_i}{m_i} \\
\dot{\mathbf{p}}_i &= \mathbf{f}_i - \frac{p_{\eta_1}}{Q_1}\mathbf{p}_i \\
\dot{\eta}_j &= \frac{p_{\eta_j}}{Q_j} \qquad\qquad\qquad\qquad\qquad\qquad j = 1, ..., M \\
\dot{p}_{\eta_1} &= \left[\sum_{i=1}^{N} \frac{\mathbf{p}_i^2}{m_i} - dNk_{\mathrm{B}}T\right] - \frac{p_{\eta_2}}{Q_2}p_{\eta_1} \\
\dot{p}_{\eta_j} &= \left[\frac{p_{\eta_{j-1}}^2}{Q_{j-1}} - k_{\mathrm{B}}T\right] - \frac{p_{\eta_{j+1}}}{Q_{j+1}}p_{\eta_j} \qquad j = 2, ..., M-1 \\
\dot{p}_{\eta_M} &= \left[\frac{p_{\eta_{M-1}}^2}{Q_{M-1}} - k_{\mathrm{B}}T\right].
\end{aligned} \tag{2.15}$$

2.4.2 Barostats

In order to control the pressure of the system, the volume must be allowed to fluctuate. A simple method analogous to rescaling the kinetic energy to control the system temperature was first proposed by Andersen[30], which involves scaling the position and momenta of each particle by the volume of the system; $\mathbf{s}_i = V^{-1/3}\mathbf{r}_i$ and $\boldsymbol{\pi}_i = V^{1/3}\mathbf{p}_i$, respectively. This introduces the volume explicitly as a dynamical variable into the phase space domain, with conjugate momentum p_V. This leads to the construction of Andersen's Hamiltonian for isobaric-isoenthalpic systems[22]

$$\mathcal{H}_{\mathrm{A}} = \sum_{i=1}^{N} \frac{V^{-2/3}\boldsymbol{\pi}_i^2}{2m_i} + U(V^{1/3}\mathbf{s}_1, ..., V^{1/3}\mathbf{s}_N) + \frac{p_V^2}{2W} + PV\,, \tag{2.16}$$

where the term PV describes the action of an imaginary external piston regulating the volume in response to fluctuations of the internal pressure about that of the external applied pressure P. The term $p_V^2/2W$, acts as the kinetic energy of the volume with fictional mass W controlling the responsiveness of the external piston to changes in the internal pressure; increasing the mass has the effect of damping the piston. The fictional mass has the form $W = (3N+1)k_{\mathrm{B}}T\tau^2$, where τ is the timescale of the volume fluctuation.

Applying Hamilton's equations of motion results in the Andersen equations of motion for the isobaric-isoenthalpic ensemble in terms of $\dot{\mathbf{s}}_i$ and $\dot{\boldsymbol{\pi}}_i$. These equations can be transformed in terms of the physical coordinates $\dot{\mathbf{r}}_i$ and $\dot{\mathbf{p}}_i$ using the previous definitions of $\mathbf{s}_i$ and $\boldsymbol{\pi}_i$, as well as $\dot{\mathbf{s}}_i = V^{-1/3}\dot{\mathbf{r}}_i - (1/3)V^{-4/3}\dot{V}\mathbf{r}_i$ and $\dot{\boldsymbol{\pi}}_i = V^{1/3}\dot{\mathbf{p}}_i +$

$(1/3)V^{-2/3}\dot{V}\mathbf{p}_i$. This results in the following equations of motion:

$$\begin{aligned}
\dot{\mathbf{r}}_i &= \frac{\mathbf{p}_i}{m_i} + \frac{\dot{V}\mathbf{r}_i}{3V} \\
\dot{\mathbf{p}}_i &= -\frac{\partial U}{\partial \mathbf{r}_i} - \frac{\dot{V}\mathbf{p}_i}{3V} \\
\dot{V} &= \frac{p_V}{W} \\
\dot{p}_V &= \frac{1}{3V}\sum_i \left[\frac{\mathbf{p}_i^2}{m_i} - \frac{\partial U}{\partial \mathbf{r}_i}\mathbf{r}_i\right] - P\,.
\end{aligned} \tag{2.17}$$

Equations (2.17) lead to the conserved quantity

$$H' = \mathcal{H}(\mathbf{r},\mathbf{p}) + \frac{p_V^2}{2W} + PV\,, \tag{2.18}$$

where $\mathcal{H}$ is the physical Hamiltonian. Consequently, the partition function generated from H' actually differs from that of the true NPH partition function by $\Delta = p_V^2/2W$ inside the delta function of equation (2.6). Andersen's approach at controlling the internal pressure of the system therefore deviates from the true constant enthalpy hypersurface. This deviation is small for large N systems and if the fluctuations in Δ are small, then the enthalpy is constrained to lie within a small shell in phase space.

Equations (2.17) can be used to generate equations of motion that replicate a full NPT ensemble. The method proposed by Martyna, Tobias and Klein (MTK)[31] correctly reproduces the volume distribution in phase space for the NPT ensemble, building on the work of Hoover[28]. Introducing the variable $\epsilon = (1/3)\ln(V)$, first implemented by Hoover, means equations (2.17) can be rewritten in terms of ϵ and $\dot{\epsilon}$, where the momentum of the volume dependence becomes $p_\epsilon = \dot{\epsilon}W$[22]. However, making only this substitution proposed by Hoover is not enough, as the modified equations of motion are compressible when they should be incompressible[22]; so as to preserve the phase space volume and ensure the correct probability distribution associated with exploring the microstates for the given ensemble. The MTK correction introduces an additional term of $-(3/N_f)p_\epsilon\mathbf{p}_i/W$ into $\dot{\mathbf{p}}_i$, where N_f is the number of degrees of freedom. They also include the additional term of $(3/N_f)\sum_{i=1}^{N}\mathbf{p}_i^2/m_i$ into the term $\dot{p}_\epsilon$. These two modifications result in equations of motion that are once again incompressible and conserve the quantity H'. The

MTK equations of motion are[22]:

$$\begin{aligned}
\dot{\mathbf{r}}_i &= \frac{\mathbf{p}_i}{m_i} + \frac{p_\epsilon}{W}\mathbf{r}_i \\
\dot{\mathbf{p}}_i &= \tilde{\mathbf{f}}_i - \left(1 + \frac{3}{N_f}\right)\frac{p_\epsilon}{W}\mathbf{p}_i \\
\dot{V} &= \frac{3Vp_\epsilon}{W} \\
\dot{p}_\epsilon &= 3V(\mathcal{P} - P) + \frac{3}{N_f}\sum_{i=1}^{N}\frac{\mathbf{p}_i^2}{m_i}\,,
\end{aligned} \tag{2.19}$$

where $\mathcal{P}$ is the internal pressure estimator, P is the applied external pressure and $\tilde{\mathbf{f}}_i$ is the total force on particle i contributing from the potential and external forces.

The MTK equations can be coupled to Nosé-Hoover thermostat chains in order to sample both the momentum of the particles and volume independently from Gaussian distributions. The particle and volume momentum are sampled separately due to the more rapid fluctuation of the particle momenta compared to that of the external piston[22] and hence require their own independent thermostats. Once coupled to a thermostat, the MTK equations correctly sample the NPT ensemble.

The thermostated version of equations (2.19) are valid only for isotropic variation in pressure. In many cases, it is desirable to allow the system volume to fluctuate according to anisotropic changes in the pressure. A method that correctly reproduces the NPT ensemble for anisotropic changes in the internal pressure of the system has also been developed by Martyna, Tobias and Klein[31] with equations of motion as follows:

$$\begin{aligned}
\dot{\mathbf{r}}_i &= \frac{\mathbf{p}_i}{m_i} + \frac{\mathbf{P}_g}{W_g}\mathbf{r}_i \\
\dot{\mathbf{p}}_i &= \tilde{\mathbf{f}}_i - \frac{\mathbf{P}_g}{W_g}\mathbf{p}_i - \frac{1}{N_f}\frac{\mathrm{Tr}[\mathbf{P}_g]}{W_g}\mathbf{p}_i \\
\dot{\mathbf{B}} &= \frac{\mathbf{P}_g\mathbf{B}}{W_g} \\
\dot{\mathbf{P}}_g &= \det[\mathbf{B}](\mathbf{P}_{\mathrm{int}} - \mathbf{I}P) + \frac{1}{N_f}\sum_{i=1}^{N}\frac{\mathbf{p}_i^2}{m_i}\mathbf{I}\,,
\end{aligned} \tag{2.20}$$

where $\mathbf{I}$ is the identity matrix and $\mathbf{P}_{\mathrm{int}}$ is the internal pressure matrix. Equations (2.20) allow for changes in the system cell matrix $\mathbf{B}$ to enter into phase space as nine independent changes in orientation and conjugate momenta $\mathbf{P}_g$. The conjugate momenta is analogous to p_ϵ in the isotropic case, where $\mathbf{P}_g = W_g\dot{\mathbf{B}}\mathbf{B}^{-1}$. Equations

(2.20) conserve the quantity

$$H' = \mathcal{H}(\mathbf{r}, \mathbf{p}) + \frac{1}{2W_g}\mathrm{Tr}[\mathbf{B}_g^T \mathbf{B}_g] + P\det[\mathbf{B}_g]\,. \tag{2.21}$$

If equations (2.20) are coupled to a Nosé-Hoover chained thermostat, similar to the isotropic case, then they accurately reproduce the NPT ensemble for anisotropic variations in internal pressure[31].

2.5 Monte Carlo

Another method for sampling various statistical ensembles is Monte Carlo (MC). Instead of evolving the system dynamically in time to explore the desired phase space, MC works on the idea of iterating a system state m, to a new system state n, by some probability. Such a method was developed by Metropolis et al.[32] and obeys the following procedure:

- A particle is selected at random from a uniform distribution in the system at state m.
- The contribution to the potential energy of the particle with all N particles, $U\big(\mathbf{r}^N\big)$, is calculated.
- A trial "move" is then performed on the particle to move the system to state n, displacing the particle so $\mathbf{r}' = \mathbf{r} + \delta$.
- The new potential energy of the system is calculated from the contribution of the particle at its new position, $U\big(\mathbf{r}'^N\big)$.
- The move is accepted with probability

$$P_{\mathrm{acc}}(m \to n) = \min\big(1, \exp\big[-\beta\big(U\big(\mathbf{r}'^N\big) - U\big(\mathbf{r}^N\big)\big)\big]\big)\,, \tag{2.22}$$

  if $P_{\mathrm{acc}}(m \to n) \geq \xi$, where ξ is a random number selected uniformly from the interval [0,1].

There are a few things to consider about the performance of the MC Metropolis method. Foremost, it is necessary that a particle is selected at random to conduct a trial move and not sequentially. This is because it should be equally likely that once a move has been completed it can also be reversed. If a move is conducted sequentially, there is no possible way to reverse the evolution of the system.

The effectiveness of the procedure is also dependent on the value for δ chosen for a particle trial move. If δ is too small, states m and n will be very similar and hence subsequent moves will be highly correlated for a long time. This will require many more MC moves to explore the phase space, resulting in long simulation times. Conversely, if δ is too big, then a particle move could get too close to other particles, resulting in very large potential energy contributions and hence a higher probability of the move being rejected. This in turn will require more trials to be made to ensure a sufficient number of moves are successful and the phase space explored. Normally, it is acceptable to choose δ so that 50% of the moves are accepted, however this not necessarily optimal[32, 33].

If a particle move is rejected, then the particle position is restored to its former position, $\mathbf{r}$, and the previous state now becomes state n. This is important, since a low energy state is more favourable than a higher energy state and therefore the system would be expected to exist more likely in these lower energy states. Hence, while no physical move has been performed, the presence of the system in its previous state should be counted as a MC move, as this more accurately weights the distribution of system states.

While the former part of this section has described MC performed for the NVT ensemble, MC can also be performed for the NPT ensemble; which is used in this research. In this case, the particle coordinates are scaled as $\mathbf{s} = V^{-1/3}\mathbf{r}$, and the simulation box is allowed to vary in size keeping the fractional coordinates of the particles constant. Performing a MC trial move allows the particles and/or the box to vary, which are accepted with a probability dependent on the external pressure of the system, P,

$$P_{\text{acc}}(m \to n) = \min(1, \exp[-\beta(\Delta U_{m\to n} + P\Delta V_{m\to n}) - N\ln(V_n/V_m)]) \,, \qquad (2.23)$$

where N is the number of particles in the system[33].

In this research, the particular MC code used actually varies the size, δ, of the MC moves over the equilibration period to tune the probability of accepting a move to 50%. This, strictly, does not obey detailed balance, and so once the equilibration period has finished, the size of δ is fixed. The advantage of this is that the system can be tuned to evolve at a rate at runtime, that doesn't require an excessive number of MC moves. It is otherwise impossible to know a priori, what value of δ would give a suitable percentage of accepting a move during the production run.

When performing a MC simulations, typically the simulation runtime is conducted in terms of MC "sweeps". A MC sweep is defined as N MC moves, and is the

number of moves expected to iterate each of the N molecule positions. In reality, in a single sweep, not every molecule will experience a MC move, since individual particles can be repeatedly chosen upon successive MC moves.

2.6 MD Practicalities

It is not enough to just know how to implement a MD algorithm to successfully perform a MD simulation. There are practicalities involved with running a simulation that must be considered if the simulation is to complete properly. This section discusses how to properly parallelise the simulation, in order to optimise the computational resources available, in addition to how to select an appropriate timestep and how to ensure a system has equilibrated.

2.6.1 Parallelisation

Large scale MD simulations can require many hours, days, months or even years of processor compute time to provide statistically significant results. Running such simulations on a single processor would be impractical if not impossible, where the processor time is the same as the actual time taken. However, MD simulations can be parallelised to run over many processors, reducing the actual time taken to complete a simulation. A rapid algorithm used in MD is spatial decomposition of the simulated systems over the physical number, p, of processors, where each processor only computes the particle attributes for the particles within that processors spatial region[34]. As a result, dozens or hundreds of particles can be updated simultaneously between timesteps, reducing the actual time taken between iterations. The "speedup" of a simulation for p processors is defined as

$$S_n = \frac{T_1}{T_n}\,, \tag{2.24}$$

while the parallel efficiency is defined as

$$E_n = \frac{S_n}{p}\,, \tag{2.25}$$

where T_1 is the actual time taken on 1 processor and T_n is the time taken on n processors[35].

The maximum theoretical achievable speedup for a simulation increases linearly with the number of processors used[35]. However, in reality, this is not possible to attain since all codes performed in parallel have a proportion of their code which

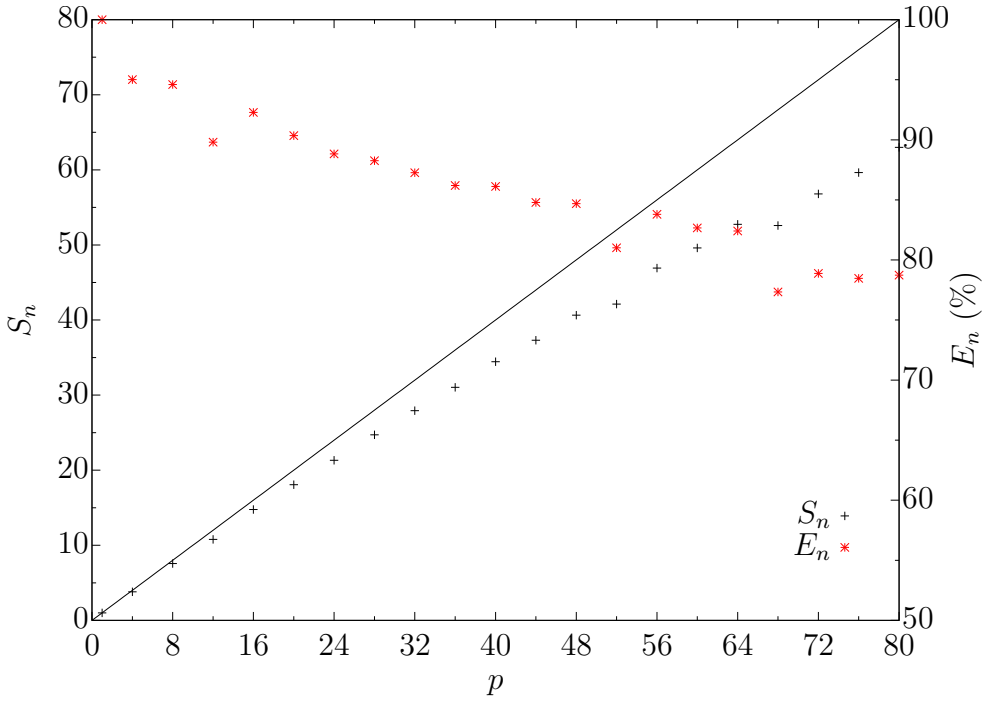

Figure 2.1: Speedup test of LAMMPS mW liquid simulation using $21,952$ particles. Black data points indicate the actual speedup fraction of the simulation, compared to perfect speedup shown by the black line. Red points indicate the efficiency of actual speedup compared with the theoretical maximum speedup for the number of processors used.

can only be executed in serial; the "serial fraction". The serial fraction can only be performed by a single thread and hence its actual time taken to execute is invariant with the number of processors available. There are also parallel overheads that arise the more processors are requested[35].

In particular, parallel codes suffer from overheads the more communication is required between processors. For example, during a MD simulation employing a spatial decomposition algorithm, particles will typically move throughout the simulated space. As these particles move, they will move from a region simulated on one processor, to a neighbouring region simulated on a separate processor. Individual processors must therefore keep track of particles near their region boundaries – the "halo" region – and communicate the particle position and attributes to the neighbouring region processor[34]. The size of this halo region will depend on the number of processors the system is decomposed over and the range of interaction potentials used. Communication between processors is significantly slower than updates to particles conducted within the core region on a single processor, due to the

necessity of having to pass a message to another processor. The time taken to pass a message relies on the time taken to copy the message to any buffers along with communication data (the "latency" time) and the time taken to actually send the data (the reciprocal of the "bandwidth")[35]. As the number of processors increases, the total halo region also increases while the core region decreases. This increases the proportion of particles that must be communicated between processors each iteration, compared to those that reside within a core region. This increases the total time spent on message passing, substantially reducing the effective parallelisation of the simulation, as shown in figure 2.1.

While a speedup is still obtained with an increasing number of processors with a LAMMPS simulation, the efficiency of the speedup achieved, steadily reduces. It is not computationally efficient, nor is it good practise as a shared user of a high performance computing resource, to request excessively large numbers of processors. What constitutes excessive is subjective and depends on several factors such as: the percentage of the machine being requested; the percentage of the machine available; and the actual time taken and the efficiency on p processors. For example, it could be considered unreasonable to request 72 processors for a simulation that would complete in one hour using 32 processors, during periods of collectively high demand for the machine. It would also be unreasonable to request p processors if only 50% efficiency was expected. Of course, different machines are administered differently and will have different acceptable tolerances.

Figure 2.1 shows that LAMMPS simulations parallelise well and that speedup is closely linear. As standard practise, the simulations conducted in this research have been conducted with approximately 85% parallel efficiency; equivalent to approximately 700 particles per processor.

2.6.2 Timesteps

To perform a MD simulation a suitable timestep must be chosen to integrate the equations of motion over. This choice is important, since choosing a timestep that is too small will result in only a small area of the system's phase space being explored between timesteps, requiring significantly more iterations to fully explore the phase space than when using a larger timestep. However, using a timestep that is too large can cause particles to be moved too far in one iteration, resulting in particles getting too close to one another and overlapping[33]. These large timesteps therefore result in unphysical behaviour, which can cause significant drifts in the total energy and deviations in the energy over short simulation durations.

Since the equations of motion are energy conserving, any large drift in the

total energy over a simulation indicates a poor choice of timestep. Typically, the choice of timestep should be no larger than the fastest fluctuations in the system[35]. Choosing a timestep close to this size allows the properties of the particles to be properly integrated over time. Smaller timesteps would result in more accurate calculation of the equations of a motion and hence a smaller rate of long term energy drift. Long term drift in the energy is unavoidable since the timestep must be finite. However, this drift is typically acceptable if it is normally by 0.01% about the mean[33]; i.e. the RMS deviation in the energy from the mean, δE_{RMS}.

The best timestep to use can therefore be estimated by plotting δE_{RMS} against timestep, δt, and checking for where the RMS fluctuations increase significantly. This is done for small mock simulations that use the same model potential and the most rapidly changing phase as the actual system of interest. These simulations are conducted from the same equilibrated starting configuration and evolved under the same conditions using different size timesteps. For Verlet algorithms, the RMS deviation in the energy at small timesteps has the relation $\delta E_{RMS} \propto \delta t^2$ [33, 36], as shown in the inset of figure 2.2 (*left*). This relationship follows directly from the maximum order of the timestep term used in the truncated Taylor expansion of the MD algorithm[36]. In the case of the Verlet algorithm, the maximum order of the step size used is two, as demonstrated in equation (2.11). The higher the order, n, of the δt term used, the smaller both the overall δE_{RMS} and maximum step size that can be used before divergence from the relationship $\delta E_{RMS} \propto \delta t^n$ is observed[36].

Figure 2.2 (*right*) also shows that the total energy clearly drifts over the duration of the simulation for timesteps $\delta t > 0.006$. There was no significant or visible drift in the value of the total energy for 0.001–0.006 δt, and so only $\delta t = 0.005$ is shown from this set of timesteps. In this simulation, the unphysical behaviour observed for $\delta t > 0.006$ involved the temperature dropping and consequently the total energy as well. This is despite the identical starting conditions where, at the initial temperature and pressure, the system is liquid.

For the simulation in figure 2.2, it was found $\delta E_{RMS} < 0.01\%$ for $\delta t \leq 0.006$. Erring on the side of caution, a timestep of 0.005 was chosen for simulations conducted with the LJ-BG potential. This method for determining the best timestep was also applied to similar mock simulations for other systems using different potentials.

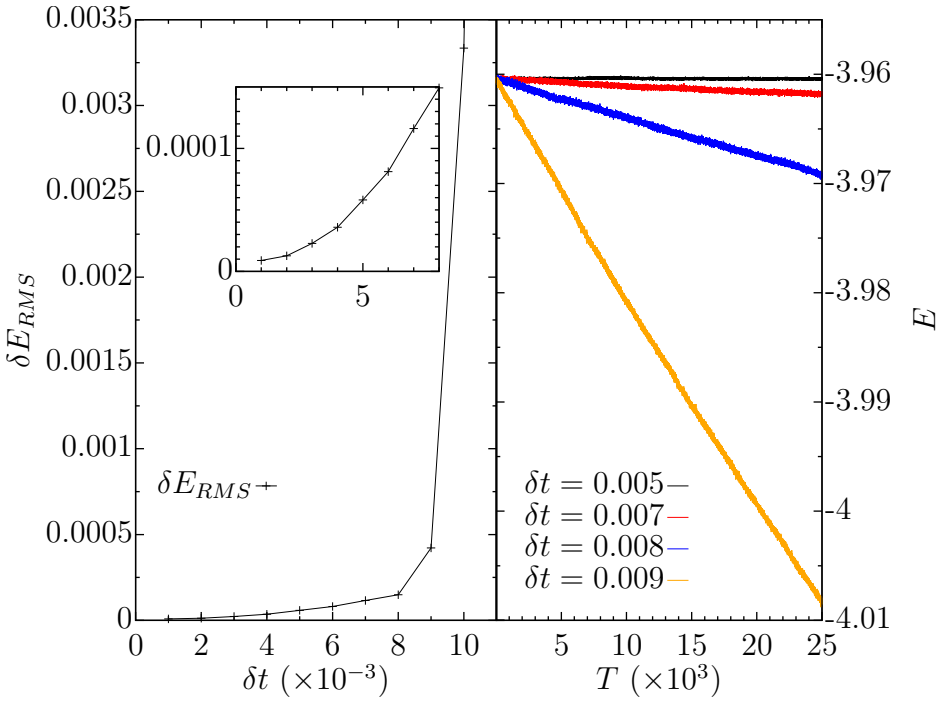

Figure 2.2: The RMS deviation in total energy with varying timestep (*left*) and the total energy as a function of simulation time for different timesteps (*right*). These results are for an 864 atom, liquid simulation at $P^* = 0$, $T^* = 0.7$, within the NVE ensemble, using the modified LJ-BG potential described in section 2.7.1. All values are in LJ reduced units for $\epsilon = \sigma = 1$.

2.6.3 Equilibration

Before being able to probe statistically meaningful values of the ensemble, the system must be set up in the state intended for examination. This requires a period of equilibration before sampling during the "production run". The duration for a simulation to equilibrate varies depending on the system simulated. In all cases though, it is required that the thermodynamic properties of the system cease to change as the system evolves in time[24]. Sampling the system before it has equilibrated would result in measuring the properties of the system over a completely different surface of the phase space than to that which is intended[33]. It is therefore necessary to allow enough time to pass for the simulation to reach the desired state and begin exploring the intended phase space surface. Such an equilibration is demonstrated in figure 2.3 for a LJ solid-liquid coexistence system using the LJ-BG potential. The simulation has been conducted in the way described in chapter 4.

The simulation shown in figure 2.3 equilibrates relatively rapidly and the equilibration period could reasonably be shorter. Both the pressure and tempera-

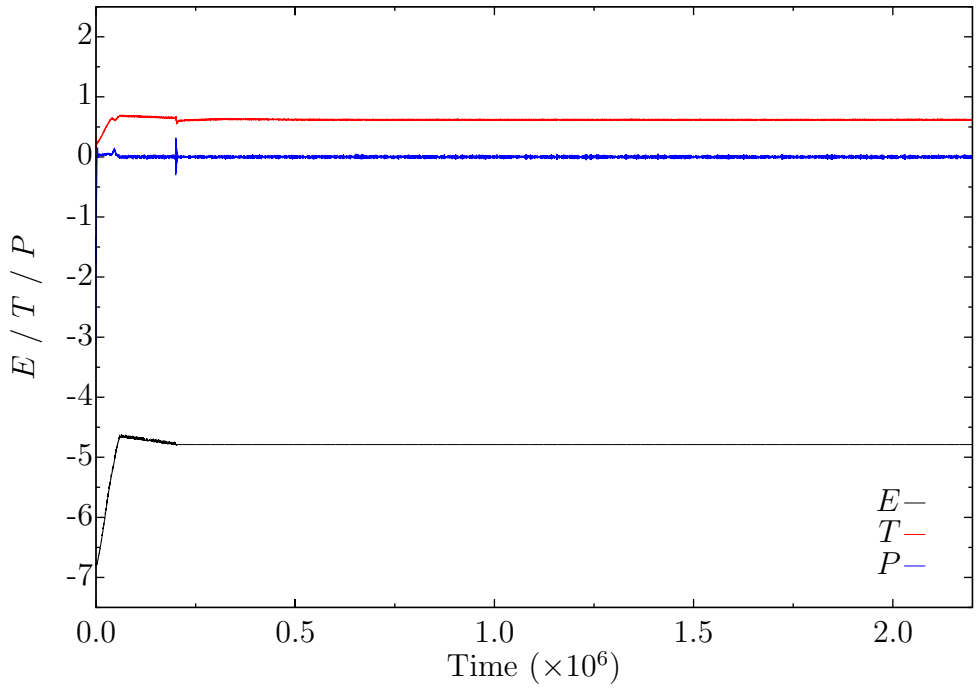

Figure 2.3: Equilibration of total energy (E), temperature (T) and pressure (P) in a LJ solid-liquid coexistence MD simulation for the (100)[001] orientation. The timestep for the simulation is $\delta t = 0.005$ and the sampling is every 100 steps. All values are in LJ reduced units for $\epsilon = \sigma = 1$.

ture display fluctuations, but no drift, while the energy remains constant for this timestep, as demonstrated in figure 2.2, over a longer duration. These fluctuations are not problematic, since only the average values are of importance and the longer the duration of the simulation, the more the fluctuations are averaged out.

2.7 Model Potentials

In order to conduct MD simulations, the particles simulated must interact with each other in some potential field. This section discusses the potentials used throughout this research.

2.7.1 Lennard-Jones

Before conducting full scale simulations on systems of research interest, it is often necessary to test any analytical techniques and procedures against simple systems that are well studied and compare obtained results against the existing literature. In MD, the Lennard-Jones (LJ) potential, is one such system. The LJ potential has

the form

$$U_{\mathrm{LJ}}(r) = 4\epsilon\left[\left(\frac{\sigma}{r}\right)^{12} - \left(\frac{\sigma}{r}\right)^{6}\right], \tag{2.26}$$

where r is the distance from a particle, ϵ is the minimum depth of the well and σ is the distance at which the potential is zero; equivalent to the diameter of the particle. The first term is just a close approximation of Pauli repulsion, which particles experience close to each other, while the second term approximates the attractive van der Waals force between particles[37]. The LJ model is a simple, computationally inexpensive approximation of gas atoms, and is therefore often used in MD simulations as a test case for new simulation principles and algorithms. This research uses the LJ model to first demonstrate simulated phase coexistence, validate the CWM, and to test the ability to identify between solid-like and liquid-like particles.

The LJ potential is an infinite range pair potential, while simulations are only of finite size. It is not possible to calculate the interaction between every particle and infinite image particle. Instead, the potential is truncated so that interactions are ignored past a cutoff radius, r_c. Beyond a certain distance, the LJ potential effectively becomes negligible and at this point, $r = r_c$, the potential can be set to zero. This is simple truncation and is usually done at a value of $r_c = 2.5\sigma$, where the potential is 1/60 of its minimum. However, simple truncation introduces a discontinuity in the potential and force field at r_c, which leads to the emergence of impulse forces at the cutoff. These impulse forces cannot be integrated in the equations of motion for MD simulations and therefore cause anomalous behaviour in the simulations[24].

An alternative to simple truncation is to use a truncated and shifted potential, $U_{\mathrm{S}}(r)$, where $U_{\mathrm{S}}(r) = U(r) - U(r_c)$ for $r \leq r_c$. Such a potential naturally tends to zero at r_c, removing any discontinuity at the cutoff. However, simply shifting the potential will still lead to a discontinuity in the force field at r_c and hence it is necessary to use a truncated force-shifted potential to remove the presence of impulse forces. Such an effect can be seen in figure 2.4, where the truncated and shifted LJ potential tends to zero at $r_c = 2.5\sigma$, but still yields a significant discontinuity in the force field at the same distance. To correct this effect, this research has implemented the truncated and force-shifted LJ-BG potential used by Broughton and Gilmer[38], which applies a smoothing function to the tail of the potential, tending both the potential and the force field to zero at r_c.

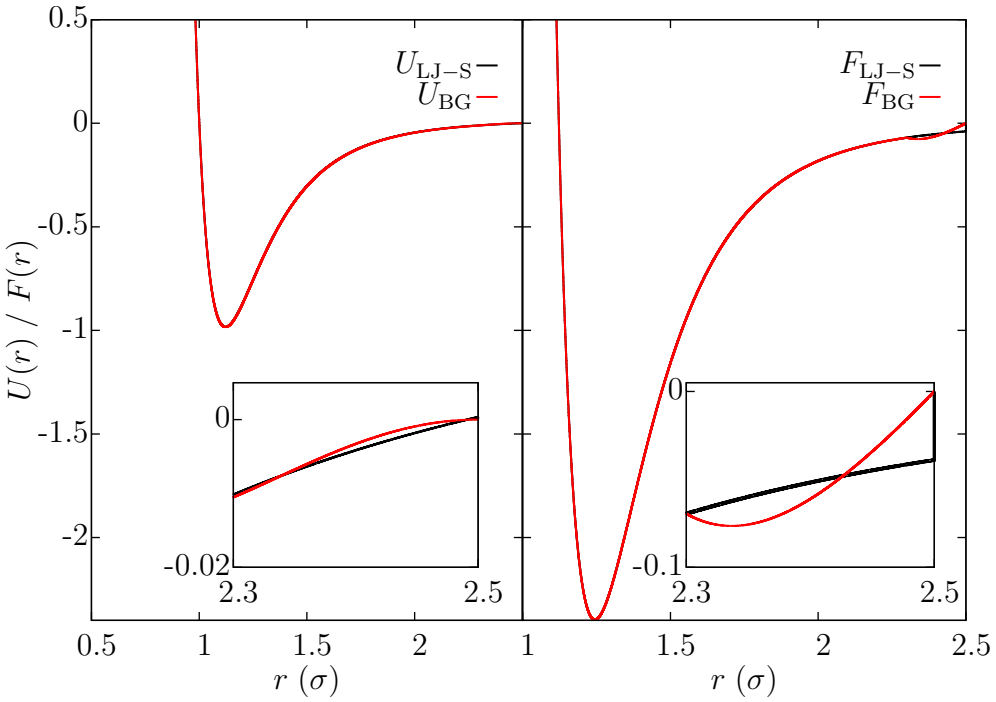

Figure 2.4: The form of the potentials (*left*) and force fields (*right*) for the shifted LJ potential (black) and the LJ-BG potential (red). The inserts show the detail in the tails for $2.3\sigma \leq r \leq 2.5\sigma$. Both potentials have $\epsilon = \sigma = 1$ and the form of the shifted LJ potential is $U_{\text{LJ-S}}(r) = U_{\text{LJ}}(r) + 1/60$ for $r < 2.5\sigma$.

The form of the truncated and shifted LJ-BG potential is:

$$U_{\mathrm{BG}}(r) = \begin{cases} 4\epsilon\left[\left(\frac{\sigma}{r}\right)^{12} - \left(\frac{\sigma}{r}\right)^{6}\right] + C_1 & r \leq 2.3\sigma \\ C_2\left(\frac{\sigma}{r}\right)^{12} + C_3\left(\frac{\sigma}{r}\right)^{6} + C_4\left(\frac{r}{\sigma}\right)^{2} + C_5 & 2.3\sigma < r < 2.5\sigma \\ 0 & 2.5\sigma \leq r \end{cases} \tag{2.27}$$

where $r \leq 2.3\sigma$ is just a shifted LJ potential and then for $2.3\sigma < r < 2.5\sigma$ the potential is smoothed to zero. The constants have the values $C_1 = 0.016132\epsilon$, $C_2 = 3136.6\epsilon$, $C_3 = -68.069\epsilon$, $C_4 = -0.083312\epsilon$ and $C_5 = 0.74689\epsilon$, as correctly reported by Davidchack and Laird[39]. It should be noted that in the original work published by Broughton and Gilmer[38], the sign of C_4 is incorrect.

The effect of introducing the corrections is shown in figure 2.4. It is clear from figure 2.4 (*right*), just how significant the discontinuity is at the cutoff for the normal LJ force field and how the correction by Broughton and Gilmer successfully adjusts this. It is also clear that the actual form of the potential differs very little,

as shown by figure 2.4 (*left*), meaning using the form of the potential introduced by Broughton and Gilmer adequately replicates a normal LJ system whilst removing any anomalous behaviour at the cutoff.

2.7.2 mW Model

The mW model is a Stillinger-Weber type potential[40] describing a monatomic form of water at 1% the computational cost of atomistic models[20]. The form of the potential[20] is:

$$U_{\mathrm{SW}}(r) = \sum_i \sum_{j>i} \phi_2(r_{ij}) + \sum_i \sum_{j\neq i} \sum_{k>j} \phi_3(r_{ij}, r_{ik}, \theta_{ijk})\,, \tag{2.28}$$

where ϕ_2 is the two body potential and ϕ_3 is the three body potential. These have the forms:

$$\phi_2(r_{ij}) = A_{ij}\epsilon_{ij}\left[B_{ij}\left(\frac{\sigma_{ij}}{r_{ij}}\right)^{p_{ij}} - \left(\frac{\sigma_{ij}}{r_{ij}}\right)^{q_{ij}}\right]\exp\left(\frac{\sigma_{ij}}{r_{ij} - a_{ij}\sigma_{ij}}\right), \tag{2.29}$$

$$\phi_3(r_{ij}, r_{ik}, \theta_{ijk}) = \lambda_{ijk}\epsilon_{ijk}\left[\cos\theta_{ijk} - \cos\theta_{0ijk}\right]^2 \exp\left(\frac{\gamma_{ij}\sigma_{ij}}{r_{ij} - a_{ij}\sigma_{ij}}\right)\exp\left(\frac{\gamma_{ik}\sigma_{ik}}{r_{ik} - a_{ik}\sigma_{ik}}\right). \tag{2.30}$$

The two body term is a similar pair-wise interaction to that the LJ potential. The three body term acts as a penalty term, increasing the energy of bond pairs between r_{ij} and r_{ik} that do not align with ideal tetrahedral crystal bonds of bond angle θ_{0ijk}[40]. The mW model is like the Stillinger-Weber potential, but includes the addition of ϵ and σ which define the energy minimum and particle radius, respectively, the same as in the LJ model. The inclusion of these parameters means that the potential and force are constrained to continuously go to zero at a value of $r = a\sigma$[20]. There is therefore no cause for concern regarding truncation effects, unlike the case with the LJ model.

The value for the parameters of the model are the same as the original Stillinger-Weber model in silicon[40], with the exception of ϵ, σ and λ, which have been altered for water[20]. The parameter values are:

$$A = 7.049556277\,, B = 0.602224558\,, p = 4\,, q = 0\,, a = 1.8\,,$$
$$\cos\theta_{0ikj} = -1/3\,, \gamma = 1.2\,, \lambda = 23.15\,, \epsilon = 6.189 \text{ kcal mol}^{-1}\,, \sigma = 2.3925 \text{ Å}\,,$$

which results in a cutoff of 4.3065 Å.

Chapter 3

Free Energy Methods

3.1 Introduction

This chapter begins with a review of classical nucleation theory, highlighting the effects of the bulk free energy and interfacial free energy involved in the process of nucleation. Thermodynamic integration (TI) is then discussed as a way to calculate the free energy difference between two states. However, TI can frequently lead to the problem of rare events and therefore a bias must be applied to the sampling of the free energy surface to overcome this. This leads to the discussion of various free energy methods, including umbrella sampling, metadynamics, the cleaving method and mold integration.

3.2 Nucleation

Classical nucleation theory (CNT) was developed initially by Volmer and Weber[41], Becker and Döring[42], and Zeldovich[43] to describe how water droplets nucleate from water vapour. The theory is, however, equally applicable to crystals nucleating in liquid[2]. An excellent review of CNT has been covered by Kalikmanov[44], while a summary is discussed here as background for understanding the significance of results obtained in chapter 6.

CNT indicates that two competing effects are important for determining nucleation: the bulk free energy difference between the solid and the liquid, $\Delta\mu = \mu_l - \mu_s$, – though strictly this is the chemical potential – and the energy associated with the formation of the interface between the solid and the liquid, γ. $\Delta\mu$ is always positive and hence nucleation is always favourable below the melting temperature

of the liquid. Hence, the Gibbs free energy for creating a solid nucleus of n nuclei is

$$\Delta G = -\frac{4}{3}\pi|\Delta\mu|n + 4\pi\gamma n^{2/3}\,. \tag{3.1}$$

This describes the formation of a spherical cluster with a vanishingly thin interface, known as the "capillarity approximation"[44]. The form of equation (3.1) produces a free energy barrier, which in order for a crystal to freely grow within a liquid, a critical nucleus of size n_c nuclei must form. If $n > n_c$ the crystal grows freely through the liquid, but if $n < n_c$, the nucleus can dissociate back into the liquid. The height of the energy barrier at $n = n_c$ is

$$\Delta G^* = \frac{16\pi\gamma^3}{3\Delta\mu^2} \equiv \alpha\frac{\gamma^3}{\Delta\mu^2}\,. \tag{3.2}$$

where α denotes the collected constants describing the anisotropy of the free energy, as it need not be spherical. If the nucleation barrier is known for two different crystal structures, A and B, then the preference of A to nucleate over B is true if the inequality $\Delta G^*_A < \Delta G^*_B$ holds. This leads to the condition

$$\frac{\gamma_A^3\alpha_A}{\gamma_B^3\alpha_B}\left(\frac{\Delta\mu_B}{\Delta\mu_A}\right)^2 < 1\,, \tag{3.3}$$

which, if the difference in bulk free energies between the two crystals, $\Delta\mu_{BA} \equiv \Delta\mu_B - \Delta\mu_A$, is known, can be rewritten as

$$\frac{\gamma_A^3\alpha_A}{\gamma_B^3\alpha_B}\left(\frac{\Delta\mu_B}{\Delta\mu_B - \Delta\mu_{BA}}\right)^2 < 1\,. \tag{3.4}$$

If the forms of the anisotropy are equivalent for both structures of nuclei, then the α terms can be ignored.

CNT can also be extended to a three parameter form

$$\Delta G = an + bn^{2/3} + cn^{1/3}\,, \tag{3.5}$$

which provides a better fit to the free energy curves associated with nucleus size. This additional term normally corresponds with a Tolman correction to the surface tension[45], but can alternatively be described by a more complicated form of nucleation. For instance in terms of ice nucleation, it has been proposed by Russo et al. that at strong supercooling, ice nucleates in a core-shell structure[17], consisting of a core of stable ice-I with radius R_1, surrounded by a shell of metastable ice-0 of thickness δR. Such a core-shell model has previously been observed in LJ sys-

tems by ten Wolde et al.[46] during homogeneous nucleation, where body centred cubic (BCC) pre-critical nuclei form before growing into structures with stable face centred cubic (FCC) cores. The core-shell model follows Ostwald's step rule[18], which states that the solid phase formed from the melt is not necessarily the most stable phase, but the phase with the smallest free energy difference with that of the liquid[47, 48].

In ice, this leads to an expression for the Gibbs free energy with both bulk ice-I and ice-0 terms, an ice-I/ice-0 interface term and an ice-0/liquid interface term

$$\Delta G = -\big|\Delta\mu_1\big|n_1 - \big|\Delta\mu_0\big|n_0 + 4\pi R_1^2\gamma_{10} + 4\pi\big(R_1 + \delta R\big)^2\gamma_0\,. \tag{3.6}$$

If the shell of ice-0 is assumed to be very thin compared to the radius of the ice-I core, then the δR^2 contribution in the final term can be ignored. Furthermore, the number of nuclei present can be rewritten in terms of

$$n_1 = \frac{4}{3}\pi R_1^3\rho_1/m \qquad\qquad n_0 = 4\pi R_1^2\delta R\rho_0/m\,, \tag{3.7}$$

where ρ is the number density of the structure and m is the mass of the water molecule. This allows equation (3.6) to be written in terms of n_1:

$$\Delta G = -\big|\Delta\mu_1\big|n_1 + 4\pi\alpha_1^{2/3}\left[\gamma_{10} + \gamma_0 - \big|\Delta\mu_0\big|\delta R\frac{\rho_0}{m}\right]n_1^{2/3} + 8\pi\alpha_1^{1/3}\delta R\gamma_0 n_1^{1/3}\,, \tag{3.8}$$

where $\alpha_1 = 3m/4\pi\rho_1$. Equation (3.8) clearly recovers the form of equation (3.5) and demonstrates the physical core-shell description of the three parameter CNT expression.

3.3 Thermodynamic Integration

To determine whether one particular system state, A, is preferential over another, B, or not – such as nucleation of different structures mentioned in section 3.2 – it is necessary to calculate the free energy difference between the two states. This can be calculated via the partition function for each of the system states. Here, the partition function is generally denoted as Z_i for state i. The change in the free energy from A to B is then

$$\Delta F_{AB} = -k_\mathrm{B}T\ln\left(\frac{Z_B}{Z_A}\right), \tag{3.9}$$

where the difference here is specifically in terms of the Helmholtz free energy: $F_i = -k_{\mathrm{B}}T \ln Z_i$. Moreover, the momentum terms are equivalent between the two states and can therefore be neglected. Hence, the partition function can be written as purely an N dimensional "configurational" quantity[22]: $Z_i = \int d\mathbf{r} \exp(-\beta U_i(\mathbf{r}))$.

However, in MD or MC simulations, it is not usually possible to perform this calculation directly since such simulations do not simulate over every possible microstate of a system, but rather sample an average across the microstates on the hypersurface[22, 24]. As required, equation (3.9) can be rewritten in terms of an observable average, by multiplying Z_B by unity,

$$Z_B = \int d\mathbf{r} \exp(-\beta U_B(\mathbf{r})) \exp(-\beta U_A(\mathbf{r})) \exp(\beta U_A(\mathbf{r}))\,, \tag{3.10}$$

and using the definition for the thermodynamic average,

$$\frac{Z_B}{Z_A} = \frac{1}{Z_A} \int d\mathbf{r} \exp(-\beta(U_B(\mathbf{r}) - U_A(\mathbf{r}))) \exp(-\beta U_A) \tag{3.11}$$

$$= \Big\langle \exp(-\beta(U_B(\mathbf{r}) - U_A(\mathbf{r})))\Big\rangle_A\,, \tag{3.12}$$

to yield the free energy difference as

$$\Delta F_{AB} = -k_{\mathrm{B}}T \ln\Big\langle \exp(-\beta(U_B(\mathbf{r}) - U_A(\mathbf{r})))\Big\rangle_A\,. \tag{3.13}$$

Equation (3.13) therefore allows for the calculation of the change in free energy from simulations by taking the difference in the potential energy between states A and B. However, if the potential difference between states A and B is large, then the expression for the average will tend to zero. Yet when this difference is small, there is a significant contribution from the average to the change in the free energy. Therefore, to calculate ΔF_{AB} between two states with very different potential energies, it is necessary to calculate ΔF_{AB} over $M-2$ intermediate states; where the potential energy is similar between two sequential intermediate states[22]. Hence, equation (3.13) can be written as the sum over the M states from A to B:

$$\Delta F_{AB} = -k_{\mathrm{B}}T \sum_{i=1}^{M-1} \ln\Big\langle \exp(-\beta(U_{i+1}(\mathbf{r}) - U_i(\mathbf{r}))\Big\rangle_i\,. \tag{3.14}$$

Hence, the calculation between M states results in the sum of $M-1$ averages.

Equation (3.14) is a discrete calculation that can be taken to the continuous limit by assuming a slow adiabatic change in the potential between states A and B with respect to some "switching parameter"[22], λ, which smoothly changes the

potential from that of the initial state to the final state. The overall form of the potential now becomes a function of λ as well, such that

$$U(\mathbf{r}, \lambda) = f(\lambda)U_A(\mathbf{r}) + g(\lambda)U_B(\mathbf{r})\,, \tag{3.15}$$

where $f(0) = 1$, $g(0) = 0$ in the initial state, and $f(1) = 0$, $g(1) = 1$ in the final state; and by extension $Z_i \equiv Z_i(\lambda)$, hence $F_i \equiv F_i(\lambda)$.

ΔF_{AB} can consequently be calculated by continuously summing the infinitesimal changes to the potential with respect to λ. Hence, from the definition of F,

$$\frac{\partial F}{\partial \lambda} = -\frac{1}{\beta Z}\frac{\partial Z}{\partial \lambda} \tag{3.16}$$

$$= \frac{1}{Z}\int d\mathbf{r}\exp(-\beta U(\mathbf{r}, \lambda))\frac{\partial}{\partial \lambda}\Big(U(\mathbf{r}, \lambda)\Big) \tag{3.17}$$

$$= \left\langle \frac{\partial U(\mathbf{r}, \lambda)}{\partial \lambda} \right\rangle_\lambda , \tag{3.18}$$

and by integrating equation (3.18), the free energy difference between the initial and final states can be recovered via thermodynamic integration (TI),

$$\Delta F_{AB} = \int_0^1 \Big\langle \frac{\partial U(\mathbf{r}, \lambda)}{\partial \lambda} \Big\rangle_\lambda d\lambda\,. \tag{3.19}$$

The success of TI rests in being able to choose appropriate functions of $f(\lambda)$ and $g(\lambda)$ that easily explore a pathway through free energy space between states A and B. In many cases, this pathway may have free energy barriers, or wells, that impede the evolution of the system from state A to state B. In these cases, MD or MC simulations would require long simulation times to observe a transition to the next state in the pathway, which is otherwise known as a "rare event"[22]. Instead of waiting a long time for a simulation to naturally evolve, there are various free energy methods that can be used to bias the system to more easily sample the pathway from A to B and encourage the occurrence of such rare events. Typically, such biasing techniques across the free energy surface are conducted in terms of a generalised "reaction coordinate"[22, 49], which is discussed in the following section.

3.3.1 Reaction Coordinates

Reaction coordinates are single valued quantities that measure the state a system is in along a reaction pathway from state A to state B[49]. Such quantities are

important when attempting to identify rare events, such as homogeneous nucleation, or transitions between states. In many complex systems, a reaction coordinate will typically be comprised of several degrees of freedom which characterise the system. It is often difficult to determine the best combination of such degrees of freedom which can accurately identify the unique system state along the reaction pathway[49]. The reaction coordinate that exactly identifies the system state is the "committor probability"[50], which indicates the number of phase space trajectories that can be initiated at a given system configuration, that will transition to state B with a given probability[49]. The probability distribution is dependent on the system itself, but – by definition – trajectories initiated at state A have a probability of transitioning to state B, P_B, of $P_B = 0$, those initiated at state B have $P_B = 1$, and transition states exist with $P_B = 0.5$[50].

The committor probability, while being able to exactly describe the likelihood of transitioning to state B from any given configuration, unfortunately does not provide any way of measuring the evolution of a system along a reaction pathway, due to its failure to link to any physical observable quantities[50]. Instead, it is necessary to find some combination of physically measurable quantities that closely reproduce the committor probability distribution. Such a method typically involves a costly and time consuming method of firstly reproducing the committor probability distribution. This is achieved by selecting systems at various configurations along the reaction pathway and then initialising the particles in each of them, multiple times, with different momenta sampled from a Boltzmann distribution. From such simulations, it is possible to count the frequency at which each initial configuration transitions to state B and recover the committor probabilities of each configuration along the reaction pathway[50]. Following this, it is then necessary to find some combination of physical observables that can be used to fit to the committor probability distribution across the entire reaction pathway. Doing so yields a single valued analytical expression for P_B in terms of the value of the observable quantities at each configuration, yet this is not trivial and requires significant care and effort.

Many methods have been investigated to combine observables to reproduce the committor probability distribution, such as using genetic neural networks[50], likelihood maximisation[49, 51] and string methods[52]. However, in simpler systems, it is often the case that a reaction coordinate can be chosen intuitively and tuned through trial and error[50]. In the case that only the end states A and B are of interest, and the full dynamical pathway is unimportant, then it is possible to characterise the two states using only a single observable. In such cases, such a

parameter is known as an "order parameter"[50]. This is true in the case of this research and the degree of crystallinity is enough to distinguish between the solid and liquid phases[53, 54]. Indeed, a full investigation of suitable order parameters used in this research is reported in chapter 5.

3.4 Umbrella Sampling

One way to overcome rare events is through the use of the umbrella sampling method[22]. The umbrella sampling method applies a biasing potential at discrete points s_i, along the reaction pathway (with reaction coordinate q), to drive the evolution of the system from the initial state towards the final state. Within a local region of states about s_i, the applied biasing potential usually has the form of that of a harmonic potential. This is known as the umbrella potential[22],

$$V(q, s_i) = \frac{1}{2}\kappa(q - s_i)^2 \,, \tag{3.20}$$

where the equilibrium point of the umbrella potential is centred on system state s_i along the reaction pathway, and κ is some constant; the total potential is then described as $U(\mathbf{r}) + V(q, s_i)$.

The addition of an umbrella potential at s_i alters the sampling across the reaction pathway to form a biased probability distribution function, $\tilde{P}(q, s_i)$. Such a biased probability distribution can be measured during a MD or MC simulation, by computing the amount of time a system spends in each state along the reaction pathway. This produces a biased histogram, $\tilde{H}_i(q)$, which yields

$$\tilde{P}(q, s_i) \approx \frac{1}{n_i \Delta q}\tilde{H}_i(q) \,, \tag{3.21}$$

where Δq is the bin width used in the biased histogram to sample a single system state along q, and n_i is the number of samples taken during the i^{th} simulation.

Once the biased probability distribution is obtained, the true distribution must be recovered by applying an unbiasing factor to $\tilde{P}(q, s_i)$, giving $P_i(q)$ for the i^{th} simulation with the i^{th} umbrella potential[22]. Doing this for each umbrella potential, results in a set of recovered probability distributions, which must be summed and weighted accordingly to obtain the overall probability distribution from the initial to the final system state. Hence the overall probability distribution

is

$$P(q) = \sum_{i=1}^{N} C_i(q) P_i(q)\,, \tag{3.22}$$

where N is the number of umbrella sampling windows (or simulations) performed and $C_i(q)$ is the weighting coefficient of the i^{th} window, which must sum to one across all umbrella windows. The degree of weighting is usually determined by minimising the error between the unbiased distribution, $P_i(q)$, and the sampled distribution, $\tilde{P}(q, s_i)$, obtained from the MD simulation[22]. Once the error is minimised, the weighting factors can be obtained for each umbrella window, allowing a full reconstruction of the original unbiased probability distribution as was described by equation (3.22).

Upon calculation of the full unbiased probability distribution, the free energy distribution is then simply

$$F(q) = -k_{\text{B}} T \ln P(q)\,. \tag{3.23}$$

This whole procedure is known as a "weighted histogram analysis method"[22]. The main restriction that must be adhered to if this method is to work, is the requirement that the sampling of each of the biased probability distributions is of equal quality. Failure to provide this, results in incomplete or uneven sampling across each umbrella window, skewing the weightings of each of the recovered probability distributions for the applied umbrella potential. Consequently, this leads to inaccurate calculation of the free energy.

Furthermore, when umbrella sampling is carried out, one does not know necessarily where all the biasing potentials should be placed along the reaction pathway to fully sample the free energy landscape. Hence, a simulation is usually carried out many times, each time noting where the simulation spent too much time in a potential well or was blocked by a potential barrier. On the next simulation, an umbrella potential is placed at the problem system state and run again. The procedure iterates until equal quality sampling of the free energy landscape is completed.

3.5 Metadynamics

Another way to calculate free energy potentials is through using metadynamics[55, 56]. Conceptually, metadynamics is relatively simple, and overcomes the rare event issue by smoothing out the free energy surface, homogenising the potential between

states A and B. How this smooth, broad sampling is achieved is by allowing the system to naturally explore the free energy surface that exists between states A and B. As this happens, the system will tend to approach states with a lower free energy than its present state, giving the effect of the system following a gradient descent approach. In order to move the system towards another state with higher free energy, encouraging further exploration of the free energy surface between states A and B, a history dependent additive biasing potential is placed onto the free energy surface at the present state. This is done during the simulation runtime, in the form of a small Gaussian potential and occurs at every iteration of the system. This has the effect of discouraging the system from exploring regions it has already visited. Continuing the gradient descent analogy, the system "rolls" away from the newly placed Gaussian. In the event that the system gets stuck in one of the local minima between the initial and final state, the continual placement of biasing Gaussian distributions will have the effect of "filling up" the local well. This smooths out the free energy potential and eventually the system escapes the local minimum. This effect of filling the free energy surface continues until the system has explored the entire range of states from A to B, producing a uniform potential, as shown pictographically in figure 3.1. The original free energy potential can be recovered by subtracting the total added Gaussian potentials from the final potential recorded at the end of the simulation.

It should also be noted that the evolution of the system, whilst always tending to a minimum in the free energy, also has some intrinsic random motion. This random motion is important as it stops the system from getting stuck at a single point on the free energy hypersurface, furthering exploration of the space. It is precisely because of this reason that the final filled-in energy surface is never completely flat.

However, there are problems with the metadynamics method, mainly being that careful selection of the reaction coordinates must be made before running the simulation, otherwise the MD simulation will generate incorrect and potentially non-physical results as the system explores an unintended free energy hypersurface[22]. It is therefore important to check, prior to running the simulation, whether the reaction coordinates selected are suitable or not. Furthermore, the time taken to fill the free energy surface from the initial to final states, is dependent upon the dimensionality of the system (scaling exponentially with the number of dimensions) and the size of the Gaussian potentials added[55]. However, the main advantage of this method, is that no a priori knowledge of the form of the free energy surface is needed before performing the computations, as opposed to methods such as umbrella

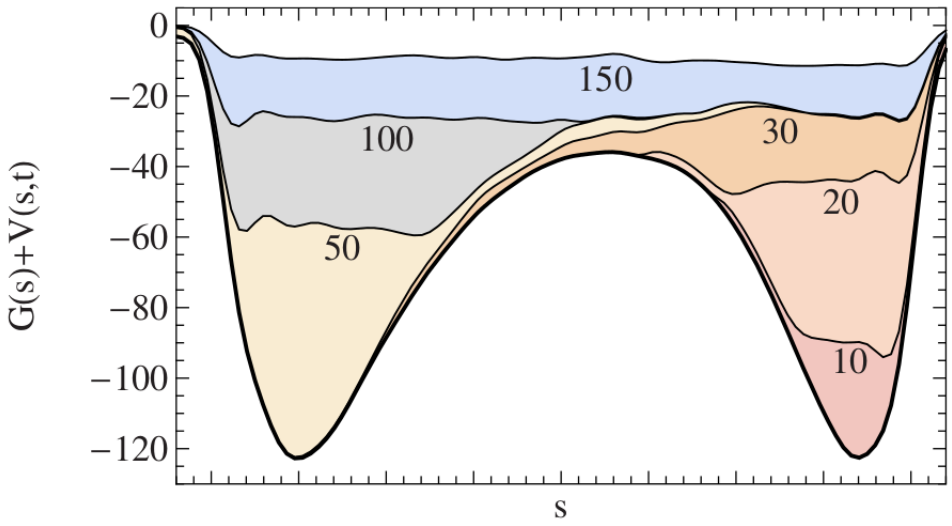

Figure 3.1: Illustration of a metadynamics algorithm exploring the free energy hypersurface; taken from ref. [56]. The underlying free energy hypersurface is shown as a function of reaction coordinate s, $G(s)$, given by the solid black curve. The accumulated biasing potential, $V(s)$, is shown at different times, denoted by different colours.

sampling discussed in section 3.4.

3.6 Cleaving Method

The cleaving method, originally proposed by Broughton and Gilmer[57], is another method for calculating the free energy, and has since been improved to resolve both the magnitude and anisotropy of the free energy[39]; although it is less precise than other methods, such as Capillary Wave Theory discussed in chapter 4, in resolving the anisotropy[1]. This method takes advantage of the thermodynamic theory proposed by Gibbs, in that a dividing mathematical surface between a system of two phases can contain all the thermodynamic properties associated with the interface, while the rest of the system accounts for the bulk thermodynamic properties of each phase[1, 56]. The total internal energy of the system can then be expressed as

$$E = \bar{E}_1 V_1 + \bar{E}_2 V_2 + eA\,, \tag{3.24}$$

where $\bar{E}_i$ is average energy associated with the i^{th} bulk phase, V_i is the volume of the i^{th} bulk phase, e is the interfacial surface excess energy and A is the surface

area between the two phases. In turn, the interfacial free energy can be defined as

$$\gamma = e - T\eta - \sum_i \mu_i \Gamma_i \,, \tag{3.25}$$

where η is the interfacial excess entropy, Γ_i is the number of particles of particle type i, and μ_i is the associated chemical potential (approximate bulk free energy), which is equivalent in both phases at coexistence[1]. The interfacial free energy is the work required to form a unit area of interface, which will be discussed in greater detail in chapter 4.

Using the definition of the interfacial free energy, the cleaving method can be used to measure such a quantity by setting up a solid-liquid interface. This solid-liquid interface is designed to be produced reversibly, allowing the reversible work, ΔW, in forming the interface to be computed via TI and using the definition that $\gamma = \Delta W/A$[1]; or by alternative means such as the Bennett acceptance ratio[58]. Reversibility is essential to ensure the TI yields the correct result for the free energy, which would otherwise be inaccurate through the existence of hysteresis loops found in irreversible processes. Hence, due to the necessity of reversibility, it is important to compute how the system is set up in the solid-liquid state slowly[1, 22, 58].

The cleaving method is implemented as follows:

- Initially, a solid crystal system is prepared and a separate liquid system is prepared.
- A cleaving potential is applied along a specified cleaving plane between two layers of the crystal structure and a similar potential is applied to the liquid system. This potential is applied slowly so as to not disrupt the crystal state nor the liquid state.
- Once the cleaving potential has been successfully applied, both systems will now be in two non-interacting halves.
- One half of the crystal system will be brought close to one half of the liquid system, essentially forming two separate non-interacting solid-liquid systems.
- The cleaving potentials between the liquid and crystal states are then slowly removed to allow the liquid and crystal regions to begin to interact. This has the effect of the systems going from being separate to completely coupled.
- After the liquid and crystal states are completely coupled, the cleaving potentials are now completely removed and the system will have formed an equilibrated solid-liquid interface.

The procedure outlined above produces a fully equilibrated solid-liquid interface. However, despite the conceptual simplicity of the procedure, the computation of the free energy at each step in the method is difficult and requires care. For instance, it is important that the introduction of the cleaving potentials do not perturb the solid or liquid, and once fully applied should instil an ordering at the liquid boundary that is compatible with the solid interface for eventual interaction[1]. These cleaving potentials are difficult to construct, and as such the alternative implementation of "cleaving walls" have been used[59]. Davidchack and Laird demonstrated such cleaving walls in hard sphere potentials, which consisted of a plane of fixed solid-like atoms in their ideal lattice positions. These were used to separate the solid and liquid systems in two and then bring the two halves together to interact by slowly removing the cleaving wall between the two halves. This is much easier to implement than fine tuning a suitable cleaving potential[59].

Furthermore, it is important to carefully calculate the reversible work done in forming the interface for all steps, in order to find the interfacial free energy of the equilibrated coexistence system. This involves accurately computing equation (3.19) along each of the stages in the method[1]. Each intermediate change in the work done is then summed together to give the total work done and compute the interfacial free energy.

3.7 Mold Integration

More recently, the mold integration method has been developed by Espinosa et al.[60] as an alternative way to directly calculate the solid-liquid interfacial free energy at coexistence conditions. Since the interfacial free energy is computed at coexistence, the bulk free energy difference between the two phases is zero. This means the interfacial free energy is

$$\gamma = \frac{\Delta G}{2A}\,, \tag{3.26}$$

where A is the area of the interface formed and ΔG is the Gibbs free energy calculated from the reversible work required to construct the crystal slab[60] within a liquid system at coexistence conditions.

The crystal plane of interest is constructed by applying a mold of fixed square well potentials, arranged such that their positions match that of the perfect crystal lattice in that plane. The wells have a radius, r_w, no larger than the radius of the particles in the simulation, ensuring only one particle can occupy a well at any

given time, and a well depth of energy ϵ. The mold of typically one or two planes, is positioned at some location along the simulation axis x, such that the crystal slab is formed in the yz plane of the simulation. The dimensions y and z of the simulation must be fixed to conform to the dimensions of the mold. The mold is then gradually applied from an initial state $\lambda = 0$, where particle interaction with the mold is zero, to a final state $\lambda = 1$, where particle interaction with the mold is maximal.

The potential energy of the system is then defined as

$$U(\lambda) = U_p(\mathbf{r_1}, ..., \mathbf{r_N}) + \lambda U_m(\mathbf{r_1}, ..., \mathbf{r_N}; \mathbf{r_{w_1}}, ..., \mathbf{r_{w_n}}) \,, \tag{3.27}$$

where U_p is the potential energy of N particles interacting with one another and U_m is the potential energy of N particles interacting with n wells in the mold. Performing TI on $U(\lambda)$ from $\lambda = 0$ to $\lambda = 1$, recovers the free energy difference, ΔG_m, between the liquid and the liquid-plus-mold system. ΔG can be recovered by removing the energy contribution between the mold and the particles from ΔG_m[60].

The method is relatively simple to implement and has the benefit of not requiring the use of any order parameters to distinguish between the solid and liquid phases, which may otherwise be difficult to define. The only caveat that exists with this technique is the choice of r_w. Espinosa et al. found that the Gibbs free energy in the liquid phase is a function of r_w; i.e. $G(r_w)$. At some value of r_w, r'_w, application of the mold to the liquid phase increases the Gibbs free energy of the liquid phase to exactly match that with the energy associated with the formation of a solid-liquid interface. However, r'_w is not known in advance. If $r_w < r'_w$, it is found that $G(r_w) > G(r'_w)$ and the solid slab instantly forms. Conversely, if $r_w > r'_w$, but still less than the particle radius, $G(r_w) < G(r'_w)$; meaning a stable liquid phase persists for some time after the activation of the mold. In principle, successive simulations varying the size of r_w can be performed to find r'_w and calculate γ; though in practise several simulations are performed for different values of $r_w > r'_w$ to underestimate γ. The resulting functional form of $\gamma(r_w)$ is then calculated and the true result computed for $\gamma(r'_w)$[60].

In summary, the steps required to implement mold integration are as follows:

- A mold of square potential wells, arranged in the structure of the plane of the solid to be examined, is constructed with dimensions y and z.
- The system is initialised in the liquid phase at coexistence conditions, with y and z dimensions that conform to that of the potential mold.
- The mold is applied to several simulations with varying r_w to bracket r'_w.

- The mold with is then gradually applied to the liquid, from initial state $\lambda = 0$ to final state $\lambda = 1$, for several simulations with varying r_w larger than the estimated value of r'_w.
- A functional form of $\gamma(r_w)$ is computed and calculated for $\gamma(r'_w)$, to yield the correct solid-liquid coexistence interfacial free energy.

Chapter 4

Capillary Wave Method

4.1 Introduction

In addition to the free energy methods discussed in chapter 3, the capillary wave method (CWM) can also be used to calculate the free energy associated with the formation of an interface between a solid and a liquid, in MD or MC simulations. This is achieved by measuring a property known as the interfacial stiffness and using its relation to the interfacial free energy; the former of which is recovered from the measurement of the local interface positions in real-space. CWM is the method used in this thesis to make such interfacial free energy measurements and is therefore discussed and validated in this chapter.

It should be noted, that when referring to system direction, x refers to the long axis of the simulation, y refers to the short axis of the simulation and z refers to the axis along the length of the interface.

4.2 Capillary Wave Theory

Consider a solid in contact with its liquid phase. Between the two bulk phases, an interface will form. Despite the fundamentally atomistic description of the solid-liquid boundary, the interface can be approximated to be continuous in the large length-scale limit. This is justified largely by the fact that the two bulk phases will have different densities and ordering. While the solid phase will form a step-wise boundary, through the presence or absence of crystal planes, the liquid phase will allow atoms to exist at irregular positions between the solid planes. Given the interface is an interaction between the two phases, the actual position of the interface over a given area element, dA, must be described by some value that

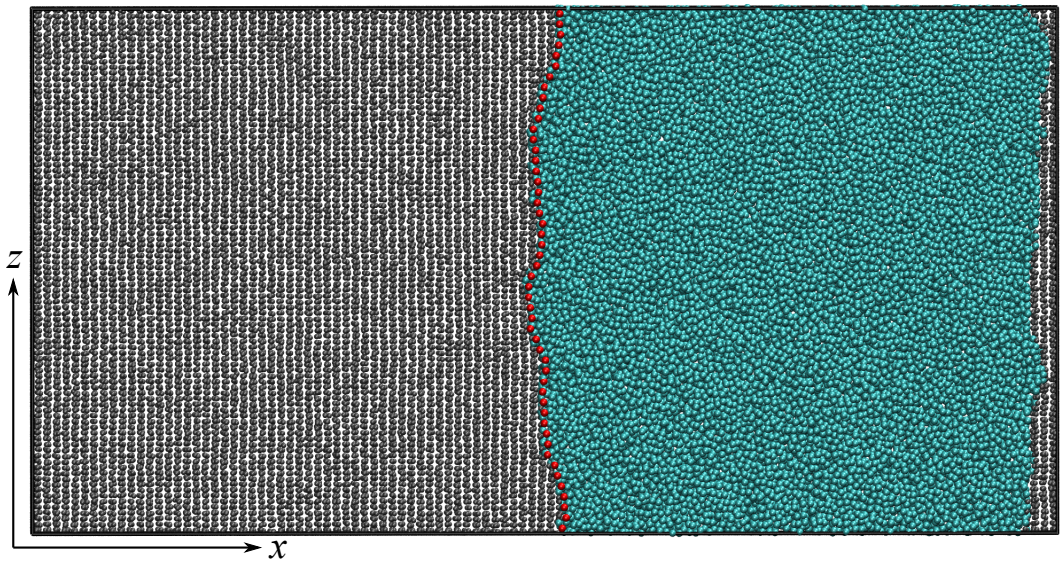

Figure 4.1: Simulation profile for the (111)[1$\bar{1}$0] system using the $q12$ order parameter and $80 \times 1 \times 50$ bins in the x, y and z directions respectively. The red points indicate the average position of the interface detected along x in a region of size Δz along z.

considers the presence of both phases. Interpolating such a quantity between area elements, results in an interface which at every point on the surface has a local real-space position and a surface normal vector. The position can be described by a single valued height function for a 2D interface by $h(y, z)$, or by $h(z)$ for a 1D interface; with subsequent normal vector to an interface line element, dl. For simplicity, capillary wave theory (CWT) is outlined here for a 1D interface, and figure 4.1 is used as reference for the real-space positions and directions of such an interface. Figure 4.1 clearly shows the discrete nature of the solid phase interface, juxtaposed with the more irregular morphology of the liquid phase interface. Figure 4.1 also shows the actual measured interface positions in red, obtained as described in section 4.3.

Due to cohesion, it is energetically favourable to minimise the surface area of the interface, and so any deviations from a flat interface will contribute to a change in the energy. Deviations from a flat interface are given by the angle between the local surface normal and the direction of the perfectly flat interface, θ[61]. For a solid-liquid interface at equilibrium, while the average temperature will remain constant, the kinetic energy of the particles in both phases will transfer heat across the interface. This interaction will cause points of localised melting of the solid and freezing of the liquid, as energy is transferred from the liquid to the solid.

These thermal fluctuations of the interface cause the deviations shown in figure 4.1; increasing the energy required to make the surface. This energy is a function of both the temperature, T, and θ, i.e. $\gamma(T,\theta)$, known as the surface tension or interfacial free energy. At constant T, the total energy of the interface can be found in 1D by integrating the contribution of the surface tension over each element, dl, of the surface contour, C,

$$E = \int_C dl\gamma(\theta)\,, \tag{4.1}$$

where $dl = \sqrt{dh^2 + dz^2}$, is a line element on the surface[62]. From the definition of θ, it is observed that $\theta = \arctan(dh/dz)$, hence equation (4.1) can be rewritten as

$$E = \int_0^L dz\gamma\left(\frac{dh}{dz}\right)\sqrt{1+\left(\frac{dh}{dz}\right)^2}\,, \tag{4.2}$$

where the integration is performed over the length of the bound surface in 1D from $z = 0$ to $z = L$. This approximation is valid assuming that the deviation of a line element is very small, i.e. the interface is continuous in the large length-scale, which implies $dh/dz \to 0$. A Taylor expansion of the integrand about zero to second order gives

$$\gamma(0) + \gamma'(0)\left(\frac{dh}{dz}\right) + \frac{(\gamma(0)+\gamma''(0))}{2}\left(\frac{dh}{dz}\right)^2\,, \tag{4.3}$$

where the first term contributes to the energy of a perfectly flat interface, the second term only contributes to the endpoints of the interface – which is of no interest – and the third term contributes to the energy fluctuation across the interface, ΔE. The third term also defines the quantity

$$\tilde{\gamma} \equiv \gamma(0) + \gamma''(0)\,, \tag{4.4}$$

which is the interfacial stiffness[62–65], linking the interfacial free energy to the interfacial stiffness.

The variation in the energy associated with the fluctuation of the interface is

$$\Delta E = \frac{\tilde{\gamma}}{2}\int_0^L dz\left(\frac{dh}{dz}\right)^2\,. \tag{4.5}$$

It is possible to measure the interfacial stiffness from equation (4.5) by decomposing the real-space fluctuations of the height function into Fourier modes and measuring the independent mean-square contribution from each mode. In 1D, the Fourier transforms used are

$$h(\mathbf{q}) = \frac{1}{A}\sum_{\mathbf{r}} h(\mathbf{r})e^{-i\mathbf{q}\cdot\mathbf{r}} \tag{4.6}$$

$$h(\mathbf{r}) = \sum_{\mathbf{q}} h(\mathbf{q})e^{i\mathbf{q}\cdot\mathbf{r}}\,, \tag{4.7}$$

where the normalisation in the forward transform is over the area, A, of the interface; which is just the length, L. $\mathbf{q}$ and $\mathbf{r}$ are defined as $\mathbf{q} = q_z\hat{\mathbf{z}}$ and $\mathbf{r} = z\hat{\mathbf{z}}$; which for brevity are equivalent to q and r in 1D. Using equation (4.7), equation (4.5) can be transformed to

$$\Delta E = \frac{\tilde{\gamma}A}{2}\sum_{q} h(q)h(-q)q^2\,. \tag{4.8}$$

Since the energy contribution of each Fourier mode is independent from one another and that the average energy contribution follows a Boltzmann distribution, then from the equipartition theorem, the average change in the surface energy for each independent surface mode is $\langle \Delta E \rangle = \frac{1}{2}k_{\mathrm{B}}T$. Hence, rearranging equation (4.8), the average transformed height becomes

$$\langle h(q)h(-q)\rangle = \langle |h(q)|^2\rangle = \frac{k_{\mathrm{B}}T}{A\tilde{\gamma}q^2}\,, \tag{4.9}$$

which is the standard result for capillary waves across a continuous interface[12, 62].

It should be noted however, that equation (4.9) does not completely describe all planar deformations of the interface. Instead, equation (4.9) can be extended to include the "bending rigidity" term, κ, to describe the overall degree of curvature of the interface, independent of thermal fluctuations[66]. A similar treatment by Turner and Sens for measuring the deformation of uniform fluid membranes[67], also includes the "elastic modulus" term, $\mathcal{E}$. This yields an equation of the form

$$\langle h(q)h(-q)\rangle = \langle |h(q)|^2\rangle = \frac{k_{\mathrm{B}}T}{A\big(\mathcal{E}q + \tilde{\gamma}q^2 + \kappa q^4\big)}\,, \tag{4.10}$$

where the interfacial stiffness term dominates at long wavelengths, the bending rigidity dominates at short wavelengths[68] and the elastic modulus dominates at very long wavelengths. Whilst fitting $\langle |h(q)|^2\rangle$ against q using equation (4.10) is

more accurate than using (4.9), this is not strictly necessary in the case of this research. It is only necessary to get an accurate measurement of the interfacial stiffness, which requires careful fitting to the long wavelength results. Attempts to include additional fitting to irrelevant short wavelengths can adversely affect the goodness of fit to the long wavelengths. Furthermore, the addition of κ complicates the distinction between long and short wavelengths that can and cannot be described by CWT; the determination of which is discussed more completely in section 4.5.

In the case of fitting using the addition of $\mathcal{E}$, it is also found that this does not provide any significant improvement to the fit of $\tilde{\gamma}$. Indeed, evidence suggests that there is no strong contribution to the elastic modulus, given the dimensions of the system sizes used in this research. Therefore, neither $\mathcal{E}$ nor κ are included in the determination of $\tilde{\gamma}$ in this work; further justification of which is provided in chapter 6.

Consequently, from the standard result of CWT, the stiffness can easily be calculated. Taking a log-log plot of the measured $\left\langle |h(q)|^2 \right\rangle$ against q, equation (4.9) can be simply rearranged to give,

$$\log\left(\frac{A}{k_{\mathrm{B}}T}\left\langle \left|h(q)\right|^2 \right\rangle\right) = -2\log q - \log\tilde{\gamma}\,. \tag{4.11}$$

Performing a simple linear regression straight line fit to equation (4.11), where the gradient must be constrained to be -2 by CWT, allows the interfacial stiffness to be recovered from the value of the fitted intercept, $c = -\log\tilde{\gamma}$.

The result derived in equation (4.5) is the 1D result, but in practise, simulations and experiments typically are conducted with surfaces that are 2D or quasi-1D (where one of the system axes is very short). The only differences in this case, is that the integration is performed over the surface element, dS, instead of the line element, resulting in the fluctuation of the surface energy more generally being defined as

$$\Delta E = \frac{1}{2}\int_S dydz...(\tilde{\gamma}_y {h_y}^2 + \tilde{\gamma}_z {h_z}^2 + ...)\,, \tag{4.12}$$

where $h_y = \partial h(y,z,...)/\partial y$, for n-dimensional interfaces[62, 63, 69]. The interfacial stiffness will generally be different along different directions in the plane of the interface. However, if such directions are orthogonal and parallel to the simulation axes, then the stiffnesses are the same[65, 70].

Within the context of simulations, the local position of the interface cannot be resolved with infinite resolution. Instead, the position must be resolved over a

discrete region. For a 2D interface, if the interface is discretised into bins in two perpendicular directions in the plane of the interface, $\hat{\mathbf{y}}$ and $\hat{\mathbf{z}}$, with bin widths, Δ_y and Δ_z, respectively, then $\mathbf{q} = q_y\hat{\mathbf{y}} + q_z\hat{\mathbf{z}}$ and $\mathbf{r} = a\Delta_y\hat{\mathbf{y}} + b\Delta_z\hat{\mathbf{z}}$; where a and b are integers. Now, applying equation (4.7) to equation (4.12) gives

$$\left\langle \left|h(\mathbf{q})\right|^2 \right\rangle = \frac{1}{4}k_{\mathrm{B}}T\left[\frac{\gamma_y}{\Delta_y^2}\sin^2\left(\frac{q_y\Delta_y}{2}\right) + \frac{\gamma_z}{\Delta_z^2}\sin^2\left(\frac{q_z\Delta_z}{2}\right)\right]^{-1}, \tag{4.13}$$

the derivation of which can be seen in full in appendix A. Observe that if the interface being simulated or measured is quasi-1D and hence $q_y \to 0$, then providing $q_z\Delta_z/2 \ll 1$, the result is the same as the "continuum limit" expression in equation (4.9)[71]. This constraint on a simulation, determines when the measurements obtained for the mean-square transformed heights can be accurately modelled by CWT.

4.2.1 Real-space Fluctuations

Whether the interface being measured in a simulation or an experiment is 1D or 2D, will determine how well the fluctuations can be measured. This can be seen by examining the real-space fluctuations of the interface. In general, the real-space fluctuations are given[63, 69, 72] by

$$\left\langle h^2(\mathbf{r})\right\rangle = \sum_{\mathbf{q}}\left\langle |h(\mathbf{q})|^2\right\rangle = \frac{1}{(2\pi)^2}\int d\mathbf{q}\left\langle |h(\mathbf{q})|^2\right\rangle. \tag{4.14}$$

The appropriate expression for $\left\langle |h(\mathbf{q})|^2\right\rangle$ can then be substituted into equation (4.14), depending on whether the system is 1D or 2D.

In 2D, after substitution, a transformation to polar coordinates reduces the integral to $\int dq/q$, while in 1D the integral performed is simply $\int dq/q^2$. The limits on the integrals are then $q = 2\pi/L$ to $q = 2\pi/a_0$. The upper limit of q is consequently the shortest wavelength fluctuation that can occur, which is proportional to $1/a_0$; where a_0 is the lattice spacing. Similarly, the lower limit of q is the largest wavelength fluctuation that can occur, which is proportional to $1/L$. In these limits, the mean-square real-space fluctuations in 1D and 2D are

$$\left\langle h^2(x)\right\rangle \propto L - a \tag{4.15}$$

$$\left\langle h^2(x,y)\right\rangle \propto \ln(L/a)\,, \tag{4.16}$$

respectively. This indicates that the real-space fluctuations increase linearly with the

length of the interface in 1D, but only logarithmically with the size of the interface in 2D; hence fluctuations are more easily identifiable for ribbon-like interfaces.

4.3 Interface Measurement

Measurement of the interface position requires being able to distinguish between the solid and the liquid. To do this, one can use an "order parameter" that can label each atom as being either solid-like or liquid-like. There are many possible order parameters that can be used and the discussion of those used in this research is left until chapter 5. Instead, at this point, the existence of a suitable order parameter is assumed, called ω, and that the value of such an order parameter, per atom, is large for particles in the solid region, small in the liquid region, and between this range near to the interface.

The difference in the value of the order parameter between solid-like and liquid-like atoms can be used to generate an order parameter profile along the length of the simulation, x. However, the system must be discretised in the direction along the length of the interface, z, into n bins of equal width. This results in a unique order parameter profile over x for each bin and allows a value for the interface position to be assigned in each bin. It would not be possible to use the individual per atom values of the order parameter to identify the interface without binning in z for two reasons. Firstly, fluctuations can exist in the simulations where atoms in one of the bulk phases can be identified as belonging to the other. This is most problematic close to the interface where the value of the order parameter, per atom, varies between solid-like values and liquid-like values and thus has the effect of broadening the interface in the x direction. This makes it difficult to definitely say where the system has transitioned from one bulk phase to the other, based on the value of individual atoms near to the interface alone. Secondly, atoms do not occupy every point in space and so there are regions along z where the order parameter is undefined. Instead, plotting the order parameter as a function of the n bins along z gives a continuous, coarse-grained form of the interface, and an average position of the interface in each bin over the bin width Δz.

Since fluctuations can occur in the bulk phases, discretising in x is also necessary. This smooths out fluctuations that occur in the system and more sharply resolves the position of the interface as a function of x for each bin n; as shown in figure 4.2. This method results in essentially splitting the system into a $m \times n$ voxels that preserve the geometry of the system; where m is the number of bins along x. Therefore, if the system is triclinic, then each voxel is also equally triclinic. This

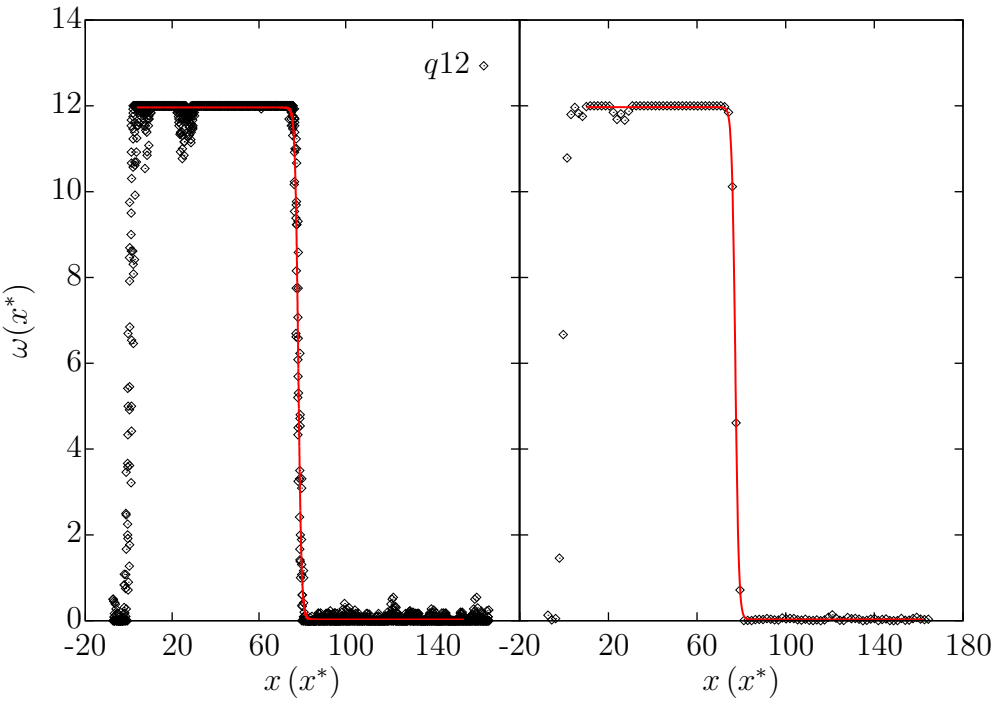

Figure 4.2: $q12$ order parameter profile and fit during an LJ-BG simulation of the (100)[001] orientation, without discretisation in x, (*left*), and when using a discretisation of 100×50 bins in the xz plane, (*right*).

constraint ensures that each voxel resides within the system boundaries and contains the same fraction of the overall system volume. Providing the density of each voxel is non-zero, then the per atom order parameter measured can be averaged over each voxel.

Having a smooth order parameter profile for each bin n in z enables, a function to be fitted to the order parameter profile of the form[70, 72]

$$\omega_n(x) = \left(\frac{\omega_\mathrm{s} + \omega_\mathrm{l}}{2}\right) - \left(\frac{\omega_\mathrm{s} - \omega_\mathrm{l}}{2}\right) \tanh\left(\frac{x - h_n}{w_n}\right), \tag{4.17}$$

where the inflexion point, h_n, defines the position of the interface for bin n, w_n is the local width of the interface in bin n, and ω_s and ω_l are the average values of the order parameter in the respective solid and liquid phases. The form of the function in equation (4.17) assumes that the system transitions from solid to liquid along x. If the reverse is true, the sign of the amplitude of the tanh function is inverted.

Figure 4.2 shows how discretising in x effects the fit of the tanh curve to the order parameter profile in a LJ system for a single bin, $n = 0$, along z. In the case of no binning along x, (*left*), the inflexion point is located at $h_0 = 78.1$, while in

the case of binning, (*right*), the inflexion point is at $h_0 = 77.3$. The Chi-Squared goodness of fit for both the unbinned and binned fits are $\chi^2 = 0.09$ and $\chi^2 = 0.004$, respectively. Hence, a better fit to the order parameter profile can be obtained by discretising along x, whilst introducing a slight shift in the measured inflexion point. Essentially, the finer the discretisation in x, the closer the measured inflexion point becomes to the interface position without binning. The effect this has on the measured interfacial stiffness is demonstrated in chapter 5. It is clear though, that coarser discretisation in x provides better fitting to the order parameter profile and more effectively removes fluctuations in the bulk phases. In the case of (*left*), there are two significant distortions in the bulk solid: a clearly visible distortion at $x = 24.7$; and a second near to the second interface at the periodic boundary, at $x = 7.5$. This second distortion could equally as likely have been at the central interface where the measurement of the interface position was made. However, in (*right*), both of these distortions are substantially reduced and conform more closely to the value of the order parameter in the bulk solid; it is also much clearer where the second interface begins.

In general, the choice for the number of voxels to use along each of the system directions is constrained by three attributes:

- Firstly, only one voxel must be used along the short direction: since the 1D CWM is applied and only capillary waves are measured along the length of the interface. Therefore, the system must be *sufficiently small* in the y direction as to exhibit no curvature of the interface in the y direction and only curvature in the z direction.

- Secondly, at least one atom must exist in each voxel along the long direction of the system. This ensures the continuity of the order parameter profile is preserved and hence the size of the voxel in x should be no smaller than the lattice parameter of the solid, a_0.

- Thirdly, the width of each voxel in z must be large enough to map the position of the solid-like particles along the length of the interface and so should also be no smaller than the lattice parameter of the solid[71]. It must also be small enough that the continuum limit in equation (4.13) is satisfied.

This final point is worth expanding on. Recall from section 4.2, that the continuum limit corresponds to $q_z\Delta_z/2 \ll 1$. Here it is imposed that this condition is satisfied when $q_z\Delta_z/2 \leq 0.5$. Given that n bins of bin width $\Delta_z = z/n$ will Fourier transform to N points as $q_z = 2N\pi/z$, then this results in only $N \leq n/2\pi$

points that can be used to both fit to find the interfacial stiffness and satisfy the continuum limit. This constraint further imposes a condition on the minimum size of the system in z for the maximum resolution of the interface. If the width is constrained to be $\Delta_z = a_0$, and at least N' data points are required for a reliable measurement of the interfacial stiffness, then a minimum of $n' = 2\pi N'$ bins are required and the minimum system size in z becomes $z' = 2\pi N' a_0$.

Overall, how the system is discretised along x is a balance between being able to reliably fit to the order parameter profile and being able to most accurately represent the true position of the interface. When validating the implementation of the CWM to measure the interfacial stiffness of several LJ systems, research has not been conducted on how the choice of binning in the x direction affects the measurement. Instead, this research follows closely the method and approximations set out by Morris, where the widths of bins in the x and z directions were chosen to be close to the lattice spacing, a_0, of the FCC LJ crystal[71]; where $a_0 \approx 1.2$, at $T^* = 0.62$ and $P^* = 0$. While the affect of binning has not been investigated in the case of the LJ systems, it has been investigated thoroughly for the case of the ice systems. These results are presented in chapter 5, as well as the results when varying the system thickness in y, in order to answer the question: "What size of y constitutes *sufficiently small*?".

4.4 Validation

Following CWT in section 4.2, and the principles for solid-like and liquid-like particle detection in section 4.3, two computational codes were written to implement the CWM; an order parameter code, and an interface analysis code. Both of these programs were bespoke and consequently needed to be validated before they could be used to measure the interfacial free energy for the ice systems of interest. The codes themselves are not discussed in this thesis, but can be found in full on the storage device submitted with this thesis. Presented here is a review of the implemented CWM, tested against LJ solid-liquid equilibrium simulations, the results of the measured interfacial stiffnesses and the comparison to existing literature results of the same systems. It should be noted, that since the simulations conducted are of LJ systems, all units are reduced; unless stated otherwise.

4.4.1 Simulation Details

Using the Large-scale Atomic/Molecular Massively Parallel Simulator (LAMMPS) MD package[34], simulations with periodic boundary conditions were conducted to

model solid-liquid coexistence of an infinite LJ system with a quasi-1D ribbon-like interface. Using the modified LJ potential suggested by Broughton and Gilmer as discussed in chapter 2, the systems used a potential cutoff of 2.5σ and were physically large enough so that self-interaction of the atoms was not possible. The truncated shifted LJ potential and force field was tabulated from $r = 0.1\sigma$ to $r = 2.5\sigma$ in steps of $1.2 \times 10^{-5}\sigma$ and smoothed by LAMMPS using linear interpolation of the potential and force fields. For these simulations it was chosen that $\epsilon = \sigma = 1$. The MD simulations were performed using velocity Verlet time integration of Nosé-Hoover style equations of motion with the adjustment proposed by Martyna, Tobias, and Klein[31].

The simulations were initialised by first creating a perfect crystal lattice and then slowly relaxing the system anisotropically. The system was then separated into a liquid half and a solid half, along x, where the atoms in the liquid half were randomly assigned velocities from a gaussian distribution to give an average liquid region temperature of 0.7. The velocities of these liquid-like atoms were chosen in such a way as to ensure the overall momentum of the system was zero. The liquid region was then allowed to evolve in the NPT ensemble, at a pressure of $P^* = 0$, raising the liquid region from a temperature of 0.7 to 1.3 while the solid region was kept frozen. As the liquid region evolved, all atoms were allowed to dilate to avoid any unphysical displacement of atoms in the solid that may be caused by only atoms dilating in the liquid region. This was done over $200,000$ iterations, with a very small timestep of 0.001 and low damping of the thermostat of 1 and low damping of the barostat of 10. These damping coefficients were 10 times the value of normal simulation damping coefficients, allowing the temperature and pressure to be less vigorously corrected over the iterations. This more delicate treatment of the system was necessary to stop the liquid region from completely freezing, or the temperature rising too quickly and causing sudden pressure spikes in the liquid region causing the system to explode.

The solid and liquid regions were then allowed to interact. The velocities of all the particles were sampled to give an average system temperature of 0.65. The whole system could then evolve in the NPH ensemble, coupling the y and z directions, to stop disproportionate deformation of the interface in the yz plane as the system equilibrated. The NPH ensemble was run over 1.75×10^6 iterations with a timestep of 0.005 and normal damping coefficients, since it was not necessary to treat the system quite so delicately. Once the simulation had completed this duration, the system was then run for a further 1.75×10^6 iterations in the fully anisotropic NPH ensemble.

Orientation	Geometry $x \times y \times z$	Atoms
(100)[001]	173.51×9.71×80.90	120,000
(110)[001]	171.71×9.71×80.11	117,600
(111)[1$\bar{1}$0]	120.34×9.92×57.25	61,000

Table 4.1: Simulation setups for the LJ-BG systems.

Sampling was conducted every 1000 iterations and only the last 1.5×10^6 iterations were used for the production run to collect data for the validation of the implemented CWM. The simulation geometries of the three systems simulated, are shown in table 4.1.

The system sizes were chosen so that the y direction was kept comparably short to the length of the short direction in the simulations conducted by Morris and Song[73]. The length of the x direction was chosen to be approximately $2z$, to ensure that capillary waves along the two interfaces in the simulation, did not interact with each other and cause correlated disturbances.

4.4.2 Results

The simulations were analysed with a discretisation resulting in bin widths close to the lattice parameter of the LJ solid, in accordance with the method proposed by Morris[71]. The discretisation is shown in table 4.2.

To validate this implementation of the CWM, three orientations were chosen that had also been computed by Morris and Song[73]. It was not necessary to simulate more since the purpose of this exercise was to check that the program developed did indeed work correctly. Furthermore, it was not necessary to calculate the interfacial free energies, since if agreement was found between the measured interfacial stiffnesses, then the free energies would also agree. The orientations chosen were the (100)[001], (110)[001] and (111)[1$\bar{1}$0]; where the notation indicates the crystal plane forming the interface, (abc), and the crystal direction, $[def]$, parallel with the y direction of the simulation. The reason these interfaces were chosen,

Orientation	Bins			
	N_z	Δ_z	N_x	Δ_x
(100)[001]	50	1.62	100	1.74
(110)[001]	50	1.60	100	1.72
(111)[1$\bar{1}$0]	35	1.64	70	1.72

Table 4.2: Analysis details for the LJ simulations.

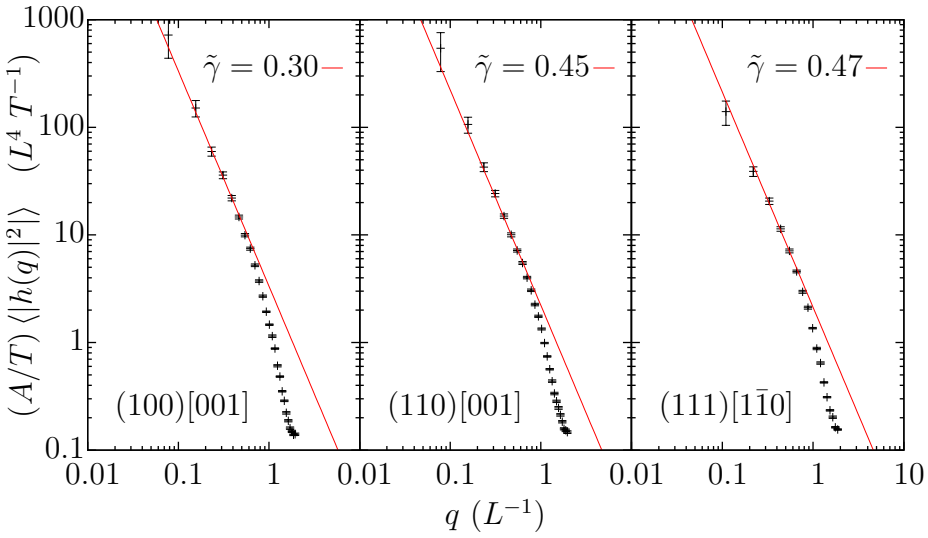

Figure 4.3: Log-log plots of the interfacial stiffness for LJ-BG systems after using the $q12$ order parameter.

was because they were relatively easy to set up and were indicated to give a clear resolution between the measured stiffness of the (100)[001] orientation and the other two.

Since the interfacial stiffness can be recovered easily by plotting $(A/T)\langle|h(q)|^2\rangle$ against q on a log-log scale, the results are presented in such a manner as shown in figure 4.3. It should be observed that CWT indicates that for low values of q where the continuum limit of the theory is valid, the data should form a straight line with a gradient of -2. This is indeed what is observed and the data deviates from this line where CWT is no longer valid. The red lines are fits to the data only where CWT is valid – using the first 6, 8 and 5 data points for the (100)[001], (110)[001] and (111)[1$\bar{1}$0] orientations, respectively – where the value of $\tilde{\gamma}$ used in the fit to equation (4.11), is stated. It should be noted that these fits are the result of using the $q12$ order parameter to identify between the liquid-like and solid-like atoms; these order parameters are discussed in detail in chapter 5, but are still reported here for completeness.

The measured interfacial stiffness results for the three orientations are also presented in table 4.3 for implementations of the $q6$ and $q12$ order parameters, along with the results for the same orientations reported by Morris and Song[73]. The number in brackets gives the error on the reported value on the last decimal place.

Between figure 4.3 and table 4.3, it is clear that there is good agreement between the results for the interfacial stiffness obtained in this research and those

Orientation	$\tilde{\gamma}$ (mJ m^{-2})		$\tilde{\gamma}_{\text{Morris}}$ (mJ m^{-2})
	$q6$	$q12$	
(100)[001]	0.302(8)	0.30(1)	0.31(5)
(110)[001]	0.41(1)	0.45(1)	0.47(7)
(111)[1$\bar{1}$0]	0.41(2)	0.47(2)	0.45(4)

Table 4.3: Measured interfacial stiffness values for LJ-BG obtained from this work and comparable values from Morris and Song[73].

obtained by Morris and Song. All results obtained are within the errors of the results quoted by Morris and Song and there is clear resolution between the (100)[001] orientation and the (110)[001] and (111)[1$\bar{1}$0] orientations; obtained with greater precision than that of Morris and Song.

While the results obtained from using either order parameter are within the errors reported by Morris and Song – which validates the implemented CWM – there is certainly a difference in the measured values between using $q6$ and $q12$, indicated from this work. The results when using $q12$ are more within errors of Morris and Song's results, than that of $q6$. Furthermore, $q12$ seems to measure a higher interfacial stiffness. While a full discussion of this appears in chapter 5, this is an early indication of the greater accuracy of $q12$.

4.5 Choice of Wavenumber

The maximum wavenumber that can be used to fit for the stiffness requires some degree of qualitative assessment. As seen in figure 4.3, CWT is only valid up to a given wavenumber, at which point the trend deviates form the linearity predicted by CWT. This sets an upper limit on the largest wavenumber that can be used to fit for the stiffness.

As discussed in section 4.2, a criterion for the validity of CWT is that $q_z\Delta_z \ll 1$. Typically, this research has considered $q_z\Delta_z \leq 0.5$ to satisfy this condition, however this is more of a rule-of-thumb and CWT can hold beyond this limit or break before. In ideal circumstances, production runs would be long enough, such that the longest wavelength fluctuations have enough time to average out sufficiently, thus reducing the error on these measurements and agreeing closer with the theory. In this long-time limit, fits to the data for any value of q, should result in the same value of stiffness up until where CWT begins to fail.

Figure 4.4 shows that fits to the data using only the largest wavelengths do not provide the same value for the stiffness as when using up to smaller wavelengths.

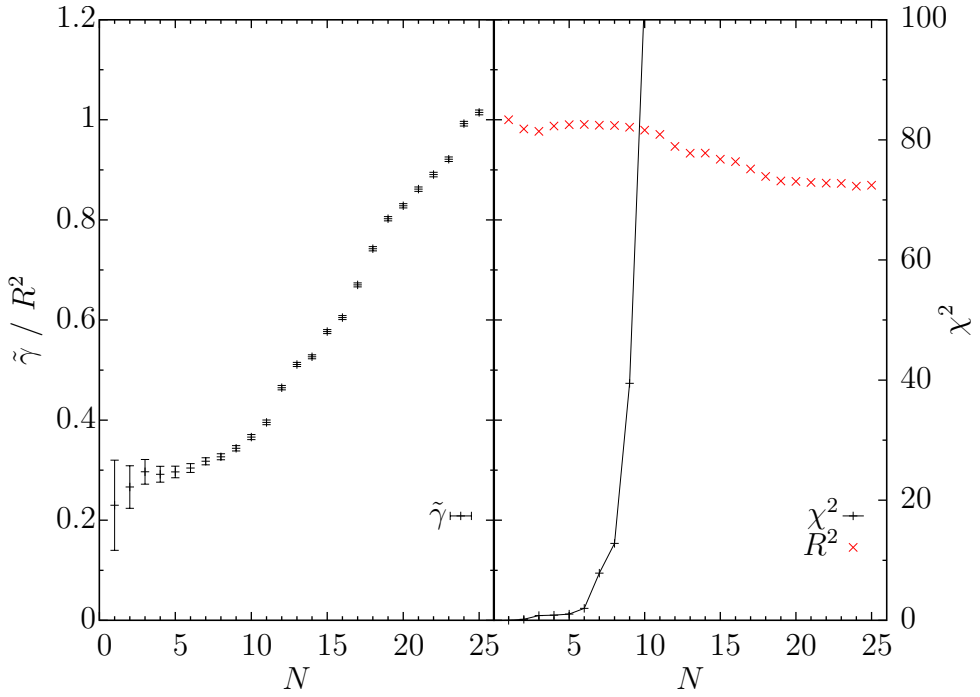

Figure 4.4: *Left:* Fitted interfacial stiffness values for the LJ (100)[001] orientation up to and including N wavenumbers. *Right:* The measured χ^2 and R^2 values for the fit up to different N wavenumbers.

This is because the long wavelength fluctuations require very long production runs to average out, which is not always achievable. This is not too problematic though, since shorter wavelength fluctuations occur much more rapidly and require substantially less time to generate statistically significant results. Furthermore, since the fit is weighted by the error on each of the N data points (where N is defined as in section 4.3), the data points with smaller errors contribute more to the fit of equation (4.11).

Performing straight line fits over N wavenumbers, as done in figure 4.4, shows that while CWT is still valid, the measured stiffness does tend to a constant the more wavenumbers are used; until the continuum limit of CWT is no longer valid. However, it is not clear precisely where deviations away from CWT begin. To aid in choosing the best number of wavenumbers to fit to, the χ^2 goodness of fit and the R^2 value are both plotted as a function of N. Normally, where the χ^2 is lowest and where R^2 is highest, indicate where the best fit is; but this will always be for using the longest wavelength only. Instead it is better to look for where the χ^2 increases sharply, indicating a sudden deviation away from a straight line fit; and also to look for where R^2 is highest away from using just the lowest wavenumber, or begins to

drop sharply. In figure 4.4, the χ^2 deviates sharply after $N = 6$, which coincides where R^2 is also highest away from $N = 1$. Therefore, in the case of the (100)[001] orientation for the LJ-BG system, this is how 6 data points were chosen to fit for the stiffness.

4.6 Error Measurements

When performing statistical sampling of observable quantities from MD simulations, it is also possible to measure errors on such quantities. It is important to calculate such errors in order to understand how accurate the results obtained are. This section therefore covers all the error calculations required in this thesis.

4.6.1 Autocorrelation Functions

When measuring certain quantities from simulations at regular intervals, it is useful to calculate how similar the values obtained are between independent measurements. This degree of similarity can be calculated through the use of the autocorrelation function. Over a measurement interval δt, the autocorrelation function for an observable is defined as

$$C(\delta t) = \frac{\left\langle \big(A(t) - \langle A \rangle\big)\big(A(t+\delta t) - \langle A \rangle\big)^* \right\rangle}{\left\langle \big(A(t) - \langle A \rangle\big)\big(A(t) - \langle A \rangle\big)^* \right\rangle}, \tag{4.18}$$

where $A(t)$ is the value of the observable measured at time t and $\langle A \rangle$ is the average value of the observable over the N measurements of the simulation[74].

For a finite set of data consisting of N measurements over a total duration of time T, the measurement interval can range from 0 to T. For instance, if $\delta t = 0$, $C(0) = 1$ as the correlation is calculated between each of the N data points and themselves. However, if $\delta t = T$, then only the correlation will be calculated between the first and last measured values. The number of calculations performed is dependent on the choice of δt; since in the former case N calculations are done, while in the latter only one calculation is performed. Hence, if the interval between each data point is δt, then the value for the autocorrelation function can be calculated for any interval $n\delta t = [0, T]$, where $n = [0, N-1] \in \mathbb{N}^0$. This means the average of the denominator in equation (4.18) is over N, while the average of the numerator is over $N - n$.

If each measurement of the observable is supposed to be independent, then it would be expected that as $\delta t \to \infty$, $C(\delta t) \to 0$. Hence, in this case, the autocor-

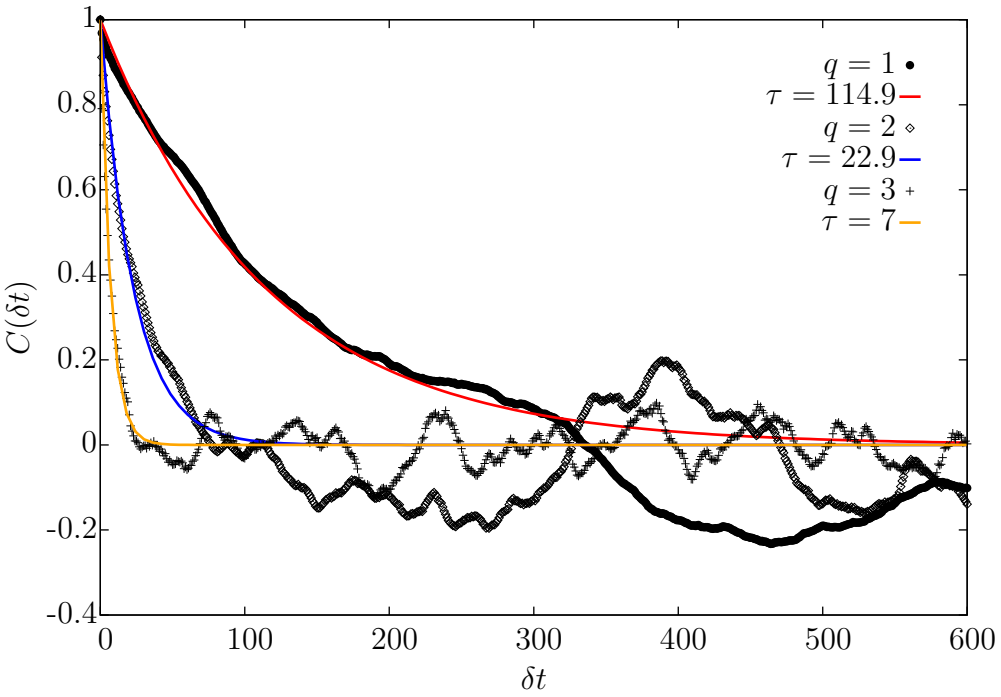

Figure 4.5: Exponential dependence of the autocorrelation function for $\langle |h(q)|^2 \rangle$ in the (100)[001] LJ-BG system for varying values of q.

relation function can be approximated as

$$C(\delta t) \approx e^{-\delta t/\tau}\,, \tag{4.19}$$

where τ is the correlation time; demonstrated in figure 4.5. The correlation time describes over what duration the results cease to be correlated and can be considered independent. In general, because there is a non-zero correlation time that exists for an interval δt, the results obtained will not be truly independent. Therefore, an error will exist on each measurement related to how correlated it is to previous measurements. The error on the equilibrium average of an observable, sampled every δt, can be found from the correlation time[33, 75]

$$\sigma\big(\langle A \rangle\big) = \left(2\sigma^2(A)\frac{\tau}{T}\right)^{\frac{1}{2}}, \tag{4.20}$$

where $\sigma^2(A)$ is the variance of the observable over T observations. If the results are uncorrelated, then $\tau \to 0$ and consequently $\sigma\big(\langle A \rangle\big) \to 0$. In the case where the measurements truly are independent of one another, it is best to use the standard error on the mean; as discussed in section 4.6.2.

A similar relationship to equation 4.20 is also true for calculating the error in average fluctuations[33], of the type $\langle \delta A^2 \rangle$, given as

$$\sigma\big(\langle \delta A^2 \rangle\big) = \left(2\langle \delta A^2 \rangle^2 \frac{\tau}{T} \right)^{\frac{1}{2}}. \tag{4.21}$$

Equation 4.21 is particularly important when considering the average fluctuations of the interface $\langle |h(q)|^2 \rangle$, which is shown in figure 4.5 for different values of q. The exponential relationship of the autocorrelation function is clearly visible as well as the varying sensitivity of correlation time for different values of q.

4.6.2 Error Calculations

The measurement of simulation quantities, taken at equilibrium, will all deviate slightly about their mean value. Hence, it is important to know what the error on these mean values are, which is calculated as

$$\sigma(\mu) = \left(\frac{1}{N(N-1)} \sum_{n=1}^{N} \big(x_n - \mu\big)^2 \right)^{\frac{1}{2}}, \tag{4.22}$$

where N is the number of data points used, x_n is the measured value of the n^{th} data point and μ is the mean value of the measured data[76].

To obtain a fit for the stiffness, given by equation (4.11), a plot of $y = \big(Lw/k_{\text{B}}T\big)\langle |h(q)|^2 \rangle$ against $x = q$ is performed on a log-log scale. This results in an error on the y axis, using basic error propagation[76], given as

$$\sigma(y) = \left(\left(\frac{y}{\langle |h(q)|^2 \rangle} \sigma\big(\langle |h(q)|^2 \rangle\big) \right)^2 + \left(\frac{y}{L}\sigma(L) \right)^2 + \left(\frac{y}{w}\sigma(w) \right)^2 + \left(-\frac{y}{T}\sigma(T) \right)^2 \right)^{\frac{1}{2}}, \tag{4.23}$$

where $\sigma(L)$, $\sigma(w)$ and $\sigma(T)$ are all calculated from equation (4.22). A straight line fit can be then be performed, so long as the data is converted to logs, hence $y \to \ln y$, $x \to \ln x$ and the error on each value becomes $\sigma(\ln y) = |\sigma(y)/y|$.

The straight line is constrained to have a gradient of $m = -2$, hence, only the parameter that defines the intercept can vary. The fit is performed using simple linear regression where the best fit minimises the quantity $\chi^2 = \big(y_i - mx_i - c\big)^2/\sigma_i^2$.

This means the intercept is fit to the equation

$$c = \frac{\sum_{i=0}^{N-1} \frac{y_i}{\sigma_i^2} - m \sum_{i=0}^{N-1} \frac{x_i}{\sigma_i^2}}{\sum_{i=0}^{N-1} \frac{1}{\sigma_i^2}}, \tag{4.24}$$

and the error on the intercept is given by $\left(\frac{1}{2}\frac{d^2\chi^2}{dc^2}\right)^{-\frac{1}{2}}$[76, 77]. This comes from the fact that errors on fit parameters can be extracted from the diagonal elements of the covariance matrix, $\mathbf{C}$, which is related to the Hessian matrix as $\mathbf{C} = \frac{1}{2}\mathbf{H}^{-1}$[76]. The Hessian is just the matrix of second order derivatives and the errors on parameters come from the square root of the diagonal elements of $\mathbf{C}$. Hence, the error on the intercept is just

$$\sigma(c) = \left(\sum_{i=0}^{N-1} \frac{1}{\sigma_i^2}\right)^{-\frac{1}{2}}. \tag{4.25}$$

Since this intercept is for the straight line fit of the form (4.11), the stiffness is therefore just $\tilde{\gamma} = 10^{-c}$ and the error on the stiffness is

$$\sigma(\tilde{\gamma}) = \left|\sigma(c)10^{-c}\right|. \tag{4.26}$$

It should be noted that when fitting a straight line to the data, no error has been assumed on the measured values on q_n. Technically, this is not true, as $q_n = 2\pi n/w$, where w is the average width of the system. Therefore, the error on q_n is simply $\sigma(q_n) = |\sigma(w)q_n/w|$. However, $\sigma(q_n)$ is negligible and so for the sake of more simplistic fitting, has been ignored from the error on the stiffness.

When fitting the measured stiffnesses to fitting functions (see chapter 5), measurements for two separate orientations may be symmetric and are therefore described by the same equation for the interfacial stiffness. In these cases, the independent measurements for the stiffness must be averaged and then the average results used to fit for the parameters in the relevant equation. Since there is an error associated with each stiffness measurement, a weighted average must be calculated along with the error on the weighted average. The error on the weighted average for N measurements is calculated as

$$\sigma(\mu_w) = \left(\sum_{i=1}^{N} \frac{1}{\sigma(x_i)^2}\right)^{-\frac{1}{2}}, \tag{4.27}$$

where μ_w is the weighted mean and $\sigma(x_i)$ is the error on the i^{th} independent mea-

sured results[76].

Once the stiffnesses have all been measured and weighted, if necessary, they are used in a general linear fit to equations that describe the interfacial stiffness for different orientations of crystal planes. This is discussed in detail in chapter 5, but it is important to consider the error on each of the fitting parameters in order to calculate the error on the free energy. A detailed discussion of how the general linear fit is performed can be found in ref. [77], while the procedure is summarised here.

For a function $y(x_i) = \sum_{j=0}^{M-1} \epsilon_j S(x_i)$, which is a linear polynomial of M functions of x, the quantity to minimise for N measurements becomes $\chi^2 = \sum_{i=0}^{N-1} \big(y_i - y(x_i)\big)^2$; where $N > M$. Now, a system of N equations must be solved. Differentiating with respect to each of the parameters ϵ_j in order to minimise χ^2, the system of equations can be expressed in terms of matrices and vectors:

$$\mathbf{A} = \begin{bmatrix} \frac{\partial y(x_0)}{\partial \epsilon_0} & \frac{\partial y(x_0)}{\partial \epsilon_1} & \cdots & \frac{\partial y(x_0)}{\partial \epsilon_{M-1}} \\ \frac{\partial y(x_1)}{\partial \epsilon_0} & \frac{\partial y(x_1)}{\partial \epsilon_1} & \cdots & \frac{\partial y(x_1)}{\partial \epsilon_{M-1}} \\ \vdots & \vdots & \ddots & \vdots \\ \frac{\partial y(x_{N-1})}{\partial \epsilon_0} & \frac{\partial y(x_{N-1})}{\partial \epsilon_1} & \cdots & \frac{\partial y(x_{N-1})}{\partial \epsilon_{M-1}} \end{bmatrix}; \quad \mathbf{b} = \begin{bmatrix} y_0 - y(x_0) \\ y_1 - y(x_1) \\ \vdots \\ y_{N-1} - y(x_{N-1}) \end{bmatrix};$$

$\boldsymbol{\epsilon}$, which is a size M vector of the fitted parameters; and $d\boldsymbol{\epsilon}$, which is the calculated difference between the parameters from the present to the next iteration of the fitting. This results in the relationship,

$$\mathbf{A}^T\mathbf{A}d\boldsymbol{\epsilon} = \mathbf{A}^T\mathbf{b}\,. \tag{4.28}$$

However, because there are errors present on the measured points y_i, then these must also be included by amending the previous equation to include a diagonal $N \times N$ weighting matrix, $\mathbf{W}$, to give

$$\mathbf{A}^T\mathbf{W}\mathbf{A}d\boldsymbol{\epsilon} = \mathbf{A}^T\mathbf{W}\mathbf{b}\,, \tag{4.29}$$

where the errors on the measurements are independent of each other and hence $W_{ii} = \frac{1}{\sigma_i^2}$[78]. Rearranging for $d\boldsymbol{\epsilon}$ allows iterative estimation of the parameters $\boldsymbol{\epsilon}$ to be calculated via $d\boldsymbol{\epsilon} = \big(\mathbf{A}^T\mathbf{W}\mathbf{A}\big)^{-1}\mathbf{A}^T\mathbf{W}\mathbf{b}$ and hence $\boldsymbol{\epsilon} \to \boldsymbol{\epsilon} + d\boldsymbol{\epsilon}$. Successively repeating this process, reduces the calculated value of $d\boldsymbol{\epsilon}$ and steadily converges $\boldsymbol{\epsilon}$ to a better estimate of the fit parameters.

The covariance matrix is defined as $\mathbf{C} = \mathbf{A}^T\mathbf{W}\mathbf{A}$ and hence the square root of each of the diagonal elements gives the error on each of the parameters, ϵ_j[77].

This is how the errors on the fit parameters are obtained.

Finally, now that the errors on the fit parameters have been established, simple error propagation recovers the error on the calculated free energy. Hence, the error on the free energy for M fit parameters is

$$\sigma(\gamma) = \left(\big(\sigma(\gamma_0)\big)^2 \left(1 + \sum_{j=1}^{M-1} \epsilon_j S(\theta_j, \phi_j) \right)^2 + \gamma_0^2 \sum_{j=1}^{M-1} \big(\sigma(\epsilon_j) S(\theta_j, \phi_j)\big)^2 \right)^{\frac{1}{2}}. \quad (4.30)$$

The form of equation (4.30) is also true for the error on the calculated stiffness, where the coefficients $S(\theta_j, \phi_j)$ will be of different values for the j^{th} measurement than those for the free energy.

Other measured quantities in this research, than the ones explicitly described here, use similar error analysis; usually standard error propagation[76]. Such calculations are not reported here, but the methods can be used equivalently; there are no other unique error calculations used in this research that have not been reported here.

Chapter 5

Measurement Details

5.1 Introduction

While the CWM was validated for LJ systems in chapter 4, the central problem of this research is applying such a method to ice-water coexistence systems, to calculate the isotropic and crystal-plane interfacial free energies in structures of ice-Ic, ice-Ih and ice-0. As such, accurate measurement of the solid-liquid interface must be conducted using appropriate order parameters that distinguish between the solid and liquid phases. Furthermore, the discretisation of the system must also be studied, as well as the size of the y direction of the interface, to understand how these affect the measurement of the interfacial stiffness. Finally, the use of symmetry adapted spherical harmonics must also be examined to recover the interfacial free energy from the interfacial stiffness. All these considerations are addressed in this chapter.

5.2 Radial Distribution Functions

In order to use order parameters to distinguish between crystal and liquid phases, a suitable spatial cutoff must be chosen within which to measure the degree of bond alignment. Since crystal structures form a regularly repeating lattice, the neighbour atoms, of every atom, will exist at specific distances. Such ordering can be measured using a radial distribution function (RDF) in each solid.

The RDF can be measured from bulk simulations of a solid at a constant temperature and pressure, and is calculated from

$$g(r) = \frac{n(r)}{\frac{4}{3}\pi\rho\big(\big(r+\delta r\big)^3 - r^3\big)}\,, \tag{5.1}$$

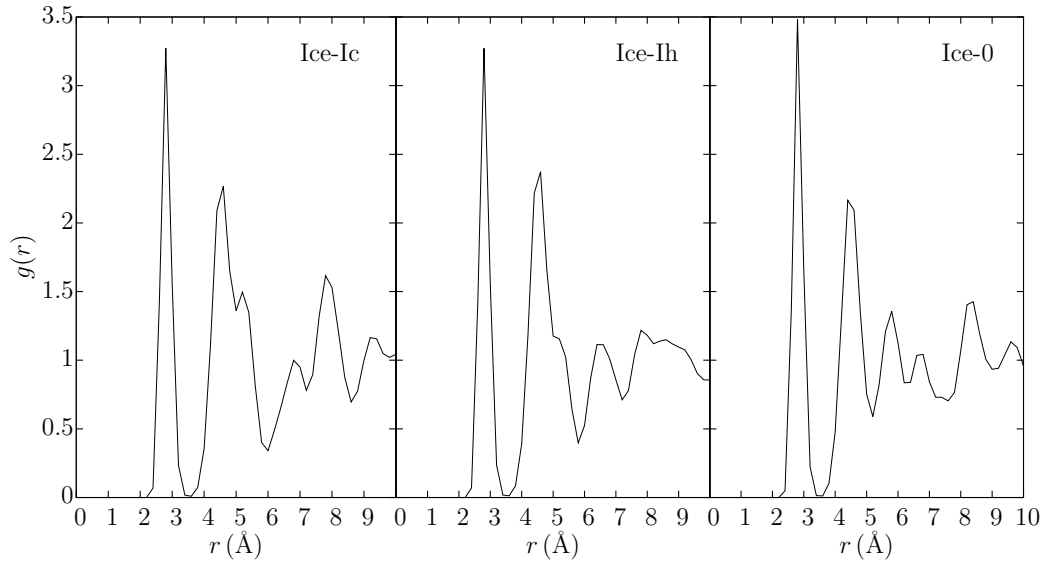

Figure 5.1: RDF plots for the three bulk solid-phase ice systems in the mW model: ice-Ic (*left*), ice-Ih (*centre*), ice-0 (*right*).

where $n(r)$ is the average number of atoms in a shell at radius r and thickness δr, and ρ is the average system density[33]. Simulations of bulk ice-Ic, ice-Ih and ice-0 were conducted over 5 ns in the NPT ensemble, sampling every 10 ps, with 1000, 896 and 1920 atoms respectively at their determined coexistence conditions; $T = 276$ K, $P = 1$ atm for ice-I and $T = 245$ K, $P = 1$ atm for ice-0, (the latter being calculated in chapter 6). This gave the resulting RDF for each structure, as shown in figure 5.1. Similar bulk liquid simulations were also performed, necessary for measuring the $c(i, j)$ values in the liquid phase; as discussed in section 5.3.

It is clear from figure 5.1 that all three structures have a first coordination shell between 2.2 Å and 3.5 Å, and that ice-0 has a more defined second coordination shell between 3.5 Å and 5.2 Å; which is otherwise blurred with the third shell in both ice-Ic and ice-Ih. These values can then be used to define the spatial cutoff for calculating the order parameters in each structure.

5.3 Ice Detection and Order Parameters

The order parameters implemented in this research, rely on representing the local bond ordering of each particle, $\mathbf{q}_{\mathrm{lm}}(i)$. Such bond ordering measures the degree of overlap between the bond orientation in the simulated system, with that of the ideal high symmetry environment. Such bond order parameters have been developed by

Steinhardt et al.[79, 80], and are mathematically described for each particle, i, as

$$\mathbf{q}_{\mathrm{lm}}(i) = \frac{1}{N_{\mathrm{b}}(i)} \sum_{j=1}^{N_{\mathrm{b}}(i)} Y_{\mathrm{lm}}(\hat{\mathbf{r}}_{ij}) \,, \tag{5.2}$$

where $N_{\mathrm{b}}(i)$ is the number of neighbours in the crystalline solid, $Y_{\mathrm{lm}}(\hat{\mathbf{r}}_{ij})$ is a spherical harmonic, $\hat{\mathbf{r}}_{ij}$ is a unit vector in the direction of the bond between particles i and j, and $\mathbf{q}_{\mathrm{lm}}(i)$ is a complex vector of size $2l+1$[47, 81]. The choice for the number of neighbours around an atom is typically the number of nearest neighbours within the first coordination shell[80]. However, this need not be the case and the number of neighbours can be the number of atoms up to any specified coordination shell, cutoff distance or imposed limit.

Taking the normalised dot product of $\mathbf{q}_{\mathrm{lm}}(i)$ with that of a neighbouring particle j, gives a measure of the bond correlation between the two atoms, $c(i,j)$,

$$c(i,j) = \frac{\mathbf{q}_{\mathrm{lm}}(i) \cdot \mathbf{q}_{\mathrm{lm}}(j)}{|\mathbf{q}_{\mathrm{lm}}(i)||\mathbf{q}_{\mathrm{lm}}(j)|} \tag{5.3}$$

$$= \frac{\sum_{m=-l}^{l} \mathbf{q}_{\mathrm{lm}}(i)\mathbf{q}_{\mathrm{lm}}(j)^*}{\left(\sum_{m=-l}^{l} \mathbf{q}_{\mathrm{lm}}(i)\mathbf{q}_{\mathrm{lm}}(i)^*\right)^{1/2}\left(\sum_{m=-l}^{l} \mathbf{q}_{\mathrm{lm}}(j)\mathbf{q}_{\mathrm{lm}}(j)^*\right)^{1/2}} \,. \tag{5.4}$$

In a bulk solid, the bond correlations should yield a distinct distribution; indicating the regularity of the crystal lattice. Conversely, the distribution obtained for a bulk liquid, should be much more uniform; indicating no particular order exists[47, 82]. It is therefore possible to bound regions of the correlation distribution that are most frequently representative of the values for the solid symmetry, and then define each correlation in this region as being a solid-like bond. Alternatively, each solid particle will also have a specific number of neighbouring particles, which if matched for a given particle with a corresponding $c(i,j)$ value in the solid region, can instead register as a single solid-like bond for the given particle.

For a given order parameter in a specific system, it is unknown what bounding criteria should be used on the distribution of $c(i,j)$ to reliably distinguish between the solid and liquid phases. This necessitates testing the order parameter against bulk solid systems and bulk liquid systems before it can be used on systems with an interface. As such, the following sections discuss the implementation of possible candidate order parameters used and the extent of their utility with the different ice structures. In what follows, for the sake of brevity, the notation used for the order

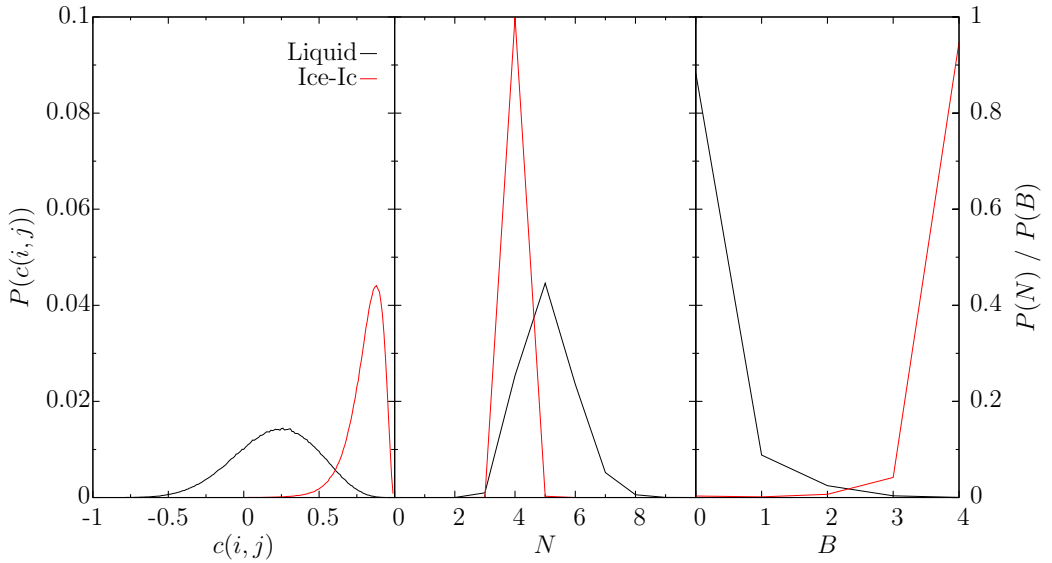

Figure 5.2: For ice-Ic and water, using an order parameter cutoff of 3.5 Å, the plot shows: (*left*) the $q6$ correlation distribution; (*centre*) the number of neighbours; (*right*) the number of solid-like bonds when using $c(i,j) \geq 0.5$ and 4 neighbours.

parameters refer to the choice of angular momentum, i.e. $q6 \equiv \mathbf{q}_{6\mathrm{m}}(i)$, where $\mathrm{l} = 6$.

5.3.1 q6 Order Parameter

In chapter 4, a way was required to detect the overall degree of crystallinity in a system between a FCC LJ crystal and its melt. In that context, $q6$ was used, which is widely known to be able to reliably distinguish between the two phases[81]. However, it is not clear if it could be suitably applied to any or all of the mW ice-water systems of interest, and so this must be checked.

The bond correlation distribution for ice-Ic, over 3.5 Å, is shown in figure 5.2 (*left*), which clearly shows that the liquid displays a broad range of correlations about a peak correlation of 0.26, while the ice-Ic is more strongly positively correlated, peaked at 0.88; the overlap of the distributions is only 11%. Correlations of $c(i,j) \geq 0.62$ are also more strongly favoured by ice-Ic, meaning correlations matching this criteria are likely solid-like. This threshold would correctly identify 94.1% of ice-Ic and incorrectly identify 5.6% of the water bond correlations as solid-like. Alternatively, a threshold of $c(i,j) \geq 0.5$ could be used, which identifies 98.4% and 14.7% of the ice-Ic and water bond correlations, respectively, as solid-like. This demonstrates it is possible to correctly identify a greater proportion of the ice-Ic correlations as solid-like by lowering the correlation threshold, while increasing the proportion of incorrectly identified water bond correlations as solid-like. This is

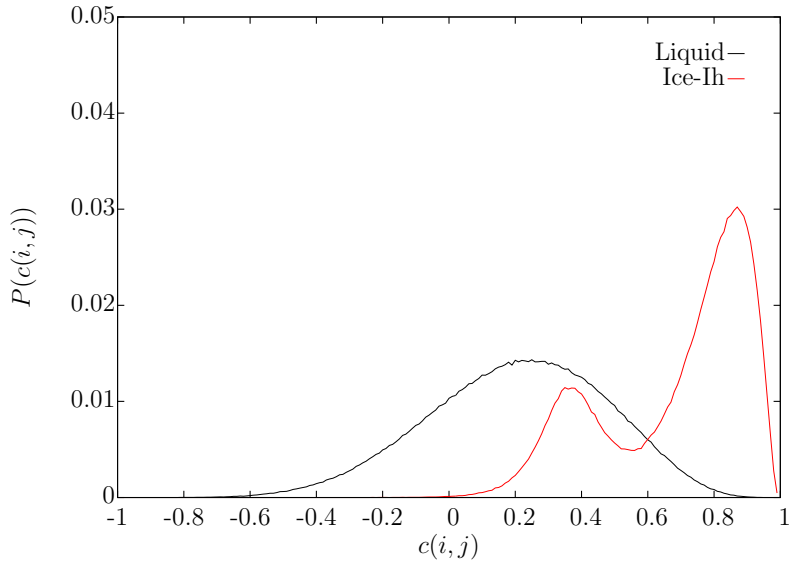

Figure 5.3: The $q6$ bond correlation distribution in ice-Ih and water over 3.5 Å.

why a second piece of criteria is required to improve upon the identification of solid particles; the number of neighbouring particles over 3.5 Å.

Using this additional criteria, as shown in figure 5.2 (*centre*), 99.6% of the solid has 4 nearest neighbours, compared to 25.3% of the liquid. When combining these two constraints, a solid-like bond can be defined if an atom has a bond correlation of $c(i,j) \geq 0.5$ with its neighbour and has a total of 4 nearest neighbours. The effect of these combined constraints in both the liquid and solid ice-Ic on the number of solid-like bonds, is shown in figure 5.2 (*right*). Now, a particle can be classified as being solid when having 3 or more solid-like bonds. This correctly identifies on average over the 5 ns bulk simulations, 98.9% of the ice-Ic as solid and 0.37% of the water as solid. This is a significant improvement on using only the criteria of $c(i,j) \geq 0.5$, since comparable correct solid identification is achieved while the amount of liquid being incorrectly identified as solid is now reduced by 97.5%. This combined criteria is consequently used for distinguishing between ice-Ic and water systems using $q6$, where particles are assigned the number of their solid-like bonds as their intrinsic order parameter value.

While $q6$ successfully distinguishes between ice-Ic and water, it suffers from limitations when applied to ice-Ih. As shown in figure 5.1, the distribution of the number density over 3.5 Å is the same in both ice-Ic and ice-Ih, which indicates that there must be the same number of neighbours in the first coordination shell for these two polytypes. This means the same criteria for the number of neighbours can be used in ice-Ih as ice-Ic. However, the bond correlation distribution for ice-Ih

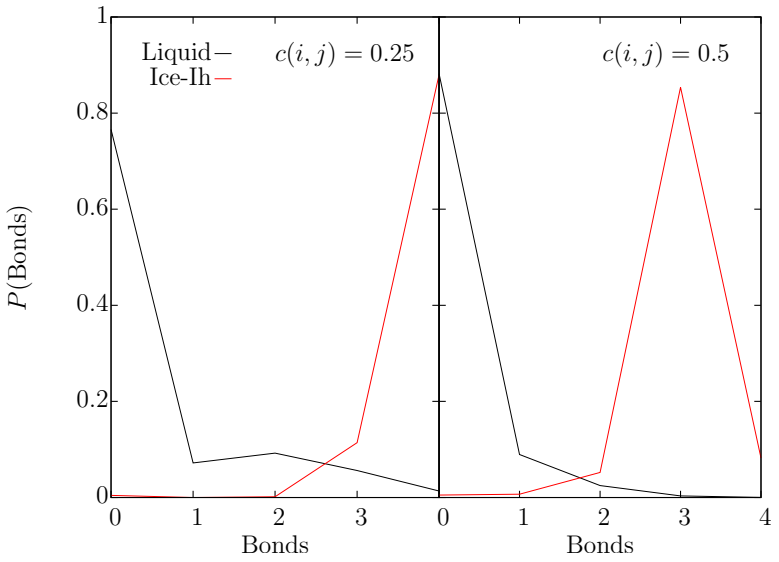

Figure 5.4: The number of solid-like bonds in ice-Ih and water over 3.5 Å when nearest neighbours = 4 and $c(i,j) \geq 0.25$ (*left*) or $c(i,j) \geq 0.5$ (*right*).

is different to that of ice-Ic, as shown in figure 5.3, where now a second lesser peak is clearly present at $c(i,j) = 0.36$.

The presence of two distinct peaks in the ice-Ih correlation distribution is indicative of the two types of bonds that form in ice-Ih: staggered bonds (s-bonds); and eclipsed bonds (e-bonds)[82]. In ice-Ic, only the peak at $c(i,j) = 0.88$ is present, which is indicative of the 4 nearest neighbour s-bonds formed within the crystal. In the ice-Ih crystal structure, each atom forms 3 s-bonds and 1 e-bond between its 4 nearest neighbours[82, 83]. In ice-Ih at least a quarter of the particle correlations have an e-bond with a correlation peak at $c(i,j) = 0.36$, increasing the distribution overlap of ice-Ih with water to 37% compared to 11% in ice-Ic. Now, if solid-like correlations are defined when $c(i,j) \geq 0.5$, only 75.3% of ice-Ih is identified as solid, compared previously to 98.4% in ice-Ic at the same cutoff. However, if using a threshold of $c(i,j) \geq 0.25$, enclosing the second peak, 97% of ice-Ih is correctly identified, while 46.3% of the water is misidentified as solid. The effect of using these cutoffs, combined with the requirement of 4 neighbour particles, is shown in figure 5.4 for the number of solid-like bonds in ice-Ih and water.

Analysis of these cutoffs show, that if 3 or more solid-like bonds are used to identify a particle as solid, then 93.6% (99.4%) of ice-Ih and 0.36% (7%) of water atoms are identified as solid when using $c(i,j) \geq 0.5$ ($c(i,j) \geq 0.25$). However, if 4 solid-like bonds are required, 8.2% (88%) of ice-Ih and 0.02% (1.3%) of water particles are registered as being solid when using $c(i,j) \geq 0.5$ ($c(i,j) \geq 0.25$). Therefore,

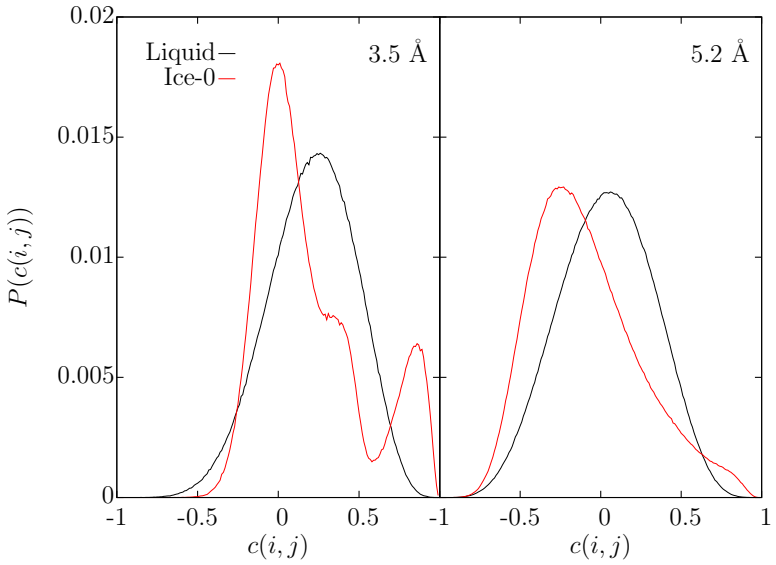

Figure 5.5: The $q6$ bond correlation distributions in ice-0 and water over the first coordination shell (*left*) and the second coordination shell (*right*).

the best criteria that can be used to correctly identify solid ice-Ih particles, is if a particle has 3 or more solid-like bonds; where a bond is only recognised if an atom has 4 nearest neighbours and the correlation with a neighbour is $c(i,j) \geq 0.5$. On average over the 5 ns bulk simulations of ice-Ih and water, 93.6% of ice-Ih and 0.36% of water is identified as being solid ice-Ih.

Since only a maximum of 93.6% of ice-Ih can, on average, be correctly identified as solid, this is not a suitable way to accurately measure the presence of ice-Ih in a system. In systems where an ice-Ih/water interface exists, the local position of the interface cannot be reliably known, compared to the accuracy of that of ice-Ic/water interface systems. $q6$ can therefore not be used to compare the interfacial free energies between ice-Ih and ice-Ic systems when in contact with water.

Ice-0 is also of interest to this research and hence an order parameter that can distinguish between ice-0 and water is of necessity. The correlation distributions for $q6$ in bulk simulations of ice-0 and water are shown in figure 5.5 over the first two coordination shells of ice-0. As can be seen, there is no way to bound the bond correlation distributions of ice-0 to distinguish between the solid and the water. The coordination shell cutoffs used result in correlation distribution overlaps of the ice-0 and water of 70% and 76% for the 3.5 Å and 5.2 Å cutoff, respectively. Hence, $q6$ can clearly not be used to distinguish between ice-0 and water.

Type	s-bonds	e-bonds	Neighbours
Ice-Ic	4	0	4
Ice-Ih	3	1	4
Interface	3 or 2	0	4
Water	Any	Any	Any

Table 5.1: Atom type identification criteria using $q3$.

5.3.2 q3 Order Parameter

The failings of $q6$ motivate the use of another order parameter that is able to work in all the structures of ice investigated and can also distinguish between the ice-I polytypes. Using $q3$, it is possible to identify between ice-Ic, ice-Ih, water and even interfacial atoms.

$q3$ is implemented through a variation of the CHILL algorithm[83]; known as CHILL+[82]. The CHILL algorithm is able to identify the crystal types of interest, however CHILL+ improves upon the percentage of ice-Ih detected. CHILL+ makes use of the different numbers of s-bonds and e-bonds formed in ice-Ic and ice-Ih[82]. While the difference in the bond correlation distributions for $q6$, between ice-Ic and ice-Ih, clearly shows the different bond types, the signal from the single e-bond in ice-Ih is not intense enough to be resolved against the bond correlation distribution of water. Comparatively, these distributions are much clearer in the case of $q3$, as shown for bulk ice-Ic and ice-Ih in figure 5.6, where the correlation distributions are measured over particles within 3.5 Å.

Following the CHILL+ algorithm, s-bonds have a correlation value $c(i,j) \leq -0.8$, where e-bonds have a correlation value $-0.35 \leq c(i,j) \leq 0.25$. Particles are defined as being interfacial (between the solid phases and water), if they have 4 nearest neighbour atoms within 3.5 Å, but only form 2 or 3 s-bonds with any of its neighbours[82]. Water may form any number of neighbour bonds of any type and may have any number of neighbour atoms. The work carried out by Nguyen and Molinero[82] also indicates that $q3$ can identify clathrates; however this is not of importance to this research and so is not discussed here. The criteria to identify an atom using $q3$ is summarised in table 5.1.

Figure 5.6 shows the bond correlation distributions of ice-Ic and ice-Ih when using $q3$, clearly indicating the presence of the respective s-bonds and e-bonds in both polytypes according to the CHILL+ algorithm. In ice-Ic, when using the full identification criteria of CHILL+, the bulk simulations identified on average, over 5 ns, 99.4% of the bulk ice-Ic and 0.006% of the bulk water as being ice-Ic particles; a significant improvement over $q6$. There is still a significant degree of overlap between

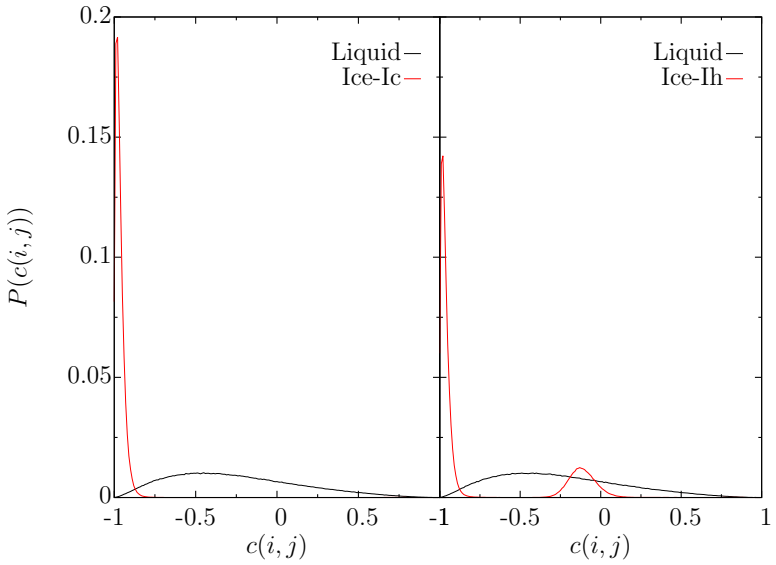

Figure 5.6: The $q3$ bond correlation distribution in ice-Ic and water (*left*) and ice-Ih and water (*right*), over an order parameter cutoff of 3.5 Å.

the water and ice-Ih correlation distribution functions of 23.8%, which compares to 37% when using $q6$. However, this difference significantly improves the probability of identifying ice-Ih e-bonds compared to using $q6$. The success of the algorithm is demonstrated in figure 5.7, where the frequency of s-bonds and e-bonds in both polytypes is clear, over a well defined narrow range. Indeed, when using the complete criteria of CHILL+ to identify ice-Ih, it is found on average over 5 ns from the bulk simulations that 98.8% of ice-Ih atoms and 0.03% of water atoms are identified as ice-Ih; again, a significant improvement over $q6$. It should be noted here, that 0.03% misidentification of water as ice-Ih compares to the previously calculated value of 0.006% misidentification of water as ice-Ic. This indicates there is a measurable bias for water to be incorrectly identified as ice-Ih over ice-Ic by a factor of 5.

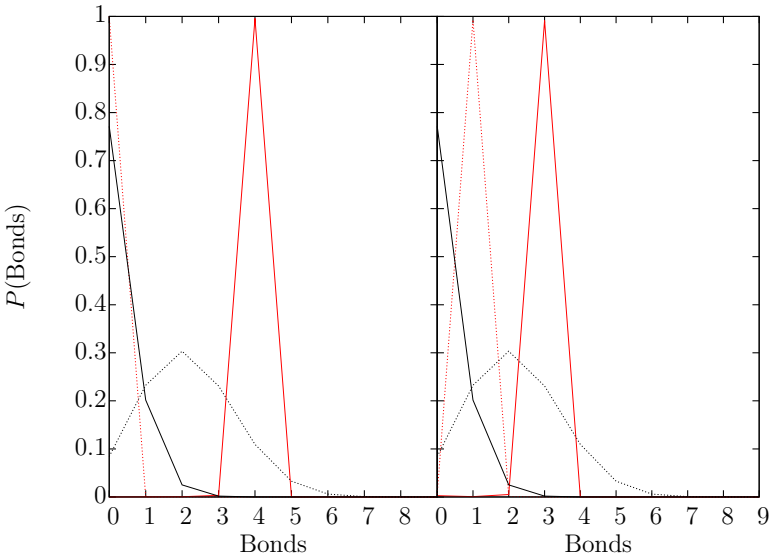

Figure 5.7: $q3$ bond types in liquid (black lines) and solid ice-I (red lines). Solid lines are s-bonds, dotted lines are e-bonds. Left shows the distributions in ice-Ic and water, right shows the distributions in ice-Ih and water.

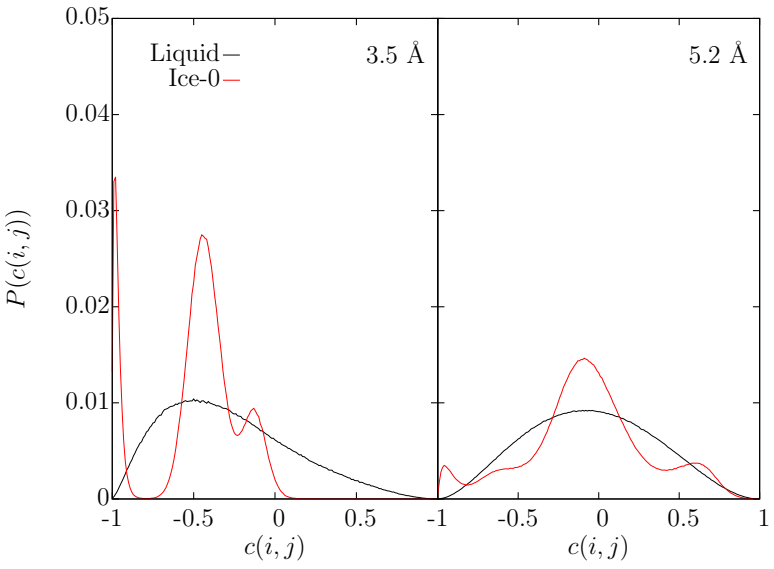

Figure 5.8: The $q3$ bond correlation distributions in ice-0 and water over the first coordination shell (*left*) and second coordination shell (*right*).

While $q3$ can distinguish between ice-Ic and ice-Ih, it is not sufficient to identify between ice-0 and water over either the first or second coordination shells, as shown in figure 5.8. There is a greater propensity to identify ice-0 when using a cutoff of 3.5 Å as opposed to 5.2 Å, but maintains ice-0/water bond correlation overlaps of 55% and 82% respectively. The distribution in the former case does show different bond peaks similar to the existence of s-bonds and e-bonds in ice-Ih. It was investigated whether $q3$ could distinguish between different bond-types in ice-0, when using a spatial cutoff of 3.5 Å, and use such bond-type distributions to distinguish between ice-0 and water. However, it was not possible to clearly resolve the secondary peak in ice-0, from that of water. This is unsurprising given $q6$ could not reliably distinguish between ice-Ih and water with an overlap of 37%, and hence the 55% overlap in this case is discouragingly high. Another order parameter is therefore necessary to clearly resolve ice-0 against water.

A further point to mention regarding $q3$ concerns the choice of the value of the order parameter in solids and liquids. Unlike $q6$ where the intrinsic atom order parameter value is the number of solid-like bonds an atom possesses, $q3$ instead identifies the type of atom directly as a combination of the number of neighbours an atom has and the proportion of different bond types. In order to obtain an order parameter profile, as discussed in chapter 4, each atom must be assigned a value based on its phase. The value assigned is an arbitrary choice, rather than a calculated quantity. It could be suggested that the choice of order parameter in different phases affects the measurement of the local position of the interface. This is demonstrated not to be the case in figure 5.9.

Figure 5.9 shows that the inflexion point, measuring the position of the interface, for the same arrangement of atoms when using ranges of 10 and 4, is $h_0 = 202.588$ Å and $h_0 = 202.799$ Å respectively. Clearly there is no significant deviation in the position of the interface measured by the two different sets of order parameter values. In the case of "Range 10", solid-like particles have been assigned a value of 10, liquid-like particles a value of 0 and interfacial particles a value of 5. The "Range 4" choice of values instead uses the number of connected bonds, where the order parameter per atom is the sum of the number of e-bonds and s-bonds; with the exception that liquid-like particles are assigned a value of 0, to keep with the convention that the order parameter is high in the solid region and low in the liquid region. This defined value in the liquid, smooths out the profile liquid region, which would otherwise have a varying number of connections per atom.

Given that there is no difference to the measurement of the inflexion point between the choice of values assigned to atoms when using $q3$, the decision was made

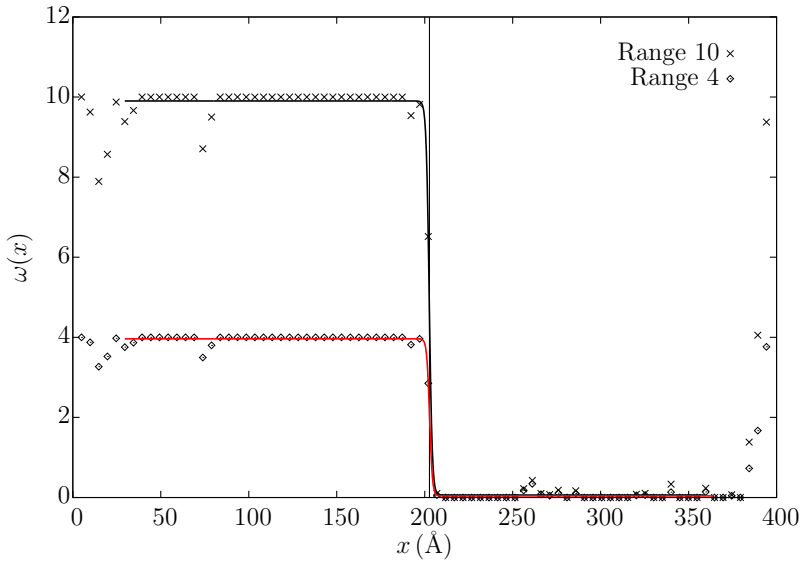

Figure 5.9: The $q3$ order parameter profile in ice-Ic (111)[1$\bar{1}$0] simulation using different assigned order parameter values to identify solid, interface and liquid particles. The vertical line is the average position of the two inflexion points ($x = 202.694$ Å).

to use the "Range 10" set of values to identify all local interface positions in ice-I. This choice was made because a larger range in the difference between atom phases allows for a clearer distinction between the solid and liquid regions when having to set thresholds in the interface identification program.

5.3.3 q12 Order Parameter

Given that both $q3$ and $q6$ cannot clearly resolve ice-0 from water, a third order parameter must be used; hence the implementation of $q12$.

While $q3$ and $q6$ both measure $c(i, j)$ over the first coordination shell in ice-I, using $q12$ over the first and second coordination shell does not yield any distinction between ice-0 and water at all; the distributions overlap by 89% and 54% respectively, as shown in figure 5.10. Instead, a modified version of the algorithm used to calculate $c(i, j)$ has been proposed by Russo et al., by using a set number of nearest neighbours for each atom i, $N_\mathrm{b}(i)$, and spatially averaging the order parameter over these neighbours[17]. The introduction of the spatially averaged vector

$$Q_{\mathrm{lm}}(i) = \frac{1}{N_\mathrm{b}(i)} \sum_{j=0}^{N_\mathrm{b}(i)} q_{\mathrm{lm}}(j)\,, \tag{5.5}$$

modifies the calculation of the bond correlation distribution, as $q_{\mathrm{lm}}(i) \to Q_{\mathrm{lm}}(i)$, in

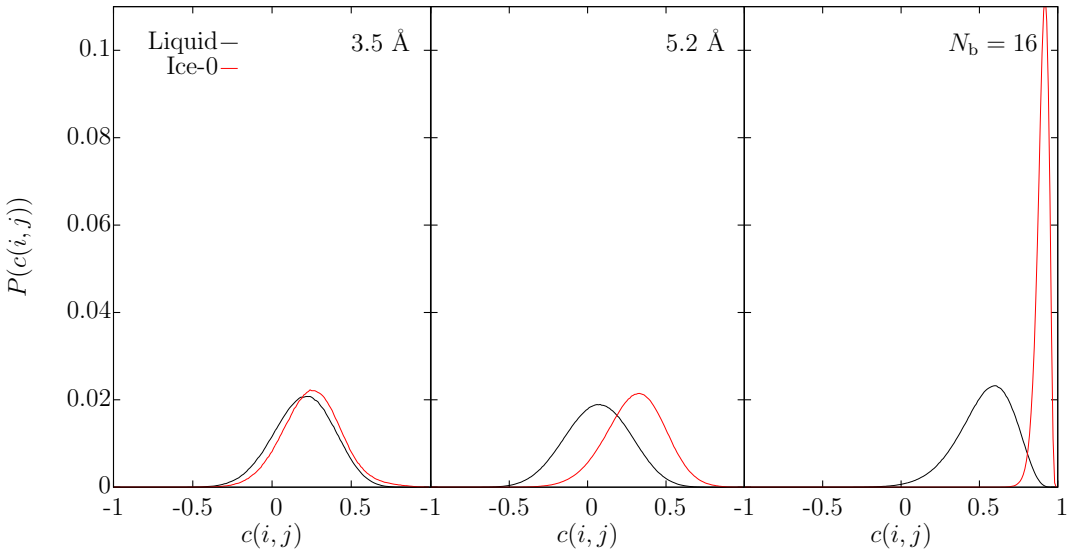

Figure 5.10: The $q12$ bond correlation distribution in ice-0 and water over 3.5 Å (*left*), 5.2 Å (*centre*) and when spatially averaging over the nearest 16 neighbours (*right*).

equation (5.3). Here, the spatial averaging is done over the constraint that for each atom $N_b(i) = 16$, which encompasses the first two coordination shells in ice-0.

When using the spatially averaged order parameter over the nearest 16 neighbours, the $q12$ bond correlation distribution in ice-0 and water are easily distinguishable with only a 6% overlap and a clear peak at $c(i,j) = 0.92$. The distributions over 3.5 Å, 5.2 Å and the 16 nearest neighbours are shown in figure 5.10.

As an aside, it is interesting to see whether applying the same spatial averaging algorithm makes any difference when using $q3$ or $q6$ to identify ice-0. As shown in figure 5.11, this does not make the distinction between ice-0 and water in the correlation distributions as well as $q12$ does, with ice-0/water bond correlation distribution overlaps of 78% and 53% for $q3$ and $q6$, respectively.

$q12$ is not just limited to distinguishing between ice-0 and water. While $q12$ is poor at distinguishing ice-Ic and ice-Ih from water over the first coordination shell – with bond correlation distribution overlaps of 72% and 76% respectively – it is excellent at identifying both ice-I polytypes when using the spatial averaging technique; with overlaps of 0.07% and 0.09% respectively. Figures 5.12 and 5.13 show the difference in the ability of $q12$ to distinguish between the respective ice-I polytype and water, when calculating the bond correlation distributions for the particles over the first coordination shell and when spatially averaging the 16 nearest neighbours. The negligible overlap obtained with $q12$ between the correlation distributions in

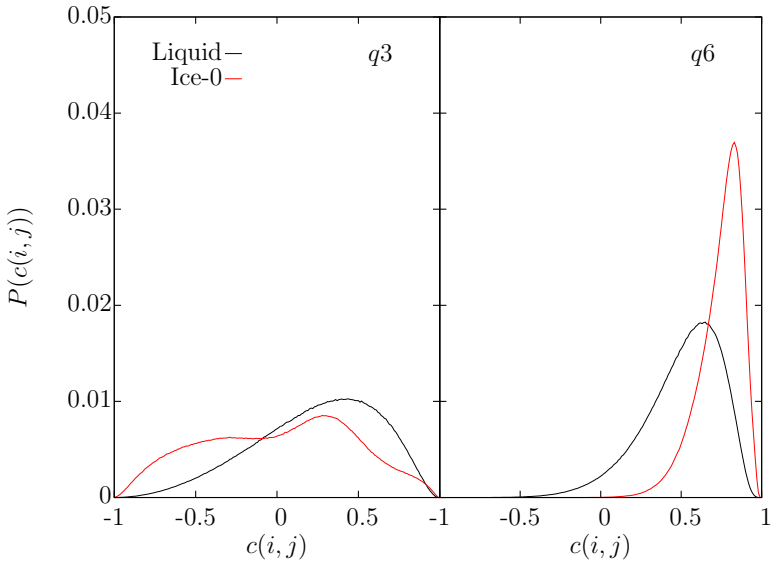

Figure 5.11: The spatially averaged bond correlation distribution in ice-0 and water over the 16 nearest neighbour atoms for $q3$ (*left*) and $q6$ (*right*).

the water and either ice-I polytype (when spatially averaging), demonstrates that $q12$ is also better than both $q3$ and $q6$ at distinguishing between ice-I and water, when using the correlation distributions alone.

Using the spatially averaged $q12$ order parameter, it is possible to identify ice-0 from water, by placing a threshold on the bond correlation distribution. Russo et al. impose that $c(i,j) \geq 0.75$ to identify solid-like particles, otherwise the particle is liquid-like[17]. This criteria is corroborated by this research as shown in figure 5.10, where this limit identifies 99.8% of bulk ice-0 and 10.3% of the bulk water as solid. In both ice-Ic and ice-Ih, 100% of ice-Ic and ice-Ih are identified as solid while 9.6% of water is misidentified as solid. Despite the complete or near complete identification of the solid, the large percentage of misidentified liquid as solid necessitates that this threshold is used to identify a solid-like bond between particles i and j. Once a particle has enough solid-like bonds between its 16 nearest neighbours, it is identified as a solid-like particle.

The bond distributions in the each of the ice structures and water are shown in figure 5.14. Choosing a threshold of 12 solid-like bonds to identify a particle as solid-like; in keeping with the algorithm used by Russo et al., should sufficiently distinguish between the solid and liquid phases. On average, over the 5 ns bulk simulations, spatially averaging $q12$ over the 16 nearest neighbours, identifies 100% of both ice-Ic and ice-Ih and 0.003% of water as solid, and identifies 99.98% of ice-0 and 0.008% of water as solid. This makes $q12$ the best choice of order parameter

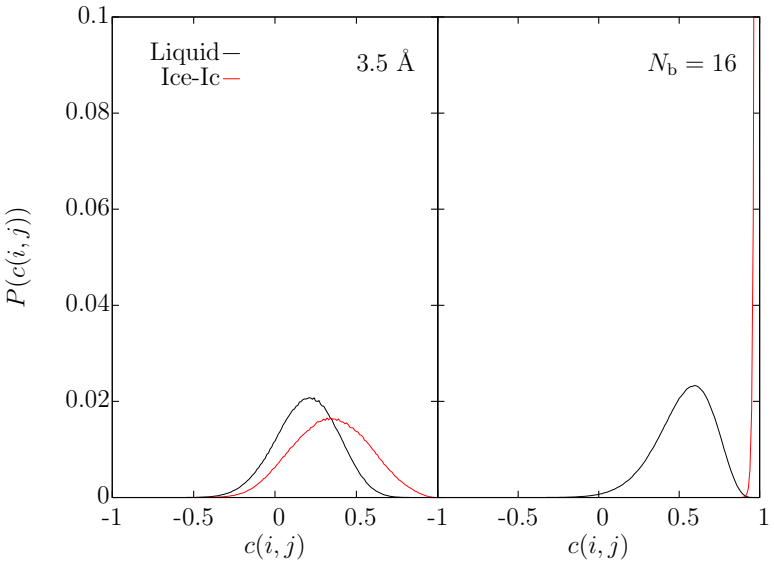

Figure 5.12: The $q12$ correlation distributions in ice-Ic and water over the first coordination shell (*left*) and spatially averaging over the 16 nearest neighbours (*right*).

to distinguish between any of the ice structures and water. Although, unlike $q3$ it cannot be used to distinguish between any of the ice structures themselves.

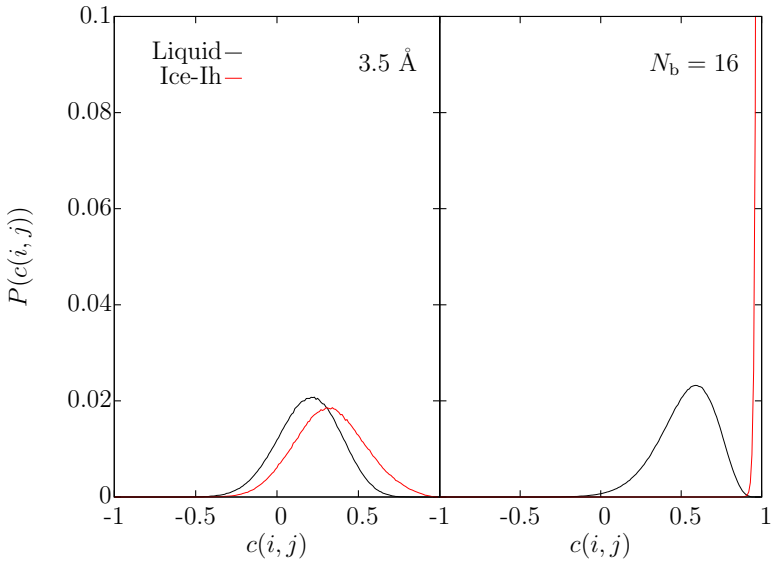

Figure 5.13: The $q12$ correlation distributions in ice-Ih and water over the first coordination shell (*left*) and spatially averaging over the 16 nearest neighbours (*right*).

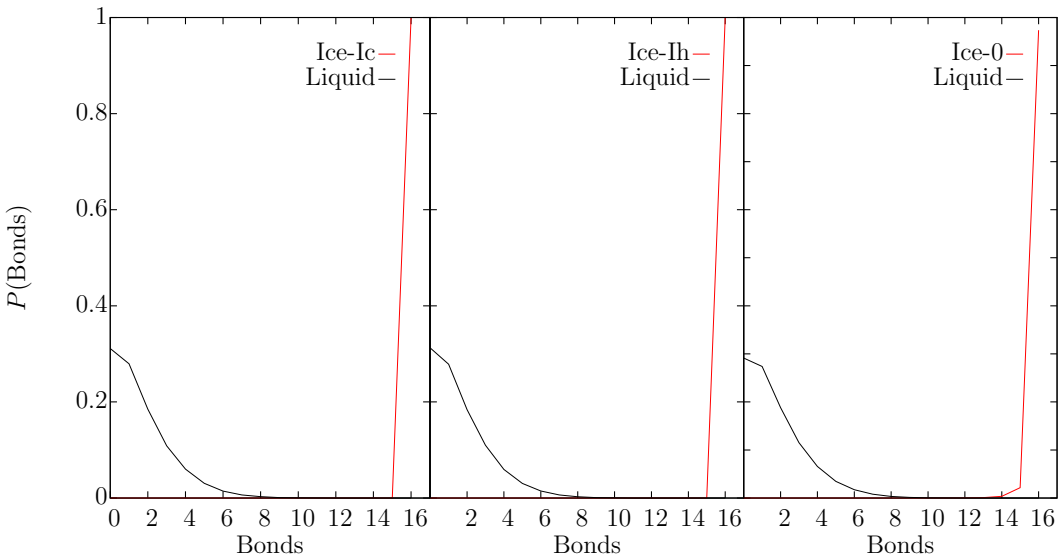

Figure 5.14: The number of solid-like bonds in ice-Ic (*left*), ice-Ih (*centre*) and ice-0 (*right*) against water when $c(i,j) \geq 0.75$ and $q12$ is spatially averaged.

5.4 Discretisation

In chapter 4 it was discussed how to measure the interface position in real-space, and the constraints that had to be considered when properly discretising the system. It was alluded to that the choice of discretisation in x and z, as well as the choice of thickness in y, would have effects on the measurement of the stiffness. In this section, such effects upon the value of the interfacial stiffness in the various ice-water coexistence systems, are discussed.

In this section, all analysis performed on the interfacial stiffness and its response to different discretisations of the system, has come from data for simulations described in chapter 6. The analysis of these simulations has been performed over the entire duration of the production runs.

5.4.1 Short Direction

Using the 1D form of CWT necessitates that only one bin can exist in the short, **y**, direction of the system. This approximates the interface to a 1D ribbon and allows a 1D Fourier transform to be performed on the real-space local interfacial positions. Therefore, the system should be simulated in such a way as to produce the best approximation of a 1D interface. However, a perfect 1D interface cannot be simulated, and it is usually desirable to avoid self interaction of particles with their own potential, which requires the simulation dimensions are no smaller than twice the potential cutoff[33]; however, this is not always a strict requirement with modern MD codes. Regardless, there must be some non-zero length to the size of the simulation in the **y** direction. How short this direction must be, and the effect it has on the measured interfacial stiffness, is important to know when setting up simulations designed to produce fluctuations in the position of the interface only along the length of the interface.

To get an idea of how flat the interface is for different lengths of y, a rough measurement of the interface position can be made by calculating the RMS deviations in the position of particles in x, in separate bins along **z**. To do this, a ribbon of solid-like atoms was identified at the interface, by selecting any particle within 4 Å of a liquid atom. This data was collected from the last timestep of the production run of the simulations outlined in chapter 6. The RMS deviations were then calculated for these particles from their mean position in x in each bin.

Figure 5.15 shows the real-space fluctuations of the (basal)$[11\bar{2}0]$ simulation at two different lengths of the short direction, y, for a single timestep. In the case of (a) $y = 22.118$ Å, while in (b) $y = 13.265$ Å. The plot shows how the atom

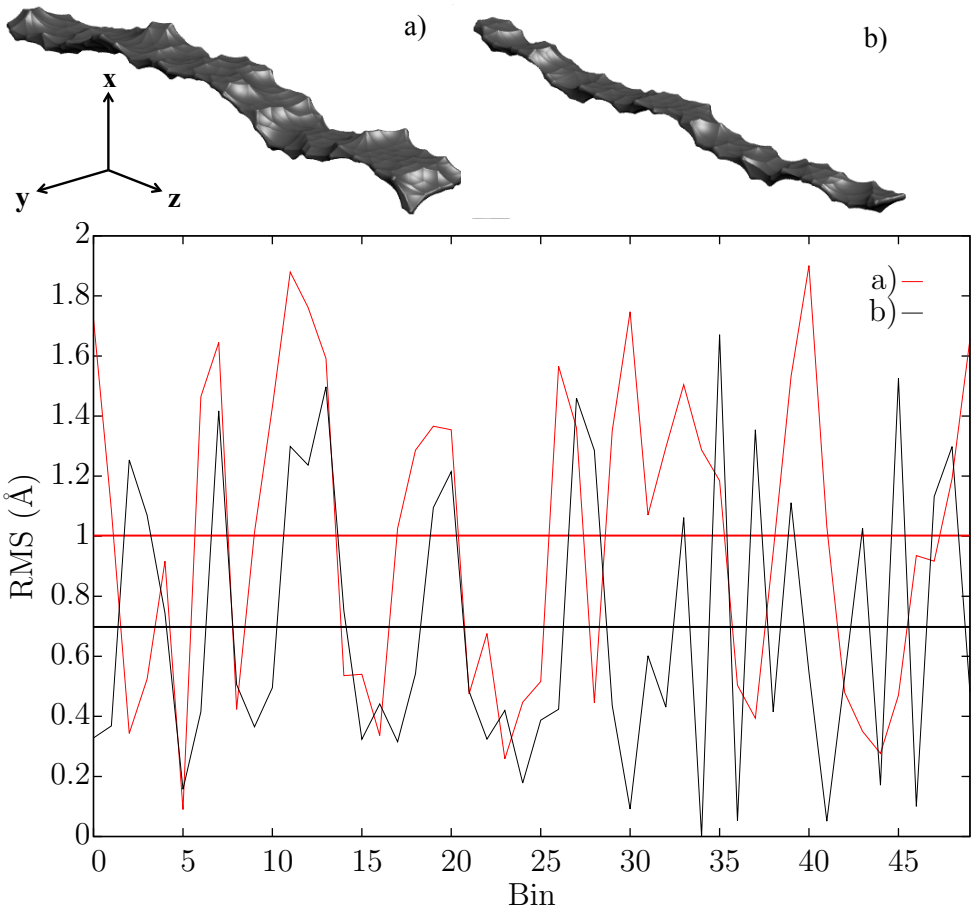

Figure 5.15: Maps of the (basal)[11$\bar{2}$0] interface in ice-Ih with varying length in **y** and the RMS displacement plots along the interface. Bin widths are approximately 3.6 Å in both (a) and (b).

positions vary in **x**, by measuring the RMS value per bin across the 50 bins along **z**, for the two different lengths of short direction within the single timestep. The spatial average RMS, $\overline{\text{RMS}}$, across all 50 bins is shown by the respective horizontal line on the plot; for (a) $\overline{\text{RMS}} = 1.0$ and (b) $\overline{\text{RMS}} = 0.7$.

To obtain an even better indication of how flat the interface is for different lengths of **y**, the $\overline{\text{RMS}}$ was calculated for the last 11 measurements of the simulation and then time averaged. The time averaged RMS values, $\langle\text{RMS}\rangle$, for $y = 22.118$ Å, $y = 17.708$ Å and $y = 13.265$ Å are 0.89(3), 0.88(3) and 0.71(3), respectively; where the error is given by the standard error on time averaging. To get an idea of whether this corresponds to an interface with no fluctuations in **y**, these measurements were compared to the $\langle\text{RMS}\rangle$ values for a "flat" interface. The flat interface consisted of 960 atoms, at 1 atm and coexistence temperature, with system dimensions of 147.2×

13.5×15.6 Å and a simulation timestep of 1 fs. The system was first equilibrated by running in the NVT ensemble at 20 K below coexistence for $50,000$ iterations, then switching to the NPT ensemble and running for a further $50,000$ iterations, and then heating half the system to 100 K above coexistence over $50,000$ iterations before then cooling it to 20 K above coexistence over $100,000$ iterations. The production run was then performed in the yz coupled NPH ensemble at coexistence for $100,000$ iterations.

The short production run provided 11 measurements, meaning only high energy fluctuations would be present on the surface. Such fluctuations are not included in the fit of the stiffness and so the measured value of $\langle \mathrm{RMS} \rangle$ would act as a reference for a flat interface. This resulted in a value of $\langle \mathrm{RMS} \rangle = 0.69(8)$, where the interface was binned along $\mathbf{z}$ with bin widths of approximately 3.6 Å, as before. Hence, the $\langle \mathrm{RMS} \rangle$ value for the (basal)$[11\bar{2}0]$ simulation with $y = 13.265$ Å is within errors of the ideal flat interface and so be considered flat in the $\mathbf{y}$ direction.

Comparing the results obtained for the $\langle \mathrm{RMS} \rangle$ with the different lengths of y to that of the flat interface, as well as the evidence from figure 5.15, it is clear there is more deviation in the position of the interface in x the greater the length of y. Since the length of z is the same in all simulations, the extra deviation must come from the presence of capillary waves forming along $\mathbf{y}$. If no capillary waves were present along $\mathbf{y}$, then it would be expected that $\langle \mathrm{RMS} \rangle$ would match that measured for the "flat interface" for all lengths of y; which instead is only observed when $y = 13.265$ Å.

The presence of capillary waves in the short direction of a simulation also affects the measured interfacial stiffness as shown in figure 5.16. It should be observed that figure 5.16 also shows an effect from varying the number of bins in z, which will be discussed further in section 5.4.3, but in general where $\Delta_z \approx a_0$, the increase in y results in a higher measured interfacial stiffness. This is not unsurprising since as previously shown, the larger y is, the more pronounced the presence of capillary waves in the short direction of the system, resulting in higher overall curvature of the interface. A more highly curved interface results in a greater free energy of formation of the interface, as discussed in chapter 4, and hence the stiffness should increase. This is exactly what is observed in figure 5.16.

When considering the measured interfacial stiffness for $n_z = 50$ bins, it should also be observed that the reduction in the measured stiffness is not linear. Reducing the thickness from 22.1 Å to 17.7 Å, results in a drop in the measured stiffness of 2.5(12) mJ m^{-2}, reducing the thickness further to 13.3 Å reduces the stiffness by a further 7.3(11) mJ m^{-2}. This non-linear drop in stiffness mirrors the non-linear

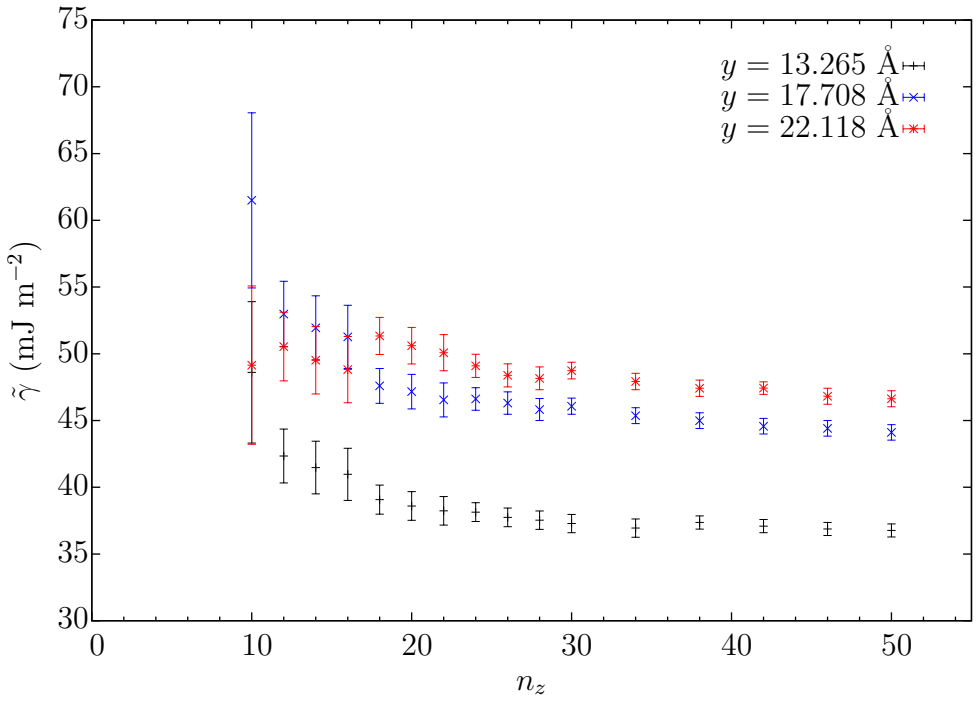

Figure 5.16: Measured interfacial stiffness for simulations of various short direction lengths, y, and number of bins along z, n_z, for the (basal)[11$\bar{2}$0] simulation. 80 bins are used along the long direction and $q12$ has been used to identify the interface.

drop in the measured $\langle \text{RMS} \rangle$ at the same lengths of y. This suggests that at 13.3 Å, the capillary waves are no longer present along **y** and the measured stiffness is due only to waves along **z**.

In essence, the choice in the length of the short direction imposes an upper estimate on the interfacial stiffness. To ensure the measured stiffness is as accurate as possible, the short direction should be chosen to be, as short as possible, or until convergence of the measured stiffness or $\langle \text{RMS} \rangle$ has been demonstrated; and is larger than twice the cutoff of the chosen potential, if particle self interaction is not desirable.

5.4.2 Long Direction

The effect of varying the bins in the long direction of the system can be seen in figure 5.17 for the ice-Ic, ice-Ih and ice-0 systems using the various relevant order parameters. In all cases, the general trend strongly indicates that the measured interfacial stiffness converges as the width of the bins $\Delta_x \to a_0$. For all three ice systems, the smallest average width of the bins used are $\langle \Delta_x \rangle = 4.96$ Å, $\langle \Delta_x \rangle = 4.81$ Å and $\langle \Delta_x \rangle = 5.23$ Å, for ice-Ic, ice-Ih and ice-0, respectively. Wider bin

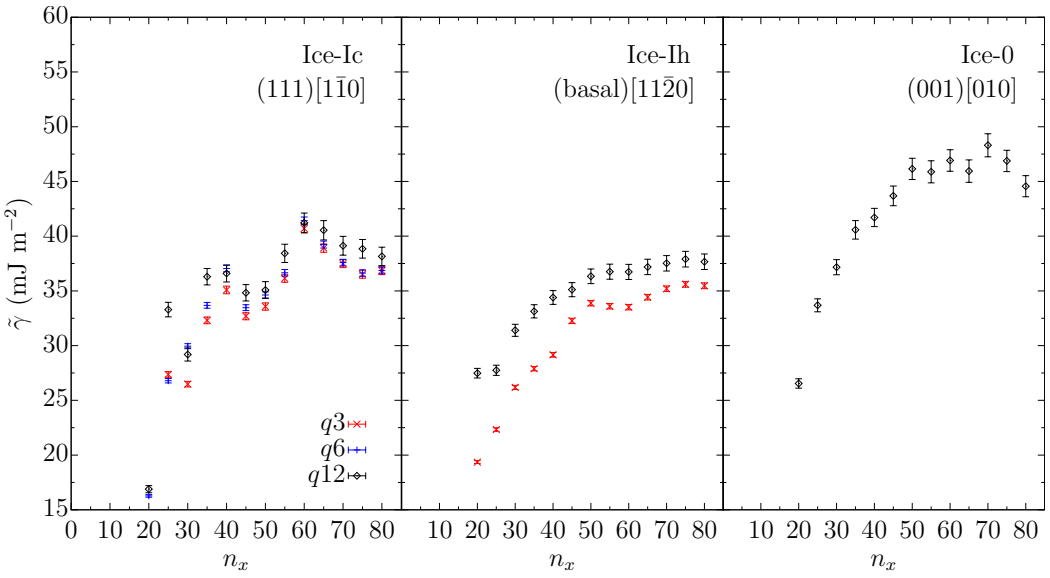

Figure 5.17: Measured interfacial stiffness for various bins in the long direction of the system, for one orientation in each of the ice structures. The number of bins along the interface is kept constant with 50, 50 and 100 bins, respectively.

widths result typically in a lower interfacial stiffness, especially if $\Delta_x \gg a_0$.

This inverse correlation between stiffness and Δ_x occurs since the wider the bins, the more particles per bin. When averaging the particles' order parameters over each bin of large width, the smaller fluctuations near to the interface are averaged out and the capillary waves across the surface become less prominent. In such a bin, change in a single particle's order parameter indicating a change of phase would not appreciably affect the average result of the order parameter of the bin. This effectively smooths the interface out and a flatter interface results in a lower free energy of formation. However, if the number of bins is large and Δ_x is small, then the fewer particles there are per bin. Any change in an individual particle's order parameter as it changes phase would more significantly affect the average result of the average order parameter in a single bin. Fluctuations near to the interface would be more noticeable in individual bins and the rougher characteristics of the interface could be resolved. A rougher interface produces a higher free energy of formation and these effects are exactly what are shown in figure 5.17.

Another effect that is present in figure 5.17 is that the stiffness does not consistently reduce in value with increasing bin width. This effect is most prominent in the case of ice-Ic where clearly the measured stiffness can be larger with larger bin sizes. A higher stiffness indicates a more highly curved interface, but the degree of curvature has not actually changed, just the choice of discretisation. Instead, this

suggests an aliasing effect when discretising the system in x. The effect observed can be attributed to fluctuations occurring on the boundaries between bins. Bins of intermediate width and low density, would be sensitive to variation in individual particle order parameters, but large enough to imply the fluctuation occurs over a larger region than in reality. For example, a single particle may update its order parameter indicating it has changed phase. The low density bin may change its average order parameters and also indicate a change of phase, which results in a change in the position of the interface by as much as Δ_x. If Δ_x is small, the change in the position of the interface is small and the measured curvature and stiffness is lower; if Δ_x is large then the inverse is true.

Overall, decreasing Δ_x converges the stiffness while large values of Δ_x artificially flatten the interface and reduce the measured stiffness. Aliasing effects may also be observed, before the stiffness actually converges, for intermediate values of Δ_x. Δ_x should be chosen such that the order parameter profile is smoothed sufficiently to effectively measure the interfacial stiffness, and hence this choice should be made from values of Δ_x that demonstrate that the stiffness has converged. Choosing larger values of Δ_x, that are within the region of convergence, are more computationally efficient, since few voxels are required to update (see the supplied "Interface_Analysis" code, provided on the digital storage medium).

5.4.3 Interface Direction

Figure 5.18 shows how varying the number of bins across the length of the interface affects the measured stiffness while keeping the maximum wave number used, q_z, constant. The average width of the bins when using the largest number of bins for ice-Ic, ice-Ih and ice-0 are $\langle \Delta_z \rangle = 4.07$ Å, $\langle \Delta_z \rangle = 3.68$ Å and $\langle \Delta_z \rangle = 5.18$ Å, respectively. It is clear when keeping q_z constant and increasing Δ_z, that the measured stiffness also increases. This trend is the result of larger bins failing to capture the more continuous change of the local interface position across $\mathbf{z}$. Larger distances between the measured local interface positions, results in a more disjointed interface, with abrupt changes in its shape; analogous to a saw-tooth interface. Such a disjointed interface requires contributions from smaller wavelengths to correctly describe its form, which contribute more energy to the formation of the interface. Conversely, smaller bins will capture fluctuations over shorter distances, rendering a smoother interface. The shortest distance that a change in the interface position can occur is between two adjacent atoms. Hence, the most accurate mapping of the local interface position is achieved as $\Delta_z \to a_0$, as shown in figure 5.18.

However, figure 5.18 is not a strictly accurate portrayal of how the measured

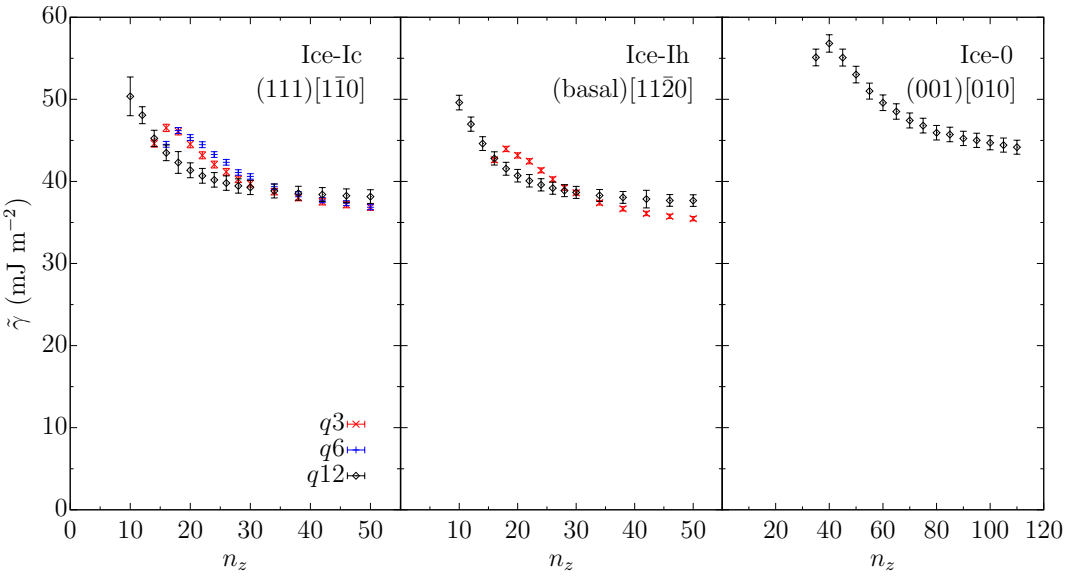

Figure 5.18: Measured interfacial stiffness for varying number of bins across z in simulations of the different ice structures. 80 bins are used along the long direction of the simulation in all cases.

stiffness changes with varying Δ_z. By keeping q_z the same for a varying number of bins, n_z, the continuum limit of CWT is not necessarily met; refer to chapter 4. For example, in figure 5.18 (*left*), using $q12$ and $n_z = 50$, $q_z\Delta_z/2 = 0.25$, and when $n_z = 10$, $q_z\Delta_z/2 = 1.26$. Considering that if CWT is to be valid, the continuum limit requires $q_z\Delta_z/2 \leq 0.5$, and the largest value of q_z that can be used cannot be the same for large values of Δ_z as that for small values of Δ_z. Correcting for this constraint is shown in figure 5.19.

When taking into consideration the effect of the continuum limit of CWT, the difference between figures 5.18 and 5.19, indicates that as q_z is reduced with increasing Δ_z, the measured stiffness is reduced from that measured in figure 5.18; it should be recalled that this was also observed in figure 5.16. Furthermore, the overall measured stiffness can be reduced to values comparable with small Δ_z, or even less.

To understand why this happens, consider continuing the analogy of the saw-tooth interface for large Δ_z. Since the true form of the interface is not actually a saw-tooth, but rather something smoother that is being coarse-grained, the smaller wavelengths that are additionally included to describe the form of the saw-tooth are actually describing a fictional interface. Hence, these high energy fluctuations must be be discounted to more accurately describe the interfacial stiffness; which is why the continuum limit is necessary and why reducing the maximum q_z reduces $\tilde{\gamma}$.

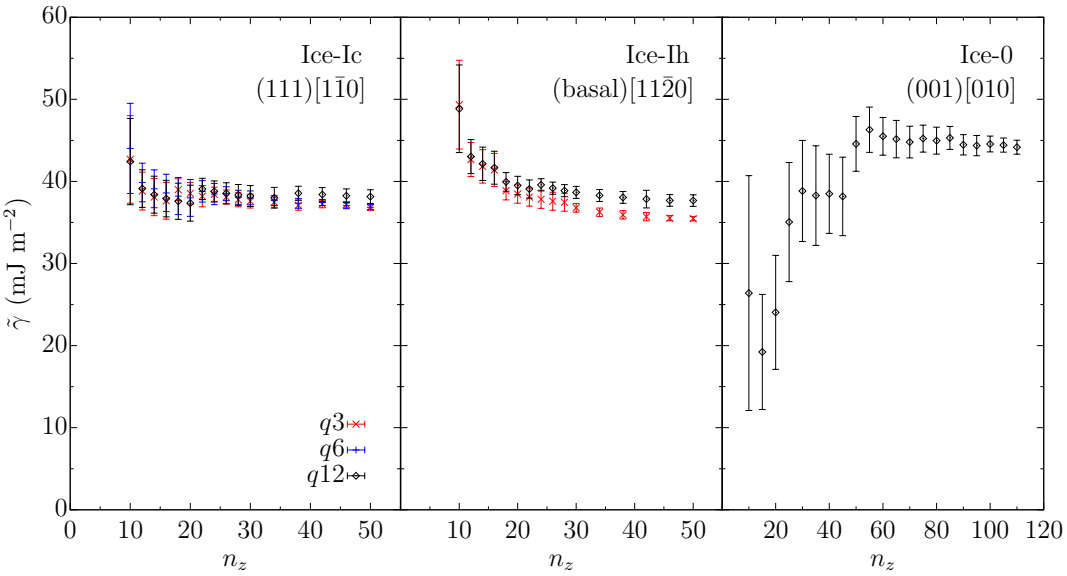

Figure 5.19: As figure 5.18, but with varying the maximum value of q_z used, ensuring the continuum limit is met.

However, the more coarse-grained a system is, the fewer possible wavelengths are available to describe the interface. Hence, when obeying the continuum limit, too little or too much "excess" energy from the shortest wavelengths can be discarded; which is why in figure 5.19, for large Δ_z, $\tilde{\gamma}$ decreases too much in ice-0, remains too high in ice-Ih, and fairly accurately describes the true interfacial stiffness in ice-Ic.

5.5 Summary

The previous two sections highlight various factors important to the measurement of the interfacial stiffness. Here, these points are briefly summarised.

The various order parameters investigated, can be used in certain cases to distinguish between different structures of ice and water. $q6$ is capable of distinguishing between ice-Ic and water. However, it cannot reliably distinguish between ice-Ih and water, nor ice-0 and water, nor between any of the ice structures. $q3$ is good at distinguishing between ice-Ic, ice-Ih and water; which is excellent for nucleation simulations where the degree of stacking disorder between ice-Ic and ice-Ih can be identified (see chapter 7). Although, $q3$ cannot reliably distinguish between ice-0 and water. $q12$ can distinguish between solid and liquid for ice-I and ice-0 with absolute or near absolute certainty. It is however, unable to distinguish between different solid structures. This makes $q12$ the most reliable order parameter to compare between measurements of quantities made in different ice structures.

It is found though, that none of the order parameters investigated can distinguish between all the different structures of ice and water.

The choice of order parameter also has an effect on the measurement of the interfacial stiffness, as can be seen throughout section 5.4. It is shown that the converged measurements of the interfacial stiffness for interfaces identified using $q12$, are consistently higher than that when using $q3$ or $q6$ as the order parameter, in ice-Ic and ice-Ih; as shown in figures 5.17, 5.18 and 5.19. The reason for this is that $q12$ more sharply defines the interface by identifying on average, more solid and less liquid, correctly as solid than either $q3$ or $q6$. Hence, finer fluctuations in the interface position are measured, resulting in a higher energy of formation of the interface. The reduced precision when using either $q3$ or $q6$, blurs the interface, smoothing out the higher energy fluctuations. Furthermore, $q3$ also identifies interfacial atoms directly, further broadening the width of the interface and making higher energy fluctuations more difficult to resolve.

The size of the short direction clearly affects the interfacial stiffness. If the short direction is insufficiently short, capillary waves form along the short direction, increasing the interfacial stiffness. The system therefore only needs to be as thin as that of an approximately flat interface along the short direction; rather than exactly 1D in order to apply the 1D form of CWT.

Discretisation along the long direction of the system can result in underestimating the value of the interfacial stiffness if the bin widths are too large. Conversely, discretisation along the interface can result in overestimating the interfacial stiffness for large bin widths when the continuum limit for CWT is not met, and is otherwise unpredictable when it is. When discretising along both axes, it is important to check for convergence of the stiffness and ensure the bin widths are sufficiently small.

5.6 Symmetry Adapted Spherical Harmonics

Recall that in order to measure the interfacial free energy, measurements must be made of the interfacial stiffness. As discussed in chapter 4, the interfacial stiffness is defined in terms of the interfacial free energy by equation (4.4). However, just knowing the stiffness for a single simulation, does not allow the free energy to be immediately recovered for that system. Instead, the idea is employed that some function exists that can describe the free energy for every crystal plane and that each crystal plane is described by a single valued equation based on its position in the function space, defined by the function variables. In turn, an equation describing the interfacial stiffness along a direction on that plane, can be derived via equation

(4.4).

The function that describes the distribution of the values of the free energy should respect the symmetry of the crystal structure and therefore be constructed of a linear combination of symmetric basis functions[84]. For example, in the case of cubic crystal symmetry, the overall function used to describe the interfacial free energy obeys a basis set of cubic harmonics, which are symmetry adapted spherical harmonics (SASH) with cubic point group symmetry[75, 85, 86]. The SASH equations define the value of the free energy of any crystal plane in spherical polar coordinates on a unit sphere identified by a unique polar and azimuthal angle, θ and ϕ respectively; where $\mathbf{r}$ is normal to the interface and hence changing that value of r points to mirror images of the same plane:

$$\gamma(\theta,\phi) = \gamma_0(1 + \epsilon_1 S_1(\theta,\phi) + \epsilon_2 S_2(\theta,\phi) + ...)\,. \tag{5.6}$$

In equation (5.6), $S_i(\theta,\phi)$ is the basis set of SASH equations, while the N coefficients, ϵ_i, parameterise the contributions of each of the basis SASH equations. These coefficients are recovered via nonlinearly fitting n interfacial stiffnesses to the set of n respective derived equations. To solve for $N+1$ coefficients, including γ_0, it is required that $n \geq N+1$.

The coordinate system used to define the crystal planes is shown in figure 5.20. Any point on the unit sphere forms a set of orthogonal polar unit vectors $\{\mathbf{e}_r, \mathbf{e}_\theta, \mathbf{e}_\phi\}$ which describe a crystal plane. These vectors can be made to align with the local simulation axes x, y and z respectively, as shown in figure 5.20. The values of θ and ϕ that align the unit vectors to a particular crystal plane are defined with respect to an underlying set of orthogonal SASH basis vectors $\{\mathbf{i}, \mathbf{j}, \mathbf{k}\}$. These basis vectors are fixed relative to the axes of the crystal unit cell $\{\mathbf{a}, \mathbf{b}, \mathbf{c}\}$, as shown in figure 5.21.

The crystal directions, $\mathbf{d}$, are characterised by Miller indices $[l\ m\ n]$ of the form $l\mathbf{a} + m\mathbf{b} + n\mathbf{c} = \mathbf{d}$ for ice-Ic and ice-0; hence the plane (001) is the plane with $\mathbf{k}$ normal to it in figure 5.21. For ice-Ih, the Miller indices are similarly $[h\ k\ p\ q]$, where $p = -(h+k)$. Hence, strictly in terms of Miller indices, the ice-Ih planes are (basal) $\equiv (0001)$ and (prism) $\equiv (10\bar{1}0)$; hence $\mathbf{j}$ is normal to the (prism) plane. Careful consideration of how the SASH basis vectors are aligned with the unit cell and how the orthogonal unit vectors are aligned with the local simulation axes, is necessary to find the correct values of θ and ϕ which generate the correct SASH equation for the crystal-plane interface between the solid and liquid phases.

In a quasi-2D system, the interface is ribbon-like and so the surface will

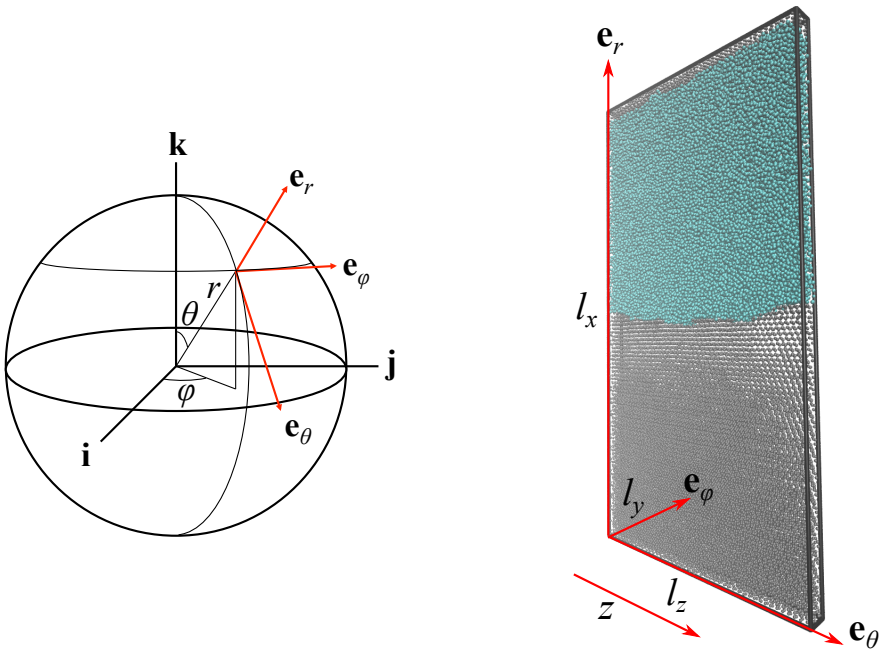

Figure 5.20: The coordinate system used (*left*) forms an orthogonal set of unit vectors from the SASH coordinates where $\mathbf{e}_r$ is always normal to the interface; demonstrated in the (111)[1$\bar{1}$0] simulation (*right*).

exhibit curvature from capillary waves only in the direction along the length of the interface. From such simulations, the interfacial stiffness is measured across the interface, corresponding to a direction unit vector $\mathbf{u} = \theta\mathbf{e}_\theta + \phi\mathbf{e}_\phi$, defined in terms of the orthogonal direction vectors on the unit sphere for the crystal plane. Since the crystal can be orientated so that the short direction of the interface is always $\mathbf{e}_\theta$ or $\mathbf{e}_\phi$, and since no fluctuations occur in this direction, then $\mathbf{u} = [1, 0]$ or $\mathbf{u} = [0, 1]$. For example, in figure 5.20, the (111) plane forms an interface with the water with a short direction along $\mathbf{y} = [1\bar{1}0]$, meaning the interface only deforms in the orthogonal $\mathbf{z} = [11\bar{2}]$ direction, which is equivalent to $\mathbf{e}_\theta$ on the unit sphere; hence $\mathbf{u} = [1, 0]$ for the (111)[1$\bar{1}$0] interface with this choice of crystal orientation to the local simulation axes.

The degree of curvature along the surface described by a function with direction $\mathbf{u}$, is given by the Hessian of that surface[88]. This means that the variation, or curvature, in the surface free energy, given by γ'' in equation (4.4), can be rewritten in terms of the Hessian and the direction vector of curvature:

$$\tilde{\gamma}(\theta, \phi) = \gamma(\theta, \phi) + \mathbf{u}^T \boldsymbol{H}_\gamma(\theta, \phi)\mathbf{u}\,, \tag{5.7}$$

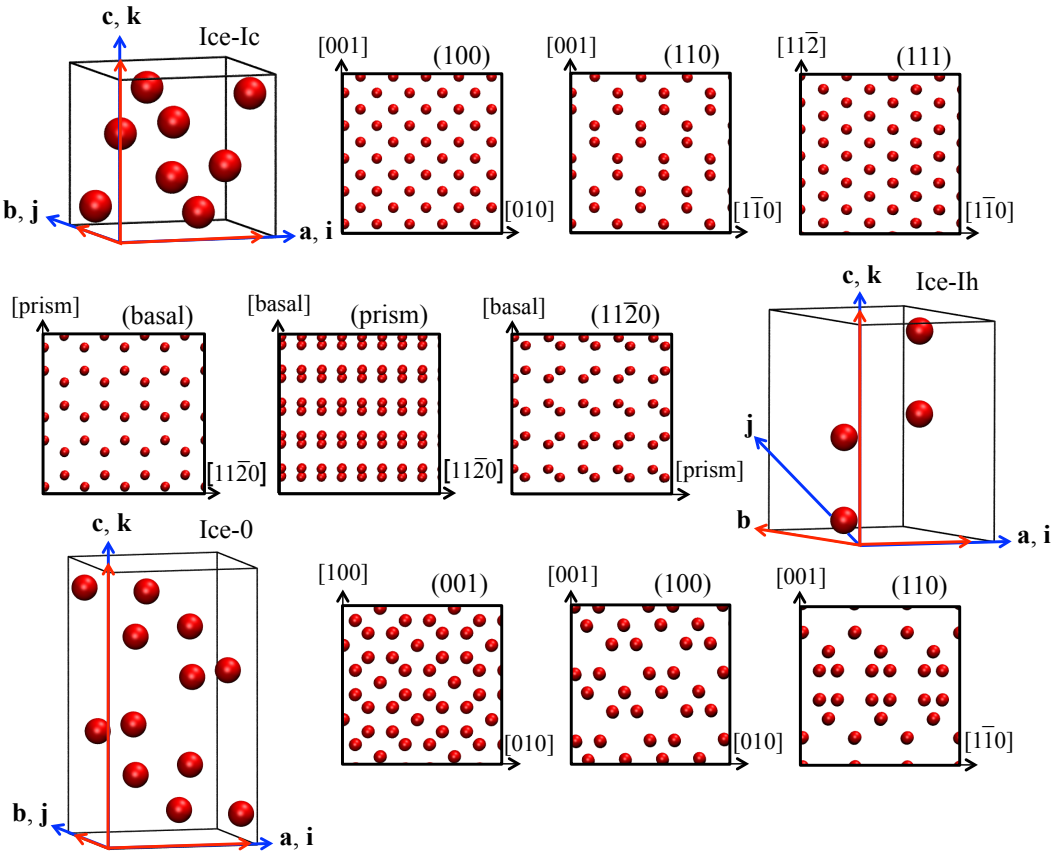

Figure 5.21: The ice-Ic (*top row*), ice-Ih (*middle row*) and ice-0 (*bottom row*) crystal unit cells and planes. The SASH basis coordinate system axes are shows in blue and the crystal cell axes are shown in red, on the unit cells, while the local simulation axes are shown in black on each of the planar images. The construction of each cell is given in (a b c α β γ) notation[87]: ice-Ic (1 1 1 $\pi/2$ $\pi/2$ $\pi/2$); ice-Ih (1 1 1.630 $\pi/2$ $\pi/2$ $2\pi/3$); ice-0 (5.905 5.905 10.674 $\pi/2$ $\pi/2$ $\pi/2$).

where the Hessian is the radially independent 2×2 matrix given as

$$\boldsymbol{H}_\gamma(\theta,\phi) = \begin{bmatrix} \frac{\partial^2\gamma}{\partial\theta^2} & \frac{1}{\sin\theta}\frac{\partial^2\gamma}{\partial\phi\partial\theta} - \frac{\cos\theta}{\sin^2\theta}\frac{\partial\gamma}{\partial\phi} \\ \frac{1}{\sin\theta}\frac{\partial^2\gamma}{\partial\theta\partial\phi} - \frac{\cos\theta}{\sin^2\theta}\frac{\partial\gamma}{\partial\phi} & \frac{1}{\sin^2\theta}\frac{\partial^2\gamma}{\partial\phi^2} + \cot\theta\frac{\partial\gamma}{\partial\theta} \end{bmatrix} . \tag{5.8}$$

This allows the equation for the interfacial stiffness to be derived for any crystal plane defined by θ and ϕ along any direction vector $\mathbf{u}$.

Using the Alloy-Theoretic Automated Toolkit (ATAT), it was possible to calculate the SASH equations for the free energy, for the three different ice unit cells[89, 90]. These were calculated up to $l = 6$ for ice-Ic, ice-Ih and ice-0. The expressions for the free energy of the various interfaces simulated in ice-Ic, ice-Ih

and ice-0 are shown in tables 5.2, 5.3 and 5.4, respectively. Similarly, the derived SASH equations for the interfacial stiffness in each of the simulated orientations are shown in tables 5.5, 5.6 and 5.7. It should be noted that in tables 5.3 and 5.6, $S_2(\theta, \phi)$ and $S_3(\theta, \phi)$ have been omitted. This is discussed in section 5.6.3.

5.6.1 Free Energy Equations

Here the equations for the interfacial free energy are tabulated for the systems of ice-Ic, ice-Ih and ice-0.

Plane	θ	ϕ	γ_{fit} Equations
(100)	$\frac{\pi}{2}$	0	$\gamma_0\big(1+\frac{2}{5}\epsilon_1+\frac{4}{7}\epsilon_2+4\epsilon_3+8\epsilon_4\big)$
(110)	$\frac{\pi}{2}$	$\frac{\pi}{4}$	$\gamma_0\big(1-\frac{1}{10}\epsilon_1-\frac{13}{14}\epsilon_2+\frac{9}{4}\epsilon_3-\frac{1}{4}\epsilon_4\big)$
(111)	$\tan^{-1}\big(\frac{2}{\sqrt{2}}\big)$	$\frac{\pi}{4}$	$\gamma_0\big(1-\frac{4}{15}\epsilon_1+\frac{64}{63}\epsilon_2+\frac{32}{27}\epsilon_3-\frac{1024}{81}\epsilon_4\big)$
(112)	$\tan^{-1}\big(\frac{1}{\sqrt{2}}\big)$	$\frac{\pi}{4}$	$\gamma_0\big(1-\frac{1}{10}\epsilon_1+\frac{37}{126}\epsilon_2-\frac{173}{108}\epsilon_3+\frac{233}{36}\epsilon_4\big)$

Table 5.2: Interfacial free energy SASH equations for ice-Ic.

Plane	θ	ϕ	γ_{fit} Equations
(prism)	$\frac{\pi}{2}$	$\frac{\pi}{2}$	$\gamma_0\big(1+0.408\epsilon_1+0.149\epsilon_4\big)$
(basal)	0	$\mathbb{R}$	$\gamma_0\big(1-0.816\epsilon_1-0.239\epsilon_4\big)$
$(11\bar{2}0)$	$\frac{\pi}{2}$	0	$\gamma_0\big(1+0.408\epsilon_1\big)$

Table 5.3: Interfacial free energy SASH equations for ice-Ih.

Plane	θ	ϕ	γ_{fit} Equations
(001)	0	$\mathbb{R}$	$\gamma_0\big(1-0.816\epsilon_1+0.216\epsilon_2+0.426\epsilon_3-0.140\epsilon_4-0.223\epsilon_5\big)$
(100)	$\frac{\pi}{2}$	0	$\gamma_0\big(1+0.408\epsilon_1+0.396\epsilon_2+0.154\epsilon_4\big)$
(101)	$\tan^{-1}\big(\frac{c}{a}\big)$	0	$\gamma_0\big(1+0.121\epsilon_1+0.128\epsilon_2-0.206\epsilon_3-0.148\epsilon_4-0.009\epsilon_5\big)$
(102)	$\tan^{-1}\big(\frac{c}{2a}\big)$	0	$\gamma_0\big(1-0.266\epsilon_1-0.015\epsilon_2-0.187\epsilon_3-0.077\epsilon_4+0.128\epsilon_5\big)$
(110)	$\frac{\pi}{2}$	$\frac{\pi}{4}$	$\gamma_0\big(1+0.408\epsilon_1-0.234\epsilon_2+0.320\epsilon_3-0.067\epsilon_4+0.139\epsilon_5\big)$

Table 5.4: Interfacial free energy SASH equations for ice-0. c=10.67425 and a=5.9045.

5.6.2 Interfacial Stiffness Equations

Here the equations for the interfacial stiffness are tabulated for the systems of ice-Ic, ice-Ih and ice-0. For some planes, the orientations measured have the same symmetry when $\mathbf{u} = [1, 0]$ or $\mathbf{u} = [0, 1]$; which gives the same expression for the interfacial stiffness. This is indicated by $\mathbf{u} = \mathbf{e}_{\theta/\phi}$, and in these cases, only the plane is listed and the equivalent orientations that were measured are indicated in the relevant table caption.

Orientation	$\mathbf{u}$	$\tilde{\gamma}_{\text{fit}}$ Equations
(100)	$\mathbf{e}_{\theta/\phi}$	$\gamma_0\big(1-\frac{18}{5}\epsilon_1-\frac{80}{7}\epsilon_2-140\epsilon_3-432\epsilon_4\big)$
(110)[1$\bar{1}$0]	$\mathbf{e}_{\theta}$	$\gamma_0\big(1-\frac{21}{10}\epsilon_1+\frac{365}{14}\epsilon_2-\frac{175}{4}\epsilon_3+\frac{1341}{4}\epsilon_4\big)$
(110)[001]	$\mathbf{e}_{\phi}$	$\gamma_0\big(1+\frac{39}{10}\epsilon_1+\frac{155}{14}\epsilon_2-\frac{455}{4}\epsilon_3-\frac{1233}{4}\epsilon_4\big)$
(111)	$\mathbf{e}_{\theta/\phi}$	$\gamma_0\big(1+\frac{12}{5}\epsilon_1-\frac{1280}{63}\epsilon_2-\frac{1120}{27}\epsilon_3+\frac{2048}{3}\epsilon_4\big)$
(112)[1$\bar{1}$0]	$\mathbf{e}_{\theta}$	$\gamma_0\big(1+\frac{19}{10}\epsilon_1+\frac{1255}{126}\epsilon_2+\frac{4795}{108}\epsilon_3-\frac{21041}{36}\epsilon_4\big)$
(112)[11$\bar{1}$]	$\mathbf{e}_{\phi}$	$\gamma_0\big(1-\frac{1}{10}\epsilon_1-\frac{2735}{126}\epsilon_2+\frac{7315}{108}\epsilon_3-\frac{4123}{36}\epsilon_4\big)$

Table 5.5: Interfacial stiffness SASH equations for ice-Ic. The orientations for (100)[010], (100)[001] and (111)[1$\bar{1}$0], (111)[11$\bar{2}$] are equivalent[70]; hence only planes (100) and (111) are given.

Orientation	$\mathbf{u}$	$\tilde{\gamma}_{\text{fit}}$ Equations
(prism)[11$\bar{2}$0]	$\mathbf{e}_{\theta}$	$\gamma_0\big(1-2.041\epsilon_1-3.430\epsilon_4\big)$
(prism)[basal]	$\mathbf{e}_{\phi}$	$\gamma_0\big(1+0.408\epsilon_1-2.535\epsilon_4\big)$
(basal)	$\mathbf{e}_{\theta/\phi}$	$\gamma_0\big(1+1.633\epsilon_1+4.772\epsilon_4\big)$
(11$\bar{2}$0)[prism]	$\mathbf{e}_{\theta}$	$\gamma_0\big(1-2.041\epsilon_1-2.684\epsilon_4\big)$
(11$\bar{2}$0)[basal]	$\mathbf{e}_{\phi}$	$\gamma_0\big(1+0.408\epsilon_1+2.684\epsilon_4\big)$

Table 5.6: Interfacial stiffness SASH equations for ice-Ih. The orientations for (basal)[prism] and (basal)[11$\bar{2}$0] are equivalent, so only the (basal) plane is given.

Orientation	$\mathbf{u}$	$\tilde{\gamma}_{\text{fit}}$ Equations
(001)	$\mathbf{e}_{\theta/\phi}$	$\gamma_0\big(1+1.633\epsilon_1-1.946\epsilon_2-3.838\epsilon_3+2.806\epsilon_4+4.454\epsilon_5\big)$
(100)[001]	$\mathbf{e}_{\phi}$	$\gamma_0\big(1+0.408\epsilon_1-4.649\epsilon_2+2.558\epsilon_3-1.613\epsilon_4+1.113\epsilon_5\big)$
(100)[010]	$\mathbf{e}_{\theta}$	$\gamma_0\big(1-2.041\epsilon_1-2.487\epsilon_2-2.558\epsilon_3-4.559\epsilon_4-1.113\epsilon_5\big)$
(101)[010]	$\mathbf{e}_{\theta}$	$\gamma_0\big(1-1.180\epsilon_1+1.034\epsilon_2+1.732\epsilon_3+3.762\epsilon_4+1.881\epsilon_5\big)$
(101)[$\bar{1}$01]	$\mathbf{e}_{\phi}$	$\gamma_0\big(1+0.695\epsilon_1-3.337\epsilon_2+1.978\epsilon_3+2.176\epsilon_4-1.515\epsilon_5\big)$
(102)[010]	$\mathbf{e}_{\theta}$	$\gamma_0\big(1-0.019\epsilon_1+2.493\epsilon_2+3.069\epsilon_3-0.279\epsilon_4-2.424\epsilon_5\big)$
(102)[$\bar{2}$01]	$\mathbf{e}_{\phi}$	$\gamma_0\big(1+1.082\epsilon_1-2.225\epsilon_2+0.305\epsilon_3+3.350\epsilon_4-2.712\epsilon_5\big)$
(110)[001]	$\mathbf{e}_{\phi}$	$\gamma_0\big(1+0.408\epsilon_1+4.811\epsilon_2-2.239\epsilon_3+1.701\epsilon_4-0.974\epsilon_5\big)$
(110)[1$\bar{1}$0]	$\mathbf{e}_{\theta}$	$\gamma_0\big(1-2.041\epsilon_1-0.595\epsilon_2-3.518\epsilon_3+0.964\epsilon_4-4.593\epsilon_5\big)$

Table 5.7: Interfacial stiffness SASH equations for ice-0. The orientations (001)[010] and (001)[100] are equivalent, so only plane (001) is given.

5.6.3 Discussion

In the context of this subsection, the terminology "S_i" refers to the i^{th} SASH basis function; where $S_i \equiv S_i(\theta, \phi)$.

The form of some of the SASH equations calculated in sections 5.6.1 and 5.6.2, do not contain the maximum number of SASH basis functions possible up to $l = 6$. As a reference, the full SASH equations for ice-Ic, ice-Ih and ice-0 generated by ATAT are reproduced in full in appendix B, where it can be seen that in the case of ice-Ic, ice-Ih and ice-0 that there are 4, 4 and 5 SASH basis functions, respectively, that can describe the free energy and stiffness. In ice-Ih, S_4 is absent from the description of the $(11\bar{2}0)$ free energy, and both S_3 and S_5 are absent from the description of the ice-0 (100) free energy. In these cases these SASH basis functions are absent because at the respective values of θ and ϕ, they equate to zero. However, in ice-Ih S_2 and S_3 have been completely omitted from the equations for the free energy and stiffness.

This research finds that it is not possible to perform a nonlinear fit to the 5 parameter SASH equations for ice-Ih with the orientations measured and so some of the parameters must be omitted in order to fit to the stiffness. It is not immediately obvious which parameters should be removed and which should be included. However, by performing a Taylor series expansion on each of the SASH basis functions to eighth order, it is found that S_1 and S_2 only have θ dependence up to fourth order with no ϕ dependence at all. S_3 has the addition of ϕ dependence at eighth order, while S_4 has ϕ dependence at sixth order. Hence, S_4 must be used to resolve the ϕ dependence in the anisotropy. There is no appreciable difference in the dependency of the other terms, but at least one of them must be used to provide a satisfactory fit to the measured stiffness. Given S_1 is the lowest order correction, this is the most sensible term to choose. Hence, the stiffness in ice-Ih is fit to γ_0, ϵ_1 and ϵ_4. Work performed by Benet et al. and Sun et al. also demonstrate a similar dependency[61, 91]. Sun et al. also find that S_1 is necessary to obtain a good fit, while S_4 is required to resolve the anisotropy of the stiffness in ice-Ih[91].

It should also be noted why the crystal planes as listed in section 5.6.1 have been chosen to be examined. This choice is motivated by picking those that were predicted to have the lowest free energy. According to the Bravais rule[92], a crystal plane's importance of formation is directly proportional to the interplanar spacing. This implies the kinetically controlled growth rate is inversely proportional to the interplanar spacing. Lower growth rates in this limit indicate a lower surface free energy of the plane, since the crystal will tend to minimise its overall surface free energy by exposing more surface area of the low energy plane[93], compared to

other planes. As a result, planes with the largest interplanar spacing typically have the lower index surfaces and so these were the chosen planes. Simulating low energy surfaces is preferential since they exhibit slower rates of change and longer wavelength fluctuations. These attributes allow for higher accuracy measurements of the interfacial stiffness than can otherwise be obtained from noisier simulations with many high energy fluctuations along rougher interfaces.

Chapter 6

Ice Results

6.1 Introduction

Following the arguments addressed in the preceding chapters, it is possible to accurately measure the interfacial free energy of solid-liquid ice-Ic, ice-Ih and ice-0 coexistence simulations using CWM. In this chapter, the results for such systems are presented and discussed.

It should be noted that results for the bulk free energy difference between ice-Ih and ice-0 have been provided by Dr D. Quigley, computed via lattice switching Monte Carlo (LSMC) simulations, which were previously partially reported in work by Quigley et al.[94].

6.2 Simulation Details

MD simulations were performed using LAMMPS to model the interface between solid-liquid equilibrium coexistence systems for ice-Ic, ice-Ih and ice-0. The systems were quasi-2D, being short in one of the directions perpendicular to the normal of the interface, but were still large enough to avoid self-interaction of particles with their own potential. The dimensions of all simulations performed are shown in table 6.1. Periodic boundary conditions were used to mimic an infinite crystal system with a quasi-1D interface. A Stillinger-Weber type potential was used to implement the mW model of water, as outlined in chapter 2, with a potential cutoff of 4.3065 Å. The simulations were run with a timestep of 1 fs and equilibrated over 5 ns before sampling the production run every 10 ps. These were performed at a pressure of 1 atm, where a five-chained Nosé-Hoover barostat was applied. Similarly, a five-chained Nosé-Hoover thermostat was applied in the applicable ensembles to control

the temperature of the systems.

Initially the entire systems were slowly relaxed either anisotropically or triclinically, depending on the orthogonality of the unit cell, forming a perfect crystal structure. For ice-I systems, particle velocities were then sampled from a Gaussian distribution, to provide an average system temperature of 253 K, whilst keeping a zero average momentum of the system. The warm solid crystal was then allowed to stabilise at 253 K in an NVT ensemble over $50,000$ iterations. The simulation then switched to an NPT ensemble and equilibrated for a further $200,000$ iterations at the same temperature.

Once equilibrated, the system was then split in half along the x direction, designating one half as the solid region and the other as the liquid region. The liquid region was melted by re-sampling the liquid particle velocities to provide an average system temperature of 473 K and zero average system momentum. The liquid region was then run at 473 K in the NPT ensemble for $50,000$ iterations, followed by cooling to 293 K over $200,000$ iterations.

Following the liquid cooling, the two halves were carefully allowed to interact with each other at coexistence by maintaining the proportions of the interface dimensions. Coupling the y and z directions to vary isotropically while permitting anisotropic variation in x, allowed the positions of the particles on the interface to vary proportionally without the interface collapsing. All particle velocities were re-sampled to produce an average temperature of 273 K with zero average system momentum, and the system run within a yz coupled NPH ensemble over 1.5×10^6 iterations. Equilibration then continued in a fully anisotropic NPH ensemble for a further 3×10^6 iterations, resulting in a stable two-phase system with the necessary quasi-1D solid-liquid interface.

Coexistence simulations of ice-0 and water were performed in a similar manner to those of ice-I and water, except the initial warm solid system was constructed at 220 K, while the liquid phase was created at 440 K and cooled to 260 K. The interaction of the two halves of the system, and final equilibration, was performed at 240 K; approximately the melting temperature (245 K) of ice-0 at 1 atm, as demonstrated in section 6.3.

Once the simulations had equilibrated over the initial 5 ns, the production runs were performed. In the ice-I systems, the production runs lasted 100 ns, while in the ice-0 systems the production runs lasted 30 ns. The difference in the durations was due to the number of particles in the simulations; as shown in table 6.1. The greater number of particles in the ice-0 systems meant it was not practical to simulate for as long as the smaller ice-I systems, nor was it necessary, so long as the measured

Structure	Orientation	Geometry $x \times y \times z$ (Å)	Particles
Ice-Ic	(100)[010]	396.32×12.50×200.07	32,768
	(100)[001]	396.36×12.50×200.07	32,768
	(110)[1$\bar{1}$0]	393.78×17.69×200.08	46,080
	(110)[001]	393.89×12.50×203.41	33,120
	(111)[1$\bar{1}$0]	396.62×15.32×203.42	40,848
	(111)[11$\bar{2}$]	396.55×17.69×183.81	42,624
	(112)[1$\bar{1}$0]	396.54×17.69×199.14	46,176
	(112)[11$\bar{1}$]	396.64×15.31×194.57	39,072
Ice-Ih	(prism)[11$\bar{2}$0]	409.72×13.28×187.24	33,696
	(prism)[basal]	409.67×14.41×194.69	38,016
	(basal)[11$\bar{2}$0]	384.90×13.28×184.00	31,104
	(basal)[prism]	384.88×15.33×194.78	38,016
	(11$\bar{2}$0)[prism]	407.51×15.33×187.26	38,688
	(11$\bar{2}$0)[basal]	407.32×14.41×183.94	35,712
Ice-0	(001)[010]	418.68×23.76×570.32	184,320
	(001)[100]	418.51×23.76×570.32	184,320
	(100)[001]	416.05×21.52×570.30	165,888
	(100)[010]	415.93×23.76×516.46	165,888
	(101)[010]	344.03×17.82×614.51	122,400
	(101)[$\bar{1}$01]	344.75×12.29×606.06	83,232
	(102)[010]	336.56×17.82×609.04	119,016
	(102)[$\bar{2}$01]	336.69×16.03×605.95	106,488
	(110)[001]	392.02×21.52×604.90	165,888
	(110)[1$\bar{1}$0]	392.18×25.20×516.53	165,888

Table 6.1: Simulation details for the different interfaces and orientations.

interfacial stiffness had converged by the end of the production run; as shown in section 6.3.

The number of bins used to discretise each system was chosen in such a way as to keep Δ_x and Δ_z approximately constant in each structure, as shown in table 6.2, while also being large enough to ensure consistently good order parameter profile fits and small enough to provide a high resolution of the interface. For these reasons, the dimensions of the bins in a single structure were kept as close to the distance of the coordination shell cutoff as possible; as discussed in chapter 5. However for the (prism)[basal] orientation, Δ_x and Δ_z had to be increased significantly compared to the other orientations of ice-Ih, in order to provide sufficient fitting to the order parameter profiles.

Structure	Orientation	Bins			
		N_z	Δ_z (Å)	N_x	Δ_x (Å)
Ice-Ic	(100)[010]	49	4.08	80	4.95
	(100)[001]	49	4.08	80	4.95
	(110)[1$\bar{1}$0]	49	4.08	79	4.98
	(110)[001]	50	4.07	79	4.99
	(111)[1$\bar{1}$0]	50	4.07	80	4.96
	(111)[11$\bar{2}$]	45	4.08	80	4.96
	(112)[1$\bar{1}$0]	49	4.06	80	4.96
	(112)[11$\bar{1}$]	48	4.05	80	4.96
Ice-Ih	(prism)[11$\bar{2}$0]	51	3.67	85	4.82
	(prism)[basal]	50	3.89	75	5.46
	(basal)[11$\bar{2}$0]	50	3.68	80	4.81
	(basal)[prism]	53	3.68	80	4.81
	(11$\bar{2}$0)[prism]	51	3.67	85	4.79
	(11$\bar{2}$0)[basal]	50	3.68	85	4.79
Ice-0	(001)[010]	100	5.70	80	5.23
	(001)[100]	100	5.70	80	5.23
	(100)[001]	100	5.70	80	5.20
	(100)[010]	90	5.74	80	5.20
	(101)[010]	108	5.69	66	5.21
	(101)[$\bar{1}$01]	106	5.72	66	5.22
	(102)[010]	107	5.69	64	5.26
	(102)[$\bar{2}$01]	106	5.72	64	5.26
	(110)[001]	106	5.71	75	5.23
	(110)[1$\bar{1}$0]	90	5.74	75	5.23

Table 6.2: Analysis details for the different interfaces and orientations.

6.2.1 Symmetric Orientations

As discussed in chapter 5, some of the SASH equations describe equivalent orientations for the measured interfacial stiffness. Consequently, two equivalent orientations cannot both be used to fit to one equation. Instead of arbitrarily choosing only one orientation to fit to, the average of the two orientations is calculated and weighted by the error on each. In this work from this point forward, when discussing the measured and fitted stiffnesses of two symmetric orientations, only the plane is stated; denoting the stiffness as a weighted average of two directions.

Orientations that have symmetric descriptions for the interfacial stiffness in ice-Ic are: (100)[001] and (100)[010]; (111)[1$\bar{1}$0] and (111)[11$\bar{2}$]. In ice-Ih, such orientations are the (basal)[prism] and (basal)[11$\bar{2}$0] directions, while in ice-0 they are the (001)[010] and (001)[100] directions.

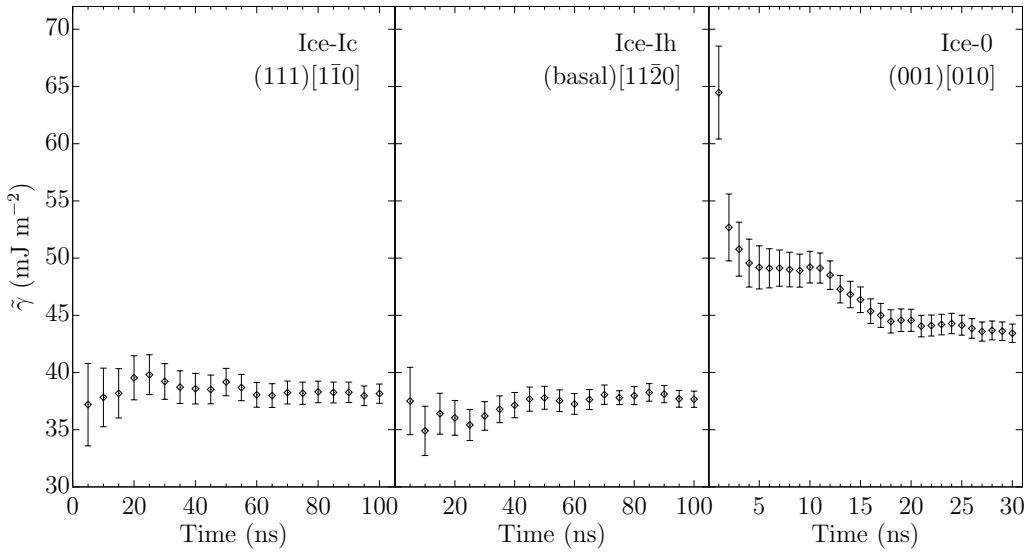

Figure 6.1: Measured interfacial stiffness for orientations in each of the ice structures against production run time.

6.3 Convergence

The measured interfacial stiffness must be converged before using the values to calculate the interfacial free energy. To check convergence, one orientation was chosen from each crystal structure and analysed over different durations of the production run. The orientations chosen were (111)[1$\bar{1}$0], (basal)[11$\bar{2}$0] and (001)[010] from ice-Ic, ice-Ih and ice-0, respectively. Since the simulation setups were all approximately equivalent for a given structure, if convergence could be adequately demonstrated for one orientation, then the other orientations were assumed to be similarly converged.

The convergence of these orientations is shown in figure 6.1, where the stiffness appears to have converged to within errors in ice-Ic beyond 40 ns. Ice-Ih also appears to have converged to within errors beyond 45 ns, in which case the results obtained for the stiffnesses at 100 ns in ice-I can be used for calculation of the free energy. Ice-0 appears to have converged, to within errors, beyond 18 ns. However, it is noted that if the production run had only extended to 11 ns, it would have been possible to mistakenly state that the orientation was converged between 5 ns and 11 ns. Given this possibility, and a production run of only 30 ns, it cannot be concluded that the ice-0 orientation is converged over the last 12 ns as confidently as that of ice-I over the last 60 ns.

Simply running the ice-0 simulations longer would increase the confidence in the convergence, but due to large simulation sizes, this is computationally unfavourable. Instead, one can reason that since different orientations will have differ-

Orientation	$\tilde{\gamma}_{20\text{ns}}$ (mJ m^{-2})	$\tilde{\gamma}_{30\text{ns}}$ (mJ m^{-2})	$\tilde{\gamma}_{30\text{ns}} - \tilde{\gamma}_{20\text{ns}}$ (mJ m^{-2})
(001)	45.6(7)	45.1(6)	-0.5(9)
(100)[001]	29.2(14)	28.4(11)	-0.8(18)
(100)[010]	28.4(14)	29.0(12)	0.6(19)
(101)[010]	30.5(12)	30.3(10)	-0.2(16)
(101)[$\bar{1}$01]	24.9(9)	25.1(8)	0.2(12)
(102)[010]	30.8(11)	30.5(9)	-0.3(14)
(102)[$\bar{2}$01]	29.5(11)	29.4(9)	-0.1(14)
(110)[001]	41.5(14)	40.8(11)	-0.7(18)
(110)[1$\bar{1}$0]	29.7(14)	29.5(12)	-0.2(19)

Table 6.3: Measured interfacial stiffness values for ice-0 at 20 ns and 30 ns and the difference between these values.

ent interfacial stiffnesses, they should also converge at different rates. By measuring the results for the stiffness for all orientations at 20 ns and again at 30 ns, it would be expected that if, in general, the stiffness in ice-0 has not converged during this duration, then one or more orientations would show a significant difference in the measured stiffness.

From table 6.3 it can be seen that the difference between the measured stiffness for each orientation at 20 ns and 30 ns, is smaller than the error on the values at either duration and smaller than the error in the difference. Any variation in the measured interfacial stiffness between 20 ns and 30 ns is therefore due to noise and one can conclude that the ice-0 orientations are converged from 20 ns onwards. Hence, the results for the stiffnesses at 30 ns can be used to calculate the interfacial free energies.

6.4 Ice-0 Coexistence

The coexistence temperature for ice-0 at 1 atm is known to be approximately 240–250 K[17, 94]. In order to perform simulations at coexistence, this temperature needed to be calculated more accurately. This was done by simply setting up a two-phase coexistence simulation, as described in section 6.2, for the (001)[010] orientation and monitoring the temperature and solid percentage, using $q12$, over the 5 ns equilibration period.

From figure 6.2, it can be seen that as the solid region of the (001)[010] simulation approaches a temperature of 245 K – and by extension the liquid – the percentage of solid in the overall system tends to a constant value of approximately 50%, during system-wide interaction within the NPH ensemble from 0.5 ns on-

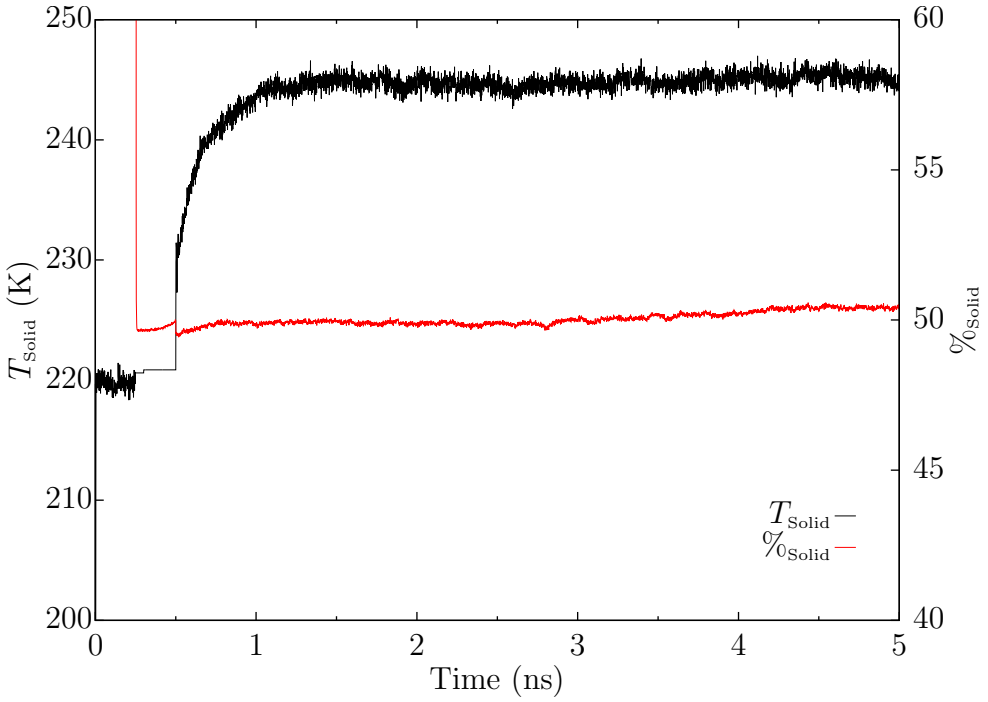

Figure 6.2: Temperature of solid region and percentage of solid in ice-0 (001)[010] simulation over the 5 ns equilibration period, sampling every 1 ps.

wards. This demonstrates that equilibrium solid-liquid coexistence occurs in ice-0 at a pressure of 1 atm and 245 K in the mW model. More precisely, measuring the temperature over the 5-30 ns production run, yields a coexistence temperature of 245.315(9) K.

6.5 Results

In this section, the tables for the measured and SASH fitted interfacial stiffnesses are presented for ice-Ic, ice-Ih and ice-0 along with tables of the calculated free energies. Log-log plots are also shown for $(A/k_{\mathrm{B}}T)\langle|h(q)|^2\rangle$ vs q with fit lines to the equation

$$\frac{A}{k_{\mathrm{B}}T}\langle|h(q)|^2\rangle = 10^{-2\log q - \log\tilde{\gamma}}\,, \tag{6.1}$$

where $\tilde{\gamma}$ is the interfacial stiffness value measured from simulations analysed using $q12$. Fit parameters found for the various measured stiffnesses are presented in section 6.6.

6.5.1 Ice-Ic

The results for the measured and fitted interfacial stiffness in ice-Ic are shown for $q3$, $q6$ and $q12$ in table 6.4, while the results for the calculated free energy are shown in table 6.5. Plots for the $q12$ stiffness fits are shown in figure 6.3.

The fits for the interfacial stiffness with 3, 4 and 5 fit parameters, result in a χ^2 goodness of fit of:

- 1.24, 0.75 and 0.47 for $q3$, respectively;
- 2.51, 0.99 and 0.42 for $q6$, respectively;
- 2.04, 0.87 and 0.63 for $q12$, respectively.

OP	Orientation	$\tilde{\gamma}$ (mJ m^{-2})	$\tilde{\gamma}_{\text{fit}}$ (mJ m^{-2})		
			$m=3$	$m=4$	$m=5$
$q3$	(100)	27.4(5)	28.2(4)	24.7(5)	26.1(6)
	(110)[1$\bar{1}$0]	24.5(4)	24.5(3)	25.4(4)	24.1(4)
	(110)[001]	34.9(4)	37.9(4)	36.5(5)	37.8(6)
	(111)	38.0(3)	40.6(4)	39.7(4)	38.2(5)
	(112)[1$\bar{1}$0]	39.8(4)	34.5(3)	37.3(3)	38.9(4)
	(112)[11$\bar{1}$]	36.2(3)	36.3(3)	38.2(4)	38.6(4)
$q6$	(100)	27.3(5)	29.7(4)	24.1(5)	26.1(6)
	(110)[1$\bar{1}$0]	24.5(4)	24.5(3)	26.0(4)	24.1(4)
	(110)[001]	34.3(4)	37.4(4)	35.2(5)	37.0(6)
	(111)	37.6(3)	41.3(4)	39.9(4)	37.8(5)
	(112)[1$\bar{1}$0]	42.0(4)	34.3(3)	38.8(3)	41.1(4)
	(112)[11$\bar{1}$]	38.8(4)	37.5(3)	40.6(4)	41.1(4)
$q12$	(100)	28.1(6)	29.1(5)	26.1(8)	27.0(9)
	(110)[1$\bar{1}$0]	25.6(6)	24.7(5)	26.4(6)	25.2(7)
	(110)[001]	35.5(7)	41.0(6)	37.2(8)	38.6(9)
	(111)	40.6(6)	44.2(6)	42.8(6)	40.6(8)
	(112)[1$\bar{1}$0]	42.6(6)	36.8(4)	40.2(5)	42.0(7)
	(112)[11$\bar{1}$]	39.0(8)	39.0(5)	42.8(6)	42.7(6)

Table 6.4: Measured and SASH fitted interfacial stiffness values for ice-Ic using the $q3$, $q6$ and $q12$ order parameters. The fitting is done to m number of fitting parameters. For $m=4$, $\epsilon_4=0$, while for $m=3$, $\epsilon_3=\epsilon_4=0$.

m	Plane	γ (mJ m^{-2})		
		$q3$	$q6$	$q12$
3	(100)	33.4(2)	33.8(2)	35.4(3)
	(110)	32.7(2)	33.3(2)	34.7(3)
	(111)	32.1(2)	32.6(2)	33.9(3)
	(112)	32.5(2)	33.0(2)	34.4(3)
4	(100)	34.6(2)	35.7(2)	37.3(3)
	(110)	33.8(2)	35.0(2)	36.6(3)
	(111)	33.2(2)	34.4(2)	35.9(3)
	(112)	33.5(2)	34.6(2)	36.2(3)
5	(100)	34.6(2)	35.7(2)	37.2(3)
	(110)	33.8(2)	35.0(2)	36.4(3)
	(111)	33.2(2)	34.4(2)	35.7(3)
	(112)	33.5(2)	34.6(2)	36.0(3)

Table 6.5: Calculated interfacial free energy for ice-Ic using the $q3$, $q6$ and $q12$ order parameters. The fitting is done to m number of fitting parameters. For $m=4$, $\epsilon_4=0$ and for $m=3$, $\epsilon_3=\epsilon_4=0$.

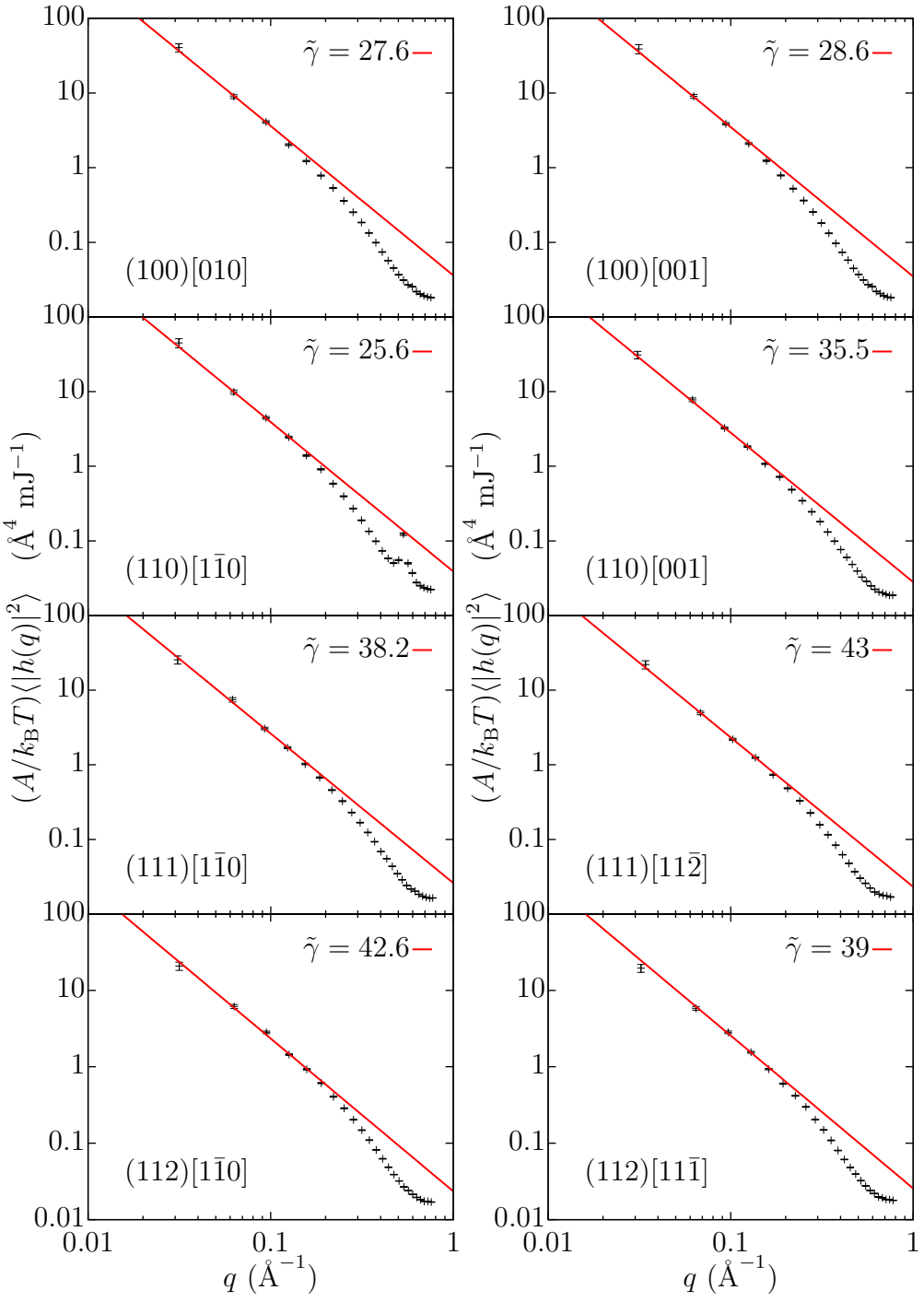

Figure 6.3: Interfacial stiffness plots for ice-Ic at various interfaces using the $q12$ order parameter and analysis geometry as specified in table 6.2.

6.5.2 Ice-Ih

The results for the measured and SASH fitted interfacial stiffness in ice-Ih are shown for $q3$ and $q12$ in table 6.6, while the results for the calculated free energy are shown in table 6.7. Plots for the $q12$ stiffness fits are shown in figure 6.4.

Orientation	$q3$		$q12$	
	$\tilde{\gamma}$ (mJ m^{-2})	$\tilde{\gamma}_{\text{fit}}$ (mJ m^{-2})	$\tilde{\gamma}$ (mJ m^{-2})	$\tilde{\gamma}_{\text{fit}}$ (mJ m^{-2})
(prism)[11$\bar{2}$0]	35.8(7)	32.4(5)	35.8(10)	34.3(9)
(prism)[basal]	36.4(3)	36.9(3)	38.3(7)	38.9(5)
(basal)	35.6(2)	34.9(6)	38.0(5)	35.7(10)
(11$\bar{2}$0)[prism]	32.1(3)	32.0(5)	34.8(6)	33.7(9)
(11$\bar{2}$0)[basal]	28.0(5)	33.7(3)	30.2(6)	34.7(5)

Table 6.6: Measured and SASH fitted interfacial stiffness values for ice-Ih using the $q3$ and $q12$ order parameters.

The χ^2 goodness of fits for the $q3$ and $q12$ fitted stiffnesses are 1.33 and 0.84, respectively.

Plane	γ (mJ m^{-2})	
	$q3$	$q12$
(prism)	35.2(2)	36.8(3)
(basal)	33.0(2)	34.4(4)
(11$\bar{2}$0)	35.3(2)	36.9(3)

Table 6.7: Calculated interfacial free energy for ice-Ih using the $q3$ and $q12$ order parameters.

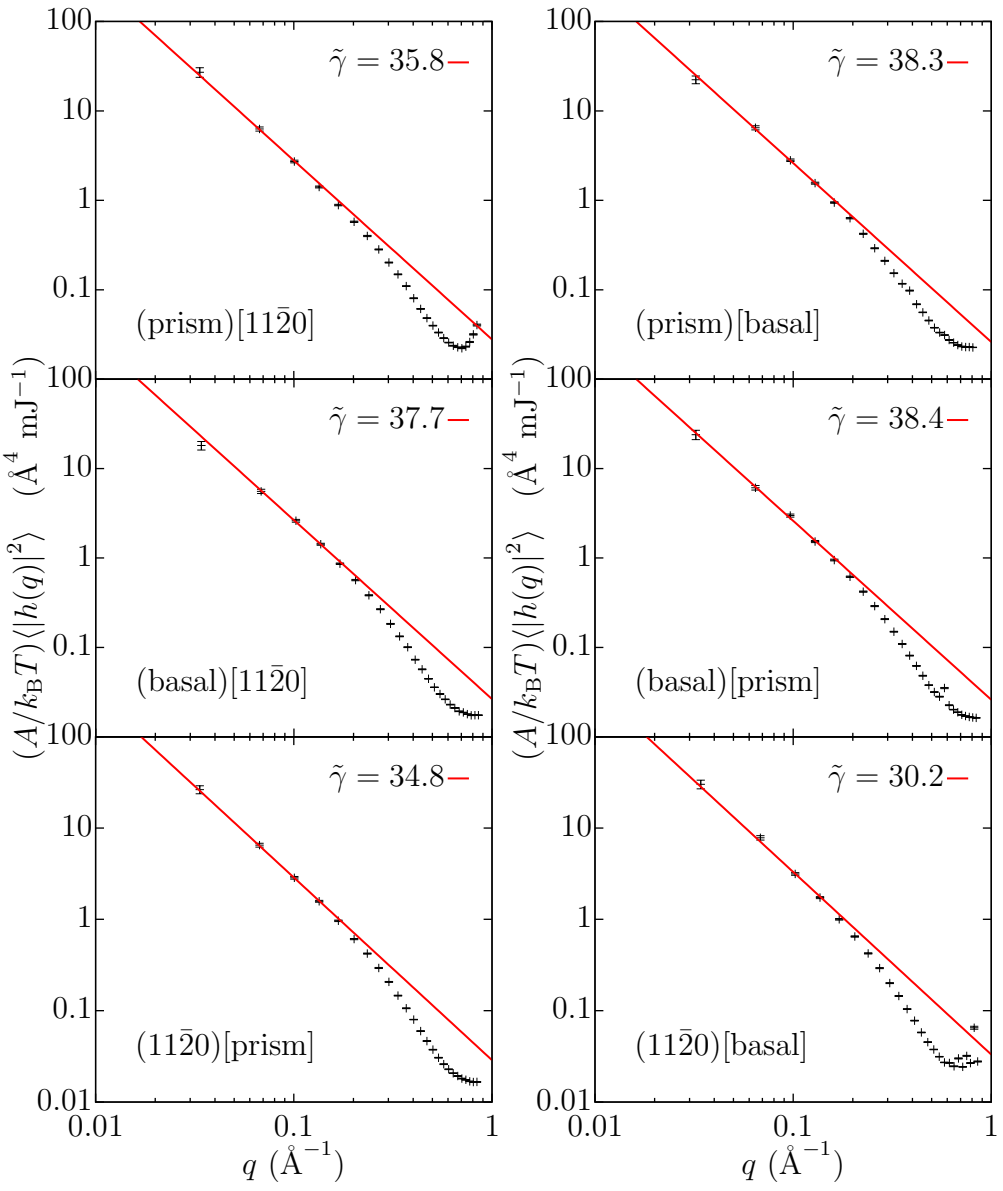

Figure 6.4: Interfacial stiffness plots for ice-Ih at various interfaces using the $q12$ order parameter and analysis geometry as specified in table 6.2.

6.5.3 Ice-0

The results for the measured and SASH fitted interfacial stiffness in ice-0 are shown for $q12$ in table 6.8, while the results for the calculated free energy are shown in table 6.9. Plots for the $q12$ stiffness fits are shown in figure 6.5.

Orientation	$\tilde{\gamma}$ (mJ m^{-2})	$\tilde{\gamma}_{\text{fit}}$ (mJ m^{-2})
(001)	45.1(6)	44.9(12)
(100)[001]	28.4(11)	27.4(8)
(100)[010]	29.0(12)	30.3(12)
(101)[010]	30.3(10)	30.5(9)
(101)[$\bar{1}$01]	25.1(8)	26.3(7)
(102)[010]	30.5(9)	29.6(7)
(102)[$\bar{2}$01]	29.4(9)	29.2(9)
(110)[001]	40.8(11)	41.9(9)
(110)[1$\bar{1}$0]	29.5(12)	28.1(11)

Table 6.8: Measured and SASH fitted interfacial stiffness values for ice-0 using $q12$.

The χ^2 goodness of fit for the fitted stiffness is 0.27.

Plane	γ (mJ m^{-2})
(001)	31.3(5)
(100)	35.2(5)
(101)	34.6(4)
(102)	33.6(4)
(110)	34.2(4)

Table 6.9: Calculated interfacial free energy for ice-0.

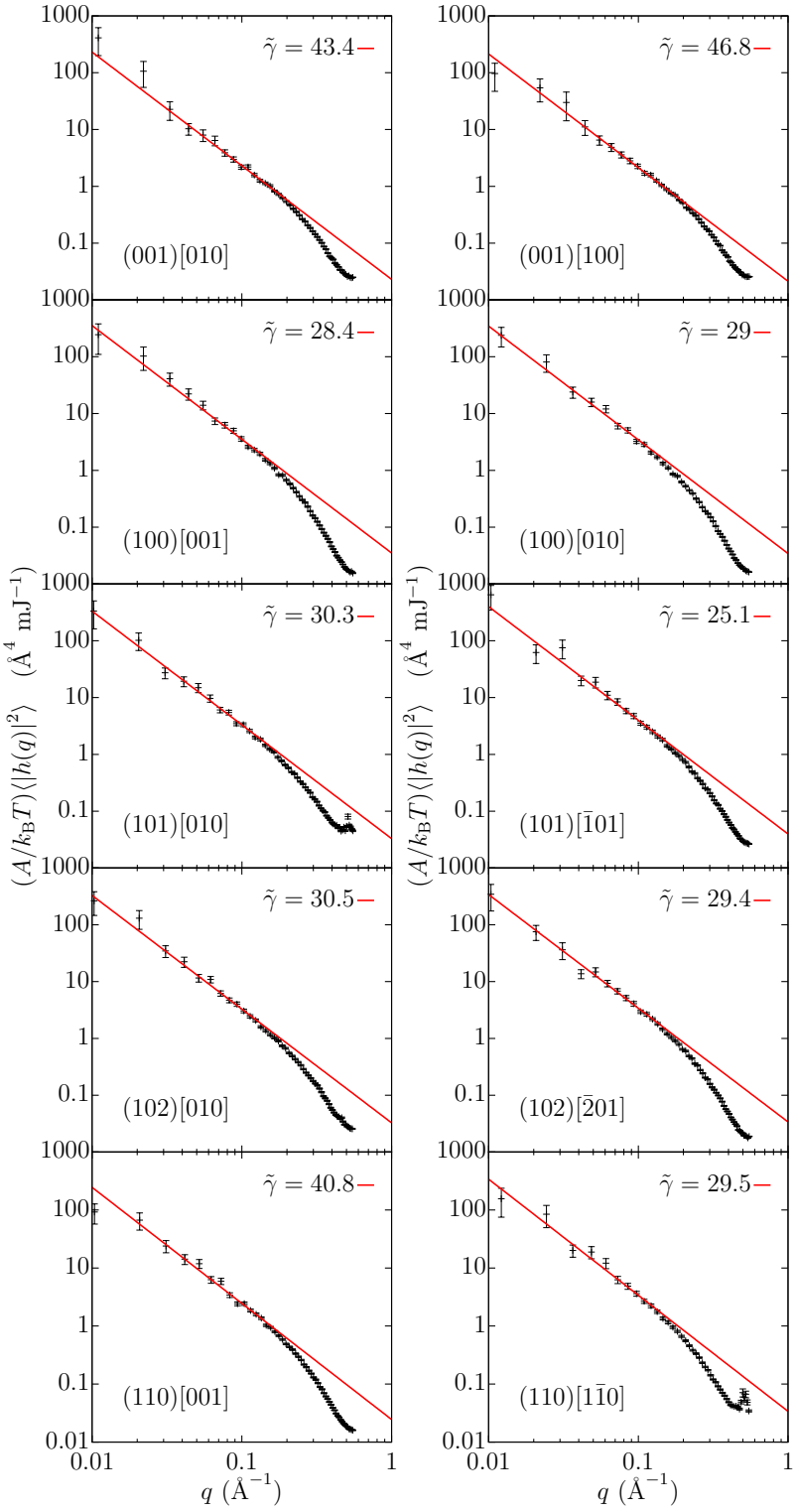

Figure 6.5: Interfacial stiffness plots for ice-0 of various interfaces using the $q12$ order parameter and analysis geometries as specified in table 6.2.

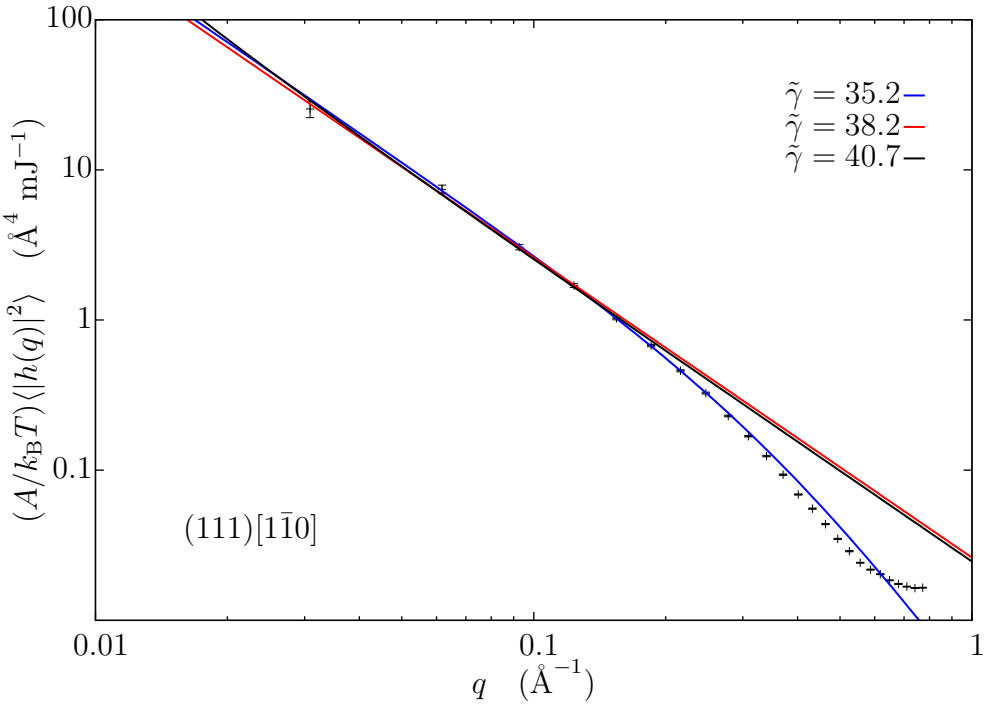

Figure 6.6: Interfacial stiffness plot for ice-Ic (111)[1$\bar{1}$0] orientation using the $q12$ order parameter. The fits have been performed with: $\tilde{\gamma}$ only, shown in red; with $\tilde{\gamma}$ and the elastic modulus ($\mathcal{E} = -0.14(14)$ mJ m^{-3}), shown in black; and also with $\tilde{\gamma}$ and the bending rigidity ($\kappa = 242(20)$ mJ), shown in blue.

6.5.4 Effects of the Elastic Modulus and Bending Rigidity

In chapter 4, the inclusion of both the elastic modulus and the bending rigidity to more completely describe the deformation of the interface, was briefly mentioned and both deemed unnecessary. To more completely justify this, it is of interest to see how the fit of $(A/k_\mathrm{B}T)\langle|h(q)|^2\rangle$ against q differs between the lack and presence of either additional terms, and consequently the effect this has on the measurement of $\tilde{\gamma}$. Figure 6.6 shows the fit of equation (6.1) (red) and the fit of equations

$$\frac{A}{k_\mathrm{B}T}\left\langle\left|h(q)\right|^2\right\rangle = 10^{-\log(\mathcal{E}q+\tilde{\gamma}q^2)}\,, \tag{6.2}$$

(black) and,

$$\frac{A}{k_\mathrm{B}T}\left\langle\left|h(q)\right|^2\right\rangle = 10^{-\log(\tilde{\gamma}q^2+\kappa q^4)}\,, \tag{6.3}$$

(blue) to the ice-Ic (111)[1$\bar{1}$0] interface; previously reported in section 6.5.1.

Given that the leading order correction to equation (6.1) is to include only

the elastic modulus, it is not unreasonable to investigate how the fitting is affected by only the $\mathcal{E}$ and $\tilde{\gamma}$ terms. The elastic modulus only dominates at wavelengths longer than those dominated by $\tilde{\gamma}$ and so fitting can be performed to the same number of data points as equation (6.1). When this is done, it is found that $\mathcal{E} = -0.14(14)$ mJ m^{-3}, which is effectively zero within errors. The subsequent value of the interfacial stiffness is $\tilde{\gamma} = 40.7(14)$ mJ m^{-2}, which is only 0.3 mJ m^{-2} outside of errors with that obtained from equation (6.1). A likely reason for the negligible contribution to $\mathcal{E}$, is due to the length of the interface not being large enough to produce wavelengths effected by the elastic modulus. Alternatively, such long wavelengths, if present, would need much longer simulation runtimes than is perhaps available in these simulations, to arise. Regardless, the practically zero value of $\mathcal{E}$ and such an insignificant effect on the value of $\tilde{\gamma}$, means that $\mathcal{E}$ can be discounted from the fitting procedure. From this, it is therefore worth examining the fitting effect produced by $\tilde{\gamma}$ and κ only.

Figure 6.6 clearly shows that the inclusion of κ allows a better fit to shorter wavelengths, than without. However, it is also clear that the inclusion of κ alters the measurement of $\tilde{\gamma}$, where the interfacial stiffness is measured to be 35.2(8) mJ m^{-2} and 38.2(8) mJ m^{-2} with and without κ, respectively.

It is not clear though, whether the value of $\tilde{\gamma}$ from the inclusion of κ is genuinely more accurate than without κ. This is brought into question for several reasons. Firstly, due to the long equilibration times of long wavelength thermal fluctuations of the interface, there is a larger error on the values obtained for small q compared to those at large q. When using a weighted fitting procedure, this gives greater flexibility in the fit to the value of $\tilde{\gamma}$, which dominates at small q, compared to the more strictly constrained fit to the value of κ, which dominates at large q. Similarly, it has already been established in chapter 4 that a fit to N data points should give a consistent value of $\tilde{\gamma}$ up until the wavelengths can no longer be considered long. It can be hypothesised that if the production run of such simulations was increased, the longest wavelengths would yield more consistent measurements of $\tilde{\gamma}$ for varying N, with smaller error bars. This would also mean that when fitting with the inclusion of κ, there would be much less flexibility in the value of the $\tilde{\gamma}$ parameter, and hence closer agreement between measurements made with and without κ.

Additionally, while work has been conducted into determining the best number of data points to fit to for measuring the interfacial stiffness without κ, it is unclear how many data points should be used in the fit when including κ. From figure 6.6 it can be seen that very short wavelengths still diverge from the fit even

with κ, which are not accurately described by the $\mathcal{O}(q^4)$ term. Extended CWT instead allows for further inclusion of higher order terms up to $\mathcal{O}(q^6)$, which dominate at very short wavelengths[66]. It is unknown where the transition between "short" and "very short" wavelengths occurs. In figure 6.6, the fit with κ has been performed over the first 8 data points; yet this may already be fitting to very short wavelengths. Attempting to fit an $\mathcal{O}(q^4)$ expression to very short wavelengths will skew the measurement of $\tilde{\gamma}$ artificially – similar to attempting to fit only the $\mathcal{O}(q^2)$ form past the continuum limit – as the very short wavelengths have even smaller error bars. To ensure an $\mathcal{O}(q^4)$ fit wasn't being performed on very short wavelengths, similar work would have to be conducted to determine the transition between short and very short wavelengths, as was done to determine the transition between long and short wavelengths in chapter 4.

Finally, it is worth noting that the difference in $\tilde{\gamma}$ when fitting either equation (6.2) or (6.3), is likely to have very little affect on the overall measurement of the interfacial free energy. It is observed, that variations of up to 3 mJ m^{-2} in fitted $\tilde{\gamma}$ vary the calculated values of γ to within errors. This can be seen from tables 6.4 and 6.5 when comparing the fitted $\tilde{\gamma}$ between $m = 4$ and $m = 5$ for all three order parameters, to the respective difference in the values of γ.

For these reasons, it is concluded that the exclusion of the bending rigidity from CWT does not adversely affect the calculation the interfacial free energies in this research. Given that this research is concerned with measuring only $\tilde{\gamma}$ to calculate γ, the ability to accurately fit to short wavelengths does not assist in more accurate fitting to long wavelengths; which is the dominant region of $\tilde{\gamma}$. The only way to improve the fit to low q values, is to increase the duration of the production runs, which can be sufficiently described in the continuum limit by equation (6.1), given negligible contribution to the $\mathcal{E}$ term in these simulations.

6.6 Parameters

The fit parameters obtained for the SASH equations of ice-Ic, ice-Ih and ice-0, are presented here.

m	Parameter	$\tilde{\gamma}_{\text{fit}}$ (mJ m^{-2})		
		$q3$	$q6$	$q12$
3	γ_0	32.8(2)	33.2(2)	34.7(3)
	ϵ_1	0.055(3)	0.049(3)	0.063(4)
	ϵ_2	-0.0053(3)	-0.0061(3)	-0.0060(5)
4	γ_0	33.8(2)	34.9(2)	36.5(3)
	ϵ_1	0.055(3)	0.049(2)	0.051(4)
	ϵ_2	-0.0037(3)	-0.0038(3)	-0.0047(4)
	ϵ_3	0.00082(7)	0.00126(7)	0.0011(1)
5	γ_0	33.8(2)	34.9(2)	36.3(3)
	ϵ_1	0.057(3)	0.052(3)	0.053(4)
	ϵ_2	-0.0041(4)	-0.0042(3)	-0.0045(5)
	ϵ_3	0.00075(9)	0.00117(8)	0.0011(1)
	ϵ_4	-0.00008(1)	-0.00012(1)	-0.00009(2)

Table 6.10: Fitted interfacial stiffness parameters for ice-Ic using the $q3$, $q6$ and $q12$ order parameters to m fit parameters.

Parameter	$\tilde{\gamma}_{\text{fit}}$ (mJ m^{-2})	
	$q3$	$q12$
γ_0	34.5(2)	36.0(3)
ϵ_1	0.059(6)	0.06(1)
ϵ_4	-0.018(3)	-0.022(4)

Table 6.11: Fitted interfacial stiffness parameters for ice-Ih using $q3$ and $q12$.

Parameter	$\tilde{\gamma}_{\text{fit}}$ (mJ m^{-2})
γ_0	33.8(4)
ϵ_1	0.07(1)
ϵ_2	0.034(3)
ϵ_3	-0.043(4)
ϵ_4	-0.010(5)
ϵ_5	0.033(4)

Table 6.12: Fitted interfacial stiffness parameters for ice-0 using $q12$.

6.7 Ice Nucleation Pathway

The isotropic component of the interfacial free energies show that $\gamma_{0_{\text{Ice-0}}} < \gamma_{0_{\text{Ice-Ih}}} \lesssim \gamma_{0_{\text{Ice-Ic}}}$; when compared using $q12$ and $m = 5$ for ice-Ic. While a lower interfacial free energy of ice-0 implies a lower nucleation barrier compared to ice-I, as discussed in chapter 3, the bulk free energy of ice-I and ice-0 must also be known to calculate the relative barrier heights. These bulk free energies were not calculated in this research. However, Dr D. Quigley performed LSMC simulations and was able to provide results for the free energy difference between bulk ice-Ih and ice-0, $\Delta\mu_{10}$, from 10-230 K at 1 atm, in steps of 20 K. It was also possible to work from results reported by Espinosa et al.[95] to obtain values for the bulk ice-Ih free energy, $\Delta\mu_1$. Using these two additional values, along with the values obtained for the interfacial free energies of ice-Ih and ice-0, the preference for ice-0 to nucleate over ice-Ih can be determined, at temperature T, by calculating $\Delta G^*_{\text{Ice-0}}/\Delta G^*_{\text{Ice-Ih}}$, as discussed in chapter 3. However, while the temperature dependence of $\Delta\mu_0$ and $\Delta\mu_1$ can be determined from the results provided by Quigley and Espinosa et al., only the values for $\gamma_{0_{\text{Ice-0}}}$ and $\gamma_{0_{\text{Ice-Ih}}}$ at coexistence are known. The temperature dependence of the interfacial free energies must first be calculated in order to then calculate the relative ice-0/ice-Ih nucleation barrier height.

The CWM implemented in this work was designed to calculate the interfacial free energy at equilibrium coexistence and hence lower temperature out-of-equilibrium simulations cannot be run to measure the interfacial free energy. Instead, the enthalpy can be measured for bulk solid, H_s, and liquid, H_l, simulations at the same temperature, repeated over a range of temperatures, in order to calculate the temperature dependence for the enthalpy of fusion; $\Delta H = H_l - H_s$. By also measuring the temperature dependence of the density, ρ, of the bulk solid, the temperature dependence of the interfacial free energy can be recovered through the use of the Turnbull correlation[96, 97]:

$$\gamma_0 = C_T \Delta H \rho^{2/3} \,, \tag{6.4}$$

where C_T is the Turnbull coefficient.

The bulk simulations conducted, required to recover the temperature dependence of ΔH and ρ, were 2.5 ns NPT simulations of 384 particles, performed using LAMMPS at 1 atm, with a timestep of 1 fs, sampled every 100 steps. The only difference between the bulk solid and liquid simulations was that the solid systems were allowed to adjust anisotropically, while the liquid systems were constrained to adjust isotropically. Solid simulations were conducted over 10-230 K in steps

T (K)	ρ (kg m^{-3})		γ_0 (mJ m^{-2})		$\Delta\mu$ (meV)		$\Delta G^*_{\text{Ice-0}}/\Delta G^*_{\text{Ice-Ih}}$
	Ice-Ih	Ice-0	Ice-Ih	Ice-0	Ice-Ih	Ice-0	
10	1002.0	963.9	14.4	-126.0	50.3	42.8	-922.7
30	1000.2	962.3	16.1	-112.3	46.5	39.1	-483.0
50	998.4	960.7	17.7	-98.6	42.7	35.5	-250.9
70	996.6	959.1	19.3	-84.9	39.0	31.8	-127.0
90	994.9	957.5	21.0	-71.3	35.2	28.2	-61.3
110	993.1	956.0	22.6	-57.7	31.4	24.5	-27.3
130	991.3	954.4	24.2	-44.1	27.6	20.8	-10.6
150	989.5	952.8	25.8	-30.5	23.8	17.2	-3.2
170	987.7	951.2	27.4	-17.0	20.0	13.5	-0.5
190	985.9	949.6	29.0	-3.5	16.2	9.9	0.0
210	984.1	948.0	30.7	10.0	12.4	6.2	0.1
230	982.3	946.4	32.3	23.4	8.6	2.5	4.4

Table 6.13: Calculated densities and free energy quantities for ice-0 and ice-Ih. Ice-0 nucleation is preferential to ice-Ih if $\Delta G^*_{\text{Ice-0}}/\Delta G^*_{\text{Ice-Ih}} < 1$.

of 20 K, while the liquid simulations were conducted over 190-310 K in steps of 20 K. The results from these simulations were sufficient to fit linear trends to the values of H_l, H_s and ρ for both ice-Ih and ice-0 simulations. The results could then be extrapolated to coexistence temperatures to calculate C_T for ice-Ih and ice-0; using the value of γ_0 known at coexistence for the respective ice structure. After recovering C_T, the temperature dependence for γ_0 could be trivially recovered using equation (6.4). The calculated values for the densities, interfacial and bulk free energies for ice-Ih and ice-0 are shown in table 6.13, along with the ice-0/ice-Ih relative nucleation barrier height.

The linear trend calculated for $\gamma_{0_{\text{Ice-Ih}}}$ is shown in comparison to that calculated by Espinosa et al. in figure 6.7. The gradient of the temperature dependence of $\gamma_{0_{\text{Ice-Ih}}}$ calculated in this work is only 51% of the gradient for that calculated by Espinosa et al. However, the dependence measured here matches the upper data points calculated by Limmer and Chandler[98] and Li et al.[6], while the fit by Espinosa et al. passes through the lower points. This suggests this research provides an upper temperature estimate on the relative ice-0/ice-Ih nucleation barrier heights. No data could be found below 200 K that further revealed the accuracy of either fit.

From table 6.13, it can be seen that ice-0 nucleates preferentially over ice-Ih at $T \leq 220$ K, where in the calculation of $\Delta G^*_{\text{Ice-0}}/\Delta G^*_{\text{Ice-Ih}}$, the degree of anisotropy in the free energy has been assumed to be equivalent between ice-0 and ice-Ih. This is not an unreasonable assumption, since the range in the anisotropy of the interfacial free energies calculated for ice-Ih and ice-0 interfaces are 2.5(5) and 3.9(7) mJ m^{-2};

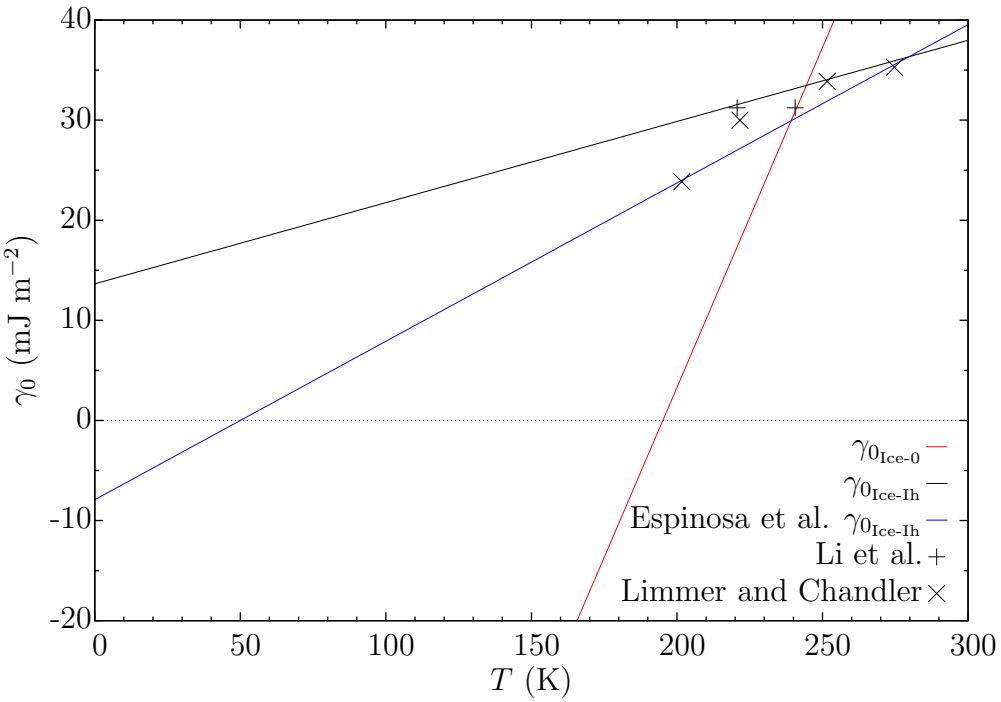

Figure 6.7: Fit lines for calculated $\gamma_{0_{\text{Ice-0}}}$ and $\gamma_{0_{\text{Ice-Ih}}}$ and the extracted trend for $\gamma_{0_{\text{Ice-Ih}}}$ from Espinosa et al. Data points are also extracted from the work by Espinosa et al. but were originally produced by Limmer and Chandler[98] and Li et al.[6].

analysed using $q12$. While the range of anisotropy is not equivalent between the two structures to within errors, the free energy is still roughly isotropic between all three structures, as can be seen in appendix C; compared to the relatively strong anisotropy of the interfacial stiffnesses.

However, as discussed in chapter 3, ice-0 is a metastable form of ice which Russo et al.[17] have proposed acts as a nucleation pathway to the formation of stable ice-I via a core-shell model. The plausibility of this nucleation method can be examined using the nucleation data produced by Russo et al.[17] at 215.2 K and the core-shell model form of CNT described in chapter 3. The three parameter form of CNT provides an expression for calculating the ice-0 shell thickness

$$\delta R = \frac{c}{8\pi\gamma_{0_{\text{Ice-0}}}} \left(\frac{4\rho_{\text{Ice-Ih}}\pi}{3m} \right)^{1/3}, \tag{6.5}$$

where the value of c is only known from fitting the three parameter form of CNT to nucleation data. Extracting the fit parameters from the plot of ΔG against n at 0 atm and 215.2 K from reference [17], the values for the CNT parameters are $a = -0.134$, $b = 0.120$ and $c = 7.404$; in units of $k_{\text{B}}T$. Hence, using equation (6.5)

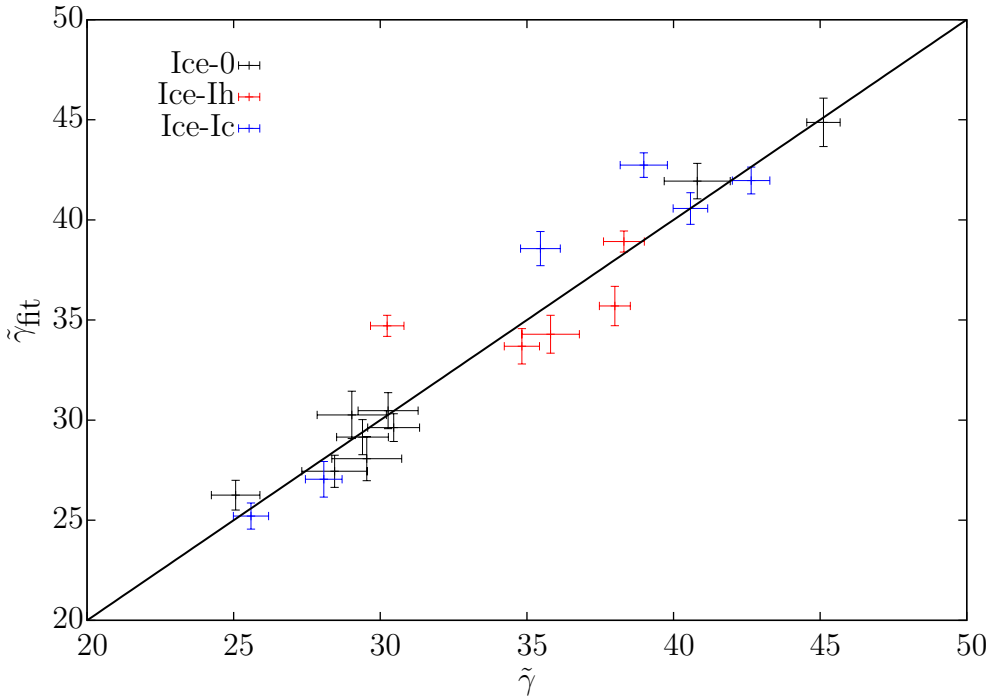

Figure 6.8: Measured versus fitted interfacial stiffness results for the three different ice structures, using the $q12$ order parameter and 5 fitting parameters for ice-Ic.

and the calculated values of $\rho_{\text{Ice-Ih}}$ and $\gamma_{0_{\text{Ice-0}}}$ at 215.2 K from this research, the thickness of the ice-0 shell is determined to be 3.3 Å.

6.8 Discussion

With regards to the results for the SASH fitted interfacial stiffness of ice-Ic, it is clear that in general a better fit can be obtained by increasing the number of fit parameters. This is indicated in figure 6.9, along with the decreasing value of χ^2 with increasing value of m for all order parameters. However, increasing m increases the uncertainty on both the fitted stiffness and calculated free energy. This is expected since more fit parameters include contributions from higher order terms in the SASH equations, which describe the finer details of the anisotropy in the interfacial stiffness. More fit parameters also gives greater flexibility in fitting to the measured values and hence results in higher error on the fit parameters when fitting to the same number of measurements.

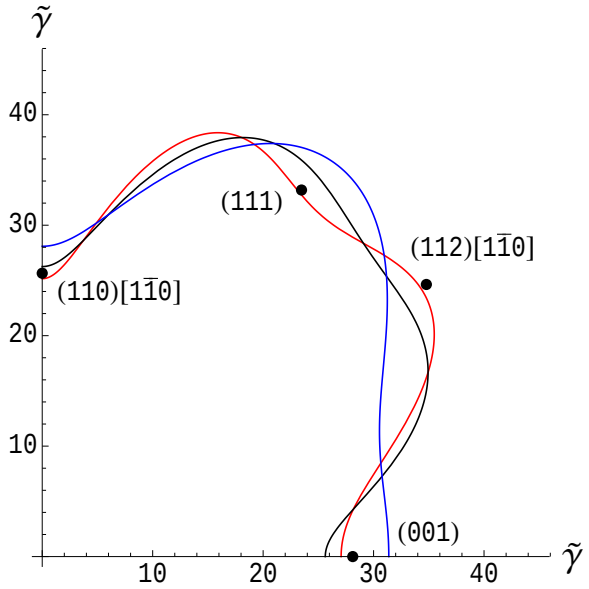

Figure 6.9: Polar plot for ice-Ic interfacial stiffness using 3, 4 or 5 fitting parameters; shown blue, black and red respectively. The plot shows the measured values of the interfacial stiffness, using $q12$, along $\mathbf{u} = [1, 0]$ at $\phi = \pi/4$. Note that the (001) is symmetrically equivalent to the (100) plane.

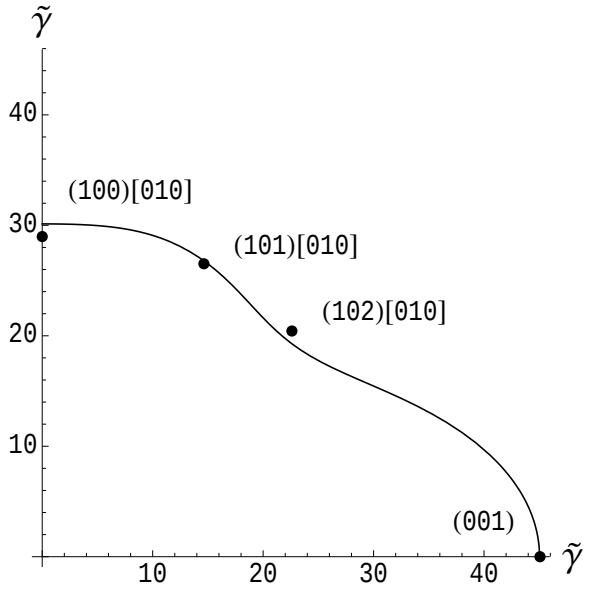

Figure 6.10: Polar plot for the ice-0 interfacial stiffness along $\mathbf{u} = [1, 0]$ at $\phi = 0$, with measured stiffnesses using $q12$.

It is observed that the choice of order parameter has an affect on the measured value of the stiffness and the calculated free energy. With regards to the stiffness, it is found that $q12$ consistently results in a value that is higher than that given by $q3$ or $q6$; in the cases of ice-Ic and ice-Ih. This is consistent with the observations in chapter 5, where $q12$ was determined to most clearly distinguish between solid-like and liquid-like particles in all ice structures studied. Since $q12$ can resolve the finer fluctuations of the interface, this results in a more highly curved interface being defined, which in turn yields higher interfacial stiffnesses. However, compared to orientations that are relatively smooth, $q12$ should yield closely similar results to the other order parameters. Consequently, $q12$ demonstrates a higher overall degree of anisotropy between finely fluctuating and smooth interfaces, while $q3$ and $q6$ will show a weaker anisotropy. This is why generally $q12$ provides good agreement between the measured and SASH fitted stiffnesses, as shown in figures 6.8, 6.9 and 6.10; although not always best agreement. In the case of ice-Ic, the range of anisotropy is higher in $q12$ than in $q3$, which suggests more fitting parameters are required for an adequate fit. However, $q6$ fits better than $q12$ when $m = 5$ and has a higher range in its anisotropy. This is surprising, since $q6$ is generally poorer at distinguishing between solid-like and liquid-like particles than $q12$.

With regards to the free energy of ice-Ic and ice-Ih, from tables 6.5 and 6.7 respectively, it is apparent that the absolute difference in the free energy between different crystal planes is the same, within errors, for each order parameter using the same value of m. Furthermore, from tables 6.10 and 6.11, the absolute difference in the isotropic component of the free energy between ice-Ic and ice-Ih is also the same, within errors, for both $q3$ and $q12$. This means that the choice of order parameter makes no difference to the form of the anisotropy of the free energy for a particular ice structure, nor does it affect the difference in the free energy between ice structures; providing such an order parameter works equally well in such ice structures. The only effect the choice of the order parameter has on the free energy, is the magnitude of the isotropic component. The isotropic component is also found to be higher when using $q12$ than either $q3$ or $q6$ for a particular ice structure, which corresponds with the higher interfacial stiffnesses measured when using $q12$. Since these systematic effects exist between the order parameters, it is therefore only sensible to compare between the free energies of different ice structures and interfaces calculated using the same order parameter. Since $q12$ works in all three structures and more accurately defines the interfaces, this research draws comparisons between ice structures largely based on analysis performed using $q12$.

In general, when using $q12$ and equation (6.1) to measure the stiffnesses, the

fits are relatively good, as shown in figures 6.3, 6.4 and 6.5. In ice-Ic and ice-Ih, the long wavelength fluctuations are typically within error of the fit to equation (6.1) and there is excellent agreement within the limits of CWT. In the case of ice-0, the longest wavelengths still conform to the linear fit of CWT and are largely within errors, except with more fluctuation about the fit. There is still good agreement to the theory and the reduced accuracy of the largest wavelengths is not detrimental to the measurement of the interfacial stiffness. The longest wavelength fluctuations require significantly longer production runs to be accurately measured, which is why the ice-I structures have better agreement with CWT than ice-0 at these wavelengths. However, the simulations for ice-0 were much larger in the z direction than those of ice-I, meaning more values for q could be used to fit for the interfacial stiffness, that still satisfied the continuum limit of CWT, than in ice-I. These smaller wavelengths have a significantly shorter equilibration time and therefore agree much better with the fit of equation (6.1). Weighting the fit more heavily to these more closely converged values results in an accurate value for the stiffness. Increasing the duration of the production run would only serve to better converge the values at the longest wavelengths, increasing the precision on the overall measured stiffness.

Analysis of the isotropic component for the free energy of ice-Ih finds good agreement with existing work. Most recently, Espinosa et al. have calculated the isotropic free energy for ice-Ih in the mW model to be 35.5(2.5) mJ m^{-2} via the seeding method[95] and 34.9(8) mJ m^{-2} via mold integration[60, 99]. Both results are in excellent agreement with the value obtained in this work from $q12$, while $q3$ only agrees with the latter result. The results reported in this research are also in agreement within the range of experimental values reported by Gránásy et al.[100], who report values of 25 to 44(10) mJ m^{-2}. There are other measured values obtained by other simulation methods that lie away from the results obtained in this research, but also within the experimental range. For instance, Limmer and Chandler[98] report 35.3 mJ m^{-2} from mean field theory, while Li et al.[6] reports 31.01(21) mJ m^{-2} using forward flux sampling; but also notes the presence of ice-Ic during the simulations. Furthermore, in an earlier study, Espinosa et al.[101] reported a value of 29.5(25) mJ m^{-2} from an earlier seeding technique. Such a range of results suggests that measurement of the interfacial free energy is highly sensitive to systematic effects in the methods used, and that there is a need to correct for such effects carefully; as demonstrated through the investigation of the order parameters used and also the simulation and analysis geometries.

Espinosa et al. also finds the interfacial free energies of ice-Ih, as this research does, to be $\gamma_{\text{basal}} < \gamma_{\text{prism}} \lesssim \gamma_{11\bar{2}0}$, with values of 34.5(8), 35.1(8) and

35.2(8) mJ m^{-2}, respectively[99]. This research instead finds that a large enough difference exists between the (basal) plane and both the $(11\bar{2}0)$ and (prism) planes to resolve the free energies, but similarly cannot distinguish between the $(11\bar{2}0)$ and (prism) planes. Work by other groups using different model potentials have also found the (basal) plane to have the lower free energy, while the $(11\bar{2}0)$ and (prism) planes have higher and unresolvable energies[61].

The free energies for ice-Ic show that while the (110) and (112) planes are indistinguishable within errors, generally it is the case that $\gamma_{111} \lesssim \gamma_{112} \lesssim \gamma_{110} < \gamma_{100}$. No existing literature could be found that has measured the interfacial free energy of ice-Ic in contact with water for the mW model, but work has been performed using FCC crystals to measure the interfacial free energy of LJ systems using the cleaving method[39] and hard-sphere potentials using CWM[73, 102]. Such works also find $\gamma_{111} < \gamma_{110} < \gamma_{100}$, in agreement with this research.

The difference in the interfacial free energy between ice-Ic and ice-Ih is difficult to definitively resolve. Depending on whether fewer or more fitting parameters are used in ice-Ic, the isotropic component of the free energy can be lower or higher, respectively, than that of ice-Ih. This is an important aspect to consider, given that typically when the CWM is applied to cubic systems, only three fit parameters are used[73, 102]. However, given that this research shows a better fit to the stiffness can be obtained by increasing the number of fit parameters, it is more reasonable to assume that the free energy for ice-Ic is comparable, to within errors, of that of ice-Ih; as indicated by $q12$, $m = 5$ in ice-Ic. Work conducted by both Hudait et al.[103] and Espinosa et al.[99] suggest the equivalency of the (basal) and (111) planes in ice-Ic and ice-Ih. Furthermore, Espinosa et al. also indicates the equivalency of the (110) and $(11\bar{2}0)$ planes. In the case of $q12$ and $m = 5$, this research finds good agreement with these observations, where the (110) and $(11\bar{2}0)$ planes are within errors, while the (111) and (basal) planes are 0.3 mJ m^{-2} outside of errors. $q3$ finds excellent agreement between the (111) and (basal) planes, but the (110) and $(11\bar{2}0)$ planes are 0.9 mJ m^{-2} outside of errors. The close agreement of such observations with measurements made using $q12$, gives sufficient support to accurately calculate the interfacial free energies of ice-0 using the CWM and $q12$, and be able to compare such results against ice-I structures.

Calculating the temperature dependency of the isotropic component of the interfacial free energy for ice-0 and ice-Ih, shows that at 240 K the interfacial free energy of ice-0 is 8.8% lower than that of ice-Ih. According to Quigley et al.[94], only an 8% difference in the interfacial free energy of ice-0 compared with that of ice-Ih, is enough to nucleate ice-0 preferentially over ice-Ih at 240 K. However,

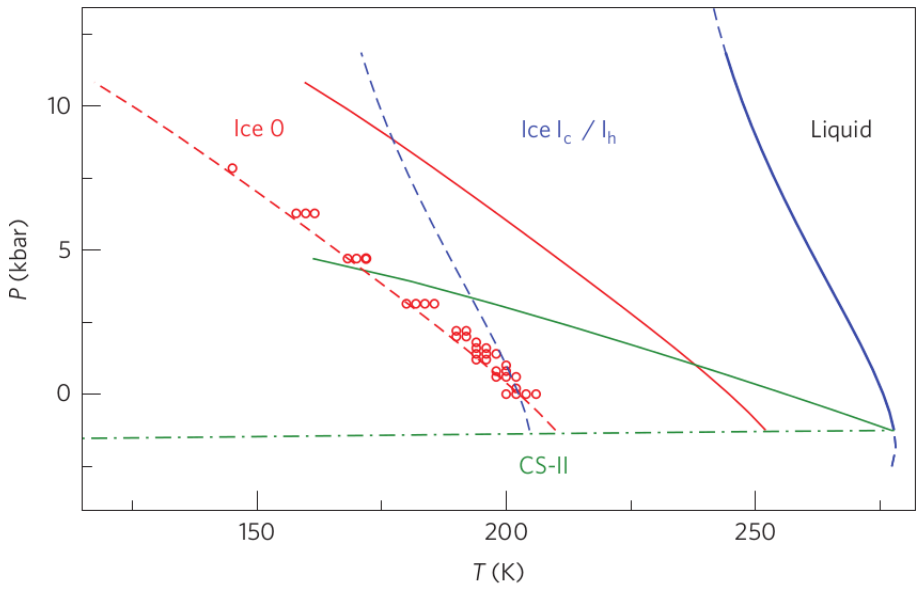

Figure 6.11: The P-T phase diagram of mW water, reproduced from ref. [17]. The solid lines demonstrate coexistence between liquid and ice-Ih/Ic (blue), and liquid and ice-0 (red). The dashed lines are constant chemical potential differences between liquid and ice-Ih/Ic (blue), and liquid and ice-0 (red). The red open circles indicate homogeneous nucleation of ice-0. The reader should refer to ref. [17] for a comprehensive description of the additional (green) information.

computing the relative nucleation barrier heights of ice-0 against ice-Ih, shows that when considering the density and bulk free energy temperature dependencies of ice-0 and ice-Ih, ice-0 preferential nucleation only occurs at $T \leq 220$ K; where the ice-0 isotropic interfacial free energy is 53.1% lower than that of ice-Ih. This is also corroborated by Russo et al. as shown in figure 6.11.

It is clear that from table 6.13, preferential ice-0 nucleation occurs above the homogeneous ice-0 nucleation temperature and below the ice-0 melting temperature, as indicated in figure 6.11. Furthermore, the quantity $\Delta G^*_{\text{Ice-0}}/\Delta G^*_{\text{Ice-Ih}} = 0$ indicates an absence of the ice-0 nucleation barrier, leading to homogeneous ice-0 nucleation. From table 6.13, this is approximately true on the interval $190 \leq T \leq 210$ K, which is consistent with the homogeneous nucleation line in figure 6.11. Hence, since the (001) plane of ice-0 has the lowest interfacial free energy of the measured interfaces at 245 K, and assuming the temperature dependence of the interfacial free energies is the same as the isotropic component found in section 6.7, the formation of a (001) interface with water should be preferential at $T \leq 220$ K.

Alternatively if ice-0 is nucleated in terms of the core-shell model proposed by Russo et al.[17], the ice-0 shell thickness surrounding a core of ice-I, is only 3.3 Å

thick at 215.2 K; which is only one molecule thick and less than the width of the ice-0 unit cell. This is also likely an upper estimate, since the temperature dependence of the calculated value of $\gamma_{0_{\text{Ice-Ih}}}$ agrees with the upper values of $\gamma_{0_{\text{Ice-Ih}}}$ reported by Limmer and Chandler[98] and Li et al.[6], while Espinosa et al. agrees with the lower values. It should be noted here, that the direct observation of such an ice-0 shell around a core of ice-Ih would be difficult using the method of ice detection used in this research. As discussed in chapter 5, ice-0 is successfully identified by spatially averaging the $q12$ order parameter over the 16 nearest neighbours, approximately equivalent to averaging over the first two coordination shells of 5.2 Å in ice-0; larger than the predicted 3.3 Å shell thickness. However, the interfacial free energy of ice-0 drops rapidly by comparison to that of ice-Ih, which would increase the thickness of any ice-0 shell formed below 215.2 K. Indeed, the ice-0 isotropic component of the interfacial free energy should drop to zero by 195 K; resulting in no nucleation barrier for ice-0. Hence, it is plausible that ice-0 does form as a precursor to stable ice-I following the core-shell model of nucleation, although it is unclear whether this is happening at 215.2 K due to such a small shell thickness.

Chapter 7

Modification of the mW Model

7.1 Ice-I Nucleation

For out-of-equilibrium liquid water systems at atmospheric pressure and below the melting temperature, ice nucleation occurs. It was thought that ice-Ic forms as a metastable precursor to ice-Ih when nucleation begins at strong supercooling, however x-ray diffraction experiments examining such systems have shown diffraction spectra that do not resemble that of either pure ice-Ic or ice-Ih[16]. Instead, it appears that a mix of pure ice-Ic and ice-Ih are present in the form of stacking disordered ice-I (ice-Isd)[104], which was previously thought to be ice-Ic. Ice-Isd consists of layers of ice-Ih and ice-Ic, stacked parallel to the plane of growth with various degrees of cubicity, i.e. presence of ice-Ic. Neutron diffraction experiments performed on ice-I formed by vapour deposited frost by Kuhs et al.[105], show ice-Isd to initially form between 175-190 K with approximately 50% cubicity, and to anneal over several hours to slowly reduce in cubicity; quicker at higher temperatures. Kuhs et al.[106] has also observed slight cubicity to persist up to almost 240 K. Additionally, work by Malkin et al.[16], shows ice-Isd to nucleate first between 237-263 K, with 50% cubicity at strong supercooling and decreasing cubicity as the temperature increases. This provides strong evidence that ice-Isd initially nucleates first at strong supercooling.

However, experiments conducted at temperatures close to the melting temperature clearly demonstrate that pure ice-Ih is the final stable crystal structure[16]. This indicates that if ice-Isd does nucleate initially at weak supercooling, then planes of ice-Ic must always anneal to become ice-Ih. This would imply the degree of cubicity in ice-Isd is therefore a kinetic effect, related to the temperature dependence of the growth rate of ice-I; i.e. slower growth rates at weaker supercooling should allow

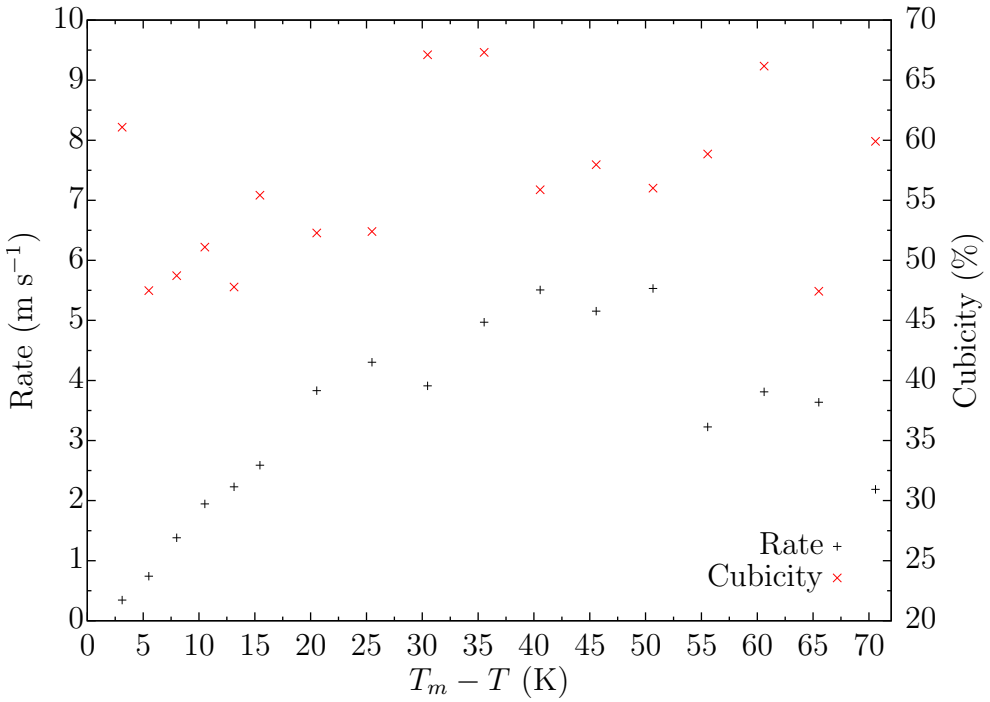

Figure 7.1: Interface growth rates (black) for an initial ice-Ih (basal) interface at various degrees of supercooling below the average melting temperature, T_m = 277.09(3) K, and 1 atm. Also shown is the relative percentage of ice-Ic (red) in the newly formed solid region at the end of the simulations.

sufficient time for planes of ice-Ic to anneal to form ice-Ih[16]. However this annealing is never observed in mW simulations, as the timescales required are beyond the computational abilities of modern MD. Consequently, the final ice-I structures grown with the mW model at weak supercooling are always ice-Isd with roughly 50% cubicity[16]; see figure 7.1. Contrary to this assumption, Quigley[107] provides a thermodynamic argument, stating that the presence of ice-Isd naturally occurs in the mW model at all supercooling, due to the small difference in the Gibbs free energy between ice-Ic and ice-Ih, which is discussed further in section 7.1.2 and is the focus of this chapter.

7.1.1 Growth Rates

The growth rates of supercooled ice-I have been examined at different temperatures for both the TIP4P/2005 model by Rozmanov and Kusalik[108], and the mW model in this research; for which simulation details are provided in section 7.1.3. Both show that a maximum growth rate exists at some temperature below the melting temperature, where either side of this temperature the growth rate is reduced. The

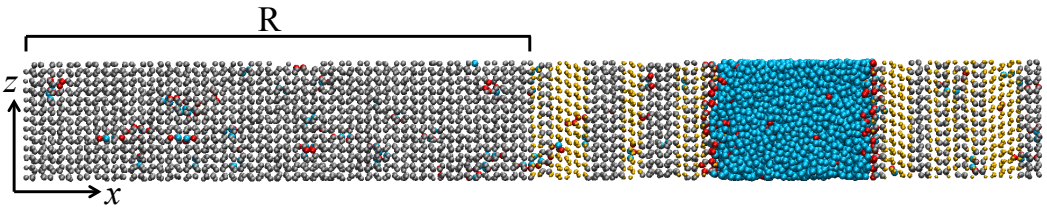

Figure 7.2: Initially a 1:1 system of ice-Ih and water, with a (basal) plane interface. This figure shows the newly formed ice-Ih (grey) and ice-Ic (orange) particles after a simulation of 5 ns at 8 K below T_m. Also present are interface (red) and water (blue) particles, as identified by $q3$. The region "R", is the original section of ice-Ih.

theoretical argument for this effect is that the growth rate is limited by the diffusion of the particles[108]. As the temperature is lowered, the liquid particles more easily bind with the solid surface, increasing the growth rate with reducing temperature. But as the temperature is lowered further, the diffusivity of the particles reduces, hence the ability for the particles to move into a solid structure is inhibited.

It is found that for the mW model, the growth rates – as shown in figure 7.1 – are much higher by almost two orders of magnitude than reported for the TIP4P/2005 model[108], and by almost an order of magnitude for other models such as the 6-site water model[109, 110]. For instance, Rozmanov and Kusalik report the maximum growth rate of ice-Ih at 12 K to be 7 cm s^{-1}, and Choi et al.[111] has recorded growth rates for ice-I at 11 K supercooling in the TIP5P-E model of 4.66 ± 1.26 cm s^{-1}, while this research finds the growth rate in the mW model at the same temperature to be approximately 2 m s^{-1}.

There are various reasons for the difference in growth rates. One such reason, as stipulated by Li et al.[6], is the diffusion coefficient is higher in the mW model than experiments by 3 times which leads to accelerated growth rates. Indeed, Espinosa et al. reports the diffusion coefficient of the mW model to be 2 orders of magnitude greater than that of the family of TIP4P water models[101]. Furthermore, the TIP4P water models are also characterised by a small solid-liquid bulk free energy difference, which results in a larger nucleation barrier[112] and hence slower growth rates. However, it has been noted that the high growth rates could be in part due to simulation effects, such as small system sizes[111] and even possibly due to heavy thermostating[113]; which can artificially remove excess heat away from the interface.

7.1.2 mW Ice-Isd

The high growth rates the mW model exhibits implies annealing is difficult, since newly formed ice-Ic particles on the surface of the interface suffer from kinetic arrest, having little time to reorganise into ice-Ih before another layer of ice-I grows on top of them. Given the comparable interfacial free energies of the ice-Ic (111) and ice-Ih (basal) planes in the mW model, this also suggests the formation of ice-Isd should occur in approximately equal concentrations of ice-Ic and ice-Ih at a range of temperatures below melting; with such planes forming parallel to the normal of the stacking plane. This has been shown to be true in the mW model by Malkin et al.[16] for initial ice-Ih (basal) planes interface with water at 274 K, for ice-Isd spontaneously forming in nanopores at 213 K and 217 K by González et al.[114] and also by Johnston and Molinero[115] between 150-200 K; reporting 60% cubicity. It has also been demonstrated via homogeneous nucleation of ice-Isd at 220 K by Reinhardt and Doye[116] and between 220-240 K by Li et al.[6], and via coexistence simulations in this work. Figure 7.2 shows the formation of ice-Isd at only 8 K below melting, while figure 7.1 demonstrates approximately equal concentrations of new ice-Ic and ice-Ih formed at the end of growth simulations, conducted over 3-70.6 K supercooling. This may anneal to form pure ice-Ih over extremely long production runs, but this is just an assumption.

An alternative model, q-TIP4P/F proposed by Habershon et al.[117], is a modified TIP4P/2005 model which includes anharmonic bond vibrations of the O-H bonds in water, and has been used to more accurately construct the ice-I/liquid, ice-I/ice-III and ice-III/liquid phase boundaries[118]. Conversely, they only report the formation of ice-Ih and make no mention of ice-Ic forming in any concentration near to the ice-I/liquid phase boundary, which is commensurate with expectations of forming pure ice-Ih at weak supercooling.

Instead of just assuming ice-Isd anneals to form ice-Ih over long durations, Quigley has investigated the propensity for the mW model to form ice-Isd at all temperatures below melting and has provided a thermodynamic argument for such an effect[107]. Moore and Molinero report that the Gibbs free energy gap between ice-Ic and ice-Ih is 0 ± 30 J mol^{-1} at 180 K[119]. However, Quigley shows from LSMC that the actual value is only 3.6(15) J mol^{-1} at $T = 240$ K[107]; decreasing with temperature. Yet first principles calculations show that the actual value should be closer to 135 J mol^{-1} at 240 K[21]. This is supported by experimental measurements of the enthalpy of transition between ice-Ih and ice-Ic, which is taken to be equivalent to the Gibbs free energy difference between the two polytypes, given a negligible entropic difference[120]. Masayasu et al.[121] measures the

average Gibbs free energy difference to be 160 J mol^{-1} between 160-210 K, which Shilling et al.[122] finds agreement with, measuring the difference to be 155 J mol^{-1} at 185 K. Many experiments forming ice-Ic from high pressure ice phases, also measure the Gibbs free energy difference to be between 13-56 J mol^{-1}[123–126], though these measurements strongly depend on the phase of ice ice-Ic was formed from.

Quigley shows that for an average interfacial free energy of $\gamma = 33$ mJ m^{-2}, $\Delta G = 50$ J mol^{-1} and latent heat of fusion $\Delta H = 6.01$ kJ mol^{-1}, that there should be almost only pure ice-Ih present for large ice nuclei at all supercooling and, at most, approximately 30% cubicity for small ice nuclei[107]. Conversely, when using a Gibbs free energy of only 2 J mol^{-1}, there should always be approximately equal quantities of ice-Ic and ice-Ih present at all supercooling and all ice nuclei sizes[107], but with a slight bias towards increasing cubicity with decreasing temperature[16].

This work hypothesises that the values of the parameters in the mW model can be altered to increase the value of ΔG and reproduce the expected formation of ice-Ih at weak supercooling, whilst still preserving the formation of ice-Isd at stronger supercooling. This is investigated by attempting to increase the Gibbs free energy gap, at 240 K, of 3.6 J mol^{-1} to the expected 135 J mol^{-1} calculated.

7.1.3 Simulation Details

With regards to the results produced in section 7.1.1, these were produced from MD simulations, explicitly designed to examine the growth rates and cubicity of ice-I nucleation in the mW model at various degrees of supercooling. Simulations were conducted at intervals 2.5 K apart, from 274 K to 206.5 K at 1 atm with a simulation timestep of 1 fs in a system of $26,880$ ice-Ih particles and an average system geometry of $400 \times 46 \times 44$ Å. These were performed by initially heating the entire system to the supercooling temperature over $100,000$ steps in the NPT ensemble. Half the system was then melted to a temperature 100 K above the supercooling temperature of the solid region by rescaling the velocities and then running in the NVT ensemble for $50,000$ steps. The remainder of the simulation was then performed in the NPT ensemble, by cooling the liquid region to the coexistence temperature over $100,000$ steps. Following this, all the atom velocities were rescaled to the supercooling temperature and the production run for was commenced for several nanoseconds. The length of the production runs varied depending on the solid temperature, since different temperatures would result in freezing at different rates.

From these simulations, the relative quantity of newly formed ice-Ic was calculated by comparing the final amount of ice-Ic and ice-Ih against the respective

initial quantities. Such initial and final measurements were possible by using the $q3$ order parameter as discussed in chapter 5. The growth rates could be established by using the $q12$ order parameter to accurately define the solid-like and liquid-like particles over the entirety of the production run. Using a discretisation of 200 bins in the **x** direction and only 1 bin in both the **y** and **z** directions, the average position of the interface was recorded every $10,000$ steps. Fitting a straight line to the plot of the average interface position against time, provided a gradient from which the growth rate of the interface could be calculated.

7.2 Free Energy Perturbation

To increase the Gibbs free energy gap between ice-Ih and ice-Ic in the mW model, the parameters of the model can be varied until the desired gap is achieved. To do this, the free energy gradient can be calculated with respect to each of the parameters in the mW potential at the values used in the systems simulated. Given that the gradient over a very small distance can be approximated to be linear, the free energy gradient for a parameter identifies whether changing such parameter by a small amount will yield a higher or lower free energy gap in a simulation using the modified parameter. In essence, one can attempt to open the Gibbs free energy gap by performing a gradient descent algorithm.

To obtain these free energy gradients, a MC code, as discussed in chapter 2, was used to simulate small single phase systems using the mW model at the same set of parameter values, also given in chapter 2. However, initially the MC algorithm had to be verified to give results consistent with those from the MD algorithm used. To check this, both an ice-Ic and an ice-Ih system were set up to run in both the MC code and in LAMMPS. The systems were set up identically for use in both algorithms, which consisted of a 512 atom ice-Ic system and an 840 atom ice-Ih system, both simulated at 253 K and 1 atm, sampling every $1,000$ steps over a production run of 1×10^6 steps; the MD simulation also having a timestep of 1 fs. The ensemble used in both algorithms was NPT and the mass of a water molecule defined to be 18.02 g mol^{-1}. Before the production run, the systems were both equilibrated over $10,000$ MC sweeps or MD iterations; in the MD simulation, the equilibration was performed in the NVT ensemble.

By calculating the average volume, $\langle V \rangle$, for a system over the production run, allowed for calculation of the average density, $\langle \rho \rangle$, of that system. The average density should be equivalent for a given polytype whether computed via the MC algorithm or LAMMPS, as should the average potential energy, $\langle U \rangle$. These values

System	Algorithm	$\langle V \rangle$ (Å^3)	$\langle \rho \rangle$ (kg m^{-3})	$\langle U \rangle$ (eV)
Ice-Ic	MC	15,623(3)	980.6(2)	-256.38(2)
	MD	15,623(2)	980.6(1)	-256.43(2)
Ice-Ih	MC	25,625(3)	980.9(1)	-420.49(3)
	MD	25,625(2)	980.9(1)	-420.59(3)

Table 7.1: Macroscopic properties of ice-Ic and ice-Ih systems as simulated via MC and MD algorithms.

are shown in table 7.1.

As shown in table 7.1, the algorithms are consistent with each other for simulating the respective ice-I mW systems. Both algorithms simulate the same densities, while the potential energies for each of the ice-Ic and ice-Ih MD simulations differ by approximately 0.02% from the potential energies of the MC simulations. While the potential energies for the MD and MC simulations are slightly outside of errors, this is not cause for concern. While both algorithms simulate at the exact applied external temperature and pressure, the MD experiences a minor drift in the internal energy over time due to the equations of motion being integrated over a discrete timestep, rather than continuously. This is the source of the minor potential energy discrepancy between the MD and the MC codes. Therefore, since the MC and MD codes give comparable results, it is possible to proceed to calculate the free energy derivatives in the MC code.

Following TI, as discussed in chapter 3, the derivative of the Hamiltonian with respect to some parameter λ, averaged over a sufficiently large production run, equates to the derivative of the free energy with respect to λ. This is demonstrated as follows for the Gibbs free energy, by first defining the free energy as

$$G = -k_{\mathrm{B}}T \ln \int_0^\infty dV \int \exp\big(-\beta \mathcal{H}(\lambda)_A + PV\big) d\mathbf{x}\,, \tag{7.1}$$

where the integration is performed over the volume V, the whole of phase space $\mathbf{x} = (\mathbf{r}, \mathbf{p})$ and $\mathcal{H}(\lambda)_A$ is the Hamiltonian of the system in state A as a function of λ. The derivative with respect to λ is then

$$\frac{\partial G}{\partial \lambda} = -k_{\mathrm{B}}T \frac{\int_0^\infty dV \int \frac{\partial}{\partial \lambda}\big(\exp\big(-\beta \mathcal{H}(\lambda)_A + PV\big)\big) d\mathbf{x}}{\int_0^\infty dV \int \exp\big(-\beta \mathcal{H}(\lambda)_A + PV\big) d\mathbf{x}} \tag{7.2}$$

$$= \frac{\int_0^\infty dV \int \frac{\partial \mathcal{H}(\lambda)_A}{\partial \lambda} \exp\big(-\beta \mathcal{H}(\lambda)_A + PV\big) d\mathbf{x}}{\int_0^\infty dV \int \exp\big(-\beta \mathcal{H}(\lambda)_A + PV\big) d\mathbf{x}}\,, \tag{7.3}$$

where equation (7.3) can be interpreted as the thermodynamic definition of the

ensemble average for the derivative of the Hamiltonian. Hence, the final form of the derivative of the free energy is

$$\frac{\partial G}{\partial \lambda} = \left\langle \frac{\partial \mathcal{H}(\lambda)_A}{\partial \lambda} \right\rangle_A , \tag{7.4}$$

where the Hamiltonian is simply $\mathcal{H}(\lambda)_A = \frac{p^2}{2m} + \Phi(\lambda)$. Since the only term dependent on λ is the potential energy, Φ, this means that in the MC code the time averaged values of the potential derivatives accurately correspond with the free energy derivatives.

In terms of the mW potential described in chapter 2, the mW model has many independent parameters that can be varied to tune the behaviour of the potential. The derivatives of the potential with respect to each of these parameters are as follows:

$$\frac{\partial \phi_2}{\partial A} = \frac{\phi_2}{A} \tag{7.5}$$

$$\frac{\partial \phi_2}{\partial \epsilon} = \frac{\phi_2}{\epsilon} \tag{7.6}$$

$$\frac{\partial \phi_2}{\partial a} = \phi_2 \left(\frac{\sigma}{r - a\sigma} \right)^2 \tag{7.7}$$

$$\frac{\partial \phi_2}{\partial B} = A\epsilon \left(\frac{\sigma}{r} \right)^p \exp\left(\frac{\sigma}{r - a\sigma} \right) \tag{7.8}$$

$$\frac{\partial \phi_2}{\partial p} = \frac{\partial \phi_2}{\partial B} B \ln\left(\frac{\sigma}{r} \right) \tag{7.9}$$

$$\frac{\partial \phi_2}{\partial q} = -A\epsilon \left(\frac{\sigma}{r} \right)^q \ln\left(\frac{\sigma}{r} \right) \exp\left(\frac{\sigma}{r - a\sigma} \right) \tag{7.10}$$

$$\frac{\partial \phi_2}{\partial \sigma} = \frac{A\epsilon}{r} \exp\left(\frac{\sigma}{r - a\sigma} \right) \left[Bp \left(\frac{\sigma}{r} \right)^{p-1} - q \left(\frac{\sigma}{r} \right)^{q-1} \right] + \frac{r}{\left(r - a\sigma \right)^2} \phi_2 \, . \tag{7.11}$$

These derivatives are from the two body term in the mW model, while those of the

three body term are:

$$\frac{\partial \phi_3}{\partial \lambda} = \frac{\phi_3}{\lambda} \tag{7.12}$$

$$\frac{\partial \phi_3}{\partial \epsilon} = \frac{\phi_3}{\epsilon} \tag{7.13}$$

$$\frac{\partial \phi_3}{\partial \cos\theta_0} = \frac{-2\phi_3}{\cos\theta - \cos\theta_0} \tag{7.14}$$

$$\frac{\partial \phi_3}{\partial \gamma} = \sigma\phi_3\left(\frac{1}{r - a\sigma} + \frac{1}{v - a\sigma}\right) \tag{7.15}$$

$$\frac{\partial \phi_3}{\partial \sigma} = \gamma\phi_3\left(\frac{r}{\left(r - a\sigma\right)^2} + \frac{v}{\left(v - a\sigma\right)^2}\right) \tag{7.16}$$

$$\frac{\partial \phi_3}{\partial a} = \gamma\sigma^2\phi_3\left(\frac{1}{\left(r - a\sigma\right)^2} + \frac{1}{\left(v - a\sigma\right)^2}\right), \tag{7.17}$$

where the notation $r_{ij} \equiv r$ and $r_{ik} \equiv v$ has been used.

7.3 Energy Gap Corrections

The Gibbs free energy gap between ice-Ic and ice-Ih is defined simply as $\Delta G(\boldsymbol{\lambda}) \equiv G_C(\boldsymbol{\lambda}) - G_H(\boldsymbol{\lambda})$, for a set of parameters $\boldsymbol{\lambda}$. By calculating the gradient of this quantity with respect to some parameter $\lambda_i \in \boldsymbol{\lambda}$, the gap can be increased by varying λ_i in the direction of the gradient. Hence,

$$\frac{\partial \Delta G(\boldsymbol{\lambda})}{\partial \lambda_i} = \frac{\partial G_C(\boldsymbol{\lambda})}{\partial \lambda_i} - \frac{\partial G_H(\boldsymbol{\lambda})}{\partial \lambda_i}\,, \tag{7.18}$$

where the terms on the right-hand-side can be obtained from the relevant equations (7.5) to (7.17).

Alternatively, the problem can be stated in terms of minimising the difference between the value for the Gibbs free energy gap with the current set of parameters, $\Delta G(\boldsymbol{\lambda})$, and the target value for the energy gap with some unknown set of parameters, ΔG_T. Hence, one must minimise the objective function

$$O(\boldsymbol{\lambda}) \equiv \left(\Delta G(\boldsymbol{\lambda}) - \Delta G_T\right)^2. \tag{7.19}$$

To do this, a set of new parameters, $\boldsymbol{\lambda'}$, is found by moving in the opposite direction to the gradient of the objective function,

$$\nabla O(\boldsymbol{\lambda}) = 2(\Delta G(\boldsymbol{\lambda}) - \Delta G_T)\left(\sum_i \frac{\partial \Delta G(\boldsymbol{\lambda})}{\partial \lambda_i}\boldsymbol{\lambda}_i\right), \tag{7.20}$$

by some small proportion, δ. Since the parameters are changing over a very small distance, the gradient of the parameter space over this region is approximately linear and the new parameters are given as $\boldsymbol{\lambda'} = \boldsymbol{\lambda} - \nabla O(\boldsymbol{\lambda})\delta$.

Since $\boldsymbol{\lambda'}$ is dependent on the value of $\Delta G(\boldsymbol{\lambda})$, it is therefore necessary to also calculate the value of $\Delta G(\boldsymbol{\lambda'})$ in order to iteratively calculate new values of $\boldsymbol{\lambda'}$ that eventually minimise the objective function. In the limit for small δ, the new Gibbs free energy gap is given by

$$\Delta G(\boldsymbol{\lambda'}) = \nabla(\Delta G(\boldsymbol{\lambda})) \cdot (\boldsymbol{\lambda'} - \boldsymbol{\lambda}) + \Delta G(\boldsymbol{\lambda})\,. \tag{7.21}$$

However, a more accurate estimate of $\Delta G(\boldsymbol{\lambda'})$ is obtained by appreciating that the function space is not necessarily going to vary linearly over an extended range from the initial set of parameters, $\boldsymbol{\lambda_0}$, to the target parameters, $\boldsymbol{\lambda_T}$. Instead, the change in the energy gap is actually

$$\Delta(\Delta G) = \int_{\boldsymbol{\lambda_0}}^{\boldsymbol{\lambda_T}} \nabla(\Delta G(\boldsymbol{\lambda})) \cdot d\boldsymbol{\lambda}\,, \tag{7.22}$$

which for discrete increments in $\boldsymbol{\lambda}$, proportional to δ, means the integral in equation (7.22) can be replaced by a summation over the number of increment steps and $d\boldsymbol{\lambda} \to \Delta\boldsymbol{\lambda} \equiv \boldsymbol{\lambda'} - \boldsymbol{\lambda}$.

The approach used to minimise the objective function could be done by moving to $\boldsymbol{\lambda'}$ in the direction of the gradient of $\Delta G(\boldsymbol{\lambda})$ at $\boldsymbol{\lambda}$, for each step. However, this approach can result in making adjustments each iteration that are too small or too large and require many iterations to yield convergence. For instance, near to the minimum, δ may be too large and result in successive values of $\boldsymbol{\lambda'}$ that orbit the actual minimum.

An alternative approach, which is used here, is to find the minimum along a search direction defined by the gradient at the initial set of parameters $\boldsymbol{\lambda_0}$. The search direction only changes once the minimum of the current search direction is found. The new direction is then defined by the gradient of the parameters at the minimum. The minimum is reached when

$$\nabla O(\boldsymbol{\lambda'}) \cdot \nabla O(\boldsymbol{\lambda_0}) = 0\,. \tag{7.23}$$

This latter method overcomes the disadvantage of the former method, since moves to $\boldsymbol{\lambda'}$ which are beyond the minimum of the line will produce negative values of equation (7.23), which clearly indicates a smaller step size is needed. The difference in execution between the two methods is that the latter doesn't require iterative

Structure	τ									
	$\partial_A G$	$\partial_a G$	$\partial_B G$	$\partial_\epsilon G$	$\partial_\sigma G$	$\partial_\lambda G$	$\partial_\gamma G$	$\partial_p G$	$\partial_q G$	$\partial_{\theta_0} G$
Ice-Ic	0.77	1.29	1.15	1.40	1.17	2.23	2.23	0.64	1.10	1.91
Ice-Ih	0.83	1.44	1.32	1.46	1.33	2.50	2.55	0.69	1.27	2.21
Interval	150	200	100	200	150	250	250	100	100	250

Table 7.2: Correlation times and sampling intervals for the derivatives of the Gibbs free energy with respect to each of the mW parameters in ice-Ic and ice-Ih. Note the condensed notation $\partial_{\theta_0} G \equiv \frac{\partial G(\boldsymbol{\lambda_0})}{\partial \cos(\theta_0)}$.

moves from $\boldsymbol{\lambda}$ to $\boldsymbol{\lambda'}$, but rather a single move from $\boldsymbol{\lambda_0}$ to $\boldsymbol{\lambda'}$ for a line search. Such a move is obtained by making iterative adjustments to the step size δ. Hence,

$$\boldsymbol{\lambda'} = \boldsymbol{\lambda_0} - \nabla O(\boldsymbol{\lambda_0})\delta\,, \tag{7.24}$$

where δ is varied until equation (7.23) is satisfied, at which point $\boldsymbol{\lambda_0} \equiv \boldsymbol{\lambda'}$ and the process is repeated. Such a method requires as many line searches as there are parameters to minimise, at which point the objective function is also minimised.

7.4 Derivative Correlations

To practically perform the gradient descent method described in section 7.3, required accurate measurements of $\partial_{\lambda_i} G(\boldsymbol{\lambda_0})$. Hence, the MC simulations had to be run long enough so that the associated error on the gradient be smaller than the value of the gradient itself. This meant each of the derivatives had to be sampled at intervals that were uncorrelated with themselves at some time t in the future from any time t_0. It was therefore necessary to calculate the degree of autocorrelation, $C(t)$, for each of the derivatives and only average over uncorrelated values; so that $C(t) \approx 0$ within n MC sweeps.

The autocorrelation of each of the derivatives was obtained from MC simulations of ice-Ic and ice-Ih using 384 particles each at $T = 240$ K, $P = 1$ atm, conducted in the NPT ensemble, using the initial set of parameters for the mW model, $\boldsymbol{\lambda_0}$, as stated in chapter 2. The systems were first equilibrated over $10,000$ MC sweeps and then sampled every 10 MC sweeps during a production run of 1×10^6 sweeps. The correlation times for each of the derivatives were then calculated over the data set obtained in the same way the correlation of $\left\langle |h(q)|^2 \right\rangle$ was obtained, as described in chapter 4. The correlation time, τ, for each of the derivatives is shown in table 7.2.

The correlation times vary significantly between each of the derivatives and

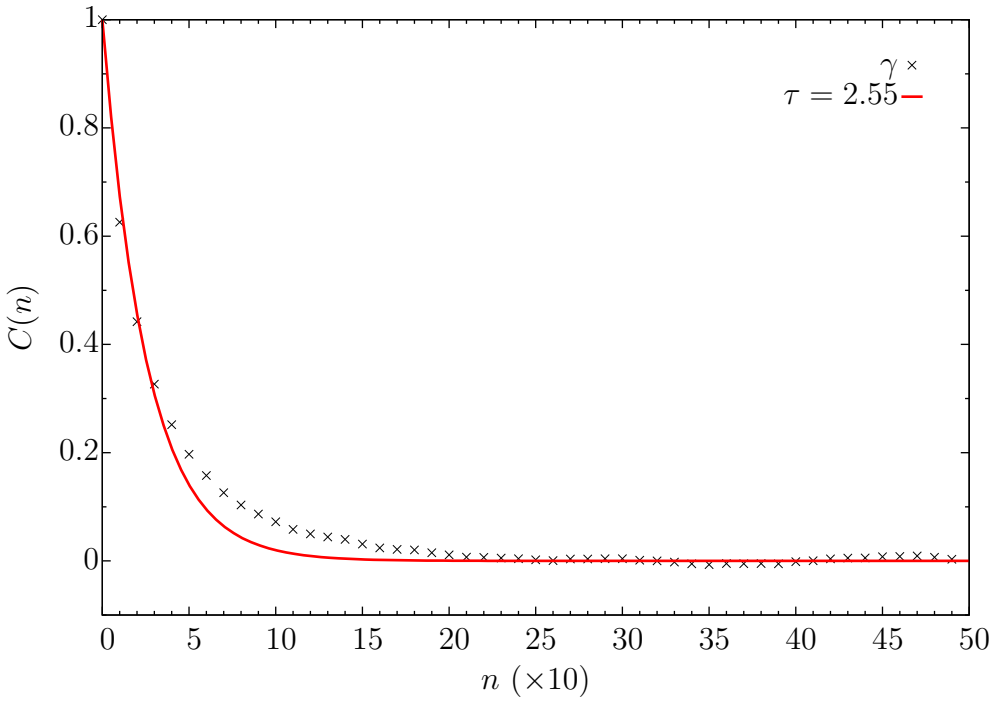

Figure 7.3: Result of the autocorrelation function for $\partial_\gamma G(\boldsymbol{\lambda_0})$ against MC sweeps, sampling every 10 sweeps over a total of 1×10^6 in ice-Ih. The red line is a fit of $\exp(-n/\tau)$.

therefore each should be sampled at intervals most suitable to the derivative. Plotting the degree of correlation for each of the derivatives against the number of MC sweeps, and the fit of $\exp(-n/\tau)$, gives a clear indication at which value of n the measurements can be considered independent. This is demonstrated in figure 7.3 for $\partial_\gamma G(\boldsymbol{\lambda_0})$ where, erring on the side of caution, samples taken every 250 MC sweeps can be considered independent. The sampling interval for each of the derivatives is also shown in table 7.2.

7.5 Gradient Descent

7.5.1 Simulations

It was found from the results of the autocorrelation, that in order to reduce the errors sufficiently on all the derivatives the MC simulations needed production runs as long as 1×10^7 MC sweeps. The other attributes of the simulations were identical to that described in section 7.4.

Once $\hat{\nabla} O(\boldsymbol{\lambda_0})$ was found, simulations were set up to construct new parameters in accordance with equation (7.24). It was discovered that the parameter ϵ,

overwhelmingly dominated the direction of the line search, contributing 98% of the gradient. A total of 43 simulations were conducted, varying δ from a value of 1×10^{-5} to 3×10^{-3}, which corresponded to a percentage change in ϵ of approximately 0.1% to 30%; while all other parameters experienced a significantly smaller percentage change. Based on the gradient of the Gibbs free energy at $\boldsymbol{\lambda_0}$, using equation (7.21) suggested that $\Delta G(\boldsymbol{\lambda'})$ would increase from 3.61 J mol^{-1} at $\delta = 1\times10^{-5}$ to 6.72 J mol^{-1} at $\delta = 3\times10^{-3}$. This predicted increase in $\Delta G(\boldsymbol{\lambda'})$ was far from the target of 135 J mol^{-1}, but it was possible the gradient could significantly change at any point along the line search.

It should be noted that even at a 30% relative change in ϵ, the absolute values for p and q changed much less than 0.5. Given that p and q are both integers, these were held constant. This meant the actual value of $\hat{\nabla}O(\boldsymbol{\lambda_0})$ was

$$\hat{\nabla}O(\boldsymbol{\lambda_0}) = 0.991\hat{\epsilon} - 0.003\hat{A} + 0.009\hat{B} + 0.018\hat{a} - 0.007\hat{\sigma} + 0.001\hat{\lambda} - 0.047\hat{\theta}_0 - 0.125\hat{\gamma}\,, \quad (7.25)$$

where the notation $\hat{\theta}_0$ is the unit vector of $\cos\theta_0$.

While varying the parameters, it is important to know if the model is still valid in terms of the quantities against which it was originally fitted. Knowing how changing the parameters affects the melting temperature of the model is of primary concern, since the Gibbs free energy gap is for ice at 240 K. Hence, if changing the parameters results in the melting temperature falling to below 240 K, then the model is no longer valid. To calculate the melting temperature, several solid-liquid coexistence MD simulations were performed along the line search. These MD simulations were performed using the parameters $\boldsymbol{\lambda'}$ for ice-Ih, using 14,976 atoms, constructing a (basal) interface at a pressure of 1 atm for values of $\delta = 5$, 10, 15, 20 and 25×10^{-4}.

The coexistence simulations were setup in a similar fashion to those previously described in chapters 4 and 6. These were initially constructed to have an average temperature such that the entire system behaved as a warm solid, simulated in the NVT ensemble over 50,000 steps with a timestep of 1 fs. Following this, the system was then switched to run in an anisotropic NPT ensemble over 50,000 steps at the same temperature. Half the system was then melted and held at high temperature for 50,000 steps. Over a further 50,000 steps, the liquid was cooled so that the average system temperature matched the predicted melting temperature. Finally, the system was equilibrated in a fully anisotropic NPH ensemble for 200,000 steps, before a production run over 5 ns.

7.5.2 Results

The results for the search for the minimum, melting temperature, density of ice-Ih and the Gibbs free energy gap, along the initial gradient are shown in figure 7.4. Firstly, from the bottom graph of figure 7.4, it can be seen that a small variation in the parameters $\boldsymbol{\lambda}$, does indeed approximate to a linear variation in the difference in the free energy gap, suggesting the method used to increase the free energy difference has been applied correctly. However, the line search fails to find a minimum as the quantity $\nabla O(\boldsymbol{\lambda'}) \cdot \nabla O(\boldsymbol{\lambda_0})$ is always ≈ 1, indicating that the direction of the gradient of ΔG does not vary along the search direction. Continuing to search past a value of $\delta = 2.8 \times 10^{-3}$ results in the MC simulations spontaneously melting. While the density of ice-Ih does not change unreasonably, MD simulations show that the melting temperature drops below 240 K at approximately $\delta = 1.4 \times 10^{-3}$; at which point $\Delta G(\boldsymbol{\lambda'}) = 5.6$ J mol^{-1}. This implies that the results obtained from the MC simulations for values $\delta > 1.4 \times 10^{-3}$ are for superheated ice only. What is more, at $\delta = 2.8 \times 10^{-3}$ the Gibbs free energy gap only manages to be increased to $\Delta G(\boldsymbol{\lambda'}) = 8.82$ J mol^{-1}, as calculated from equation (7.22) plus $\Delta G(\boldsymbol{\lambda_0})$, being significantly lower than the 50 J mol^{-1} reported by Quigley necessary to reproduce ice-Ih nuclei at temperatures close to melting[107].

The fact that the melting temperature drops is not unsurprising, since ϵ is responsible for the potential well depth. As this parameter decreases a relatively large amount, so too does the depth of the potential well. This results in pairs of atoms becoming more loosely bound and therefore less energy is required to break the solid bonds, resulting in melting at lower temperatures.

Given that the gradient of the objective function is dominated by the change in ϵ, it was expected that only a small change would be necessary to satisfy equation (7.23); hence the justification for changing ϵ by 0.1% up to 1%. However, figure 7.4 shows no appreciable difference. From $\boldsymbol{\lambda_0}$ to $\boldsymbol{\lambda'}$, the gradients of other parameters change sign, but their magnitudes are negligible compared to that of ϵ.

It must therefore be concluded that the Gibbs free energy gap cannot be opened sufficiently in the mW model to reproduce the larger experimental values, or the expected first principles value discussed in section 7.1.2. Consequently, the formation of ice-Isd in the mW model, at all degrees of supercooling, appears to be an artefact of the model. The small value of the Gibbs free energy gap, allows either ice-Ic or ice-Ih to form readily on an ice-I interface. Combined with the characteristic high growth rates of the mW model, results in insufficient time for ice-Ic to anneal to form ice-Ih. Hence, ice-Isd readily forms in the mW model at weak supercooling, compared to models with slower growth rates such as q-TIP4P/F.

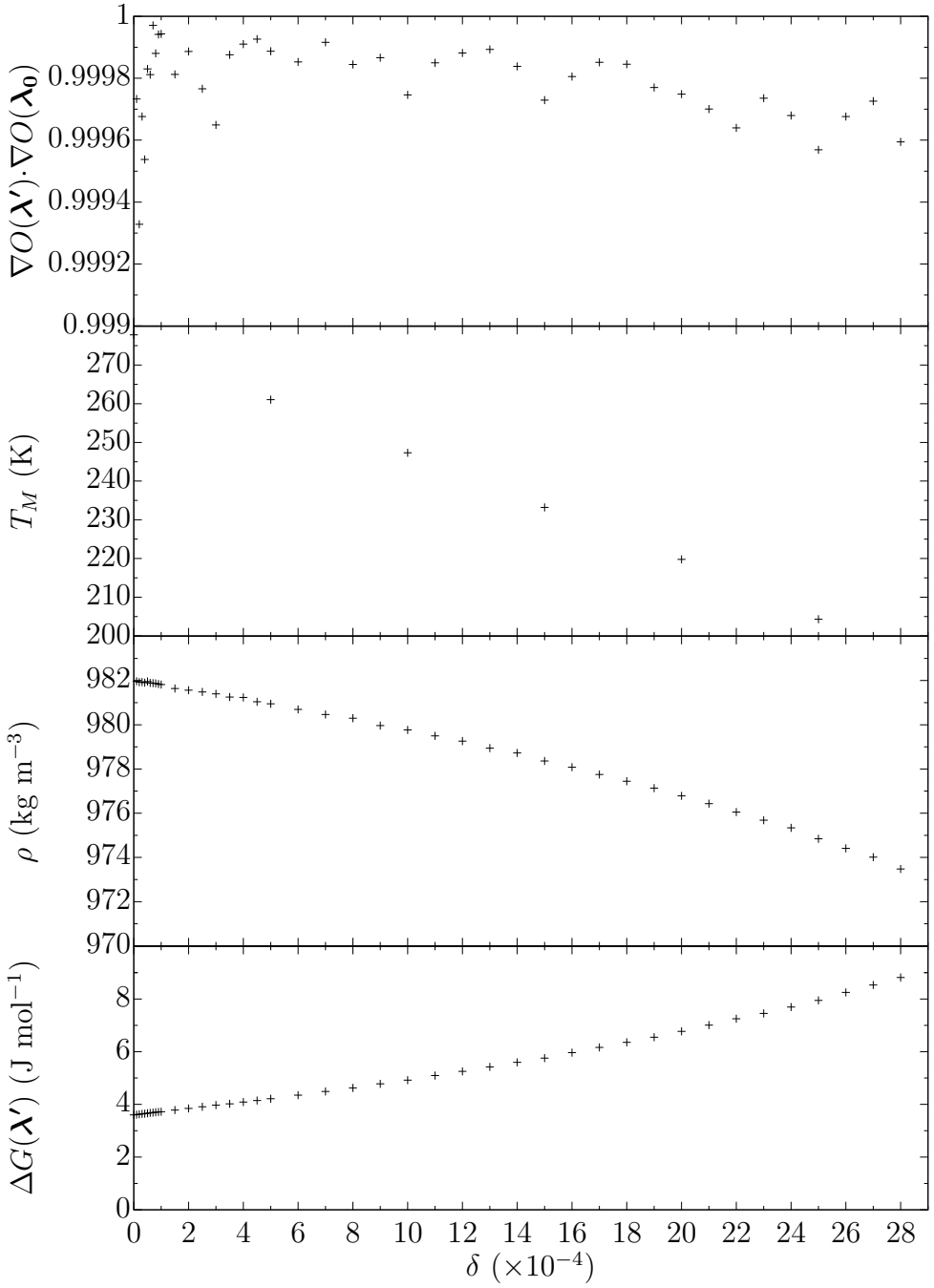

Figure 7.4: Quantities for the mW model at different parameter sets, $\boldsymbol{\lambda}'$, for varying δ. *Top:* The result of equation (7.23). *Upper middle:* The melting temperature of ice-Ih obtained from coexistence MD simulations. *Lower middle:* The density of ice-Ih obtained from the MC simulations. *Bottom:* The Gibbs free energy gap as calculated by equation (7.22), plus the initial gap.

Chapter 8

Conclusion

This research primarily dealt with the application of the CWM to calculate the interfacial free energy of ice-Ic, ice-Ih and ice-0 structures interfaced with water. The development of various software was necessary in order to conduct such research, which needed validating. Work began with the development of an interface analysis code, which was able to map the position of the interface at individual timesteps and construct the relative contributions of wave vectors present in the fluctuations across the length of the interface. In chapter 4, the interfacial analysis code was applied to coexisting systems of LJ FCC solids in contact with their melt at $P^* = 0$, for (100)[001], (110)[001] and (111)[$1\bar{1}0$] orientations. The code produced measured values of $\langle |h(q)|^2 \rangle$ which were used to calculate the interfacial stiffness for each orientation using the CWM. These were then compared directly to calculations previously conducted by Morris and Song[73] and were found to be in excellent agreement and to higher precision.

Following the successful implementation of the CWM in FCC LJ systems, focus shifted to applying the method to ice systems. However, before interfacial free energy results could be obtained, development of reliable ice detection order parameters and software was required, followed by a clear understanding of how discretising the system affected the interfacial stiffness results; as discussed in chapter 5.

$q3$, $q6$ and $q12$ order parameters were investigated to check the suitability of ice detection. While $q6$ was good at distinguishing between FCC solid-like and liquid-like particles, it did not perform well at determining which were ice-Ih solid-like and liquid-like particles. $q6$ was also unable to distinguish between the two ice-I polytypes, whilst completely failing at ice-0 detection and hence was of extremely limited use for ice detection. The failings of $q6$ prompted the investigation into $q3$, which, using the CHILL+ algorithm developed by Nguyen and Molinero[82],

was excellent at distinguishing between the ice-I polytypes, water and interfacial atoms. However, it could not identify the difference between solid-like and liquid-like ice-0 particles. To identify ice-0 particles, $q12$ was required, which had the exceptional ability to distinguish between the solid-like particles of each of the ice structures and water. $q12$ however, could not distinguish between the different solid-like particles of the ice structures themselves. Hence, one concludes that $q3$ is useful for ice-I polytype identification, necessary for observing the growth of ice-Isd, while $q12$ is useful for solid-like and liquid-like particle distinctions, necessary for ice-0 identification.

After choosing an appropriate order parameter capable of defining a boundary between the solid and liquid phases, the system had to be discretised in such a way as to correctly measure the local interfacial positions. Changing the discretisation of the system in the long and interfacial directions, as well as changing the thickness of the system, had profound effects on the measurement of the interfacial stiffness. It was discovered that if the system is not discretised sufficiently in the long direction of the system, the measured interfacial stiffness is lower than actual; due to the interface having a similar position in the long direction at every point across the interface, appearing smoother than it actually is. If discretisation was too coarse across the interfacial direction of the system, then, when ignoring the continuum limit, the interfacial stiffness was higher than actual; due to the interface appearing rougher than in reality. Thicker systems also exhibited higher interfacial stiffnesses than in reality, due to the presence of capillary waves across the short direction of the interface; corroborated by RMS deviation measurements for the interface position, which were larger for thicker systems than shorter systems. The interfacial free energy results obtained for ice, were from simulations that were as thin as possible for ice-0, while for ice-I were thin enough to have removed any capillary waves across the short direction. However, since the interfacial stiffness increases with thickness, the results obtained form this research can be considered to be at least upper limits on the interfacial free energies.

The results for the interfacial free energies of ice-Ic, ice-Ih and ice-0, discussed in chapter 6, could only be compared using $q12$ since it was the only order parameter that worked with all three structures. Analysis conducted for ice structures where the other order parameters could distinguish between solid-like and liquid-like particles, found that $q12$ actually gave a higher estimate for the interfacial stiffness than either $q3$ or $q6$. Hence a systematic effect exists dependent upon the choice of order parameter. This was attributed to the exceptional ability for $q12$ to distinguish between solid and liquid phases close to the interface, meaning the interface appeared

rougher when using $q12$ compared to the other two order parameters.

Measurements of the interfacial free energies find for ice-Ih $\gamma_{\text{basal}} < \gamma_{\text{prism}} \lesssim \gamma_{11\bar{2}0}$, while generally for ice-Ic $\gamma_{111} \lesssim \gamma_{112} \lesssim \gamma_{110} < \gamma_{100}$; found to be in agreement with other research conducted[39, 61, 73, 99, 102]. Furthermore, it is found that between ice-Ic and ice-Ih, $\gamma_{110} \approx \gamma_{11\bar{2}0}$ and $\gamma_{\text{basal}} \approx \gamma_{111}$ to 0.3 mJ m^{-2} outside of errors, which supports the equivalency of such interfaces previously reported[99, 103]. Such agreement of ice-I results with literature implies the results of the CWM conducted in this research are highly reliable when considering new results for ice-0.

The isotropic components of the free energy are found to be $\gamma_{0_{\text{Ice-0}}} < \gamma_{0_{\text{Ice-Ih}}} \lesssim \gamma_{0_{\text{Ice-Ic}}}$. With regards to ice-Ih specifically, excellent agreement is found between this work and previous work conducted using alternative methods. Most notably, here it is found $\gamma_{0_{\text{Ice-Ih}}} = 36.0(3)$ mJ m^{-2}, while it is also reported as being 34.9(8) and 35.5(25) mJ m^{-2} for mold integration[99] and the seeding method[95], respectively. In this research, it is also found that the isotropic component of the free energy is more strongly dependant on the temperature in ice-0 than in ice-Ih, resulting in a preferential ice-0 nucleation barrier over ice-Ih at $T < 220$ K. From the core-shell model of nucleation, this should result in a 3.3 Å thick ice-0 shell around a core of ice-Ih at 215.2 K; with increased thickness at lower temperatures. However at 215.2 K, it is unclear whether ice-0 definitively does form, as the shell thickness is smaller than the width of the ice-0 unit cell and cannot be microscopically verified using the ice detection methods employed in this research. It is plausible that ice-0 does nucleate as a precursor to ice-I and is even more likely at $T < 215.2$ K, possibly forming a (001) interface with water as this has the lowest interfacial free energy.

The final part of this research, reported in chapter 7, investigated the failure of the mW model to reproduce experimentally observed pure ice-Ih near to the melting temperature of ice-I. The Gibbs free energy gap between ice-Ic and ice-Ih in the mW model had been calculated to be 3.6 J mol^{-1} at 240 K and 1 atm by Quigley[107], while it was actually expected to be closer to 135 J mol^{-1}[21]. The small difference in the Gibbs free energy between the two polytypes had been identified as the cause for always generating ice-Isd, in the mW model, when nucleating ice-I at all temperatures below melting by Quigley[107]. The formation of ice-Isd was corroborated by Malkin et al.[16] between 220-240 K, by Li et al.[6], and demonstrated further in this research from 3-70 K below melting.

This research also found that the high growth rate of ice is the kinetic reason ice-Ic has no time to anneal to form ice-Ih during nucleation, since newly formed ice-Ic is kinetically arrested by the growth of more ice-Isd on top of it. As a consequence of such kinetics, it was found that ice-Ic forms in approximately equal quantities

during the formation of ice-Isd; also observed by Malkin et al.[16]. The high growth rates observed in this research corroborated independent work by Espinosa et al.[101] who report the diffusion coefficient of the mW model to be at least 2 orders of magnitude greater than that of slower growing TIP4P water models; one of which (q-TIP4P/F)[117] didn't report the presence of any ice-Ic forming near to the melting temperature of ice-I[118].

In an attempt to increase the Gibbs free energy gap between ice-Ic and ice-Ih, first order thermodynamic perturbation theory was applied to the mW model. By varying the parameters of the mW model following a gradient descent algorithm, with the exception of p and q since they were integers, it was found that ϵ had the most profound effect on the value of the Gibbs free energy difference. However, despite varying the value of the ϵ by approximately 28%, the energy gap could only be increased to 8.82 J mol^{-1} before the MC simulations, used to calculate the free energy derivatives, spontaneously melted. Most significantly, it was found that varying the parameters to reflect a 14% change in ϵ, reduced the melting temperature of the mW model to approximately 240 K at 1 atm; resulting in a Gibbs free energy gap of only 5.6 J mol^{-1}. Consequently, this research indicates that it is unlikely that the parameters of the mW model can be modified such that the Gibbs free energy gap can be sufficiently opened to reproduce nucleation of ice-Ih at weak supercooling, whilst maintaining ice-Isd nucleation at strong supercooling; without changing the melting temperature of the model appreciably. Hence, it can be argued that the mW model is not a reliable model to use for the investigation of the formation of ice-Isd, since its manifestation is an artefact of the model, rather than as a result of the true underlying mechanics during nucleation.

Appendix A

Derivation of Capillary Waves

As discussed in chapter 4, in general, the total change in the surface energy of an interface due to thermal fluctuations can be equated to

$$\Delta E = \frac{1}{2}\int d\mathbf{r}\big(\gamma_{\mathbf{r}}\big(\nabla h(\mathbf{r})\big)^2\big). \tag{A.1}$$

The above equation was derived with the consideration that the deviation in the height function over an infinitesimal element is continuous. While this is true analytically, with most numerical techniques it is not possible to measure the smooth infinitesimal change in the height over real-space. In practise, we are limited to the size of the discrete spacing the surface is broken up into. Considering a 2D interface, a position in $\mathbf{r}$ can be defined discretely as $\mathbf{r} = a\Delta_x\hat{\mathbf{x}} + b\Delta_y\hat{\mathbf{y}}$. Here, Δ_x and Δ_y are the size of the bins the surface is being discretised into along the surface directions $\hat{\mathbf{x}}$ and $\hat{\mathbf{y}}$, respectively, and $\{a, b\} \in \mathbb{Z}$. Similarly for $\mathbf{q}$, this is defined as $\mathbf{q} = q_x\hat{\mathbf{x}} + q_y\hat{\mathbf{y}}$. This means, the height function in equation (A.1) must be differentiated discretely from the definition of differentiation

$$\frac{\partial h(\mathbf{r})}{\partial x} = \frac{h((a+1)\Delta_x) - h(a\Delta_x)}{\Delta_x}. \tag{A.2}$$

It is then possible to derive an expression for the height-height correlation function $\langle h(\mathbf{q})h(-\mathbf{q})\rangle = \langle |h(\mathbf{q})|^2\rangle$, by directly applying the Fourier transforms

$$h(\mathbf{r}) = \sum_{\mathbf{q}} h(\mathbf{q})e^{i\mathbf{q}\cdot\mathbf{r}} \tag{A.3}$$

$$h(\mathbf{q}) = \frac{\Delta_x\Delta_y}{\sqrt{A}}\sum_{\mathbf{r}} h(\mathbf{r})e^{-i\mathbf{q}\cdot\mathbf{r}} \tag{A.4}$$

to equation (A.1).

Hence,

$$\frac{\partial h(\mathbf{r})}{\partial x} = \frac{1}{\Delta_x}\sum_{q_x,q_y} h(q_x,q_y)\big(e^{iq_x(a+1)\Delta_x} - e^{iq_x a\Delta_x}\big)e^{iq_y b\Delta_y} \tag{A.5}$$

$$= \frac{1}{\Delta_x}\sum_{q_x,q_y} h(q_x,q_y)e^{iq_x a\Delta_x}\big(e^{iq_x\Delta_x} - 1\big)e^{iq_y b\Delta_y}, \tag{A.6}$$

and similarly for $\frac{\partial h(\mathbf{r})}{\partial y}$ where $x \to y$, $y \to x$, $a \to b$ and $b \to a$. Then from (A.1),

$$\frac{1}{2}\int dxdy\left(\gamma_x\left(\frac{\partial h(\mathbf{r})}{\partial x}\right)^2 + \gamma_y\left(\frac{\partial h(\mathbf{r})}{\partial y}\right)^2\right) =$$
$$\frac{1}{2}\sum_{a,b}\Bigg[\left(\frac{\gamma_x}{\Delta_x^2}\sum_{q_x,q_y} h(q_x,q_y)e^{iq_x a\Delta_x}\big(e^{iq_x\Delta_x} - 1\big)e^{iq_y b\Delta_y}\right)$$
$$\left(\sum_{k_x,k_y} h(k_x,k_y)^* e^{-ik_x a\Delta_x}\big(e^{-ik_x\Delta_x} - 1\big)e^{-ik_y b\Delta_y}\right) + ...\Bigg] \tag{A.7}$$

$$= \frac{1}{2}\sum_{a,b}\Bigg[\frac{\gamma_x}{\Delta_x^2}\sum_{q_x,q_y,k_x,k_y} h(q_x,q_y)h(k_x,k_y)^* e^{i(q_x-k_x)a\Delta_x}e^{i(q_y-k_y)b\Delta_y}$$
$$\big(e^{iq_x\Delta_x} - 1\big)\big(e^{-ik_x\Delta_x} - 1\big) + ...\Bigg], \tag{A.8}$$

where "..." denotes the derivative with respect to y, following the transformation rules outlined previously. Note also that

$$\sum_n e^{i(x-y)n} = \delta_{x,y}\,, \tag{A.9}$$

so from equation (A.9), equation (A.8) becomes

$$= \frac{1}{2}\sum_{q_x,q_y}\frac{\gamma_x}{\Delta_x^2}\big|h(q_x,q_y)\big|^2\big|e^{iq_x\Delta_x} - 1\big|^2 + ... \tag{A.10}$$

$$= \sum_{q_x,q_y}\frac{\gamma_x}{\Delta_x^2}\big|h(q_x,q_y)\big|^2\big(1 - \cos(q_x\Delta_x)\big) + ...\,, \tag{A.11}$$

and making use of half angles of sine,

$$= 2\sum_{q_x,q_y}\frac{\gamma_x}{\Delta_x^2}\big|h(q_x,q_y)\big|^2\sin^2\left(\frac{q_x\Delta_x}{2}\right) + ...\,. \tag{A.12}$$

As from chapter 4, taking the average of equation (A.1) and treating the

modes independently,

$$\frac{1}{2}k_{\mathrm{B}}T = 2\left\langle \left|h(\mathbf{q})\right|^2 \right\rangle \left(\frac{\gamma_x}{\Delta_x^2}\sin^2\left(\frac{q_x\Delta_x}{2}\right) + \frac{\gamma_y}{\Delta_y^2}\sin^2\left(\frac{q_y\Delta_y}{2}\right)\right), \tag{A.13}$$

the height-height correlation function is recovered for a 2D interface,

$$\left\langle \left|h(\mathbf{q})\right|^2 \right\rangle = \frac{1}{4}k_{\mathrm{B}}T\left[\frac{\gamma_x}{\Delta_x^2}\sin^2\left(\frac{q_x\Delta_x}{2}\right) + \frac{\gamma_y}{\Delta_y^2}\sin^2\left(\frac{q_y\Delta_y}{2}\right)\right]^{-1}. \tag{A.14}$$

Appendix B

SASH Equations

The SASH equations derived in chapter 5 are the result of substituting the corresponding values of θ and ϕ that define the crystal plane, into the SASH basis functions $S_i(\theta, \phi)$. These basis functions were obtained from ATAT and are reproduced here in terms of Cartesian coordinates up to $l = 6$. The components x, y and z, have the respective vectors on the unit sphere **i**, **j** and **k** as defined in chapter 5. Simply converting to spherical polar coordinates will recover the basis functions in terms of θ and ϕ when setting $r = 1$, i.e.

$$x = \cos(\phi)\sin(\theta) \quad y = \sin(\phi)\sin(\theta) \quad z = \cos(\theta)\,. \tag{B.1}$$

For ice-Ic, the basis functions are defined as follows:

$$S_1(x,y,z) = x^4 + y^4 + z^4 - \frac{3}{5} \tag{B.2}$$

$$S_2(x,y,z) = 3\big(x^4 + y^4 + z^4\big) + 66\big(x^2y^2z^2\big) - \frac{17}{7} \tag{B.3}$$

$$S_3(x,y,z) = 65\big(x^4 + y^4 + z^4\big)^2 - 94\big(x^4 + y^4 + z^4\big) - 208\big(x^2y^2z^2\big) + 33 \tag{B.4}$$

$$S_4(x,y,z) = 7106\big(x^4 + y^4 + z^4\big)\big(x^2y^2z^2\big) + 187\big(x^4 + y^4 + z^4\big)^2 - 264\big(x^4 + y^4 + z^4\big) - 3190\big(x^2y^2z^2\big) + 85\,. \tag{B.5}$$

For ice-Ih, the basis functions are:

$$S_1(x,y,z) = 0.408248\big(x^2+y^2\big) - 0.816497z^2 \tag{B.6}$$

$$S_2(x,y,z) = 0.179284\big(x^4+y^4\big) + 0.358569\big(x^2y^2\big) - 1.43427\big(x^2z^2+y^2z^2\big) + 0.478091z^4 \tag{B.7}$$

$$S_3(x,y,z) = 0.194972x^6 - 0.125587y^6 - 0.111016z^6 + 2.50827\big(x^2y^4\big) - 2.30011\big(x^4y^2\big) - 0.624465\big(x^4z^2+y^4z^2\big) - 1.24893\big(x^2y^2z^2\big) + 0.832621\big(x^2z^4+y^2z^4\big) \tag{B.8}$$

$$S_4(x,y,z) = 1.34224\big(x^4y^2 - x^4z^2 - y^4z^2\big) - 0.894825\big(x^2y^4\big) + 0.149137y^6 - 2.68447\big(x^2y^2z^2\big) + 1.78965\big(x^2z^4+y^2z^4\big) - 0.23862z^6\,. \tag{B.9}$$

For ice-0, the basis functions are:

$$S_1(x,y,z) = 0.408248\big(x^2+y^2\big) - 0.816497z^2 \tag{B.10}$$

$$S_2(x,y,z) = 0.396412\big(x^4+y^4\big) + 0.216225z^4 - 0.648675\big(x^2z^2+y^2z^2\big) - 1.7298\big(x^2y^2\big) \tag{B.11}$$

$$S_3(x,y,z) = 1.2792\big(x^2y^2 - x^2z^2 - y^2z^2\big) + 0.426401z^4 \tag{B.12}$$

$$S_4(x,y,z) = 0.154303\big(x^6+y^6\big) - 0.140276z^6 - 0.420827\big(x^4y^2+x^2y^4\big) - 1.89372\big(x^4z^2+y^4z^2\big) + 1.05207\big(x^2z^4+y^2z^4\big) + 5.04993\big(x^2y^2z^2\big) \tag{B.13}$$

$$S_5(x,y,z) = 0.556702\big(x^4y^2+x^2y^4 - x^4z^2 - y^4z^2\big) + 1.67011\big(x^2z^4+y^2z^4\big) - 6.68043\big(x^2y^2z^2\big) - 0.222681z^6\,. \tag{B.14}$$

Appendix C

SASH Plots

In support of the results given in chapter 6, presented here are 3D polar plots of the fitted interfacial stiffness and free energy for ice-Ic, ice-Ih and ice-0. In all three cases, the plots are made from the parameters found when using the $q12$ order parameter. Specifically, in the case of ice-Ic, the plots are also made when using $m = 5$ fitting parameters. These figures clearly demonstrate how insensitive to anisotropy the free energy is when compared to the stiffness.

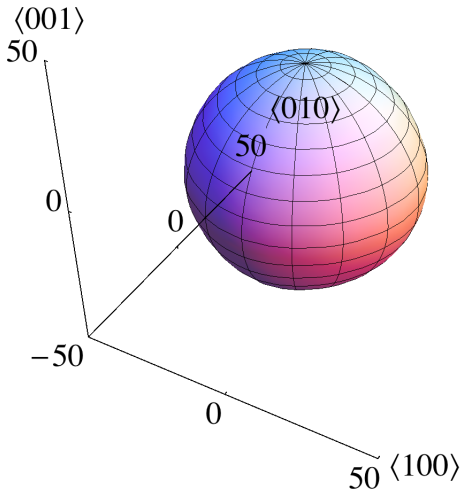

(a) Free energy SASH for ice-Ic.

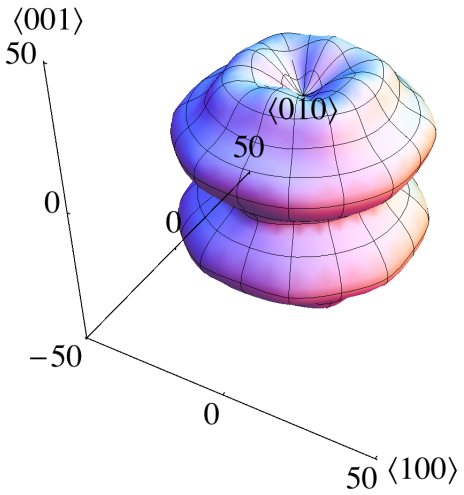

(b) Stiffness SASH for ice-Ic, $\mathbf{u} = \mathbf{e}_\theta$.

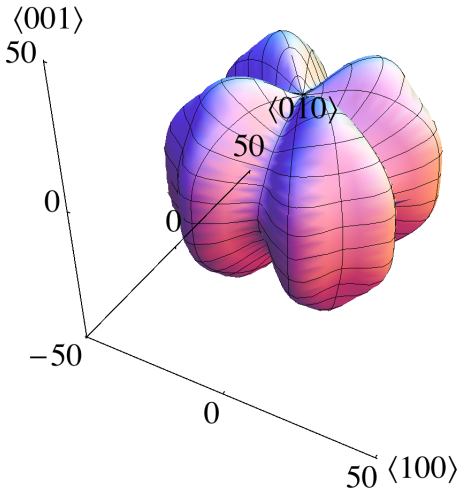

(c) Stiffness SASH for ice-Ic, $\mathbf{u} = \mathbf{e}_\phi$.

Figure C.1: Plots of the SASH equations for ice-Ic representing the free energy and the interfacial stiffness with unit vectors $\mathbf{u} = \mathbf{e}_\theta$ and $\mathbf{u} = \mathbf{e}_\phi$ as shown.

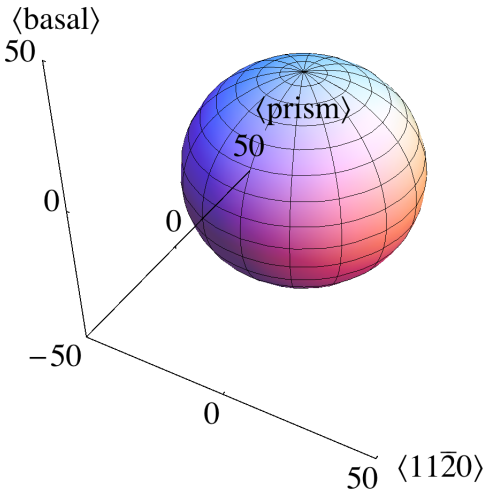

(a) Free energy SASH for ice-Ih.

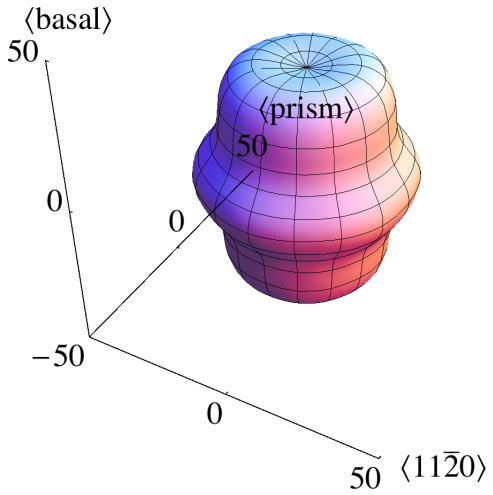

(b) Stiffness SASH for ice-Ih, $\mathbf{u} = \mathbf{e}_\theta$.

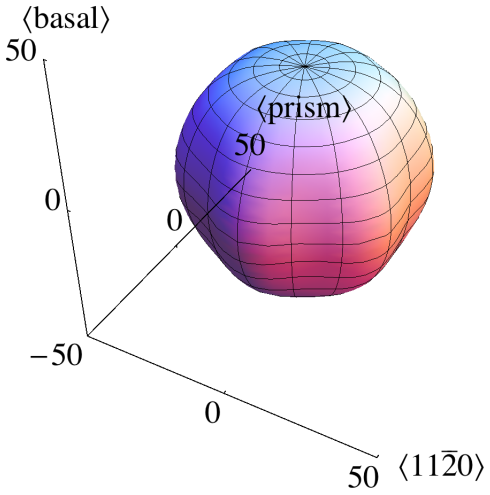

(c) Stiffness SASH for ice-Ih, $\mathbf{u} = \mathbf{e}_\phi$.

Figure C.2: Plots of the SASH equations for ice-Ih representing the free energy and the interfacial stiffness with unit vectors $\mathbf{u} = \mathbf{e}_\theta$ and $\mathbf{u} = \mathbf{e}_\phi$ as shown.

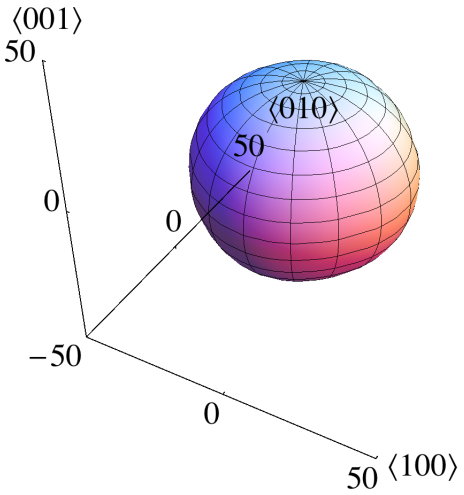

(a) Free energy SASH for ice-0.

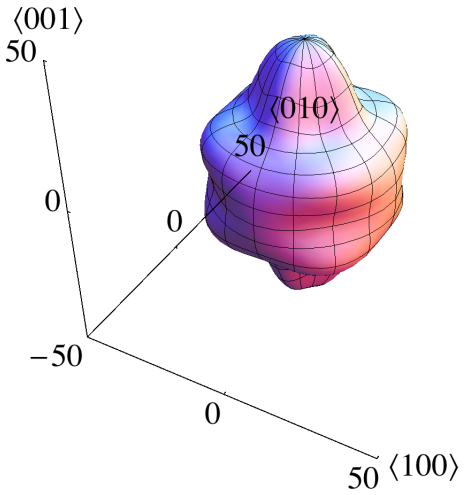

(b) Stiffness SASH for ice-0, $\mathbf{u} = \mathbf{e}_\theta$.

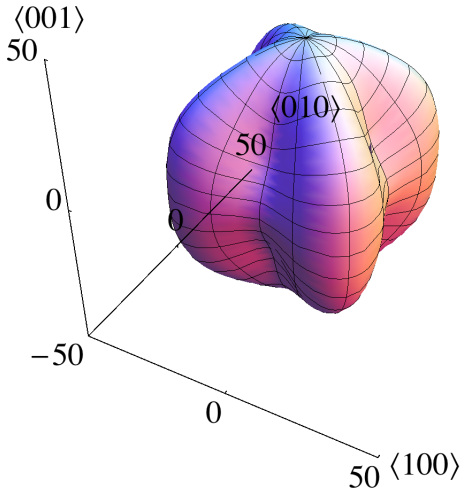

(c) Stiffness SASH for ice-0, $\mathbf{u} = \mathbf{e}_\phi$.

Figure C.3: Plots of the SASH equations for ice-0 representing the free energy and the interfacial stiffness with unit vectors $\mathbf{u} = \mathbf{e}_\theta$ and $\mathbf{u} = \mathbf{e}_\phi$ as shown.

Abbreviations

ATAT — Alloy Theoretic Automated Toolkit.

BCC — Body centred cubic.

CNT — Classical nucleation theory.

CWM — Capillary wave method.

CWT — Capillary wave theory.

FCC — Face centred cubic.

Ice-Ic — Cubic phase of ice-I.

Ice-Ih — Hexagonal phase of ice-I.

Ice-Isd — Stacking disordered phase of ice-I.

LAMMPS — Large-scale Atomic/Molecular Massively Parallel Simulator.

LJ — Lennard-Jones.

LJ-BG — Broughton and Gilmer modified LJ.

LSMC — Lattice switching Monte Carlo.

MC — Monte Carlo.

MD — Molecular dynamics.

mW — Monatomic water.

RDF — Radial distribution function.

RMS — Root mean square.

SASH — Symmetry adapted spherical harmonic.

TI — Thermodynamic integration.

x — The local simulation axis denoting the long direction of the system.

y — The local simulation axis denoting the short direction of the system.

z — The local simulation axis denoting the direction along the length of the interface.

Bibliography

[1] B. B. Laird and R. L. Davidchack, "Direct Calculation of the Crystal-Melt Interfacial Free Energy via Molecular Dynamics Computer Simulation," *The Journal of Physical Chemistry B*, vol. 109, no. 38, pp. 17802–17812, 2005.

[2] G. C. Sosso, J. Chen, S. J. Cox, M. Fitzner, P. Pedevilla, A. Zen, and A. Michaelides, "Crystal Nucleation in Liquids: Open Questions and Future Challenges in Molecular Dynamics Simulations," *Chemical Reviews*, vol. 116, no. 12, pp. 7078–7116, 2016.

[3] W. Boettinger, S. Coriell, A. Greer, A. Karma, W. Kurz, M. Rappaz, and R. Trivedi, "Solidification microstructures: recent developments, future direction," *Acta Materialia*, vol. 48, no. 1, pp. 43 – 70, 2000.

[4] J. P. Hirth, "The influence of grain boundaries on mechanical properties," *Metallurgical Transactions*, vol. 3, no. 12, pp. 3047–3067, 1972.

[5] A. Tabazadeh, Y. S. Djikaev, and H. Reiss, "Surface crystallization of supercooled water in clouds," *Proceedings of the National Academy of Sciences*, vol. 99, no. 25, pp. 15873–15878, 2002.

[6] T. Li, D. Donadio, G. Russo, and G. Galli, "Homogeneous ice nucleation from supercooled water," *Phys. Chem. Chem. Phys.*, vol. 13, no. 44, pp. 19807–19813, 2011.

[7] G. L. Stephens, S.-C. Tsay, P. W. S. Jr., and P. J. Flatau, "The Relevance of the Microphysical and Radiative Properties of Cirrus Clouds to Climate and Climatic Feedback," *Journal of the Atmospheric Sciences*, vol. 47, no. 14, pp. 1742–1754, 1990.

[8] Q. Fu and K. N. Liou, "Parameterization of the Radiative Properties of Cirrus Clouds," *Journal of the Atmospheric Sciences*, vol. 50, no. 13, pp. 2008–2025, 1992.

[9] K. E. Zachariassen and E. Kristiansen, "Ice nucleation and Antinucleation in Nature," *Cryobiology*, vol. 41, no. 4, pp. 257 – 279, 2000.

[10] T. Koop and B. Zobrist, "Parameterizations for ice nucleation in biological and atmospheric systems," *Phys. Chem. Chem. Phys.*, vol. 11, no. 46, pp. 10839–10850, 2009.

[11] M. G. Potapczuk, "Aircraft Icing Research at NASA Glenn Research Center," *Journal of Aerospace Engineering*, vol. 26, no. 2, pp. 260–276, 2013.

[12] J. J. Hoyt, M. Asta, and A. Karma, "Method for Computing the Anisotropy of the Solid-Liquid Interfacial Free Energy," *Phys. Rev. Lett.*, vol. 86, no. 24, pp. 5530–5533, 2001.

[13] M. Muschol, D. Liu, and H. Z. Cummins, "Surface-tension-anisotropy measurements of succinonitrile and pivalic acid: Comparison with microscopic solvability theory," *Phys. Rev. A*, vol. 46, no. 2, pp. 1038–1050, 1992.

[14] K.-K. Koo, R. Ananth, and W. N. Gill, "Tip splitting in dendritic growth of ice crystals," *Phys. Rev. A*, vol. 44, no. 6, pp. 3782–3790, 1991.

[15] T. Bartels-Rausch, V. Bergeron, J. H. E. Cartwright, R. Escribano, J. L. Finney, H. Grothe, P. J. Gutiérrez, J. Haapala, W. F. Kuhs, J. B. C. Pettersson, S. D. Price, C. I. Sainz-Díaz, D. J. Stokes, G. Strazzulla, E. S. Thomson, H. Trinks, and N. Uras-Aytemiz, "Ice structures, patterns, and processes: A view across the icefields," *Rev. Mod. Phys.*, vol. 84, no. 2, pp. 885–944, 2012.

[16] T. L. Malkin, B. J. Murray, C. G. Salzmann, V. Molinero, S. J. Pickering, and T. F. Whale, "Stacking disorder in ice I," *Phys. Chem. Chem. Phys.*, vol. 17, no. 1, pp. 60–76, 2015.

[17] J. Russo, F. Romano, and H. Tanaka, "New metastable form of ice and its role in the homogeneous crystallization of water," *Nat Mater*, vol. 13, no. 7, pp. 733–739, 2014.

[18] W. Ostwald, "Studies on formation and transformation of solid materials," *Z. Phys. Chem*, vol. 22, pp. 289–330, 1897.

[19] J. Russo and H. Tanaka, "The microscopic pathway to crystallization in supercooled liquids," *Scientific Reports*, vol. 2, no. 505, 2012.

[20] V. Molinero and E. B. Moore, "Water Modeled As an Intermediate Element between Carbon and Silicon," *The Journal of Physical Chemistry B*, vol. 113, no. 13, pp. 4008–4016, 2009.

[21] E. A. Engel, B. Monserrat, and R. J. Needs, "Anharmonic Nuclear Motion and the Relative Stability of Hexagonal and Cubic ice," *Phys. Rev. X*, vol. 5, no. 2, p. 021033, 2015.

[22] M. E. Tuckerman, *Statistical Mechanics: Theory and Molecular Simulation*. Oxford University Press, New York, 2012.

[23] D. Quigley, *Constant Pressure Langevin Dynamics: Theory and Application to the Study of Phase Behaviour in Core-Softened Systems*. 2005.

[24] D. Frenkel and B. Smit, *Understanding Molecular Simulation: From Algorithms to Applications*. Academic Press, 2nd ed., 2002.

[25] L. Verlet, "Computer "Experiments" on Classical Fluids. I. Thermodynamical Properties of Lennard-Jones Molecules," *Phys. Rev.*, vol. 159, no. 1, pp. 98–103, 1967.

[26] G. D. Quinlan and S. Tremaine, "On the reliability of gravitational N-body integrations," *Monthly Notices of the Royal Astronomical Society*, vol. 259, no. 3, pp. 505–518, 1992.

[27] S. Nosé, "A unified formulation of the constant temperature molecular dynamics methods," *The Journal of Chemical Physics*, vol. 81, no. 1, pp. 511–519, 1984.

[28] W. G. Hoover, "Canonical dynamics: Equilibrium phase-space distributions," *Phys. Rev. A*, vol. 31, no. 3, pp. 1695–1697, 1985.

[29] G. J. Martyna, M. L. Klein, and M. Tuckerman, "Nosé–Hoover chains: The canonical ensemble via continuous dynamics," *The Journal of Chemical Physics*, vol. 97, no. 4, pp. 2635–2643, 1992.

[30] H. C. Andersen, "Molecular dynamics simulations at constant pressure and/or temperature," *The Journal of Chemical Physics*, vol. 72, no. 4, pp. 2384–2393, 1980.

[31] G. J. Martyna, D. J. Tobias, and M. L. Klein, "Constant pressure molecular dynamics algorithms," *The Journal of Chemical Physics*, vol. 101, no. 5, pp. 4177–4189, 1994.

[32] N. Metropolis, A. W. Rosenbluth, M. N. Rosenbluth, A. H. Teller, and E. Teller, "Equation of State Calculations by Fast Computing Machines," *The Journal of Chemical Physics*, vol. 21, no. 6, pp. 1087–1092, 1953.

[33] M. P. Allen and D. J. Tildesley, *Computer Simulation of Liquids*. New York, NY, USA: Clarendon Press, 1989.

[34] S. Plimpton, "Fast Parallel Algorithms for Short-Range Molecular Dynamics," *Journal of Computational Physics*, vol. 117, no. 1, pp. 1 – 19, 1995.

[35] P. S. Pacheco, *Parallel Programming with MPI*. San Francisco, CA, USA: Morgan Kaufmann Publishers Inc., 1997.

[36] W. F. van Gunsteren and H. J. C. Berendsen, "Algorithms for macromolecular dynamics and constraint dynamics," *Molecular Physics*, vol. 34, no. 5, pp. 1311–1327, 1977.

[37] J. E. Lennard-Jones, "Cohesion," *Proceedings of the Physical Society*, vol. 43, no. 5, p. 461, 1931.

[38] J. Broughton and G. Gilmer, "Surface free energy and stress of a Lennard-Jones crystal," *Acta Metallurgica*, vol. 31, no. 6, pp. 845 – 851, 1983.

[39] R. L. Davidchack and B. B. Laird, "Direct calculation of the crystal-melt interfacial free energies for continuous potentials: Application to the Lennard-Jones system," *The Journal of Chemical Physics*, vol. 118, no. 16, pp. 7651–7657, 2003.

[40] F. H. Stillinger and T. A. Weber, "Computer simulation of local order in condensed phases of silicon," *Phys. Rev. B*, vol. 31, no. 8, pp. 5262–5271, 1985.

[41] M. Volmer and A. Weber, "Nucleus formation in supersaturated systems," *Z. phys. Chem*, vol. 119, no. 1926, 1926.

[42] R. Becker and W. Döring, "Kinetische Behandlung der Keimbildung in übersättigten Dämpfen," *Annalen der Physik*, vol. 416, no. 8, pp. 719–752, 1935.

[43] J. B. Zeldovich, "On the theory of new phase formation: cavitation," *Acta physicochim. URSS*, vol. 18, no. 1, pp. 1–22, 1943.

[44] V. I. Kalikmanov, *Classical Nucleation Theory*, pp. 17–41. Dordrecht: Springer Netherlands, 2013.

[45] D. W. Heermann, "Classical nucleation theory with a tolman correction," *Journal of Statistical Physics*, vol. 29, no. 3, pp. 631–640, 1982.

[46] P. R. ten Wolde, M. J. Ruiz-Montero, and D. Frenkel, "Numerical calculation of the rate of crystal nucleation in a Lennard-Jones system at moderate undercooling," *The Journal of Chemical Physics*, vol. 104, no. 24, pp. 9932–9947, 1996.

[47] P. R. ten Wolde, M. J. Ruiz-Montero, and D. Frenkel, "Simulation of homogeneous crystal nucleation close to coexistence," *Faraday discussions*, vol. 104, pp. 93–110, 1996.

[48] M. Santra, R. S. Singh, and B. Bagchi, "Nucleation of a Stable Solid from Melt in the Presence of Multiple Metastable Intermediate Phases: Wetting, Ostwald's Step Rule, and Vanishing Polymorphs," *The Journal of Physical Chemistry B*, vol. 117, no. 42, pp. 13154–13163, 2013.

[49] B. Peters and B. L. Trout, "Obtaining reaction coordinates by likelihood maximization," *The Journal of Chemical Physics*, vol. 125, no. 5, p. 054108, 2006.

[50] A. Ma and A. R. Dinner, "Automatic Method for Identifying Reaction Coordinates in Complex Systems," *The Journal of Physical Chemistry B*, vol. 109, no. 14, pp. 6769–6779, 2005.

[51] B. Peters, G. T. Beckham, and B. L. Trout, "Extensions to the likelihood maximization approach for finding reaction coordinates," *The Journal of Chemical Physics*, vol. 127, no. 3, p. 034109, 2007.

[52] L. Maragliano, A. Fischer, E. Vanden-Eijnden, and G. Ciccotti, "String method in collective variables: Minimum free energy paths and isocommittor surfaces," *The Journal of Chemical Physics*, vol. 125, no. 2, p. 024106, 2006.

[53] W. Lechner, C. Dellago, and P. G. Bolhuis, "Reaction coordinates for the crystal nucleation of colloidal suspensions extracted from the reweighted path ensemble," *The Journal of Chemical Physics*, vol. 135, pp. –, 2011.

[54] L. A. Fernández, V. Martín-Mayor, B. Seoane, and P. Verrocchio, "Equilibrium Fluid-Solid Coexistence of Hard Spheres," *Phys. Rev. Lett.*, vol. 108, no. 16, p. 165701, 2012.

[55] A. Laio and M. Parrinello, "Escaping free-energy minima," *Proceedings of the National Academy of Sciences*, vol. 99, no. 20, pp. 12562–12566, 2002.

[56] S. Angioletti-Uberti, M. Ceriotti, P. D. Lee, and M. W. Finnis, "Solid-liquid interface free energy through metadynamics simulations," *Phys. Rev. B*, vol. 81, no. 12, p. 125416, 2010.

[57] J. Q. Broughton and G. H. Gilmer, "Molecular dynamics investigation of the crystal-fluid interface. VI. Excess surface free energies of crystal-liquid systems," *The Journal of Chemical Physics*, vol. 84, no. 10, pp. 5759–5768, 1986.

[58] R. Handel, R. L. Davidchack, J. Anwar, and A. Brukhno, "Direct Calculation of Solid-Liquid Interfacial Free Energy for Molecular Systems: TIP4P Ice-Water Interface," *Phys. Rev. Lett.*, vol. 100, no. 3, p. 036104, 2008.

[59] R. L. Davidchack and B. B. Laird, "Direct Calculation of the Hard-Sphere Crystal/Melt Interfacial Free Energy," *Phys. Rev. Lett.*, vol. 85, no. 22, pp. 4751–4754, 2000.

[60] J. R. Espinosa, C. Vega, and E. Sanz, "The mold integration method for the calculation of the crystal-fluid interfacial free energy from simulations," *The Journal of Chemical Physics*, vol. 141, no. 13, p. 134709, 2014.

[61] J. Benet, L. G. MacDowell, and E. Sanz, "A study of the ice-water interface using the TIP4P/2005 water model," *Phys. Chem. Chem. Phys.*, vol. 16, no. 40, pp. 22159–22166, 2014.

[62] V. Privman, "Fluctuating Interfaces, Surface Tension, and Capillary Waves: An Introduction," *International Journal of Modern Physics C*, vol. 03, no. 05, pp. 857–877, 1992.

[63] S. A. Safran, *Statistical Thermodynamics of Surfaces, Interfaces, and Membranes*. Perseus Publishing Services, 1994.

[64] M. P. A. Fisher, D. S. Fisher, and J. D. Weeks, "Agreement of Capillary-Wave Theory with Exact Results for the Interface Profile of the Two-Dimensional Ising Model," *Phys. Rev. Lett.*, vol. 48, no. 5, pp. 368–368, 1982.

[65] D. S. Fisher and J. D. Weeks, "Shape of Crystals at Low Temperatures: Absence of Quantum Roughening," *Phys. Rev. Lett.*, vol. 50, no. 14, pp. 1077–1080, 1983.

[66] E. M. Blokhuis, "On the spectrum of fluctuations of a liquid surface: From the molecular scale to the macroscopic scale," *The Journal of Chemical Physics*, vol. 130, no. 1, p. 014706, 2009.

[67] M. Turner and P. Sens, "Inclusions on Fluid Membranes Anchored to Elastic Media," *Biophysical Journal*, vol. 76, no. 1, pp. 564–572, 1999.

[68] H. Kellay and J. Meunier, "Elastic properties of monolayers of soluble surfactants at oil - brine interfaces," *Journal of Physics: Condensed Matter*, vol. 8, no. 25A, p. A49, 1996.

[69] D. Jasnow, "Critical phenomena at interfaces," *Reports on Progress in Physics*, vol. 47, no. 9, p. 1059, 1984.

[70] R. E. Rozas and J. Horbach, "Capillary wave analysis of rough solid-liquid interfaces in nickel," *EPL (Europhysics Letters)*, vol. 93, no. 2, p. 26006, 2011.

[71] J. R. Morris, "Complete mapping of the anisotropic free energy of the crystal-melt interface in Al," *Phys. Rev. B*, vol. 66, no. 14, p. 144104, 2002.

[72] K. Binder and M. Müller, "Computer Simulations of Profiles of Interfaces Between Coexisting Phases: Do We Understand Their Finite Size Effects?," *International Journal of Modern Physics C*, vol. 11, no. 06, pp. 1093–1113, 2000.

[73] J. R. Morris and X. Song, "The anisotropic free energy of the Lennard-Jones crystal-melt interface," *The Journal of Chemical Physics*, vol. 119, no. 7, pp. 3920–3925, 2003.

[74] H. Gould and J. Tobochnik, *An introduction to computer simulation methods: applications to physical systems.* Reading, Mass. : Addison-Wesley, 2nd ed., 1996.

[75] J. J. Hoyt and M. Asta, "Atomistic computation of liquid diffusivity, solid-liquid interfacial free energy, and kinetic coefficient in Au and Ag," *Phys. Rev. B*, vol. 65, no. 21, p. 214106, 2002.

[76] I. Hughes and T. P. A. Hase, *Measurements and their uncertainties: a practical guide to modern error analysis.* Oxford : New York, NY: Oxford University Press, 2010.

[77] W. H. Press, S. A. Teukolsky, W. T. Vetterling, and B. P. Flannery, *Numerical Recipes 3rd Edition: The Art of Scientific Computing.* New York, NY, USA: Cambridge University Press, 3rd ed., 2007.

[78] D. Birkes and Y. Dodge, *Alternative Methods of Regression.* John Wiley & Sons, Inc., 1993.

[79] P. J. Steinhardt, D. R. Nelson, and M. Ronchetti, "Icosahedral bond Orientational Order in Supercooled Liquids," *Phys. Rev. Lett.*, vol. 47, no. 18, pp. 1297–1300, 1981.

[80] P. J. Steinhardt, D. R. Nelson, and M. Ronchetti, "Bond-orientational order in liquids and glasses," *Phys. Rev. B*, vol. 28, no. 2, pp. 784–805, 1983.

[81] P. R. ten Wolde, M. J. Ruiz-Montero, and D. Frenkel, "Numerical Evidence for bcc ordering at the Surface of a Critical fcc Nucleus," *Phys. Rev. Lett.*, vol. 75, no. 14, pp. 2714–2717, 1995.

[82] A. H. Nguyen and V. Molinero, "Identification of Clathrate Hydrates, Hexagonal Ice, Cubic Ice, and Liquid Water in Simulations: the CHILL+ Algorithm," *The Journal of Physical Chemistry B*, vol. 119, no. 29, pp. 9369–9376, 2015.

[83] E. B. Moore, E. de la Llave, K. Welke, D. A. Scherlis, and V. Molinero, "Freezing, melting and structure of ice in a hydrophilic nanopore," *Phys. Chem. Chem. Phys.*, vol. 12, no. 16, pp. 4124–4134, 2010.

[84] W. R. Fehlner and S. H. Vosko, "A product representation for cubic harmonics and special directions for the determination of the Fermi surface and related properties," *Canadian Journal of Physics*, vol. 54, no. 21, pp. 2159–2169, 1976.

[85] S. L. Altmann and A. P. Cracknell, "Lattice Harmonics I. Cubic Groups," *Rev. Mod. Phys.*, vol. 37, no. 1, pp. 19–32, 1965.

[86] M. Asta, J. J. Hoyt, and A. Karma, "Calculation of alloy solid-liquid interfacial free energies from atomic-scale simulations," *Phys. Rev. B*, vol. 66, no. 10, p. 100101, 2002.

[87] E. J. W. Whittaker, *Crystallography: An Introduction for Earth Science (and Other Solid State) Students.* Pergamon Press, Oxford, 1981.

[88] M. Masi, "On compressive radial tidal forces," *American Journal of Physics*, vol. 75, no. 2, pp. 116–124, 2007.

[89] A. van de Walle, M. Asta, and G. Ceder, "The alloy theoretic automated toolkit: A user guide," *Calphad*, vol. 26, no. 4, pp. 539 – 553, 2002.

[90] A. van de Walle, Q. Hong, L. Miljacic, C. B. Gopal, S. Demers, G. Pomrehn, A. Kowalski, and P. Tiwary, "*Ab initio* calculation of anisotropic interfacial excess free energies," *Phys. Rev. B*, vol. 89, no. 18, p. 184101, 2014.

[91] D. Y. Sun, M. I. Mendelev, C. A. Becker, K. Kudin, T. Haxhimali, M. Asta, J. J. Hoyt, A. Karma, and D. J. Srolovitz, "Crystal-melt interfacial free energies in hcp metals: A molecular dynamics study of Mg," *Phys. Rev. B*, vol. 73, no. 2, p. 024116, 2006.

[92] J. D. H. Donnay and D. Harker, "A new law of crystal morphology extending the law of Bravais," *Am. Mineral*, vol. 22, no. 5, pp. 446–467, 1937.

[93] R. Docherty, G. Clydesdale, K. J. Roberts, and P. Bennema, "Application of Bravais-Friedel-Donnay-Harker, attachment energy and Ising models to predicting and understanding the morphology of molecular crystals," *Journal of Physics D: Applied Physics*, vol. 24, no. 2, p. 89, 1991.

[94] D. Quigley, D. Alfè, and B. Slater, "Communication: On the stability of ice 0, ice i, and Ih," *The Journal of Chemical Physics*, vol. 141, no. 16, p. 161102, 2014.

[95] J. R. Espinosa, C. Vega, C. Valeriani, and E. Sanz, "Seeding approach to crystal nucleation," *The Journal of Chemical Physics*, vol. 144, no. 3, p. 034501, 2016.

[96] D. Turnbull, "Formation of Crystal Nuclei in Liquid Metals," *Journal of Applied Physics*, vol. 21, no. 10, pp. 1022–1028, 1950.

[97] S. R. Wilson, K. G. S. H. Gunawardana, and M. I. Mendelev, "Solid-liquid interface free energies of pure bcc metals and B2 phases," *The Journal of Chemical Physics*, vol. 142, no. 13, p. 134705, 2015.

[98] D. T. Limmer and D. Chandler, "Phase diagram of supercooled water confined to hydrophilic nanopores," *The Journal of Chemical Physics*, vol. 137, no. 4, p. 044509, 2012.

[99] J. R. Espinosa, C. Vega, and E. Sanz, "Ice-Water Interfacial Free Energy for the TIP4P, TIP4P/2005, TIP4P/Ice, and mW Models As Obtained from the Mold Integration Technique," *The Journal of Physical Chemistry C*, vol. 120, no. 15, pp. 8068–8075, 2016.

[100] L. Gránásy, T. Pusztai, and P. F. James, "Interfacial properties deduced from nucleation experiments: A Cahn–Hilliard analysis," *The Journal of Chemical Physics*, vol. 117, no. 13, pp. 6157–6168, 2002.

[101] J. R. Espinosa, E. Sanz, C. Valeriani, and C. Vega, "Homogeneous ice nucleation evaluated for several water models," *The Journal of Chemical Physics*, vol. 141, no. 18, p. 18C529, 2014.

[102] Y. Mu, A. Houk, and X. Song, "Anisotropic Interfacial Free Energies of the Hard-Sphere Crystal "Melt Interfaces"," *The Journal of Physical Chemistry B*, vol. 109, no. 14, pp. 6500–6504, 2005.

[103] A. Hudait, S. Qiu, L. Lupi, and V. Molinero, "Free Energy Contributions and Structural Characterization of Stacking Disordered Ices," *Phys. Chem. Chem. Phys.*, vol. 18, no. 14, pp. 9544–9553, 2016.

[104] T. L. Malkin, B. J. Murray, A. V. Brukhno, J. Anwar, and C. G. Salzmann, "Structure of ice crystallized from supercooled water," *Proceedings of the National Academy of Sciences*, vol. 109, no. 4, pp. 1041–1045, 2012.

[105] W. F. Kuhs, C. Sippel, A. Falenty, and T. C. Hansen, "Extent and relevance of stacking disorder in "ice Ic"," *Proceedings of the National Academy of Sciences*, vol. 109, no. 52, pp. 21259–21264, 2012.

[106] W. F. Kuhs, G. Genov, D. K. Staykova, and T. Hansen, "Ice perfection and onset of anomalous preservation of gas hydrates," *Phys. Chem. Chem. Phys.*, vol. 6, no. 21, pp. 4917–4920, 2004.

[107] D. Quigley, "Communication: Thermodynamics of stacking disorder in ice nuclei," *The Journal of Chemical Physics*, vol. 141, no. 12, p. 121101, 2014.

[108] D. Rozmanov and P. G. Kusalik, "Temperature dependence of crystal growth of hexagonal ice (Ih)," *Physical Chemistry Chemical Physics*, vol. 13, no. 34, pp. 15501–15511, 2011.

[109] H. Nada and J. P. J. M. van der Eerden, "An intermolecular potential model for the simulation of ice and water near the melting point: A six-site model of H2O," *The Journal of Chemical Physics*, vol. 118, no. 16, pp. 7401–7413, 2003.

[110] M. A. Carignano, P. B. Shepson, and I. Szleifer, "Molecular dynamics simulations of ice growth from supercooled water," *Molecular Physics*, vol. 103, no. 21-23, pp. 2957–2967, 2005.

[111] S. Choi, E. Jang, and J. S. Kim, "In-layer stacking competition during ice growth," *The Journal of Chemical Physics*, vol. 140, no. 1, p. 014701, 2014.

[112] A. Haji-Akbari and P. G. Debenedetti, "Direct calculation of ice homogeneous nucleation rate for a molecular model of water," vol. 112, no. 34, pp. 10582–10588, 2015.

[113] V. C. Weiss, M. Rullich, C. Köhler, and T. Frauenheim, "Kinetic aspects of the thermostatted growth of ice from supercooled water in simulations," *The Journal of Chemical Physics*, vol. 135, no. 3, p. 034701, 2011.

[114] E. González Solveyra, E. de la Llave, D. A. Scherlis, and V. Molinero, "Melting and Crystallization of Ice in Partially Filled Nanopores," *The Journal of Physical Chemistry B*, vol. 115, no. 48, pp. 14196–14204, 2011.

[115] J. C. Johnston and V. Molinero, "Crystallization, Melting, and Structure of Water Nanoparticles at Atmospherically Relevant Temperatures," *Journal of the American Chemical Society*, vol. 134, no. 15, pp. 6650–6659, 2012.

[116] A. Reinhardt and J. P. K. Doye, "Free energy landscapes for homogeneous nucleation of ice for a monatomic water model," *The Journal of Chemical Physics*, vol. 136, no. 5, p. 054501, 2012.

[117] S. Habershon, T. E. Markland, and D. E. Manolopoulos, "Competing quantum effects in the dynamics of a flexible water model," *The Journal of Chemical Physics*, vol. 131, no. 2, p. 024501, 2009.

[118] S. Habershon and D. E. Manolopoulos, "Free energy calculations for a flexible water model," *Phys. Chem. Chem. Phys.*, vol. 13, no. 44, pp. 19714–19727, 2011.

[119] E. B. Moore and V. Molinero, "Is it cubic? Ice crystallization from deeply supercooled water," *Physical Chemistry Chemical Physics*, vol. 13, no. 44, pp. 20008–20016, 2011.

[120] B. J. Murray, S. L. Broadley, T. W. Wilson, S. J. Bull, R. H. Wills, H. K. Christenson, and E. J. Murray, "Kinetics of the homogeneous freezing of water," *Phys. Chem. Chem. Phys.*, vol. 12, no. 35, pp. 10380–10387, 2010.

[121] S. Masayasu, S. Hiroshi, and S. Syûzô, "Calorimetric Study of the Glassy State. IV. Heat Capacities of Glassy Water and Cubic Ice," *Bulletin of the Chemical Society of Japan*, vol. 41, no. 11, pp. 2591–2599, 1968.

[122] J. E. Shilling, M. A. Tolbert, O. B. Toon, E. J. Jensen, B. J. Murray, and A. K. Bertram, "Measurements of the vapor pressure of cubic ice and their implications for atmospheric ice clouds," *Geophysical Research Letters*, vol. 33, no. 17, pp. n/a–n/a, 2006.

[123] O. Yamamuro, M. Oguni, T. Matsuo, and H. Suga, "Heat capacity and glass transition of pure and doped cubic ices," *Journal of Physics and Chemistry of Solids*, vol. 48, no. 10, pp. 935 – 942, 1987.

[124] E. Mayer and A. Hallbrucker, "Cubic ice from liquid water," *Nature*, vol. 325, no. 6105, pp. 601–602, 1987.

[125] Y. P. Handa, D. D. Klug, and E. Whalley, "Energies of the phases of ice at low temperature and pressure relative to ice Ih," *Canadian Journal of Chemistry*, vol. 66, no. 4, pp. 919–924, 1988.

[126] C. G. Salzmann, E. Mayer, and A. Hallbrucker, "Thermal properties of metastable ices IV and XII: comparison, isotope effects and relative stabilities," *Phys. Chem. Chem. Phys.*, vol. 6, no. 6, pp. 1269–1276, 2004.